KU LEUVEN

ARENBERG DOCTORAL SCHOOL
Faculty of Engineering Science

Operation and control of power systems with low synchronous inertia

Pieter Tielens

Supervisor:
Prof. dr. ir. D. Van Hertem

Co-supervisor:
Prof. dr. ir. R. Belmans

Dissertation presented in partial fulfillment of the requirements for the degree of Doctor in Engineering Science (PhD): Electrical Engineering

November 2017

Operation and control of power systems with low synchronous inertia

Pieter TIELENS

Examination committee:
Prof. dr. ir. P. Wollants, chair
Prof. dr. ir. D. Van Hertem, supervisor
Prof. dr. ir. R. Belmans, co-supervisor
Prof. dr. ir. J. Driesen
Prof. dr. ir. J. Poortmans
Prof. dr. ir. W. D'haeseleer
Prof. dr. ir. M.A.M.M. van der Meijden
(Delft University of Technology)
Dr. ing. T. Ackermann
(Energynautics GmbH)

Dissertation presented in partial fulfillment of the requirements for the degree of Doctor in Engineering Science (PhD): Electrical Engineering

November 2017

© 2017 KU Leuven – Faculty of Engineering Science
Uitgegeven in eigen beheer, Pieter Tielens, Kasteelpark Arenberg 10 B2445, B-3001 Heverlee (Belgium)

Alle rechten voorbehouden. Niets uit deze uitgave mag worden vermenigvuldigd en/of openbaar gemaakt worden door middel van druk, fotokopie, microfilm, elektronisch of op welke andere wijze ook zonder voorafgaande schriftelijke toestemming van de uitgever.

All rights reserved. No part of the publication may be reproduced in any form by print, photoprint, microfilm, electronic or any other means without written permission from the publisher.

Voorwoord

"Pleasure in the job puts perfection in the work."
- Aristotle

Waar het voorwoord voor iedere lezer meestal het begin inluidt van een doctoraatstekst, betekent het schrijven ervan voor mij net het einde van een belangrijke periode. Het biedt me de gelegenheid om even terug te blikken op mijn tijd als doctoraatsstudent en hierbij alle mensen te bedanken die dit werk mogelijk hebben gemaakt.

In de eerste plaats wil ik mijn promotor, professor Dirk Van Hertem, van harte bedanken. Dirk, zonder jouw kennis, advies en enthousiasme was dit boekje nooit tot stand gekomen. Daarom, bedankt om niet alleen promotor te zijn van dit werk, maar vooral van de weg ernaar toe. Bedankt voor je menselijke aanpak, je vertrouwen en je beschikbaarheid tijdens en buiten de werkuren (letterlijk 24/7).

Verder wil ik mijn co-promotor, professor Ronnie Belmans, bedanken. Bedankt voor alle ondersteuning, voor het gedetailleerd nalezen van deze tekst en de waardevolle commentaar op mijn werk. Een speciaal woordje van dank gaat ook uit naar professor Johan Driesen. Als promotor van mijn masterthesis heeft u de kiem van dit doctoraat gelegd. Bedankt om ook nu in de jury te zetelen en doorheen de jaren mijn doctoraat op te volgen. De andere leden van de jury, professor Jef Poortmans, professor Mart van der Meijden en professor William D'haeseleer bedank ik voor alle pertinente vragen en opmerkingen, alsook professor Patrick Wollants voor het voorzitterschap.

I would also like to express my gratitude to Dr. Thomas Ackermann for his valuable comments on my work and for giving me the opportunity to be part of the scientific committee of the wind integration workshops.

Zoals het citaat hierboven stelt, is een aangename werksfeer uitermate belangrijk om iets te kunnen verwezenlijken. Daarom wil ik alle collega's van ELECTA bedanken voor de fijne samenwerking. In het bijzonder de mensen van de Power groep: bedankt Steven, Willem, Hakan, Kristof, Jef, Simon, Evelyn, Robert, Thomas, Tom en Alejandro voor al jullie hulp en advies, voor de ontspannende koffiepauzes, voor de aangename en inspirerende discussies tijdens en na de Kundursessies en voor de avontuurlijke kanotocht tussen de Canadese beren. Alle leden van de IEEE student branch wil ik verder bedanken voor de vele leerrijke activiteiten en toffe reizen. Words of appreciation go also to Simon, Barry, Willem, Steven, Hakan, Jayachandra, Mian, Mudar, Firew and Tuan Anh for our scientific collaboration on different research papers.

Verder wil ik de mensen van het secretariaat en het labo nog bedanken. Bedankt Katleen, Nathalie, Veronica en Veerle voor alle mogelijke ondersteuning, voor het reguliere ‘tooghangen’ en toffe babbels tijdens de vele koffiepauzes. Ook Roland, Johan en Luc, bedankt voor alle technische en praktische hulp.

Bedankt ook aan alle mensen van het LAL-forum, een hechte vriendengroep die ontstaan is tijdens het middelbaar onderwijs en doorheen de jaren samen is gebleven. De vele activiteiten en samenkomsten zorgden steeds voor de nodige ontspanning. Ik kijk alvast uit naar de volgende LAL-weekenden, uitstapjes, trouwpartijen en andere feesten. Moge er nog velen volgen!

Mijn voormalige huisgenoten van Villa Leopolda verdienen ook een speciale vermelding in dit voorwoord. Jullie waren natuurlijk meer dan gewoon huisgenoten. Ik denk dan ook nog vaak met weemoed terug aan de Villa-feestjes, de legendarische shoppingmaandagen, het samen koken en plezier maken. Het klinkt allemaal banaal, maar het maakte mijn periode als Leuvenaar een tijd om nooit te vergeten. Bedankt Ruben, Kenny, Paul, Fleur en Philippe!

Ook wens ik heel oprecht mijn ouders en familie te bedanken voor alles wat ze voor mij de voorbije jaren hebben gedaan. Voor op de juiste momenten al dan niet te vragen hoe het met mijn doctoraat gaat, voor alle aanmoedigingen, steun en kansen die ik van jullie heb gekregen, een dikke merci!

Tot slot wil ik natuurlijk Anne bedanken. Bedankt voor je geduld, liefde en steun. Het is een rijkdom om met jou het leven te mogen delen. Laten we samen uitkijken naar alles wat nog volgt!

Pieter Tielens
November 2017

Abstract

Power systems are facing some tremendous challenges for the next decades to come. While dealing with an ageing infrastructure and an ever increasing demand for electric power, the projected increase of electricity generation coming from renewable energy sources will put an even higher stress to the already highly loaded power systems.

From a system perspective, renewable electricity generation behaves quite differently from traditional, centralized generation facilities equipped with synchronous generators. Contrary to these generators, most of the renewable energy units do not contribute to the total inertia perceived by the system. This inertia is often considered as one of the vital system parameters upon which the synchronized operation of current day power systems is based. It determines the frequency response with respect to inequalities in the overall power balance. The lower the inertia, the more nervous the grid frequency reacts on abrupt changes in generation and load patterns. As it can be expected that more and more conventional power plants will be replaced by renewable energy generation, such as photovoltaic installations and wind farms, the power system will evolve to a system that will have to be less dependent on this physical inertia. New approaches to control the grid and its components are therefore required.

This work covers the complete transition from a traditional power system towards an inertialess, converter based system. The focus lies in understanding the role of synchronous inertia and to provide potential pathways to improve overall system behaviour. To this end, both the quantification and measurement of inertia, together with its impact on the different forms of power system stability, are assessed in detail. Furthermore, distinct control strategies for low inertia systems as a whole, as well as for the provision of so-called ‘virtual inertia’ by renewable energy sources, are presented and evaluated. By applying these advanced controllers to deliver virtual inertia, the use of the otherwise masked (kinetic) energy stored in converter connected units is facilitated in order to improve system stability. Finally, also future approaches for the operation and control of large-scale power systems with zero synchronous inertia are given.

Samenvatting

Het huidig elektriciteitsnet komt in de volgende decennia voor enorme uitdagingen te staan. Naast een verouderde infrastructuur en een steeds stijgende vraag naar elektrische energie, zal de voorspelde toename van elektriciteitsproductie uit hernieuwbare bronnen het elektriciteitsnet nog meer belasten.

Vanuit een systeemperspectief verschillen de hernieuwbare energiebronnen, zoals zon- en windenergie, namelijk sterk van de traditionele, gecentraliseerde eenheden. In tegenstelling tot deze eenheden, draagt het merendeel van de hernieuwbare energiebronnen niet bij tot de inertie van het net. Deze inertie wordt vaak beschouwd als één van de fundamentele systeemparameters waarop de gesynchroniseerde werking van ons huidig net is gebaseerd. Het bepaalt in grote mate de frequentierespons na een onevenwicht in generatie en vraag van elektrisch vermogen. Naarmate de inertie verlaagt, zal de frequentie sneller fluctueren na abrupte wijzigingen in last- en generatiepatronen. Indien meer en meer conventionele eenheden vervangen worden door productie uit hernieuwbare energiebronnen, zal ons toekomstig elektriciteitsnet minder afhankelijk moeten worden van de inertie van synchrone generatoren. Hiervoor zijn nieuwe controletechnieken voor het net en zijn componenten noodzakelijk.

Dit doctoraat analyseert de complete transitie van een traditioneel naar een omvormer gebaseerd systeem. De rol, kwantificering en meting van de inertie, samen met de invloed ervan op verschillende vormen van netstabiliteit, zijn hierbij gedetailleerd besproken. Daarnaast worden ook verschillende controlestrategieën voor netten met lage inertie, alsook voor de levering van zogenaamde ‘virtuele inertie’ door hernieuwbare energiebronnen gepresenteerd en geëvalueerd. Met behulp van deze geavanceerde controlemechanismen kan de (kinetische) energie opgeslagen in de hernieuwbare energiebronnen aangewend worden om de stabiliteit van het net te verbeteren. Tenslotte reikt dit werk ook algemene controleprincipes aan voor de uitbating en werking van grootschalige inertieloze elektriciteitsnetten.

List of Abbreviations

AC	Alternating Current
AGC	Automatic Generation Control
CCA	Critical Clearing Angle
CCGT	Combined Cycle Gas Turbine
CCT	Critical Clearing Time
CHP	Combined Heat and Power
CIGRE	Conseil International des Grands Réseaux Électriques
CSB	Current Source Based
DC	Direct Current
DFIG	Doubly Fed Induction Generator
DG	Distributed Generation
EAC	Equal Area Criterion
EMF	Electromotive Force
EMT	Electromagnetic Transient
ENTSO-E	European Network of Transmission System Operators for Electricity
EU	European Union
FFR	Fast Frequency Response
FRT	Fault Ride Through
GB	Gear Box
Gm	Gain Margin

GSC	Grid Side Converter
HVDC	High Voltage Direct Current
IEEE	Institute for Electrical and Electronics Engineers
IG	Induction Generator
MPPT	Maximum Power Point Tracking
OCGT	Open Cycle Gas Turbine
PCC	Point of Common Coupling
PLL	Phase Locked Loop
PMSG	Permanent Magnet Synchronous Generator
PSS	Power System Stabilizer
PV	Photovoltaic
PWM	Pulse Width Modulation
RES-e	Renewable Energy Sources for electricity
RfG	Requirements for Generators
RHC	Receding Horizon Control
ROCOF	Rate Of Change Of Frequency
SCADA	Supervisory Control And Data Acquisition
SCR	Short Circuit Ratio
SG	Synchronous Generator
SMIB	Single Machine Infinite Bus
SOGI	Second Order Generalized Integrator
SRF	Synchronous Reference Frame
TSO	Transmission System Operator
UC	Unit Commitment
VSB	Voltage Source Based
VSC	Voltage Source Converter

List of Symbols, Subscripts and Superscripts

Symbols

β	Pitch angle
δ	Electrical angle
λ	Tip speed ratio
ω	Rotational speed
τ	Time constant
θ	Mechanical angle
φ	Phase angle between voltage and current
c	Capacitance
E	Energy
f	Frequency
H	Inertia constant
J	Moment of inertia
l	Inductance
P	Active power
p	Pole pairs
R	Droop constant/Radius

r	Resistance
S	Apparent power
s	Laplace operator
T	Torque
u	Voltage
v	Speed

Subscripts

e	Electrical
G	Generated
g	Grid
L	Load
m	Mechanical
V	Virtual
0	Rated
COI	Centre Of Inertia
cv	Converter
d	Direct
gen	Generator
kin	Kinetic
q	Quadrature
ss	Steady state
sys	(Power) System
wt	Wind turbine
w	Wind

Superscripts

$*$	Reference

Contents

Abstract **iii**

Contents **xi**

List of Figures **xvii**

List of Tables **xxv**

1 Introduction **1**

1.1 Context and motivation 1

1.2 Scope and objectives of the work 6

1.3 Outline 8

2 Inertia in power systems **11**

2.1 Introduction 11

2.2 Basic considerations: inertia from a power system perspective . 12

2.2.1 Swing equation and inertia of a single synchronous machine 12

2.2.2 System inertia in a traditional power system 15

2.2.3 System inertia in future power systems 18

2.3 Quantification of resources providing inertia 23

2.3.1 Conventional power plants 23

2.3.2 Synchronous condensers 24
2.3.3 Distributed generation units 24
2.3.4 Power system load 30
2.4 Estimating available system inertia 31
2.4.1 Retroactive approach: analysing frequency transients . . 31
2.4.2 Real time inertia estimation 34
2.5 Conclusion 36

3 Relevance of inertia in power system operation and control 37

3.1 Introduction 37
3.2 Inertia and power system stability 38
3.2.1 Time scales of power system dynamics 38
3.2.2 Stability and control actions of interest 40
3.3 Impact of inertia on rotor angle stability 41
3.3.1 Power system modelling and methods of analysis 41
3.3.2 Inertia and transient stability 45
3.3.3 Inertia and small-signal stability 50
3.4 Impact of inertia on frequency stability 53
3.4.1 Mechanisms for frequency stability and control 53
3.4.2 Frequency and ROCOF operating ranges 56
3.4.3 Inertial response 59
3.4.4 Primary control action 61
3.5 Reduced inertia: how low can we go? 66
3.5.1 Minimum inertia for the continental Europe and Nordic power system 67
3.5.2 Inertia and share of converter connected generation . . . 69
3.6 Options to operate a system with low synchronous inertia . . . 70
3.7 Conclusion 72

4 Control and modelling of converter connected units 73

4.1 Introduction 73

4.2 General control structure 74

4.2.1 Overview 74

4.2.2 Classification of GSC control 76

4.3 Current source based (CSB) control of grid side converters . . . 79

4.3.1 Control implementation 79

4.3.2 Grid synchronization and frequency estimation 81

4.4 Voltage source based (VSB) control of grid side converters . . . 89

4.4.1 Control concept 89

4.4.2 Control implementation 90

4.5 Wind turbine modeling 92

4.5.1 Aerodynamic model 93

4.5.2 Two mass mechanical model & filter 94

4.5.3 Pitch controller 95

4.5.4 Maximum Power Point Tracking (MPPT) 96

4.6 Conclusion 99

5 Inertia support by converter connected units 101

5.1 Introduction 101

5.2 Quantifying available energy buffers 102

5.3 Inertia support in an optimal operating point: wind power . . . 105

5.3.1 Virtual inertia control 107

5.3.2 Fast frequency response control 110

5.4 Inertia support in a deloaded operating point: deloading wind and PV units 114

5.5 Transfer of inertia by HVDC links 117

5.5.1 Inertia support by HVDC point-to-point links 117

5.5.2 Potential of HVDC link energy storage in inertia support 121
5.5.3 Inertia support within HVDC grids 123
5.6 Large scale implementation of inertia support 124
5.6.1 Inertia support within current grid codes 125
5.6.2 Future pathways for inertia support 127
5.6.3 Discussion & Guidelines for TSOs 133
5.7 Conclusion 134

6 Receding horizon control of wind power to provide frequency regulation 135

6.1 Introduction 135
6.2 Motivation and methodology 136
6.3 Convex formulation of wind turbine and power system model . 137
6.3.1 Wind turbine model 138
6.3.2 Power system model 141
6.4 Potential of wind power kinetic reserves to damp frequency variations 142
6.5 Receding horizon controller 145
6.6 Simulation results 146
6.6.1 Random load profile 146
6.6.2 Influence of control parameters and load forecast errors 148
6.6.3 Multiple turbines with variable wind speed profile . . . 150
6.7 Discussion 152
6.8 Conclusion 153

7 Pathways to a converter based power system 155

7.1 Introduction 155
7.2 From synchronous machine based towards an empty grid 156

7.3 Limits to provision of inertia support by CSB converters 157
7.3.1 Test system and methodology 157
7.3.2 Minimum required synchronous inertia and SCR to deliver virtual inertia support 159
7.3.3 Discussion 163
7.4 Providing virtual inertia by VSB converters 165
7.4.1 Swing equation emulation 165
7.4.2 Discussion 167
7.5 Converter based test system 168
7.6 Conclusion 172

8 Conclusion 173

8.1 General summary and conclusions 173
8.2 Recommendations to different stakeholders 175
8.3 Future work 176

A Power system and power plant modelling 179

A.1 Classical multi-machine system representation 179
A.2 Aggregated single machine equivalent for load-frequency studies 180
A.3 Turbine and governor models 182

B System data 184

B.1 Test system 184
B.2 Wind turbine model 187
B.3 HVDC model 187

Bibliography 189

Curriculum Vitae 211

List of Figures

1.1 RES-e share of installed capacity and electricity generation within the EU-28 member states [1, 2, 3] 2

1.2 Projection for 2050 of the installed capacity and electricity generation within the EU-28 member states, converter connected generation is coloured in grey [2] 3

1.3 High-level comparison of present and future power systems . . 5

1.4 Operational security challenges associated with the distinct RES-e (wind and PV) characteristics 7

1.5 Outline of the work, main contributions are coloured in grey . . 8

2.1 Schematic example of the main elements within a drive system of a thermal unit with three pressure stages (HP, IP and LP), the synchronous machine is equipped with a rotating exciter . . 13

2.2 Representation of an elementary three-phase, two-pole synchronous generator (generator convention) 14

2.3 Synchronization mechanism in a small power system ($H_1 = 6\ s$, $H_2 = 3\ s$, $H_3 = 9\ s$ and $H_4 = 3\ s$) 16

2.4 Inertia and (kinetic) energy storage in power systems 19

2.5 (Kinetic) energy exchange in traditional and future power systems after a power imbalance 22

2.6 Inertia constants for conventional power plants (derived from data in [4]) 24

2.7 Interfacing technology for (distributed) generation 25

2.8 Common wind turbine topologies (GB: Gearbox) 26

2.9 Inertial response for a fixed speed wind turbine using an induction generator, parameters are taken from [5] 28

2.10 Retroactive approach 32

2.11 Estimation of historic kinetic energy in Sweden, Finland and Norway [6] 34

2.12 Kinetic energy in the Nordic system for a week in June (2015) [6] 35

3.1 Different time frames of power system phenomena and controls in today's power system [7] (VC: Voltage Control, ULTC: Under Load Tap Changer, FACTS: Flexible AC Transmission Systems) 39

3.2 Classification of power system stability (Types of stability of interest are coloured in grey) [8] 40

3.3 Equal area criterion for a three-phase fault on a SMIB system . 44

3.4 Critical clearing time in function of inertia for the network and fault considered in Figure 3.3(a) ($P_m = 0.8\, p.u.$ and $\delta_0 = 0.594\, rad$) 45

3.5 Critical clearing times for a simplified two area system in function of inertia 46

3.6 Transient stability assessment after a three-phase fault on the modified test system (system base is taken equal to the total synchronous generator capacity of the base case) 48

3.7 Eigenvalue loci of the electro-mechanical modes for the two area system as depicted in Figure 3.5(a). $H_1 = 4\ s$ and H_2 is varied from 4 to 8 s in steps of 0.5 s. 51

3.8 Typical frequency response after a substantial loss in active power generation 55

3.9 Frequency capability curve for synchronous areas within ENTSO-E (a) and North American Electric Reliability Corporation (NERC) (b) 57

3.10 Inertial response: Rate of change of frequency (a) and frequency (b) at the center of inertia after a power imbalance 60

3.11 Frequency response due to primary control action (a) and minimum frequency in function of inertia (b) ($\Delta P_L = 0.1\ p.u.$, $R_{sys} = 0.05$, $D_{sys} = 1$ and $\tau_{sys} = 0.8\ s$) 61

3.12 Variation of frequency control parameters in order to keep $f_{min} \geq$ 49 Hz (○) and 49.2 Hz (◇) 62

3.13 Frequency (a) and turbine response (b) for three different type of power plants ($\Delta P_L = 0.1$ $p.u.$, $R_{sys} = 0.05$, $D_{sys} = 1$ and $H_{sys} = 8$ s) 64

3.14 Minimum frequency and |ROCOF| after a load step of $\Delta P_L = 0.10$ $[p.u.]$ ($D_{sys} = 1$, $R_{sys} = 0.05$) 65

3.15 Minimum required kinetic energy in function of maximum allowed ROCOF 68

3.16 Minimum required kinetic energy in function of maximum τ_{sys} in order to $f \geq f_{min}$ 69

3.17 Inertia in function of the penetration of converter connected generation 69

3.18 Options to operate system with high penetration of converter connected generation: scenario A and B (see Figure 3.17) 71

4.1 Overview of the control structure of a PV, Wind, HVDC and energy storage system (CH: chopper, GB: gearbox, GSC: grid side converter, MPPT: maximum power point tracking) 74

4.2 Simplified model of PV and wind (Type 4) GSC converter for power system stability studies 76

4.3 Classification of GSC control approaches: simplified representation (based on [9]) 77

4.4 Simplified control model of GSC: current source based control . 79

4.5 Voltage vector representation in the dq synchronous reference frame 80

4.6 General structure of PLL [10] 82

4.7 Block diagram of SRF-PLL [10] 84

4.8 Block diagram of DSOGI-PLL/FLL [11, 10] 85

4.9 Frequency response of DSOGI ($k = \sqrt{2}$ to obtain a good trade-off between settling time and overshoot) [10] 85

4.10 Voltage waveforms as input to PLL/FLL: frequency drop with ROCOF of 4 Hz/s applied at t=0.5 s 86

4.11 Frequency and ROCOF measurements for the voltages given in Figure 4.10 ($\tau_s = 100\ ms$), the results of the SRF-PLL are not given for the case of unbalanced voltages due to the high oscillating measurements 87

4.12 Comparison of the mean absolute error of the frequency measurements in function of the total settling time (with $k = \sqrt{2}$, the settling time of the DSOGI loop is fixed, equal to 18 ms) . 88

4.13 Power control of voltage-source base converter connected to a power system 89

4.14 Simplified control model of GSC: voltage source based control . . 91

4.15 Block diagram of wind turbine model 93

4.16 Power coefficient as a function of β and λ 94

4.17 Block diagram of pitch controller (AWU: Anti-windup) 96

4.18 Power-speed control curves for MPPT and ideal operation. The latter connects the points of highest efficiency of the power-speed curves corresponding to a fixed wind speed (shown in grey) . . 96

4.19 Power, rotor speed and pitch angle in function of wind speed . 97

4.20 Wind turbine active power, speed and pitch angle for a varying wind profile 98

5.1 Overview of available energy buffers in converter connected units (a) and the required exchanged energy during a frequency transient (b) 103

5.2 Test system: Frequency response after the outage of G_4 (27MW) with and without G_3 providing synchronous inertia (equivalent converter power is constant during frequency transient, equal to 50 MW) 106

5.3 Virtual inertia control 107

5.4 Results for a wind farm equipped with a virtual inertia controller ($v_w = 10\ \frac{m}{s}$ and $\tau_V = 0.2\ s$), wind farm covers 30% of total load 108

5.5 Influence of virtual inertia control on ROCOF (Assuming that the converter can be overloaded by 10%) 109

5.6 Results for a wind farm equipped with a virtual inertia controller ($v_w = 14\ \frac{m}{s}$, $H_V = 10\ s$ and $\tau_V = 0.2\ s$), wind farm covers 60% of total load 109

5.7 Fast frequency response control 110

5.8 Results for a wind farm equipped with a fast frequency response controller ($v_w = 10\ \frac{m}{s}$, $t_{up} = 8\ s$, $P_{up} = 0.05\ p.u.$ and $P_{down} = 0.025\ p.u.$), controller is triggered at 49.8 Hz 111

5.9 Results for a wind farm equipped with a fast frequency response controller ($v_w = 10\ \frac{m}{s}$, $t_{up} = 1\ s$, $P_{up} = 0.1\ p.u.$ and $P_{down} = 0.05\ p.u.$) 111

5.10 Correlation between FFR control paramters 112

5.11 Droop and virtual inertia control 114

5.12 Results for converter units equipped with droop and virtual inertia support (power imbalance of 27 MW at t = 0 s) 114

5.13 Providing a 10% power margin by underspeeding (A), pitching (B) or overspeeding (C) 115

5.14 Inertia support by a PV unit [12] 116

5.15 Inertia support from system B to A by point-to-point HVDC links: control overview 118

5.16 Results strategy 1 119

5.17 Results strategy 2 120

5.18 Required H_{DC} to deliver inertia support 122

5.19 Inertia support by HVDC grids 123

5.20 Active power frequency response characteristic according to ENTSO-E RfG network code (type C) [13] 125

5.21 Assumed decrease of inertia as a function of the penetration of converter connected generation (without any support) 128

5.22 Results case 1: Deloading approach 129

5.23 Results case 2: Optimal power point approach 131

5.24 Results case 3: Optimal tuning of inertia support (H_V and R_V) for scenario B (expressed on a system base equal to 100 GVA) 132

6.1 Normalized maximum available aerodynamic power as a function of kinetic energy for different wind speeds (a) and concave approximation for $v_w = 8\ \frac{m}{s}$ (b), the grey lines indicate the limits of the kinetic energy 140

6.2 Schematic of the kinetic energy reserves and power margin referred to MPPT operation taken into account wind turbine operating limits. 142

6.3 Damping potential of wind turbines over the whole wind speed range (a), for $v_w = 9$, 10 and 11 m/s (b) 144

6.4 Optimization results for the point indicated in Figure 6.3(b) over a time horizon of 100 s 145

6.5 Overview of the implemented receding horizon control 146

6.6 Results for a random measured and forecasted load profile (RHC parameters: $\epsilon = 0.8$ & $t_{RHC} = 60\ s$) 147

6.7 Sensitivity analysis of parameters t_{RHC} with $\epsilon = 0.8$ (a) and ϵ with $t_{RHC} = 60\ s$ (b), with perfect load forecast (solid lines) and load forecast errors (dotted lines) 149

6.8 Sensitivity analysis of load forecast errors ($\epsilon = 0.8$ & $t_{RHC} = 60\ s$)150

6.9 Results for two aggregated wind turbines with a variable wind profile 151

7.1 From synchronous machine based to an empty grid (assuming a linear relationship between converter connected penetration and inertia from synchronous machines) 157

7.2 CSB converter connected to a weak grid: test system 158

7.3 Feedback control system equivalent of test network 159

7.4 Bode plot of $G(s)$ and $G(s) \cdot H(s)$ (see Figure 7.3) for case 1 ($D_{sys} = 1$, $\tau_V = 0.2\ s$ and $\tau_{s,pll} = 0.1\ s$), dashed lines correspond to a converter with an infinite control bandwidth 160

7.5 Bode plot of $G(s) = \frac{\Delta\omega_{e,pll}}{\Delta P^*}$ for different grid parameters 161

7.6 Simplified mechanical equivalent of the test system shown in Figure 7.2 162

7.7 Maximum H_V and $\frac{1}{R_V}$ in function of the SCR at point A ($D_{sys} = 1$, $H_{sys} = 5\ s$ and $\tau_V = 0.2\ s$) 163

7.8 Maximum H_V and $\frac{1}{R_V}$ in function of H_{sys} ($D_{sys} = 1$, $SCR_A = 5$ and $\tau_V = 0.2\ s$) 163

7.9 Root locus of the most critical poles (for test system as shown in Figure 7.2) using a VSB converter with virtual inertia H_V swept from 0.1 to 10 s ($R_P = 0.05$, $H_{sys} = 5\ s$, $D_{sys} = 1$ and $SCR_A = 2$)166

7.10 Frequency and converter active power variation after $\Delta P_{sys} = 0.1\ p.u.$ ($R_P = 0.05$, $H_{sys} = 5\ s$, $D_{sys} = 1$ and $SCR_A = 2$) . . . 167

7.11 From synchronous to converter (CV) based system: test system and test cases (VSB: Voltage source based, CSB: Current source based) 170

7.12 Frequency results after an outage of the line connecting G_4/CV_4 for the different test cases presented in Figure 7.11, $|ROCOF|$ is measured over 500 ms 171

A.1 Classical multi-machine system representation to study a sudden load change at node L [14, 4] 180

A.2 Power system equivalent for load-frequency studies 181

A.3 Steam turbine and governor model 182

A.4 Hydro turbine and governor model 183

A.5 Gas turbine and governor model 183

B.1 Test system with power flow results 185

B.2 HVDC link 187

List of Tables

2.1 Interfacing technology for different energy source types [15] . . 25

B.1 Generator parameters 184
B.2 Line parameters 185
B.3 Exciter and governor parameters 186
B.4 Load and transformer parameters 186
B.5 Aerodynamic parameters 187
B.6 Wind turbine GSC parameters 187
B.7 VSC HVDC link parameters [16] 188

Chapter 1

Introduction

1.1 Context and motivation

The growing concerns related to the depletion of fossil fuels and the environmental impacts of global warming due to human activities, have reinforced the need to steer our energy system on a more sustainable and cost-effective path. This energy transition is one of the main challenges that countries worldwide face in the decades to come, as it is vital for future prosperity and for the well-being of the people, industry and economy.

The European Union (EU) can be considered as the precursor in this quest for a low-carbon energy supply, since it has already set ambitious energy and climate objectives through its 20-20-20 targets which were enacted in legislation in 2009. These targets aim at reducing the greenhouse gas emissions by 20% compared to the 1990 level, 20% increase in energy efficiency and 20% share of renewable energy in the overall energy consumption of the European Union by the year 2020 [17]. Also beyond 2020, renewable energy sources will continue to play a key role in the energy transition, since the European countries already have agreed upon a new renewable energy target of 27% of the final energy consumption by 2030 [18].

As shown in Figure 1.1, the various efforts in promoting the use of renewables, e.g. through national financial support mechanisms, has facilitated the vast growth of Renewable Energy Sources for electricity (RES-e) within the EU. By the end of 2015, 422 GW of cumulative RES-e capacity was installed, providing 29% of the total electricity consumption [3]. Hydropower still covers the main share of RES-e, with a capacity of 152 GW, closely followed by wind accounting for 141.5 GW, including 11 GW offshore. Solar PV power has been the fastest growing RES-e technology during the past decade, going from 3.3 GW in 2005 to 94.8 GW in 2015. During 2016, an estimate capacity of 6.1 GW of solar PV and 12.1 GW of wind power has been added. Within the European Union, Germany is currently taken the lead in terms of cumulative capacity both with respect to wind and solar PV power, corresponding to respectively 50 GW and 41 GW by the end of 2016 [19, 20].

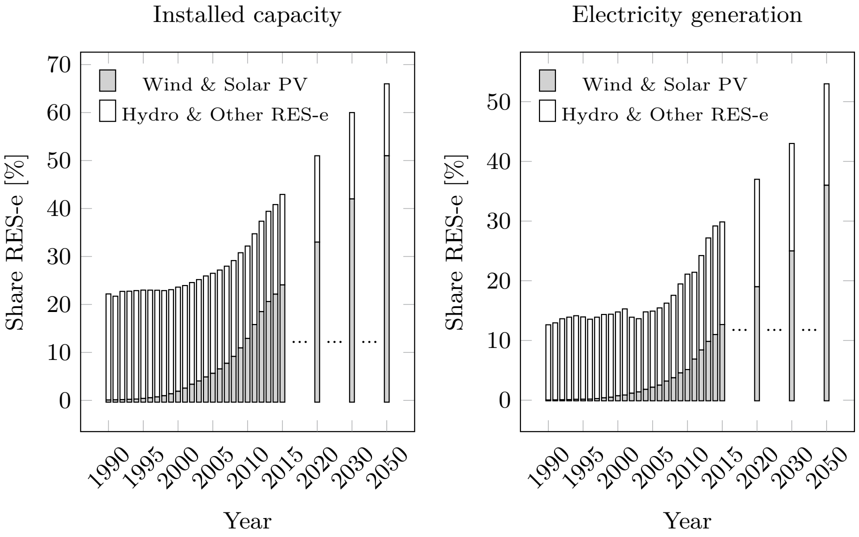

Figure 1.1: RES-e share of installed capacity and electricity generation within the EU-28 member states [1, 2, 3]

Looking at the projections for the EU as given in Figure 1.1, the steady growth of electricity coming from renewable energy sources is expected to continue even further into the future. By 2050 for instance (Figure 1.2), it is estimated that approximately 62% of the installed capacity will be covered by RES-e units [2]. However, as the capacity factors of solar PV and wind power units are relatively low compared to conventional generation, it only corresponds to a share of 47% of the total electricity production.

Similar trends are noticeable elsewhere in the world, with an increasing growth of RES-e in North America and Asia. China is currently the forerunner in terms of absolute numbers, having a total installed solar PV capacity of 77.42 GW and 168.7 GW of wind. Almost 50% of this solar PV capacity has been added during 2016 [19, 20].

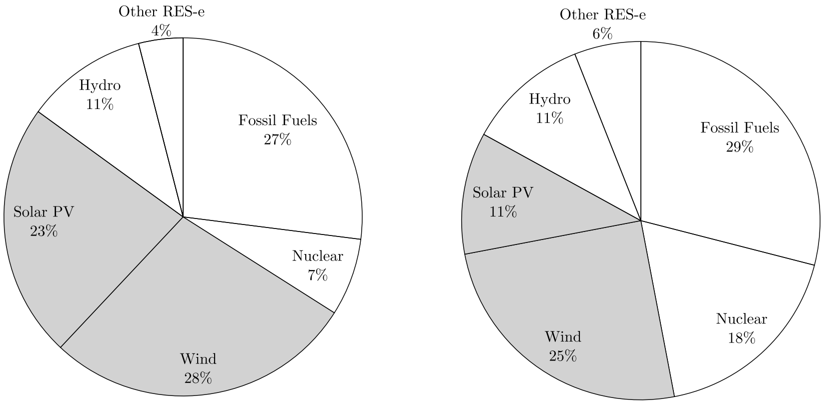

Installed capacity 2050
Total: 1283 GW

Electricity generation 2050
Total: 4064 TWh

Figure 1.2: Projection for 2050 of the installed capacity and electricity generation within the EU-28 member states, converter connected generation is coloured in grey [2]

Along with the transition towards more RES-e, a shift is generally taken place in the way generation units are connected to the grid. Traditional large-scale power systems are currently still mainly powered by a relative small number of synchronous generators, installed in conventional power plants. The unique characteristics of these machines have determined how power systems have been planned and operated since the development of the first alternating current (AC) transmission network at the dawn of the electricity era, more than a century ago. These large generators are centrally located, either close to the load centres or near the primary energy sources, and connected through an extensive transmission and distribution grid providing energy to the different electric loads in the system.

RES-e units on the other hand are often more distributed in the network and, aside from hydro and other technologies such as geothermal energy, interface with the grid through a power electronic converter. Referring back to Figures 1.1 and 1.2 and assuming that the vast majority of solar PV and wind power units is equipped with such a converter, the share of these converter connected units in the total electricity capacity within the EU experienced a significant growth from merely 1.2% in 2000 to 24% in 2015 and will increase to an approximately estimated 51% in 2050 [1, 2, 3]. During favourable wind and sun conditions, combined with a low system load, the instantaneous penetration can even reach higher numbers than the one indicated in grey in both figures.

From a physics point of view, the synchronous generators and coupled rotating machinery, such as e.g. steam turbines, have mechanical inertia and therefore, are capable of storing kinetic energy in their rotating mass. Since the terminals of the generator are directly linked with the network, this energy is inherently exchanged with the system during disturbances which makes it less prone to frequency fluctuations in case of an imbalance between load and generation [21].

On the contrary, converters typically transform direct current (DC) electricity to AC power by controlling semiconductor devices at a high switching frequency. Due to this intermediate DC link which decouples the generator from the grid and the lack of any mechanical inertia in case of PV units, no energy is normally exchanged with the grid to limit power imbalances. Instead of physical characteristics, the control strategy of the converter predominately determines the electrical dynamic interaction with the system.

The distinct grid interface together with the intermittent and variable generation output of these RES-e unit poses not only additional challenges with respect to the operation of today's power system, but the massive integration of renewables also sets the directions for future grid planning and reinforcements. A substantial share of the renewable electricity generation will be concentrated in locations far from the main population and load centres, such as in the North Sea or the European periphery. Therefore, fundamental upgrades to the current networks are required to accommodate the high and volatile power flows from generation to load [22]. The need for such additional transmission grid investments within Europe is further reinforced by the liberalization and unbundling of the energy market which has been implemented in order to promote the competition. As a consequence, the European power system is operated closer to its limits and in order to not impede the development towards a single energy market, new interconnections have to be built [23, 24].

At the same time, Transmission System Operators (TSOs) are faced with complex and difficult permitting processes as a result of the increasing public opposition against the construction of new overhead lines, mainly due to environmental, perceived health or political reasons. In order to resolve this conflict of interest, reinforcing and upgrading the network by building new High Voltage Direct Current (HVDC) links is considered to be one of the options since it allows to build long underground cable connections, with less public resistance. Moreover, also for the connection of offshore wind farms which are remotely located from the mainland, HVDC technology is the preferred technology [25].

As a consequence, an increasing number of new HVDC links are currently constructed or planned, not only as interconnections of asynchronous zones or to link offshore wind farms at the periphery of the system, but also becoming

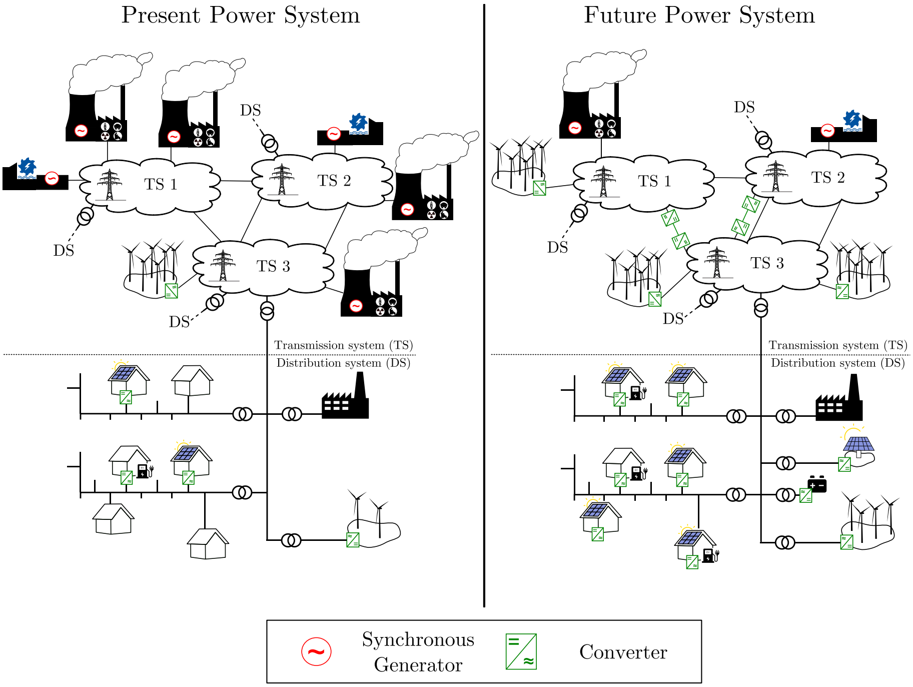
Present Power System
Future Power System
TS 1
TS 2
TS 3
DS
Transmission system (TS)
Distribution system (DS)
Synchronous Generator
Converter

Figure 1.3: High-level comparison of present and future power systems

increasingly embedded in the current AC network. The Alegro link between Belgium and Germany for instance, currently in the permitting process, will be the first (DC) connection between Belgium and Germany [26]. Within Germany itself, even more progressive plans are currently under investigation to construct three major HVDC corridors to transport the vast amounts of wind power in the north to the main load centres located in the south. This major grid reinforcement is part of the German energy transition towards 2022, including a phase-out of all nuclear power plants [27, 28].

Looking further into the future, these large embedded HVDC corridors could eventually be linked together which would pave the way for an extensive overlay DC grid, or a so called supergrid. Such a grid could possibly be applied to reach a zero carbon electricity supply, by transporting large amounts of energy on a continental scale, transferring energy from wind turbines in the North Sea, hydropower in Scandinavia and solar energy in the Southern countries towards the main load centres in the heart of continental Europe [29].

The different transitions described are summarized and highlighted in Figure 1.3. A high-level comparison is made between a present and future power system. This future power system will be realized as RES-e increases and large conventional synchronous generators are gradually displaced by converter coupled units providing zero inertia to the system. Also the grid itself will undergo a transformation, from mainly AC networks to more and more HVDC links used to reinforce the connection between the different transmission networks.

Although not yet touched upon, other changes in the power system such as an increasing electrical load at household level, due to for instance the increase in the number of electric vehicles, and the rising application of converter connected storage in the form of batteries are displayed in the figure as well.

1.2 Scope and objectives of the work

In light of this shift towards a substantial penetration of RES-e, some tremendous challenges will be encountered in the decades to come with respect to operation, control and planning of our power system in order to maintain current levels of security of supply.

This security of supply corresponds, according to Eurelectric, to the "ability of the system to provide electricity to the end-user with a specified level of continuity and quality in a sustainable manner" [30]. Security of supply covers many aspects and is generally subdivided in long-term security, corresponding to for instance fuel availability and system adequacy, and short-term security, i.e. operational security. In this work, it is assumed that there is sufficient generation and transmission capacity available and the operational security of systems with increasing amounts of converter connected generation is mainly addressed. This operational security refers to the capability to withstand sudden disturbances and therefore acts on a much shorter time scale.

A non-exhaustive overview of the different operational security issues linked to the specific characteristics of RES-e (wind and solar PV) is given in Figure 1.4, with the main scope of this research coloured in grey. Although their are many challenges associated with the integration of RES-e in power systems, this thesis deals mainly with those related to the distinct converter interface as introduced in the former section. More specifically, it addresses the influence of the decreasing inertia provided by synchronous machines and the way to mitigate possible issues in order to maintain system stability. To this end, new approaches to control the grid and its components are developed and analysed.

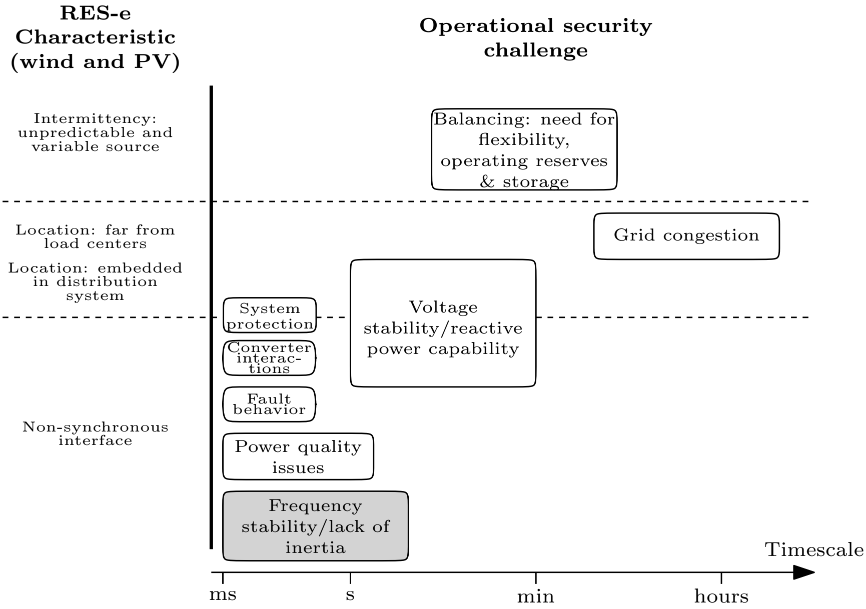
RES-e Characteristic (wind and PV)
Operational security challenge
Intermittency: unpredictable and variable source
Balancing: need for flexibility, operating reserves & storage
Location: far from load centers
Grid congestion
Location: embedded in distribution system
System protection
Voltage stability/reactive power capability
Converter interactions
Fault behavior
Non-synchronous interface
Power quality issues
Frequency stability/lack of inertia
Timescale
ms
s
min
hours

Figure 1.4: Operational security challenges associated with the distinct RES-e (wind and PV) characteristics

The main research objectives associated with the reducing system inertia are threefold:

- Investigate how the current power system operation and control is influenced by the decreasing inertia and assess to what extent system stability is ensured
- Develop control methods to provide additional support by converter connected RES-e units and HVDC links in order to improve frequency stability
- Propose systematic control approaches on system level to enable the shift towards a converter dominated system

As such, this work covers the complete transition with respect to the provision of inertia for system stability, from a synchronous machine based power system towards a system in which all generation units are interfaced with a converter.

1.3 Outline

An outline is presented in Figure 1.5, with the chapters coloured in grey (3, 5, 6 and 7) containing the main contributions. Chapters 2 and 4 are introductory.

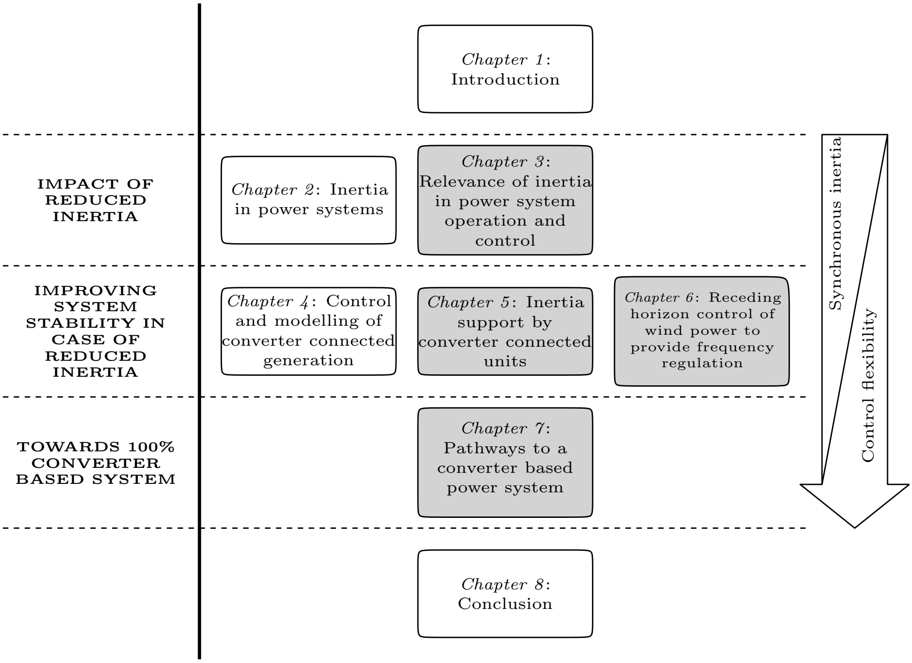
Chapter 1: Introduction
IMPACT OF REDUCED INERTIA
Chapter 2: Inertia in power systems
Chapter 3: Relevance of inertia in power system operation and control
IMPROVING SYSTEM STABILITY IN CASE OF REDUCED INERTIA
Chapter 4: Control and modelling of converter connected generation
Chapter 5: Inertia support by converter connected units
Chapter 6: Receding horizon control of wind power to provide frequency regulation
TOWARDS 100% CONVERTER BASED SYSTEM
Chapter 7: Pathways to a converter based power system
Chapter 8: Conclusion
Synchronous inertia
Control flexibility

Figure 1.5: Outline of the work, main contributions are coloured in grey

Chapter 2 starts with giving a general introduction to the fundamentals of inertia in powers systems. The different sources contributing to the total inertia are described and their contribution is quantified. An overview of the different approaches to estimate and measure inertia is given.

In *Chapter 3*, the role and influence of reducing the inertia on power system operation and control is further elaborated. The different forms of power stability are separately dealt with and the main challenges are identified. Furthermore, some possible solutions are introduced to operate today's power system with lower inertia.

Before describing different controllers to offer support by converter connected generation, the control and modelling of such converter connected RES-e units is described in more detail in *Chapter 4*. Special attention is given to different control approaches of the grid side converter and the way synchronization with the grid is achieved as this mechanism provides the inputs to the inertia support controller.

Chapter 5 starts with a quantification of the available energy buffers within RES-e. Based on this analysis, different inertia support mechanisms are proposed, which are further grouped depending whether they are applied under optimal or under deloaded operation. Moreover, the control of HVDC links to transfer inertia between two asynchronous areas is presented. The provision of inertia at scale is addressed in the final section of this chapter.

As the kinetic energy of wind turbines can be exploited to deliver support on longer time scales than the methods proposed in the former chapter, a receding horizon control approach to provide frequency regulation by wind turbines is presented in *Chapter 6*. The influence on forecast errors of both wind speed and electric load is elaborated.

In *Chapter 7*, the limits to the control approach presented in chapter 5 are further investigated. New ways of operating a system with very high of even 100% of converter connected RES-e are presented and analysed.

Chapter 8 presents the main conclusions together with some recommendations for future research.

The appendices support the main chapters by providing more detail on the modelling (*Appendix A*) and parameters of the different test cases applied in this work (*Appendix B*).

Chapter 2

Inertia in power systems

“Life leaps like a geyser for those who drill through the rock of inertia.”
- Alexis Carrel

2.1 Introduction

The concept of inertia is one of the well-known and fundamental principles of classical mechanics used to describe the motion of objects and how they are affected by applied forces. In general, it is defined in its elementary form as the resistance of a physical object to a change in its state of motion, including changes in speed and direction [31].

Within an alternating current electrical power system, an inherent close coupling exists between the speed of the grid connected rotating machinery and the electrical frequency at their terminals. Consequently, the total mechanical inertia of these machines provides the system the capability to oppose sudden variations in electrical frequency after a disturbance in the grid occurs. It is therefore considered as a vital parameter upon which the synchronized operation of current day systems is based.

The fundamentals of power system inertia are recapitulated in this chapter. The main sources of inertia in current systems are identified and quantified. Furthermore, the impact of the expected increase of converter connected units on inertia is shortly addressed. An overview is also given of the different approaches to measure and estimate the available power system inertia.

2.2 Basic considerations: inertia from a power system perspective

Although every motor or generator unit directly connected to the grid provides to some extent inertia to the system, the major share of the inertia in current power systems comes from conventional power plants. In these power plants, synchronous generators are commonly applied to convert primary energy sources such as water, chemical or nuclear energy to electrical energy via a mechanical intermediate link, the turbine. Since they still form the main source of electrical power generation, these generators can be considered as the cornerstone of current power system operation.

2.2.1 Swing equation and inertia of a single synchronous machine

Neglecting damping, the mechanical dynamics of such a synchronous machine installed within a conventional power plant, are governed by its torque equation, embodied by Newton's second law of motion:

$$J\frac{\mathrm{d}^2\theta}{\mathrm{d}t^2} = T_m - T_e \tag{2.1}$$

with

$$\omega_m = \frac{\mathrm{d}\theta}{\mathrm{d}t} \tag{2.2}$$

where J defines the moment of inertia which opposes any change in the angular acceleration of the rotor resulting from an imbalance in mechanical and electromagnetic torque, respectively denoted by T_m and T_e. The rotor angular position and the mechanical rotational speed with respect to a stationary reference frame are given by θ and ω_m.

The moment of inertia in (2.1) represents the total equivalent inertia of the drive train within the power plant. This drive train is a very complex mechanical structure, sometimes exceeding 50 m in length and weighing several hundred tons, usually composed out of a number of masses mounted on the same shaft as illustrated in Figure 2.1 for a thermal power plant consisting out of a high-pressure, intermediate and low pressure steam turbine. The entire drive shaft rotates at the same speed, governed by (2.1), with J the sum of the individual moments of inertia. The complete generator/turbine system has therefore several torsional vibration modes depending on the relative inertia and the damping of each rotor mass together with the shaft stiffness of the sections connecting adjacent elements. However, as these oscillations lie in the sub-synchronous frequency range, the drive train can be represented by a lumped single mass model in dynamic power system studies, except when sub-synchronous resonance is analysed [32].

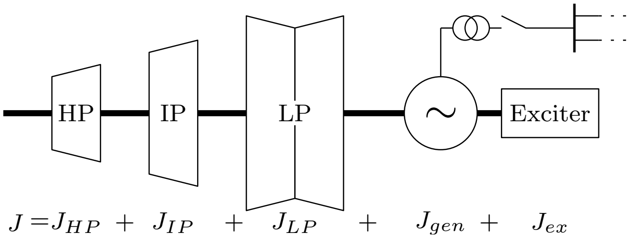

Figure 2.1: Schematic example of the main elements within a drive system of a thermal unit with three pressure stages (HP, IP and LP), the synchronous machine is equipped with a rotating exciter

The flux (ψ) produced by the rotating field windings within the synchronous machine induces an electromotive force (EMF) in the armature windings of the stator. For a generator with a single pole pair, the EMF (also called internal voltage) lags the rotor in steady state by $\frac{\pi}{2}$ rad (Figure 2.2). The electrical angle δ of this EMF is usually expressed with respect to a synchronously rotating reference frame and therefore relates to the absolute angular position of the rotor as:

$$\delta = p \cdot (\theta_m - \frac{\pi}{2}) - \omega_{e,0} \cdot t \tag{2.3}$$

with $\omega_{e,0}$ the rated electrical angular frequency. The number of pole pairs, p, largely depends on the generation technology. In general, synchronous machines in thermal power plants have a low number of pole pairs corresponding to a high operational speed (3000 or 1500 rpm in a 50 Hz grid). Hydropower plants, on the other hand, are running at low speed, incorporating a large number of pole pairs.

Equation (2.1) can further be expressed in terms of power and electrical angles:

$$\frac{J \cdot \omega_e}{p^2} \frac{\mathrm{d}^2\delta}{\mathrm{d}t^2} = P_m - P_e \tag{2.4}$$

is the so-called swing equation of the synchronous machine, used to determine the rotor dynamics in stability studies. P_m represents the mechanical input power to the shaft and P_e the electrical output power. The left-hand side of

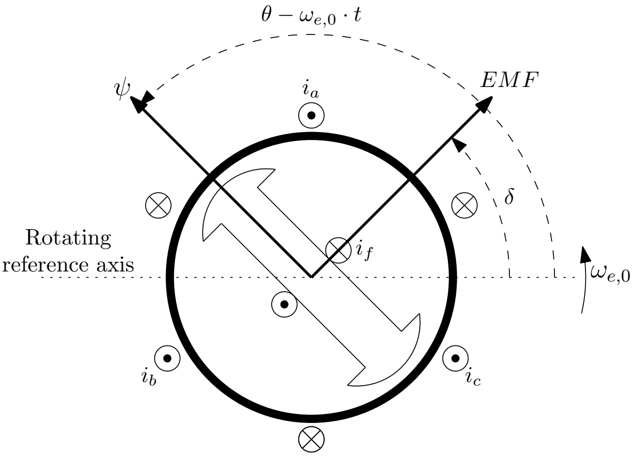

Figure 2.2: Representation of an elementary three-phase, two-pole synchronous generator (generator convention)

(2.4) is the derivative of the kinetic energy (E_{kin}) stored in the drive train. The energy at rated speed is often expressed proportional to the power rating of the generator and is called the inertia constant H, i.e. the time in seconds a generator can provide rated power solely using the kinetic energy stored in the rotating mass [32]:

$$H = \frac{\frac{J \cdot \omega_{e,0}^2}{2 \cdot p^2}}{S} = \frac{E_{kin}}{S} \tag{2.5}$$

with S the rated apparent power of the generator. The inertia of a single unit is often also defined by the mechanical time constant ($2H$), which is equal to the time in seconds it takes to accelerate a generator from standstill to rated speed when a constant torque equal to $\frac{S \cdot p}{\omega_{e,0}}$ is applied [33].

The second order swing equation (2.4) can be converted to per unit ($\bar{\ }$) and rewritten as two first order equations. Taking the rated machine power and system frequency as base values and assuming only small deviations from rated frequency ($\omega_e \approx \omega_{e,0}$), yields[1]:

$$2H \frac{\mathrm{d}\bar{\omega}_e}{\mathrm{d}t} = \bar{P}_m - \bar{P}_e \tag{2.6}$$

---

[1] In the remainder of the text, the ($\bar{\ }$) notation for per unit values is omitted as it is clear from the context whether or not the quantities are expressed in per unit.

$$\frac{\mathrm{d}\delta}{\mathrm{d}t} = \omega_{e,0} \cdot (\bar{\omega}_e - 1) \tag{2.7}$$

The inertia of a single machine expresses thus the resistance to the change in rotational speed, inherently translated to a change in the frequency of the internal voltage induced by the rotating field flux.

2.2.2 System inertia in a traditional power system

To transfer the concept of rotational inertia provided by a single generator or power plant to the total inertia perceived by a power system, it is important to understand the synchronization mechanism between interconnected machines.

The way these machines exert synchronizing forces in order to acquire the same rotational speed is demonstrated by applying a sudden load change within the power system given in Figure 2.3(a). This system is used as a test network throughout this work and a more detailed description can be found in appendix B.1.

Initially, all machines are at steady state, rotating at synchronous speed equal to 50 Hz. At $t_L = 0.1\ s$, the active power demand at load bus L is suddenly increased with $\Delta P_L = 6.5\ MW$. The rotational speed and change in active power of each machine after the event can be analysed based on the classical multi-machine modelling (Appendix A.1). Using this approach, the grid is reduced to the internal machine nodes and load node L. Furthermore, all generator control actions are neglected and although it only leads to approximate results, yet they are quite instructive.

The variation in rotational speed of the three synchronous machines are given in Figure 2.3(b), which results are based on a phasor time domain simulation within DIgSILENT Power Factory (disabling governor and exciter controllers).

Load change at $\mathbf{t = t_L^+}$

Immediately after the load step is applied (t_L^+), the rotor angles remain constant due to the inertia of the machines. The energy to balance the load can therefore not come from the stored energy in the rotating mass, but is supplied by the energy stored in their magnetic fields. The angle deviation on each bus of the reduced network is:

$$\Delta\delta_i(t_L^+) = 0 \quad \text{for} \quad i \neq L \tag{2.8a}$$

$$\Delta\delta_i(t_L^+) = -\frac{\Delta P_L}{\sum_{j=1}^{n} P_{S,Lj}} \quad \text{for} \quad i = L \tag{2.8b}$$

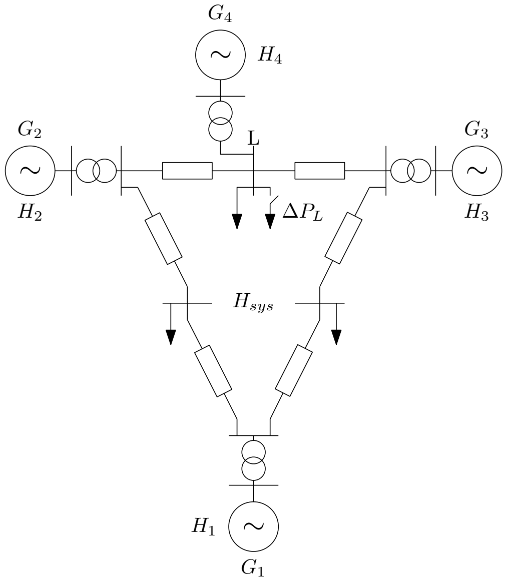
G_4
H_4
G_2
H_2
L
G_3
H_3
ΔP_L
H_{sys}
H_1
G_1

(a) Test system

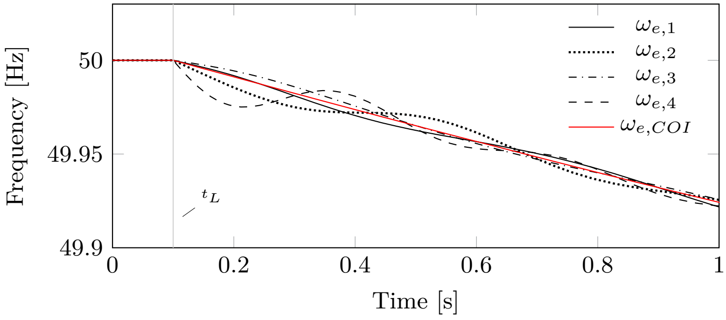

(b) Speed of synchronous machines

Figure 2.3: Synchronization mechanism in a small power system ($H_1 = 6\ s$, $H_2 = 3\ s$, $H_3 = 9\ s$ and $H_4 = 3\ s$)

Consequently, the load impact is immediately distributed among the generators depending on their synchronizing power coefficient, $P_{S,ij}$ (power values are expressed in per unit with respect to a common system base S_{sys} equal to the sum of the rated power of all connected machines):

$$\Delta P_{e,i}(t_L^+) = \frac{\Delta P_L \cdot P_{S,iL}}{\sum_{j=1}^{n} P_{S,Lj}} \tag{2.9}$$

This way, taking into account the swing equation governing the motion of each machine, all machines start to decelerate at different rates, according to their inertia constant and electrical distance to the node L as given by $P_{S,iL}$:

$$\frac{d\Delta\omega_{e,i}(t_L^+)}{dt} = -\frac{\Delta P_{e,i}(t_L^+)}{2 \cdot H_i'} = -\frac{\Delta P_L \cdot P_{S,iL}}{2 \cdot H_i' \sum_{j=1}^{n} P_{S,Lj}} \tag{2.10}$$

With H_i' the inertia constant of a single machine referred to the common system base S_{sys}:

$$H_i' = \frac{H_i \cdot S_i}{S_{sys}} \tag{2.11}$$

For $\mathbf{t < t_{gov}}$

Before governor action is fully initiated at $t = t_{gov}$, an overall deceleration of all machines occurs, represented by the decrease of frequency at the inertial centre of the system, $\omega_{e,COI}$. This frequency at the centre of inertia is defined as:

$$\omega_{e,COI} = \frac{\sum_{i=1}^{n} H_i' \cdot \omega_{e,i}}{\sum_{i=1}^{n} H_i'} \tag{2.12}$$

Adding up the deceleration of each individual machine (2.10), yields:

$$\frac{d\Delta\omega_{e,COI}}{dt} = -\frac{\Delta P_L}{\sum_{i=1}^{n} 2 \cdot H_i'} \tag{2.13}$$

This equation gives the mean deceleration of the system at its centre of inertia. Each machine individually however follows a different oscillatory motion around this centre of inertia governed by its swing equation. The synchronizing forces between the machines tend to pull them together and because of the damping provided by rotor damper windings, grid losses or external control devices such as a power system stabilizers (PSS), all machines eventually acquire the same deceleration. At that moment, each machine covers a share of the load imbalance depending only on their inertial constants:

$$\Delta P_{e,i} = -\frac{H_i' \cdot \Delta P_L}{\sum_{j=1}^{n} H_j'} \tag{2.14}$$

Due to this inherent synchronization mechanism within the transmission network, all individual machines can actually be aggregated into a single unit, which mechanical behaviour is governed by a single swing equation to represent the coherent response of all generators:

$$2H_{sys}\frac{\mathrm{d}\omega_{e,COI}}{\mathrm{d}t} = P_G - P_L = -\Delta P_L \tag{2.15}$$

with

$$H_{sys} = \sum_{i=1}^{n} H_i' = \frac{\sum_{i=1}^{n} H_i \cdot S_i}{S_{sys}} \tag{2.16}$$

the equivalent inertia constant of the whole power system. The equivalent unit is driven by the combined mechanical outputs of the individual turbines of the generators ($P_G = \sum_{i=1}^{n} P_{m,i}$) and the output power is set equal to the total load in the system, represented by P_L. Both values are expressed in per unit on a common system base S_{sys} mostly equal to the total synchronous generation capacity connected to the system. Looking at this swing equation, the system inertia can thus be interpreted as the resistance in the form of kinetic energy exchange from all synchronous machines to oppose changes in the frequency at the centre of inertia resulting from power imbalances in generation and demand. The system inertia is not a constant system parameter as the number and type of grid connected machines, both at load and generation side, varies in time. The inertia provided from the generation side is for instance directly linked to the type and number of the operating conventional power plants determined by the unit commitment (UC) and merit order [34, 35].

2.2.3 System inertia in future power systems

In a future power system, many of these conventional units will be displaced or switched off in favour of renewable generation units with lower marginal costs as introduced in the former chapter of this work. Focusing on the context of inertia, most of these renewable electricity generation units behave differently from traditional, centralized generation facilities. They are in general connected through a power electronic converter, which fully or partly electrically decouples the generator from the grid. The link between the rotational speed of the generator and the system frequency is therefore removed. As a result, these converter connected generation units do not inherently contribute to the total system inertia [34]. Secondly, the (kinetic) energy buffer available in conventional power generation units to counteract frequency changes is often missing. For instance in photovoltaic (PV) power generation, no rotating parts are involved and only a very small amount of energy can be stored in the capacitors.

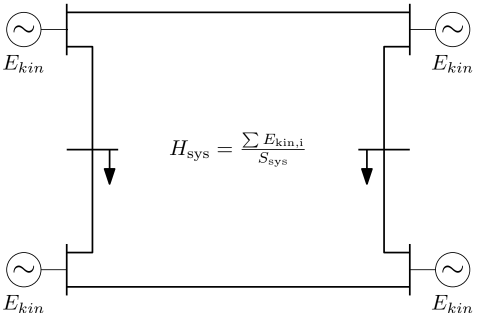
E_{kin}
E_{kin}
$H_{\mathrm{sys}} = \frac{\sum E_{\mathrm{kin,i}}}{S_{\mathrm{sys}}}$
E_{kin}
E_{kin}

(a) Traditional power system

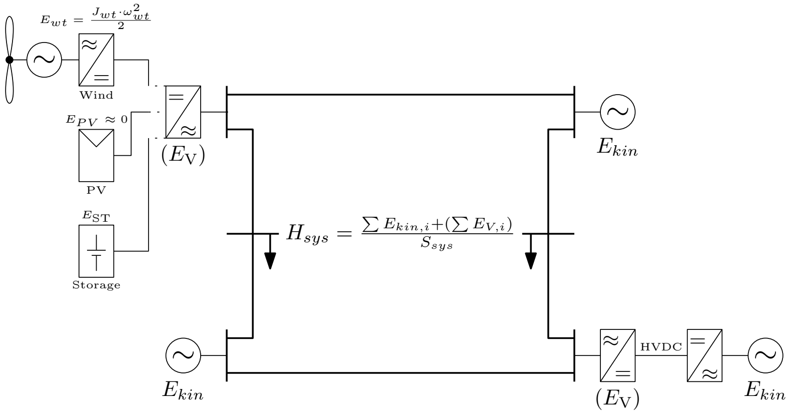
$E_{wt} = \frac{J_{wt} \cdot \omega_{wt}^2}{2}$
Wind
$E_{PV} \approx 0$
PV
E_{ST}
Storage
(E_{V})
E_{kin}
$H_{sys} = \frac{\sum E_{kin,i} + (\sum E_{V,i})}{S_{sys}}$
E_{kin}
HVDC
(E_{V})
E_{kin}

(b) Future power system

Figure 2.4: Inertia and (kinetic) energy storage in power systems

Furthermore, it is expected that more and more high voltage direct current (HVDC) links will be installed since they are an interesting option to transport large amounts of renewable energy from the remote sources to the load centres and to fundamentally upgrade the existing AC network [25]. As these HVDC links electrically decouple two or more interconnected systems, the inertia of one system is not directly accessible to the other.

With respect to inertia, the worst case therefore corresponds to a high penetration of converter connected generation together with a high import from HVDC transmission links during times of low residual system load as the number of conventional power plants providing inertia will be significantly reduced.

In Figure 2.4(b), a future power system is depicted in which part of the synchronously connected generation of the traditional system is displaced by converter connected generation. Assuming the same system base (S_{sys}), the system inertia (2.16) decreases which makes the system more prone to fast frequency deviations after imbalances in generation and load.

One of the options to change this behaviour comprises a modification of the converter control. Converters, connecting the generator or power source to the grid, are normally not managed in a way to react to variations in grid frequency, hence decoupling the generator from grid side variations. However, the control of the converter can be modified to vary the energy exchange with the grid in a controlled way depending on the (measured) grid frequency. One such possible control action is to mimic the natural behaviour of a synchronous machine [36, 37, 38].

The energy exchange corresponding to this control action is called the virtual (or synthetic) inertial response and is characterized by a virtual moment of inertia J_V and virtual inertia constant H_V. In a system where both synchronous machines and converters deliver respectively synchronous (H) and virtual inertia (H_V) to the grid, H_{sys} can now be expressed as [39][2]:

$$H_{sys} = \frac{\sum E_{kin,i} + \sum E_{V,i}}{S_{sys}} = \frac{\sum H_i \cdot S_i + \sum H_{V,i} \cdot S_i}{S_{sys}} \tag{2.17}$$

As the converter controls instead of the generators determine the power exchange with the system, any type of power source or energy buffer can in principle be used to contribute to the system inertia (flywheels, batteries, capacitors, ...). In wind turbines, the kinetic energy from the blades, gearbox and generator can be extracted. In a PV system, additional storage can for instance be added in the form of batteries. A second source of energy can come from deloading the generation units to have an upward power reserve available. However, this energy exchange is restricted to certain limits, e.g. converter operating limits, minimum rotor speeds, DC capacitor voltage, maximum deceleration and acceleration of the blades, ... and highly depends on the operating point [40].

---

[2] While the total kinetic energy of the conventional power plants decreases, S_{sys} is in this work always kept equal to the total generation capacity of the (original) synchronous machine based power system, unless stated otherwise.

The inertia in future systems can thus be described as the resistance in the form of any kind of energy exchange from synchronously connected machines and converter connected generation to counteract the changes in system frequency resulting from power imbalances in generation and demand.[3]

The energy exchange in a power system immediately after a power imbalance is schematically illustrated in Figure 2.5. The area of each block is equal to the available kinetic energy within the system as the width and height are respectively proportional to $\sum \frac{J}{p^2}$ and to $\frac{\omega_e^2}{2}$. The grey area defines the stored kinetic energy at rated frequency ($\omega_{\mathrm{e},0}$). Since the power system is designed to operate within a certain frequency band, the stored kinetic energy always varies between the boundaries set by $\omega_{\mathrm{e,min}}$ and $\omega_{\mathrm{e,max}}$. When for instance a negative imbalance in a traditional power system (system A) occurs, the deficit is initially compensated by the kinetic energy released by the conventional generation units, indicated by the hatched area. As a result, the system frequency declines and reaches a certain value at time t_1 (Figure 2.5(b)). The frequency decline as well as the exchanged energy (ΔE) as a function of time are given in this figure. If no further actions are taken to arrest the frequency drop by increasing the power setpoints of the generation units, the stored kinetic energy gets depleted and the system collapses.

The effect of this decreasing system inertia in future systems is presented in Figure 2.5 (system B). The stored kinetic energy available to the system (grey area) is reduced. Assuming the same power imbalance as before and thus also the same amount of exchanged energy ($\sum \Delta E$), the decrease in system inertia results in a lower frequency at $t = t_1$ and a higher rate of change of frequency (ROCOF), see Figure 2.5(b). By using available converter connected generation to deliver a virtual inertial response and therefore compensate for the reduction in synchronous inertia, the frequency deviation is less compared to a system in which converter connected units do not respond to frequency changes. This can also be explained based on the schematic representation in Figure 2.5 (system C). A part of the required energy is coming from converter connected

---

[3] The terms synchronous inertia (H) and virtual inertia (H_V) are used in the remainder of this work to clearly highlight the difference between the type of generation unit providing inertia.

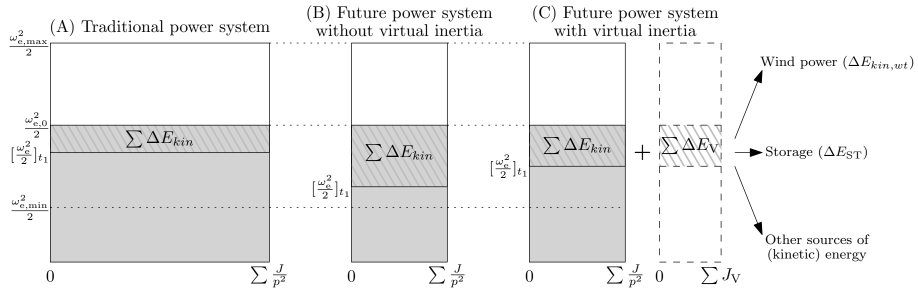
(A) Traditional power system
(B) Future power system without virtual inertia
(C) Future power system with virtual inertia
$\frac{\omega_{e,\max}^2}{2}$
$\frac{\omega_{e,0}^2}{2}$
$[\frac{\omega_e^2}{2}]_{t_1}$
$\frac{\omega_{e,\min}^2}{2}$
$\sum \Delta E_{kin}$
$\sum \Delta E_V$
+
Wind power ($\Delta E_{kin,wt}$)
Storage (ΔE_{ST})
Other sources of (kinetic) energy
0
$\sum \frac{J}{p^2}$
$\sum J_{\mathrm{V}}$

(a) Schematic representation of (kinetic) energy exchange

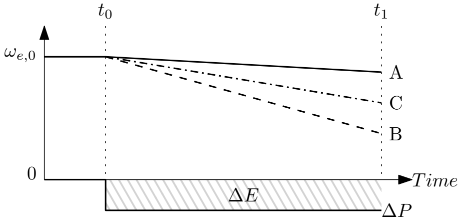

(b) Influence on power system frequency

Figure 2.5: (Kinetic) energy exchange in traditional and future power systems after a power imbalance

generation by means of a virtual inertial response ($\sum \Delta E_V$). Therefore, the reduction in stored kinetic energy from the synchronous connected units is partially compensated, which results in a higher frequency at $t = t_1$ compared to a future system without virtual inertial support. The actual source of energy depends on what is behind each converter participating in the virtual inertial control and can consist of a combination of storage, kinetic energy from wind, power reserves, kinetic energy from other systems connected through HVDC, ...

In the former analysis, a large number of simplifications are made. For instance, network topology, voltage dependency of load and generation and losses are all omitted. Furthermore, also the inertia coming from the load and other types of electrical machines (e.g. induction machines) was not taken into account. In future systems however, it is expected that this inertia will decrease as well since more and more of frequency dependent load such as motors and pumps are controlled using variable frequency drives.

In the next chapter, a more detailed analysis is performed to assess the relevance and influence of this inertia on the stability and operation of a power system.

2.3 Quantification of resources providing inertia

The amount of total inertia at each moment in time will depend on the number and characteristics of every load and generation unit connected to the power system. In order to have a clear overview of the different sources and their contribution to the system inertia, the amount of inertia from conventional power plants, distributed generation units and system load is quantified. In the remainder of this chapter, only the inertia that is naturally provided to the system is discussed, without considering the modified control of converter connected generation.

2.3.1 Conventional power plants

Large conventional units like e.g. coal fired, nuclear and hydropower plants using synchronous machines to convert the mechanical power from their turbine to electrical power are the main sources of inertia in today's power system. Their inertia (2.5) is expressed proportional to its power rating and falls typically in the wide range of 2-9 s [41, 4]. The constant covers the total kinetic energy stored in the drive train of the power plant, comprising the rotors of the synchronous generator and the prime mover. For steam turbo generators roughly 30 to 60% of the total inertia comes from this prime mover, whereas only 4 to 15% of the total kinetic energy of a hydro power unit is usually stored in the water wheel (including the water itself) [42].

In Figure 2.6, the inertia constants for a number of steam and hydropower plants with different power ratings are given. The values for the steam units tend to be inversely proportional to their rating, however no strong correlation can be noted [4]. A more elaborate study on published inertia values can be found in [15]. Also in this work, based on data from numerous sources in the literature, it is concluded that no clear consistency can be found in the inertia constants of large power plants. However, with respect to thermal power plants, units equipped with a four-pole synchronous generator (1500 rpm in a 50 Hz power system) generally have larger inertia constants than units using a two-pole generator running at a higher speed (3000 rpm in a 50 Hz power system). For large thermal units using a four-pole generator, the inertia constant can even exceptionally reach values up to 10 s [15].

The amount of inertia of a power plant is thus very much case specific and strongly depends on the design of both the generator and turbine. Moreover, most of the available system data on inertia constants seems to be unreliable and inaccurate, as many machines appear to have the same integer value for their inertia constants in the transmission system operator (TSO) databases.

The inertia constants are thus likely just an estimate of the real values and they should therefore be verified or determined more accurately [43].

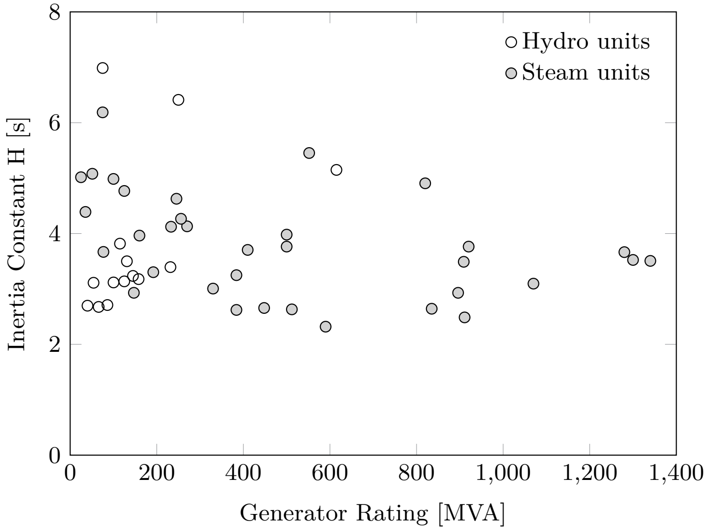

Figure 2.6: Inertia constants for conventional power plants (derived from data in [4])

2.3.2 Synchronous condensers

Synchronous condensers (or synchronous compensators) are devices that comprise a freely spinning synchronous machine connected to the high voltage network via a step-up transformer. By regulating the excitation current of the machine, dynamic voltage and reactive power support is provided. As they are synchronously connected to the system, they will also contribute to the total inertia. However, as they do not generate any active power, no prime mover is driving the synchronous machine. Consequently, the stored kinetic energy is rather low with an inertia constant around 1 s [32].

2.3.3 Distributed generation units

In contrast to the large conventional power plants which mostly use synchronous generators, different interfacing technologies to transfer the power from the prime mover to the grid are applied for (small) distributed generation units.

Depending on the energy source, a direct generator coupling, a partial power electronic or a full power electronic coupling is made. A schematic representation of the options is given in Figure 2.7 and an overview of some common energy sources and their preferred interfacing technologies are summarized in Table 2.1.

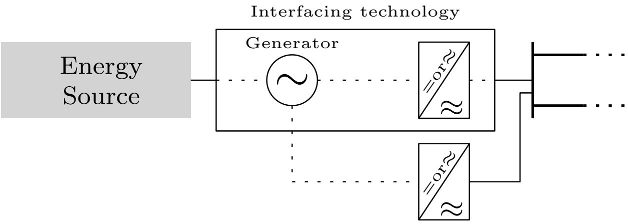

Figure 2.7: Interfacing technology for (distributed) generation

Energy Source Type	Generator	Power electronics
Wind power	IG	/
	SG, PMSG	AC/AC
	DFIG	AC/AC to rotor windings
Photovoltaic	/	DC/AC
Internal Combustion Engines	SG, IG	Optional: AC/AC
Microturbines	SG, IG	Optional: AC/AC
Hydropower	SG	/
Flow of river	PMSG	AC/AC
Fuel Cell/Battery storage	/	DC/AC

DC (Direct current), SG (Synchronous generator), PMSG (Permanent magnet synchronous generator), IG (Induction generator) and DFIG (Doubly fed induction generator)

Table 2.1: Interfacing technology for different energy source types [15]

Direct machine coupling

A direct machine coupling is often applied for units that convert mechanical into electrical power. If a constant mechanical power is supplied to the shaft, resulting in a steady speed operation, a synchronous generator can be used. Considering the energy source type, a directly connected synchronous machine is often applied in (small) hydropower units, internal combustion engines and some low-speed microturbines, in which the motor or turbine is optimally designed to operate at constant speed. Looking at the inertia of these small hydro and thermal units equipped with a synchronous machine, it is indicated in [15] that the inertia constants are much lower (about 50%) compared to large conventional units of the same type. Furthermore, in case of internal combustion engines for instance, a power electronic interface is sometimes included to offer an increased fuel efficiency as the engine speed can be optimized depending on the load [44]. Also for high-speed single shaft microturbines, becoming widely popular as energy producers in combined heat and power (CHP) systems, a converter is used to transfer the power from the generator operating at high speed ranging from 50000-120000 rpm [45]. The converter decouples the generator from the power system and consequently, no inertia is provided.

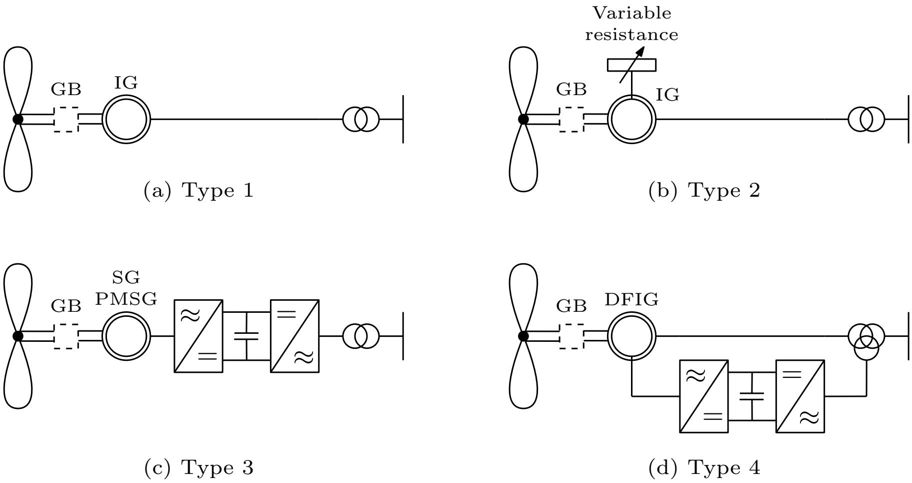

(a) Type 1 (b) Type 2

(c) Type 3 (d) Type 4

Figure 2.8: Common wind turbine topologies (GB: Gearbox)

In case the mechanical power and speed from the primary source fluctuates, an induction generator is more suitable as an inherent damping is provided through the speed difference between rotor and stator [15]. This direct induction generator coupling is for instance used in fixed speed wind turbine units as it offers a cheap and robust way to convert the wind power into electrical power (Type 1 & 2 Wind turbine[4], see also Figure 2.8). The main disadvantages are the need for reactive power compensation and the limited ability of varying its rotational speed with the wind speed resulting in a low efficiency over the whole wind speed range [5]. Also a gearbox is required in this topology in order to increase the low rotational speed of the rotor blades to the high-speed shaft driving the generator.

---

[4] Type 1 includes a standard induction generator while a type 2 wind turbine employs a wound rotor induction generator with adjustable external resistors to increase its allowed speed range

Due to the direct coupling, distributed generation units equipped with a synchronous or an induction generator provide inertia to the system. However, the way this inertia is delivered slightly differs for both machine types (Figure 2.9). The variation in active power output of an induction machine due to a changing system frequency is given in this figure. This (inertial) response is compared to a synchronous generator of the same rating. An inertia constant equal to 5 s is taken for both machine types and the voltage amplitude at the terminals is assumed to be constant during the frequency transient.

A fifth-order model is used to represent the dynamics of the induction generator. For this model, the electrical torque can be expressed as a function of the slip [32]:

$$T_{\mathrm{e}} = 3p\frac{r_r}{sl \cdot \omega_{e,0}} \cdot \frac{u_{eq}^2}{\left(r_{eq} + \frac{r_r}{s}\right)^2 + \left(x_{eq} + x_r\right)^2} \tag{2.18}$$

with

$$u_{eq} = \frac{j \cdot x_{mg} u_s}{r_s + j \cdot (x_s + x_{mg})} \qquad r_{eq} + j \cdot x_{eq} = \frac{j \cdot x_{mg}\left(r_s + j \cdot x_s\right)}{r_s + j \cdot (x_s + j \cdot x_{mg})}$$

where sl is the slip and u_s the stator voltage. r_s, r_r, x_s and x_r denote the resistance and reactance, of respectively the stator and rotor, referred to the stator of the induction machine. x_{mg} is the magnetizing reactance.

At $t = 2\ s$, the frequency starts to decline (Figure 2.9(a)) immediately resulting in an increased power output of the synchronous generator (ΔP_{SG}) releasing its kinetic energy. For the induction generator on the other hand, the change in mechanical speed lags the changing electrical frequency due to its inertia. Consequently, the slip becomes more negative. As a result, the electrical torque increases according to (2.18). The inertial response from the induction generator (ΔP_{IG}) is therefore slightly slower and lower, corresponding to the results in [46, 47, 48]. Once the frequency is stabilized, the difference between electrical and mechanical torque becomes zero and a new equilibrium is reached at a lower rotational speed.

In the studied case, the mechanical torque was also slightly influenced since the change in rotational speed affects the aerodynamic efficiency of the wind turbine. Similar results would be obtained for a constant mechanical torque.

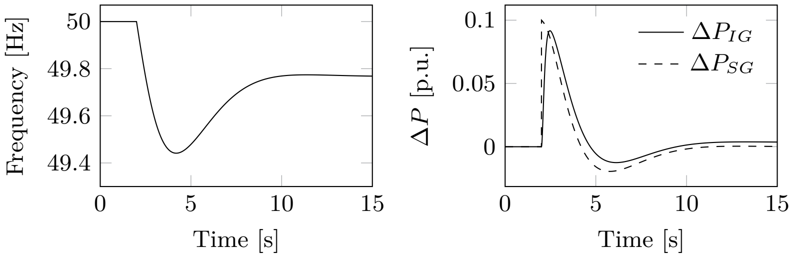

(a) Frequency profile

(b) Inertial response

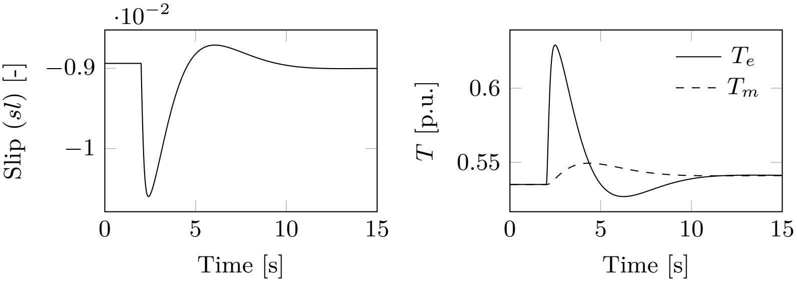

(c) Slip of IG

(d) Electrical and mechanical torque of IG

Figure 2.9: Inertial response for a fixed speed wind turbine using an induction generator, parameters are taken from [5]

Partial power electronic coupling

When an increased variable speed range is required, a partial power electronic coupling using a doubly fed induction generator (DFIG) can be applied. A converter rated for a certain percentage of the apparent power of the generator feeds the rotor windings while the stator is directly connected to the grid (Type 3 wind turbine, see Figure 2.8). Due to this partial decoupling, a variable speed operation with a range of ± 30 % of the synchronous speed can be reached [49]. The topology is mostly used in wind power units, allowing the rotor blades to optimally vary their rotational speed depending on the wind speed, resulting in an overall increasing efficiency compared to a fixed speed wind turbine.

Although this topology provides a partial direct grid coupling via the stator windings of the machine, the inertial response from these units seems to be almost negligible, mainly due to the fast acting converter controller which is usually designed to regulate the electrical torque. Hence, during a frequency transient, it will control the rotor current in order to keep the electrical torque equal to its pre-disturbance value. In [47], the influence of the bandwidth of this controller on the inertial response is further investigated. Only if a low controller bandwidth is assumed, a small inertial response can be noticed. A low controller bandwidth would however adversely affect the control capability during normal operation where a fast current controller is desired. Finally, in [50], it is demonstrated that in case the stator power is controlled instead of the electrical torque, an inertial response is provided by the turbine through the changing rotor power. This control strategy is considered quite uncommon though and is only reported in a few research articles [51, 52].

Full power electronic coupling

Finally, for all other types of distributed generation, a full power electronic coupling is applied. In a PV system for instance, a DC/AC with an intermediate DC/DC conversion stage is included to regulate the DC voltage in order to extract the maximum available power [15]. Also for wind power units, a back-to-back configuration comprising an AC/DC and DC/AC converter (full scale converter) can be applied, which allows an extended variable speed operation in order to obtain maximum efficiency (Type 4 wind turbine, see Figure 2.8). The concept can accommodate different generator types, but mostly a synchronous generator is used, either with permanent magnets or electrical excitation [53]. In case a direct driven multipole generator with a large diameter is applied, the generator and the blades can operate at the same speed so that the gearbox can be omitted [54]. The generator is completely decoupled in this case due to the separate controls of the generator and grid side converter linked by a DC capacitor. Due to this decoupling, no inertia to the power system is provided.

Summary

The amount of inertia inherently provided by distributed generation is thus limited to the inertia from direct connected internal combustion engines and microturbines (used for instance in CHP systems) together with the inertia from fixed speed wind turbines equipped with induction machines.

Regarding the latter type of wind turbines, it should be noted that although there is still a large amount of these fixed speed wind turbines in operation (mainly in the pioneer countries e.g. Germany, Spain and Denmark), they are gradually squeezed out of the market as new installations or the repowering of old turbines consist predominantly of wind turbines equipped with a DFIG or full scale converter interface [55].

Already in 2010, it was estimated that these two types combined covered a market share of almost 80% in Europe [56]. Also worldwide estimates indicate an increasing trend of variable speed wind turbines due to their flexible control and grid support capabilities [57].

2.3.4 Power system load

Whether the load will contribute to the system inertia, depends on the dynamics and type of the load. Directly connected motor loads in the form of fans, drives, pumps, ... deliver inertia just like generators do. Motor loads are present in both residential, commercial and industrial areas and cover a fundamental share of the total system load, generally consuming 60-70% of the total energy supplied by a power system [32]. The heavy rotating machinery of large industrial consumers mainly contributes to the system inertia. The small and medium sized motors on the other hand, installed in residential and commercial areas (e.g. used in air conditioning and refrigeration units), are characterized by a low inertia constant between 0.1-0.3 s [58].

Motor loads equipped with a variable speed drive (VSD) on the other hand do not provide inertia due to the electrical decoupling of the motor. Although some industry studies show that only 15-20% of the motors use such a VSD today, it is expected that this share will further increase [59]. All other load types do not react on frequency variations such as resistive or power electronic coupled loads.

To determine the aggregated inertia from the total system load, a detailed representation and estimation of the load composition is required. However, due to the large number of devices involved together with the spatial distribution, the time-varying and stochastic nature of the load, it is very complicated to assess the exact share of each type, and to develop a simple model correctly representing the dynamic behaviour of the load aggregated over a certain area.

The inertia from the load is therefore often assumed to be fixed or mostly even neglected in power system stability studies. In general, load models are regarded as of secondary importance and the emphasis is mainly been placed on the modelling of power generation units. The key findings from a survey conducted by the CIGRE[5] working group C4.605 “Modelling and aggregation of loads in flexible power networks” clearly highlights that in industry the load is generally modelled in a very simplified way [60]. Results of the questionnaire, administered by 160 utilities and system operators, showed that only 30% of the system operators use some form of motor load model for their power system stability analysis. By moving towards a system with less inertia coming from the generation side, the load inertia will become increasingly important to correctly model the frequency dynamics in the system and this assumption will therefore be no longer valid [61].

---

[5] CIGRE (Conseil International des Grands Réseaux Électriques) is a global organization in the field of high voltage electricity

2.4 Estimating available system inertia

Although inertia is generally considered an important parameter in the operation of current power systems, it appears a difficult task to accurately estimate the available system inertia. In the literature, two main approaches can be distinguished.

A first one analyses frequency transients directly after major generator outages or contingencies to determine the total inertia of an existing power system. As shown in the following section, this approach only gives a rough indication of the amount of inertia since many factors related to filtering, measurement errors, ... significantly influence the accuracy of the applied method. Moreover, this method is not considered to be relevant for real time system operation due to its retroactive approach of analysing past frequency transients.

A second approach uses Supervisory Control And Data Acquisition (SCADA) measurements together with the available operational data from generation units to track the inertia in real time. This method was implemented for the first time by the TSOs of the Nordic power system. Their real time inertia estimation could be a useful support tool in future system operation and control, but it needs to be developed further as not all units are yet included in the tool. More research is also required to verify the reliability and accuracy of the estimation.

2.4.1 Retroactive approach: analysing frequency transients

The different steps of the approach are illustrated in Figure 2.10. Firstly, the frequency after a major contingency is measured at a single or multiple locations in the system. Thereafter, the measurements are filtered to remove noise. In case frequency variations on multiple locations in the system are applied, the frequency at the centre of inertia is estimated using additional system data, e.g. system layout, inertia constants from synchronous generation and location of the contingency. Subsequently, the resulting frequency trajectory is fitted by a polynomial function and the time derivative is taken to determine the ROCOF.

Finally, by including information of the contingency and/or estimated frequency and voltage behaviour of the load, the system inertia is calculated.

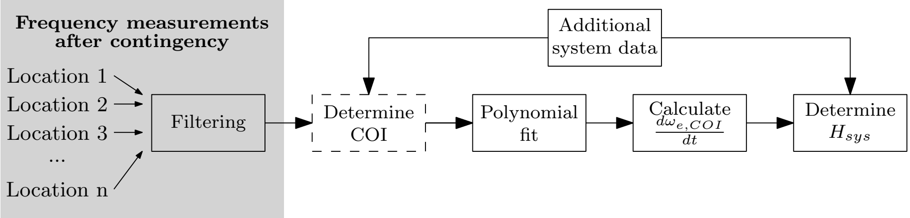

Figure 2.10: Retroactive approach

In [62], a first attempt to estimate the inertia of the 60 Hz system of Japan, using this retroactive approach, is presented. Ten over- and under-frequency events from 1992 were evaluated. The frequency from one location in the system is filtered and a fifth-order polynomial with respect to time is fitted to the measured frequency using a least square approximation. The influence of a superimposed oscillatory component resulting from an inter-area oscillation is removed. Taking the system load as base power, the inertia is estimated between 14 and 18 s. However, it remains difficult to assess the accuracy of the results since only one measurement location is used.

A more theoretical approach is developed in [63, 64]. In this work, the inertia is estimated by taking the ROCOF and active power flow at each generator bus during an event as given input variables. The authors state that their method is accurate and robust since it produces, by using different noise profiles and simulated data from generator disturbances, estimates with a median error of 1.68%. However, the method requires many measurements at different locations in the power system and can only deliver accurate results for large frequency events.

In [65], an algorithm to simultaneously perform an estimate of the time of a disturbance in a power system and the inertia immediately after a disturbance, is presented. It is demonstrated that the proposed algorithm could accurately estimate both variables if suitable tuning parameters, depending on the noise level and size of disturbance, are taken. The algorithm was applied to the data recorded by National Grid (UK) during the sequential loss of two generating units on May 7, 2008. Results show that the inertia of the system was about 9 s on a basis of 43 000 MW. The method should however be further developed to automatically adapt the tuning parameters depending on the system characteristics and to include the spatial variation of system inertia incorporating frequency measurements from different locations.

The inertia constant of the power system of Great Britain is also calculated in [66]. A similar method as presented in [62] is applied to fit the frequency transient. The study used multiple phase measurement units (PMU) spread over the system to measure the rate of change of frequency after 22 genuine generation loss events. Taking into account the inertia constants of the synchronous generators, it was estimated that the residual inertia from embedded generation and load comprises between 8 and 25% of the total system inertia.

The retroactive approach is finally applied to calculate the inertia of the Western Interconnection in North America [67]. 388 major plant outages during the study period from May 2002 through June 2004 are analysed and it is illustrated that the inertia varied over a broad range, ranging from 2-13 s on a 100 GW base. Furthermore, a linear correlation between system load, valid in the range of 70 to 115 GW, and system inertia is derived:

$$H_{\text{sys}} = 31.2 \cdot 10^{-3} \cdot P_L + 3.415 \tag{2.19}$$

with a standard deviation of 2.07 s. H_{sys} is expressed here on a 100 GW basis and the system load P_L is given in GW. The authors acknowledge that further research is required to improve the accuracy of their method.

From these studies, it can be concluded that the retroactive approach can only be used to get a rough estimate of the system inertia during a disturbance. The results are highly sensitive to the data available and to the calculation method itself. Several practical issues arise, like filtering the frequency measurements, sampling the frequency to determine the ROCOF, identifying the precise starting instance of the event, ... which makes it very hard to estimate the exact system inertia [67, 62, 68, 66]. Moreover, the swing equation (2.15), only gives a good approximation of the system frequency transient a few seconds after the power imbalance occurs. Thereafter, other control actions like the governor response, are initiated and additional parameters besides the inertia determine the subsequent frequency trajectory.

The main factors that influence the accuracy are [66]:

- Accuracy of the frequency measurement
- Location(s) of the measurements
- Identification of exact event start time
- Precise data on the size of the power loss
- Voltage and frequency dependent characteristics of the load

2.4.2 Real time inertia estimation

In 2015, a tool was developed by the Nordic Analysis Group (NAG) to estimate the inertia of the Nordic power system, comprising the synchronously interconnected power systems of Norway, Finland, Sweden and Eastern Denmark [6]. To monitor the inertia in real time, each TSO performs an estimate of its own control area, thereafter all inertia values are combined to perform an estimation on Nordic system level.

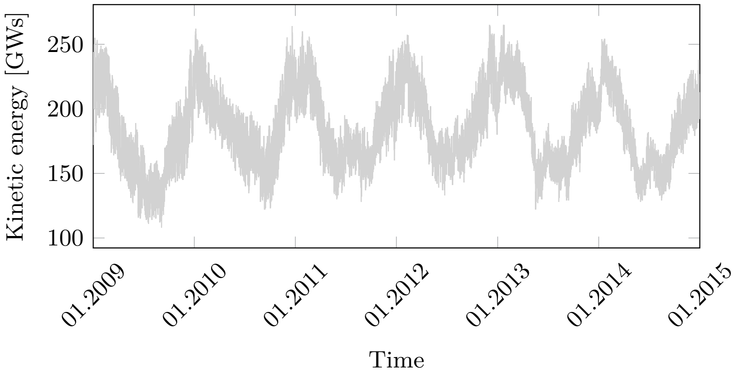

(a) Kinetic energy in Sweden, Finland and Norway

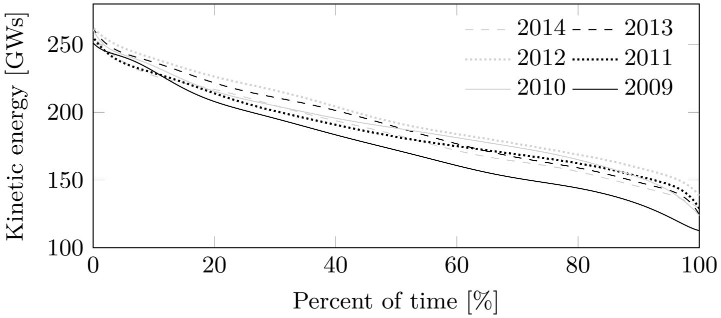

(b) Duration curves

Figure 2.11: Estimation of historic kinetic energy in Sweden, Finland and Norway [6]

In the Swedish power system, the inertia is estimated based on the circuit breaker position and corresponding inertia constant of each generator. 421 generators are included in the study which all combined have a total stored kinetic energy of 166.5 GWs. However, for 125 generators, no SCADA measurements are available to distinguish whether or not they are connected to the system. Furthermore, from 173 small generators, inertia data is missing. Therefore, the estimate from SCADA measurements is complemented with estimates of missing machines based on their production type and total system load. A similar method is applied by the Finnish TSO.

The kinetic energy for the Norwegian system on the other hand is currently estimated based on the total production corresponding to different consumptions levels. A more accurate approach as used by the Swedish and Finish TSOs is postponed to the implementation of a new SCADA system. The final tool will approximately include 2000 generating units.

Finally, in the Danish system, SCADA measurements for each generating unit over 1.5 MW are included. If the circuit breaker position of a generator unit is not known, power measurements are used to determine whether or not they are synchronized.

The results for the combined inertia values are given in Figures 2.11 and 2.12. By analysing the kinetic energy of the system within the time period of 2009 to 2015, the seasonal variation of system inertia is illustrated. The lowest kinetic energy was 115 GWs during the summer of 2009 which could be explained due to the low availability of nuclear power during that year [6].

The time dependency of inertia and the close link with system load are clearly visible, as the inertia significantly drops during night time due to the reduced number of generators connected to the power system (Figure 2.12).

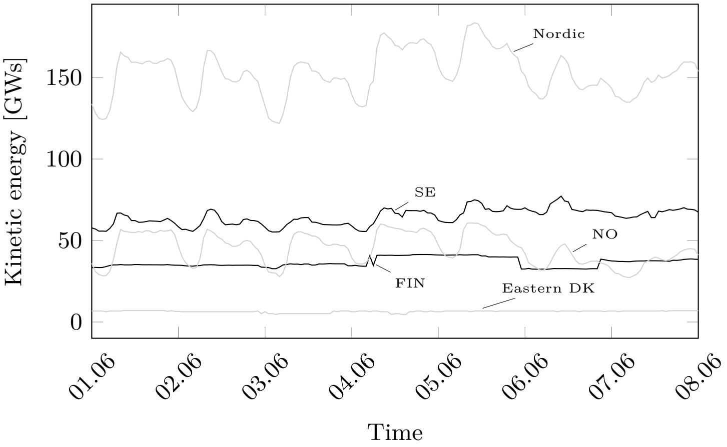

Figure 2.12: Kinetic energy in the Nordic system for a week in June (2015) [6]

Although the tool can be considered as an important first step to measure the inertia of power systems in real time and to include it in other power system operational tools, some improvements to increase the accuracy are required:

- Take into account the contribution from the load
- Increase the number of production units included
- Improve the quality of the inertia data from each unit

2.5 Conclusion

The role, quantification and measurement of inertia in a power system are discussed. The inertia perceived by the system can be considered as the resistance in the form of (kinetic) energy exchange to oppose the change in electrical frequency resulting from power imbalances in the system. With the increase of renewable power generation units, more and more of the traditional generation is displaced by converter connected generation which do not inherently provide inertia to the power system. However, novel control strategies can be developed in order to control the converter to deliver virtual inertia.

Looking at the inertia from conventional power plants and distributed generation, the inertia they provide varies over a wide range and is very technology and case specific. When reviewing the literature, no consistent values for the inertia from different generation sources can be found.

The way the total inertia of a power system can be measured is also elaborated. Different methods are presented and discussed, but none of them seems to give accurate and reliable results. Nevertheless, the real time inertia estimation tool implemented in the Nordic system can be considered as a major step towards the inclusion of inertia estimation in operation and control of a power system.

Chapter 3

Relevance of inertia in power system operation and control

“If a man will begin with certainties, he shall end in doubts; but if he will be content to begin with doubts, he shall end in certainties.”
- Francis Bacon

3.1 Introduction

An electrical power system comprises a large number of interconnected elements with different characteristics resulting in an extensive, complex and dynamic system. As it is operated in a constantly changing environment subject to varying load and generation patterns, control actions, grid disturbances, ... different dynamic interactions occur, affecting several elements or even the system as a whole.

With the expected decrease in inertia due to the displacement of conventional generation by converter connected units, it is important to assess the influence of reduced inertia on these dynamics and in this way determine the relevance of inertia in the stability, control and operation of a power system. The main challenges with respect to the different forms of power system stability are therefore identified in this chapter and some possible solutions are introduced to operate today’s power system with lower inertia.

This chapter is based on: P. Tielens and D. Van Hertem, “The Relevance of Inertia in Power Systems,” *Renewable and Sustainable Energy Reviews*, vol. 55, pp. 999-1009, 2016.

Although an increased penetration of converter connected units is considered, it is assumed that the power system still mostly relies on synchronous machines for the generation of electrical power. Current operating and control principles are therefore still applicable and the use of well-established tools and study methods to assess the impact of inertia on system stability is still feasible.

3.2 Inertia and power system stability

In order to specify the role of inertia in the changing dynamic behavior of the system due to the increased share of converter connected generation, it is important to firstly assess which types of stability or control actions could possibly be influenced if inertia is reduced. In this respect, it is examined on what time scales inertia acts and which form of stability is affected by looking at the main system variables in which the potential instability can be observed. It serves as a basis for the different stability studies presented in the following sections.

3.2.1 Time scales of power system dynamics

The dynamic interactions in today's system and the accompanied control actions are characterized by a wide spectrum of time constants (Figure 3.1). The time frame involved closely relates to the physical nature of the dynamics. These dynamics can be divided into four groups: wave, electromagnetic, electromechanical and the non-electric dynamics [33].

The fastest dynamics comprise the wave effects corresponding to the propagation of electromagnetic waves caused by lightning strikes or switching actions, ranging from microseconds to milliseconds. Slower electromagnetic phenomena occurring in the synchronous machine windings following a disturbance, fall typically within the time frame less than a second. The rotor speed of the generators connected to the system can be considered to remain almost constant within this time frame, as the inertia of the machines prevent the rotor to significantly change its speed. The oscillations in which kinetic energy is exchanged between the generators are much slower, ranging from a second to several seconds. Other dynamics within this time frame are related to the voltage and the prime mover control. Finally, the slowest dynamics given in the figure comprise for instance the thermodynamic phenomena in the boiler and the dispatch of power plants.

While inertia is not considered to play a major role in the electromagnetic phenomena, as it mainly involves damper and armature windings of the machine without influencing speed, the electromechanical oscillations alter as inertia changes. Therefore, the time frame of interest ranges from a couple of milliseconds to several seconds as indicated by the grey band. In this frame, the system dynamics are mainly governed by the natural electromechanical behaviour of the synchronous machines connected to the system. The inertia still plays a part in the much slower dynamics, though they are influenced to a much greater extent by the applied control actions.

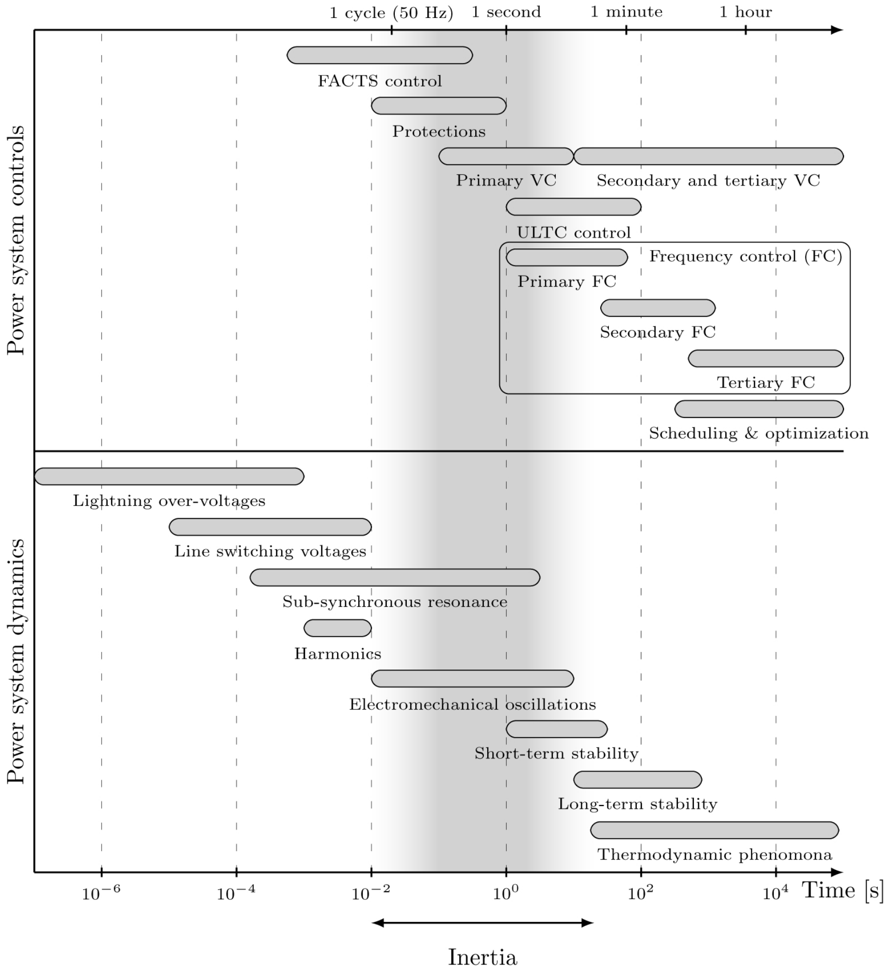

Figure 3.1: Different time frames of power system phenomena and controls in today's power system [7] (VC: Voltage Control, ULTC: Under Load Tap Changer, FACTS: Flexible AC Transmission Systems)

3.2.2 Stability and control actions of interest

Within the time frame of interest, different system controls are initiated to ensure stability after a disturbance in the system occurs. Depending on the initial operating point, the magnitude and type of disturbance, small transients or large oscillations are excited which can endanger system stability. In general, the stability is associated with the capability of the system to damp the oscillations in order to continue the operation of the system without any major impacts for the consumers connected to the network.

More formal definitions for power system stability are often applied [69]. The following definition was elaborated by IEEE/CIGRE[1] task force: "Power system stability is the ability of an electric power system, for a given initial operating condition, to regain a state of operating equilibrium after being subjected to a physical disturbance, with most system variables bounded so that practically the entire system remains intact." This stability can be applied to a part of the interconnected system or the system as a whole. The system stability can be further classified depending on the time scale and driving force of instability (generator or load) as illustrated in Figure 3.2.

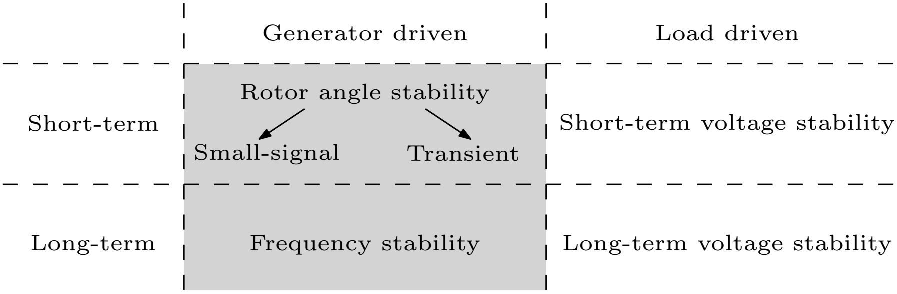

Figure 3.2: Classification of power system stability (Types of stability of interest are coloured in grey) [8]

The first type of stability that is mainly generator driven, is rotor angle stability related to the electromechanical oscillations between generators. Instability can be encountered in the form of undamped oscillations or a monotonic acceleration of the rotor leading to the loss of synchronism. Depending on the size of the disturbance, we refer to transient or small-signal stability for respectively large and small system disturbances. For the analysis of small-signal stability, it is sufficient to consider a linear model of the system around a certain operating point. The eigenvalues of the system matrix indicate the different oscillatory modes and characterize the small-signal stability [32]. For transient stability on the other hand, as large disturbance involves significant excursions of generator rotor angles, one has to take into account the nonlinear behaviour.

---

[1] IEEE (Institute for Electrical and Electronics Engineers)

Once these short-term dynamics are stabilized, the system enters a slower time frame. Looking at electromechanical oscillations, they eventually die out and a common frequency over the whole system is reached, allowing to model the system as a single bus equivalent (section 2.2.2). Frequency stability can therefore be considered as the long-term counterpart of rotor angle stability. Its stability is directly related to the capability of the system to maintain the frequency between certain limits by adjusting the power outputs of the turbines after an imbalance in active power between generation and load occurs.

As the inertia directly influences the angles and frequency in the system through the swing equation of each synchronous machine ((2.6) and (2.7)), the main focus is on angle and frequency stability.

The influence of lower system inertia on voltage stability is not considered. This voltage stability is mainly load driven, and associated with the ability of the system to keep the voltage at every node within the desired range, both during normal conditions as well as following a disturbance. Undervoltages are in this respect far more common than overvoltages and mostly occur when the reactive power demand is beyond the reactive power capacity of the resources controlling the voltage. Instability is reached when the voltage progressively and uncontrollable declines leading to the loss of load in a certain area or tripping of transmission lines. Contrary to frequency and rotor angle stability, it is mostly a phenomenon occurring locally. Nevertheless, voltage problems can spread through the system causing major blackouts [8, 32].

3.3 Impact of inertia on rotor angle stability

3.3.1 Power system modelling and methods of analysis

As introduced in the former section, rotor angle stability denotes the ability of the power system to maintain synchronism after a disturbance in the grid occurs, i.e. to keep the angular separation between the synchronous machines within certain bounds. Different distinct study methods and approaches can be applied to assess each type of rotor stability, i.e. small-signal or transient stability. The time domain approach on the other hand, is applicable to both types.

Time domain approach

From a mathematical point of view, the analysis of rotor angle stability is a strongly, nonlinear and high dimensional problem which can be accurately assessed by a time domain simulation of the whole power system. To study the electromechanical dynamics, the power system is usually represented by a set of differential algebraic equations (DAE) [7, 70][2]:

$$\frac{\mathrm{d}\mathbf{X}}{\mathrm{d}t} = F(\mathbf{X}, \mathbf{Y}, \mathbf{P}) \tag{3.1a}$$

$$0 = G(\mathbf{X}, \mathbf{Y}, \mathbf{P}) \tag{3.1b}$$

where $\mathbf{X}$ ($\mathbf{X} \in \mathbb{R}^{n_x}$) denotes the vector of state variables and $\mathbf{Y}$ ($\mathbf{Y} \in \mathbb{R}^{n_y}$) indicates the vector of instantaneous (algebraic) variables. $\mathbf{P}$ ($\mathbf{P} \in \mathbb{R}^{n_p}$) explicitly represents the vector of parameters, which influence the dynamics under study. Algebraic equations are used to describe the network, the generator's stator equations and static loads. The remaining equipment and the dynamics of the synchronous machines are represented by the set of differential equations (e.g. the swing equation, damper windings, ...).

Although this time domain approach can exactly assess the stability after a disturbance by step-by-step solving (3.1), and is in some way indispensable for an in-depth analysis of the angle stability of a system, it is often unable to provide sound stability margins or clear guidelines for the control to improve stability [71]. Furthermore, for small-signal stability analysis, it may not capture the poorly damped modes in the system in case the disturbance or input parameters are not properly chosen, which could lead to misleading results [72].

Transient stability assessment: Direct methods

In addition to the time domain approach, direct (Lyapunov-like) methods are often applied in transient stability studies.

These methods attempt to assess the stability of the power system by constructing a Lyapunov function $V(\mathbf{X}) : \mathbb{R}^{n_x} \mapsto \mathbb{R}$ for the dynamic system model. A function representing the total energy of the system is mostly taken, usually referred to as Transient Energy Function (TEF) [71]. By evaluating the function at the disturbance clearing time (post-fault system), and comparing this value with the value of the Lyapunov function on the boundary of its stability domain, the transient stability of the system can be evaluated.

---

[2] Matrices and vectors are denoted in bold throughout the remainder of the text

The transient stability assessment of the multi-variable system of (3.1) is in this way reduced to the study of a scalar function. Furthermore, contrary to numerous repetitive runs required in the time domain approach, only a single time domain simulation during the fault period is mostly required.

The main drawbacks are the practical application in large complex power systems, as the TEF and its associated stability region can not be computed easily, except for comparatively simple systems. Furthermore, if losses are included in the system model, the stability test provided by the TEF is only sufficient, not necessary [71].

One of the simple, yet powerful graphical application of the Lyapunov's direct method is the equal area criterion (EAC), which can help in understanding the main factors influencing the transient stability of an (equivalent) two-machine system [73, 41]. The equal area criterion is illustrated in Figure 3.3 for a fault with zero fault resistance on a single machine infinite bus system (SMIB), where the classical machine model (second order) with zero damping is used to represent the synchronous machine.

In case the network resistance is neglected, the swing equation of the machine during pre-fault and post-fault operation is:

$$\frac{\mathrm{d}^2\delta}{\mathrm{d}t^2} = \frac{P_m \cdot \omega_{e,0}}{2H} - \frac{P_e \cdot \omega_{e,0}}{2H} = \frac{P_m \cdot \omega_{e,0}}{2H} - \frac{P_{max} \cdot sin(\delta) \cdot \omega_{e,0}}{2H} \tag{3.2}$$

Both the mechanical input and electrical output power in function of the rotor angle are shown in Figure 3.3(b), the initial operating point (δ_0) is located at the crossing of both curves. When a three-phase fault with zero fault impedance is applied at the generator terminals, the electrical output (P_e^{DF}) during the fault becomes zero until the fault is cleared and the machine starts to accelerate ($\frac{\mathrm{d}^2\delta}{\mathrm{d}t^2} > 0$). If the system is capable of regaining synchronism after fault clearance, the rotor angle finally returns back to its pre-fault state.

In essence, the EAC states that the faulted system can still reach this equilibrium and recover stability as long as the kinetic energy gained during the fault (represented by the area A_1) is smaller than the kinetic energy lost during deceleration after fault clearance (A_2). The borderline case ($A_1 = A_2$) is shown in Figure 3.3(b).

In this case, the fault is cleared at a critical angle at which the requirement of the EAC can still be satisfied, called the critical clearing angle (CCA) which is for this particular system:

$$\delta_{cr} = cos^{-1}((\pi - 2\delta_0) \cdot sin\delta_0 - cos\delta_0) \tag{3.3}$$

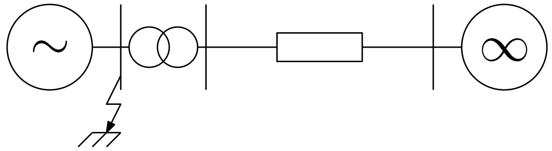

(a) SMIB

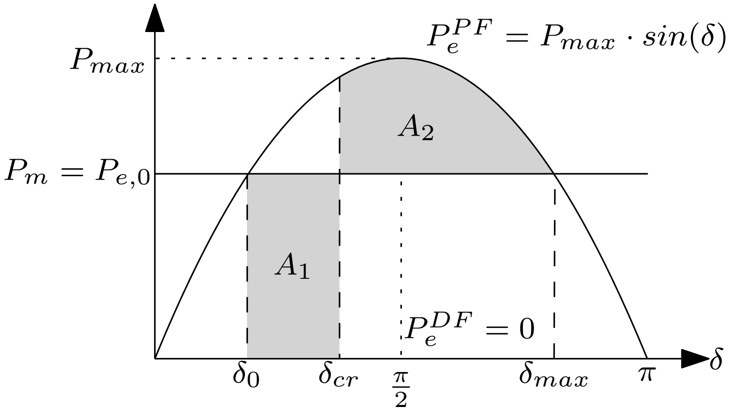

(b) Power angle curves before, during and after the fault: A_1 is equal to A_2 corrsponding to a fault cleared at the critical clearing angle δ_{cr}

Figure 3.3: Equal area criterion for a three-phase fault on a SMIB system

By integrating (3.2), the time to reach this CCA which is defined as the critical clearing time (CCT), is determined:

$$t_{cr} = \sqrt{\frac{4(\delta_{cr} - \delta_0)}{P_m \cdot \omega_{e,0}}} \cdot \sqrt{H} \tag{3.4}$$

Both the CCT and CCA are often used as system stability indicators since the difference between the actual clearing angle and clearing time and respectively the CCT and CCA defines the transient stability margin of the system [73].

Small-signal stability assessment: Eigenvalue analysis

Small system stability analysis concerns the study of the stability of the system given in (3.1) for small disturbances around its stationary or equilibrium point $(\mathbf{X_0}, \mathbf{Y_0})$. Analyzing the small-signal stability is typically done through an eigenvalue analysis of its state matrix [32, 7]. The state matrix is obtained from the Jacobian matrix ($\mathbf{J}$), determined by linearizing the DAE system around the equilibrium point:

$$\begin{bmatrix} \frac{\mathrm{d}\mathbf{\Delta X}}{\mathrm{d}t} \\ \mathbf{0} \end{bmatrix} = \begin{bmatrix} \frac{\mathrm{d}\mathbf{F}}{\mathrm{d}\mathbf{X}} & \frac{\mathrm{d}\mathbf{F}}{\mathrm{d}\mathbf{Y}} \\ \frac{\mathrm{d}\mathbf{G}}{\mathrm{d}\mathbf{X}} & \frac{\mathrm{d}\mathbf{G}}{\mathrm{d}\mathbf{Y}} \end{bmatrix} \begin{bmatrix} \mathbf{\Delta X} \\ \mathbf{\Delta Y} \end{bmatrix} = \begin{bmatrix} \mathbf{F_X} & \mathbf{F_Y} \\ \mathbf{G_X} & \mathbf{G_Y} \end{bmatrix} \begin{bmatrix} \mathbf{\Delta X} \\ \mathbf{\Delta Y} \end{bmatrix} = \mathbf{J} \begin{bmatrix} \mathbf{\Delta X} \\ \mathbf{\Delta Y} \end{bmatrix} \tag{3.5}$$

The state matrix ($\mathbf{A}$) is calculated by eliminating the algebraic variables:

$$\mathbf{A} = \mathbf{F_X} - \mathbf{F_Y} \cdot \mathbf{G_Y^{-1}} \cdot \mathbf{G_X} \tag{3.6}$$

The eigenvalues of $\mathbf{A}$ correspond to the natural modes of the system. To ensure small-signal stability, all eigenvalues need to have negative real parts.

For a conjugated pair of complex eigenvalues ($\alpha \pm \omega j$), corresponding to an oscillatory mode, the real part gives the damping and the imaginary part represents the frequency of oscillation. The damping ratio is finally defined as:

$$\zeta = \frac{-\alpha}{\sqrt{\alpha^2 + \omega^2}} \tag{3.7}$$

3.3.2 Inertia and transient stability

It is clear that inertia is directly linked to the CCT of the synchronous machine in the SMIB case (3.4). The increase in inertia leads to higher critical clearing times (Figure 3.4). However, if this network is extended to a simple two area system, represented by two synchronous machines and two loads, also the distribution of the inertia plays an important role.

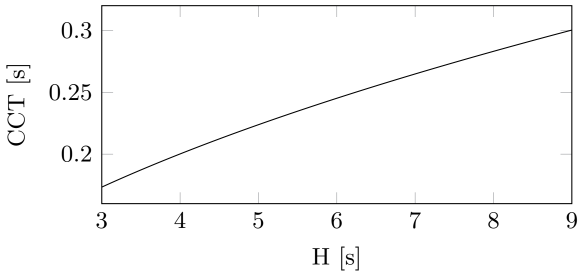

Figure 3.4: Critical clearing time in function of inertia for the network and fault considered in Figure 3.3(a) ($P_m = 0.8$ $p.u.$ and $\delta_0 = 0.594$ rad)

Consider for example the system shown in Figure 3.5(a), with area 1 the exporting and area 2 the importing area. If a fault is applied in the middle of the line, the voltage drop at the load buses predominantly determines the electromechanical power balance within each area. In case constant power loads are assumed, the generators in area 1 and 2 respectively accelerate and decelerate. Increasing the inertia in both areas will improve the stability since the rate at which the rotor angles deviate during the fault is reduced. This corresponds with the calculated CCT values given in Figure 3.5(b). The CCT is determined by applying the (extended) equal area criterion, which can be used to asses the stability of a two machine equivalent of a power system [74].

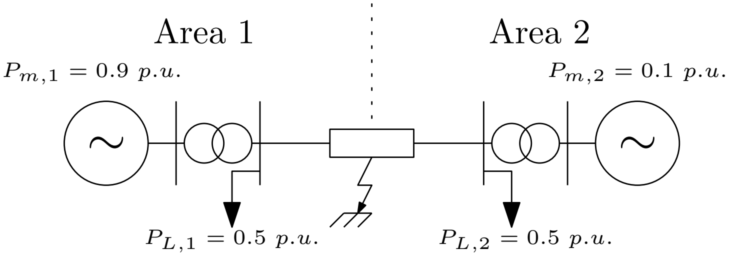

(a) Simplified two area system

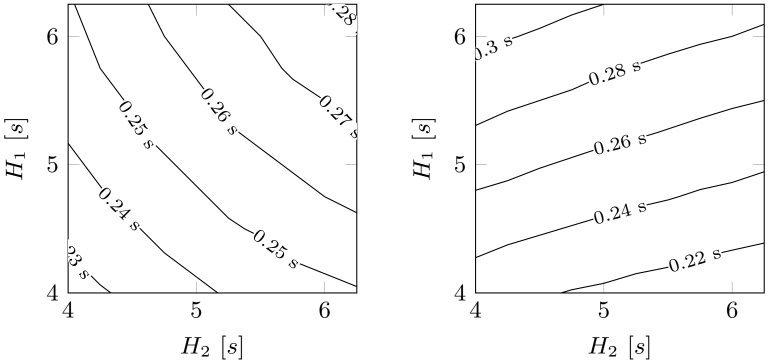

(b) Constant power loads: Contour plot of CCT

(c) Constant impedance loads: Contour plot of CCT

Figure 3.5: Critical clearing times for a simplified two area system in function of inertia

On the other hand, if the loads are modelled as constant impedances, the voltage drop leads to a substantial reduction in demand, causing both equivalent machines to accelerate during the fault. To acquire an equal acceleration in both areas, the inertia should be scaled according to the power imbalance. Therefore, contrary to the case of constant power loads, the highest CCT is now obtained with a low inertia in area 1 and a high inertia in area 2 (Figure 3.5(c)). Looking at this simplified model, an increased system inertia is thus not directly linked to an improvement of the transient stability.

Although the application of the equal area criterion to these simplified cases can give a first insight in the role of inertia in the transient stability of a power system, it does not take into account the generator controllers and protection mechanisms. Furthermore, only the inertia constant of the generators is varied, while the decrease of inertia within a part of the system or the system as a whole actually goes hand in hand with the replacement of synchronous generators by converter connected generation. To study the effect of these converters and the generator controllers, a more detailed model of the power system is required and time domain simulations are needed to assess the transient stability.

Therefore, as a final study case, the original test system (appendix B.1) is modified (Figure 3.6(a)), in order to assess the transient stability including detailed generator and converter models. One of the load buses of the original system is connected to a strong external system through a double transmission line. The three loads now each have a power demand of 3 MW and the power generation is distributed equally among three generation centres ($G_{1,2,3}$ and G_4 is switched off) to obtain a power export to the external system of 70 MW. In order to stepwise displace the synchronous units by the converter connected generation, the remaining generation centres are assumed to comprise three equal synchronous machines (a, b and c), each having an inertia constant of 3 s and equipped with a governor and exciter. In the base case, all synchronous units are connected to the system providing spinning reserve, the converters do not produce any power. Gradually, some of the synchronous units from each generation center are disconnected resulting in a decreased inertia of the power system (the spinning units are listed in Figure 3.6(b)). The lost power generation is compensated by an increased power output from the remaining generators or from the converter connected generation. The CCT for a fault on one of the lines linked to the external system is given in Figure 3.6(b).

Looking at the case without converter connected generation, represented by the grey bars, similar results as for the former SMIB system are obtained. A reduction in inertia leads to lower CCT's.

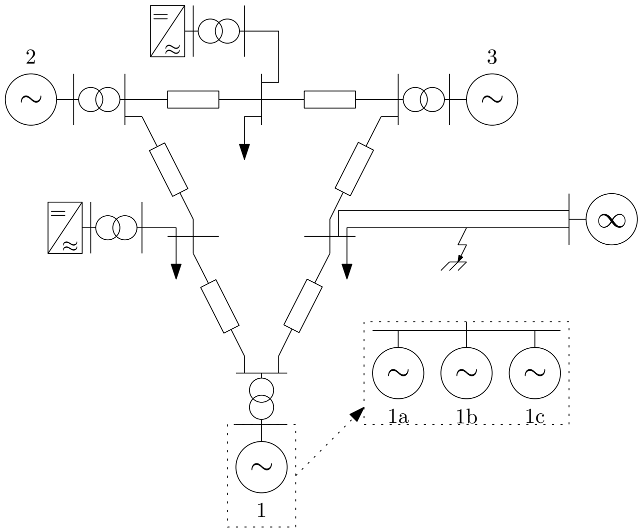

(a) Modified test system

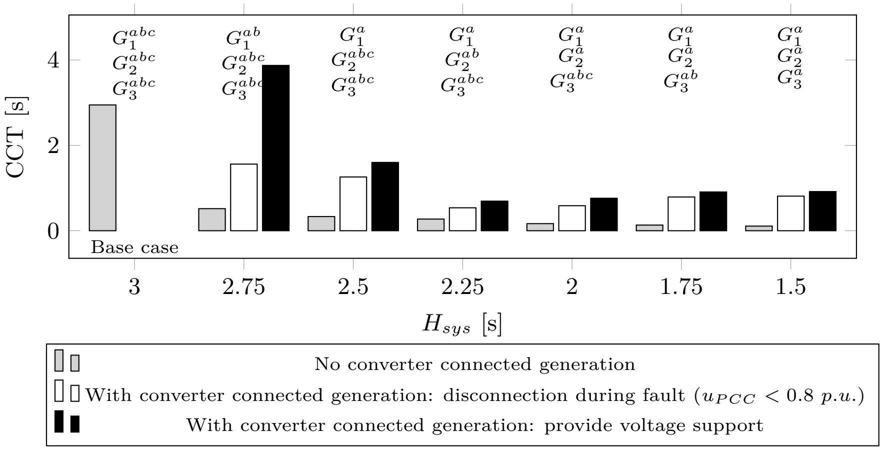

(b) CCT of different scenarios

Figure 3.6: Transient stability assessment after a three-phase fault on the modified test system (system base is taken equal to the total synchronous generator capacity of the base case)

When the converter connected generation compensates for the reduced power output due to the disconnection of the synchronous generation units, the CCT also depends on the way the converters react during and after the fault, typically defined in the grid code. This grid code generally sets some requirements to the converters, such as the voltage ride through in terms of minimum voltage magnitude and recovery slope the converter should be able to withstand without disconnection, also denoted as the fault ride through (FRT) capability of the unit. Additionally, also voltage support is often required by means of reactive current injection during fault and recovery [10]. As the detailed behaviour of these converters under grid faults and the accompanied fault current contribution strategies is out of the scope of this work, only two basic cases are considered[3].

Firstly, it is assumed that the converters are allowed to disconnect during the fault (white bars in Figure 3.6(b)). Secondly, the converters stay connected and offer voltage support during the fault by increasing their reactive power output proportionally to the voltage deviation at the point of common coupling (PCC) (black bars in Figure 3.6(b)). Both options result in a substantial increase in CCT compared to the case without converters. For this system, the impact of the reduced inertia on the transient stability after a fault on the tie-line is in some way compensated by the behavior of the converters, improving the transient stability of the remaining generators, although a general trend in decreasing CCT for decreasing inertia can still be noticed.

Additionally, due to the displacement of synchronous generators by converter connected generation, not only the applied technology, but also the location of the generation changes. Assuming that the load centers are not altered, flow patterns on the system can be substantially impacted. The power flows on individual transmission lines, and more importantly, on interregional paths are critical for the transient stability. Also the dynamic behavior of all converter units, in terms of voltage support and FRT capability, along with the accompanied transmission reinforcements, substantially impact the bulk power system [76]. It is therefore difficult to draw general conclusions on the influence of inertia on transient stability and a more case specific approach is often required.

A more elaborated study on the effect of this increasing distributed generation (DG), considering both induction motors and inertialess converter connected units, on transient stability can be found in [73]. A maximum penetration level of converter connected generation in terms of transient stability cannot be solely based on the amount of synchronous inertia in the system, but significantly depends on the reactive power scheme and the network topology. Increasing the reactive power and fault ride through capability from distributed generators, can help to reach high levels of non-synchronous generation without jeopardizing transient stability. Another option to improve stability, is assigning certain classical power plant as synchronous condensers that can provide synchronous inertia and in addition also deliver the necessary amount of reactive power [73]. Furthermore, it is concluded that, as most of the DG is installed in distribution grids close to the load, the power flows in the transmission grid can be reduced compared to the case with only conventional generation. This inherently improves the transient stability of the transmission system as large power flows may have a detrimental effect on the damping of oscillations.

---

[3] More information on different fault current contributions strategies can be found in [75] and an overview of the grid requirements for converter systems during faults can be found in [10]

Focusing on converter connected wind power, similar conclusions hold. It is shown that doubly fed induction generators connected wind turbines can have both beneficial as detrimental effects on transient stability depending on the grid layout and location of the wind turbines [77, 78, 79]. The optimal control, during and after the fault, to stabilize the grid and increase the stability is investigated in more detail in [80, 78, 49]. Using the capability of converters to deliver voltage and reactive power support after a fault, the transient stability margin of the remaining generators increases.

Less research is being conducted to reveal the impact of the integration of PV units on transient stability. The fault ride through capability of PV units is highly important to ensure transient stability as the loss of distributed PV units may result in large oscillations during moments of high PV penetration as observed in [81]. Other research illustrates both the beneficial as well as the adverse effects on stability of increasing PV penetration depending on system layout, location of PV units, ... [82, 83].

3.3.3 Inertia and small-signal stability

Power systems contain a large number of natural oscillatory modes due to a variety of interactions of its components. Many modes are related to the swinging of the generator rotor masses relative to one another. These modes are typically located in the sub-synchronous frequency range and may be either global or local in nature. Local modes are often associated with a single generator oscillating with respect to the rest of the system or involve the oscillations between a few generators close to each other. Global oscillations on the other hand include the interactions among large groups of generators (so called inter-area mode oscillations).

For a reliable system operation, all modes should be sufficiently damped under all expected system conditions. The damping of these modes however depends on many system parameters and may be negatively influenced in the presence of controls, such as high responsive AVRs (Automatic Voltage Regulators), which are practically the only source of negative damping [84]. In practice, the damping of a mode is considered to be satisfactory in case the damping ratio $\zeta \geq 0.05$ [33].

The effect of decreasing the inertia is mainly reflected in the frequency of these electromechanical modes. Referring back to the SMIB case (Figure 3.3(a)), the undamped natural frequency and damping ratio of the rotor angle mode using the classical machine model are equal to [85]:

$$\omega = \sqrt{\frac{P_{max} cos\delta_0 \cdot \omega_{e,0}}{2}} \cdot \sqrt{\frac{1}{H}} \tag{3.8}$$

$$\zeta = \frac{K_D}{2\sqrt{2P_{max} cos\delta_0 \cdot \omega_{e,0}}} \cdot \sqrt{\frac{1}{H}} \tag{3.9}$$

with K_D the damping torque coefficient, accounting for the mechanical rotational losses and the damping due to damper windings [33]. Both damping ratio and frequency of the mode decreases for increasing inertia values.

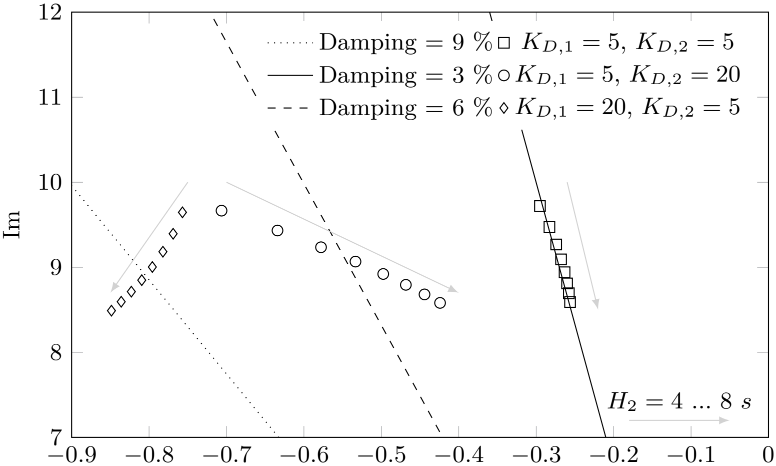

Figure 3.7: Eigenvalue loci of the electro-mechanical modes for the two area system as depicted in Figure 3.5(a). $H_1 = 4\ s$ and H_2 is varied from 4 to 8 s in steps of 0.5 s.

By calculating the eigenvalue of the two area system (Figure 3.5(a)) associated with the electromechanical mode between the two generators, it is clear that the inertia mainly determines the frequency of the mode (Figure 3.7). H_1 is kept constant and the eigenvalue loci for varying H_2 are plotted for different damping torque coefficients. The damping ratio not only depends on these damping torque coefficients, but also on the power transfer and inertia constants.

In case of reduced system inertia due to an increased penetration of converter connected units, not synchronously linked to the system, several studies confirm that the electromechanical modes of the system are altered [86, 87, 77]. There is however no general consensus about the specific impact of the increased penetration of inertialess units on these modes and on small-signal stability in general.

In [88], the effect of large scale wind power on small-signal stability is discussed. The influence of converter connected wind generation mainly depends on the location, operating mode and penetration of wind power together with the loading level of the system and the control of the converter.

Looking at the research related to the impact of PV on small-signal stability [82, 89, 90], no convergent results are visible as well. In [82], the impact of different penetration levels of large-scale and distributed PV generation on small-signal stability, using real network data of the power system of Ontario and its neighbouring systems, is investigated. The performed eigenvalue analysis shows that there is no major effect on the small-signal stability. The study presented in [89] on the other hand concluded that in case system inertia decreases due to the decommitment of conventional units, the eigenvalues are moved toward the right half plane, resulting in a deteriorated damping performance. Moreover, stability is highly sensitive to the location of the utility scale PV units. In this work, the IEEE 39-bus New England system was chosen as test system. Finally, in a study on the western North American power system, the frequency of the north south inter-area modes increases in frequency while the damping ratio was almost unaltered as renewable generation increases [90].

Similar conclusions as for the transient stability assessment can therefore be drawn, i.e. the decrease in inertia is in most cases directly linked to the increase of converter connected generation which can both improve as well deteriorate the small-signal stability depending on many system parameters, such as the control and location of the units together with the changing flow patterns within the system.

3.4 Impact of inertia on frequency stability

3.4.1 Mechanisms for frequency stability and control

The frequency within an AC interconnected power system, also denoted by synchronous area, is dedicated by the speed of the synchronous generators connected to it. In steady state, this frequency is the same throughout the system, equal or close to its rated value (e.g. 50 Hz in Europe and 60 Hz in North America). At the instant an imbalance between the generated and consumed active power occurs, the frequency alters as the power deficit or surplus is not instantaneously compensated by a corresponding increase or decrease in mechanical turbine power of the connected power plants.

The imbalances in generated and consumed power causing the frequency to deviate can generally be classified into two groups [14]:

- Power imbalances during normal (continuous) operation: due to the random on and off switching of load devices, intermittent power generation from renewable energy sources or even market driven events (e.g. the scheduling of energy market contracts [91])
- Contingency: undesirable power imbalance after an event, e.g. power plant outage or a large load step

For satisfactory operation of the system, the frequency has to remain at all times within a narrow range around the rated value as specified in the grid codes [92]. A substantial drop in the frequency will not only lead to high magnetization currents in transformers and induction motors, but may also detrimentally affect the performance of conventional power plants. Operating at a reduced frequency results for instance in a decreased ventilation of the synchronous generator and leads to additional vibrational stresses on the turbine blades. As the effects are cumulative with time, the frequency has to be quickly restored [93]. Additionally, since the speed of all grid connected motors is directly linked to the frequency, also the performance of the auxiliary equipment (fuel, feed-water and combustion air supply systems) is impacted [94]. In case of combined cycle gas turbines (CCGT) for instance, a drop in frequency leads to a reduction of the airflow into the combustion chamber, since the compressor synchronously rotates with the system frequency. Especially at base load, when the inlet guide vanes are already fully open and can not offset the reduction in airflow, the exhaust temperature quickly rises. As this temperature increases, the temperature control system reduces the fuel flow and the power output is decreased [95].

The critical frequency at which the performance of the equipment will affect the plant capability highly depends from plant to plant, but additional safeguards should be considered in order to protect the plant and trip the unit in case of an excessive frequency excursion [96]. Furthermore, as the frequency might be applied for timing purposes, there are also requirements on the discrepancy between the actual time and the time corresponding to the integrated frequency from the system [32].

Accordingly, in order to stabilize and restore the frequency after a power imbalance, different control mechanisms are activated in a power system (see Figure 3.8 for an underfrequency event). The response from the moment of the disturbance to the restoration of the frequency can roughly be divided into four stages:

1. Inertial response
    (a) Distribution of initial power impact and rotor swings
    (b) Synchronized frequency drop
2. Primary (governor) control action
3. Secondary control action
4. (Tertiary control action)

As indicated by the hatched area in the figure, immediately after the power balance in generated (P_G) and consumed (P_L) power is disturbed (in this case a substantial loss in power generation), the synchronous connected units release their kinetic energy in the grid to counteract the frequency deviation and to provide a natural time delay for the governors of the power plants. Within this first phase, the power impact is distributed over all synchronous machines each experiencing a different change in rotor angle and speed. Once these oscillations are damped out, a common frequency decline among the whole system is reached [14].

Meanwhile, all generators equipped with a speed controller or governor, jointly act as soon as the frequency exceeds a certain dead band (± 20 mHz within the synchronous grid of Continental Europe [97]), by increasing the power output of the prime mover proportional to the speed deviation of the machine. Depending on the type of governor and turbine, several time delays in the order of seconds are introduced in this process [92]. Consequently, because of this local control action, also known as primary control, the frequency deviation is limited and the balance between power generation and load is restored. Due to the proportional action, the frequency is stabilized during this process, yet still deviates from its rated value with an offset equal to Δf_{ss}.

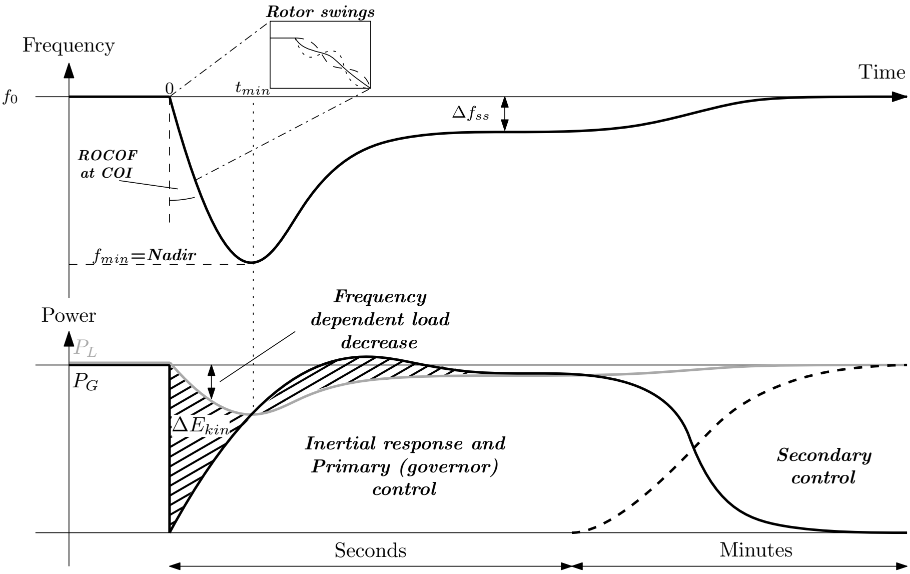
Rotor swings
Frequency
Time
f_0
0
t_{min}
Δf_{ss}
ROCOF at COI
f_{min}=Nadir
Power
Frequency dependent load decrease
P_L
P_G
ΔE_{kin}
Inertial response and Primary (governor) control
Secondary control
Seconds
Minutes

Figure 3.8: Typical frequency response after a substantial loss in active power generation

The restoration of the frequency is accomplished in the next stage, also called secondary control, by further adjusting the power setpoints of prime movers within selected units. This extra control action is much slower than the governor action, with a time constant in the range of 10-15 min. Depending on the system, a manual adjustment of the setpoints is made (e.g. the Nordic system [98]) or the control is automated, typically the case in large systems such as the synchronous grid of Continental Europe [97]. Here, the secondary control is actually part of an integrated platform called the automatic generation control (AGC). This AGC actuates on system level and, besides regulating the frequency back to rated, also adjusts the power references of the generation units to maintain the power exchange between different control areas at their scheduled values [14]. For the sake of completeness, generally also a tertiary control action is implemented, which restores the secondary control reserves used or provides the most economically allocation of these reserves within the set of generating units in service [32].

All operating reserves, both at the demand as the generation side, that need to be allocated to adequately control the frequency in order to maintain it between strict boundaries, are contracted by the TSO who has the final responsibility to ensure frequency stability. Reserves can be categorized depending on the type of power imbalances they correspond to (during normal operation or contingency), the direction of response (up- or downward) or on the timescale of their activation which can be directly linked to the previously described control mechanisms [99, 100]. In Europe for instance, in an ongoing harmonization process within the ENTSO-E (European Network of Transmission System Operators for Electricity) zone, the different operating reserves are defined as Frequency Containment Reserves (FCR), Frequency Restoration Reserves (FRR) and Replacement Reserves (RR) corresponding to respectively the primary, secondary and tertiary control action [101][4]. The required FCR are usually sized to assure that the frequency is properly stabilized after a reference incident, corresponding to the maximum expected instantaneous power deviation between generation and demand within the synchronous area. In continental Europe, the present reference incident corresponds to the loss of the two largest nuclear units, equal to a total power capacity of 3000 MW [101].

In case there are insufficient reserves available or a poor coordination between the control and protection equipment exists, a severe imbalance in generation and load can lead to frequency instability, defined as the inability to maintain the system frequency within the specified operating limits [69]. This may result in a cascade tripping of (renewable) generation units, system splitting and/or load shedding, which can be considered as a last resort measure to stabilize the frequency and thereby prevent widespread outages or even a total blackout of the system.

3.4.2 Frequency and ROCOF operating ranges

The frequency operating range is defined in the grid codes and sets a certain tolerance around the nominal frequency within which generators should remain connected to the transmission grid. For large interconnected systems, this tolerance is mostly around ±2 %, while in smaller or island systems, slightly larger bands are required as frequency control is more challenging. Outside these frequency bands, generators must remain connected for a certain amount of time or may disconnect immediately [102]. An overview of the frequency bands defined by a number of TSOs within ENTSO-E and North America is given in Figure 3.9. In Figure 3.9(a), ENTSO-E Requirements for Generators (RfG) refers to the recently established European network code on the requirements for the grid connection of new generator facilities. It covers the requirements for different type of power plants with the aim of harmonizing the connection rules within each synchronous area. This network code is in force under European law since may 2016 and will be adopted by each country and hence TSO in the coming years [13].

---

[4] As a result of the harmonization, the different control actions are nowadays denoted within ENTSO-E by frequency control, frequency containment and frequency restoration process. However, as the traditional terminology is still widely used by many TSOs, the terminology of primary, secondary and tertiary control action is adopted in this work.

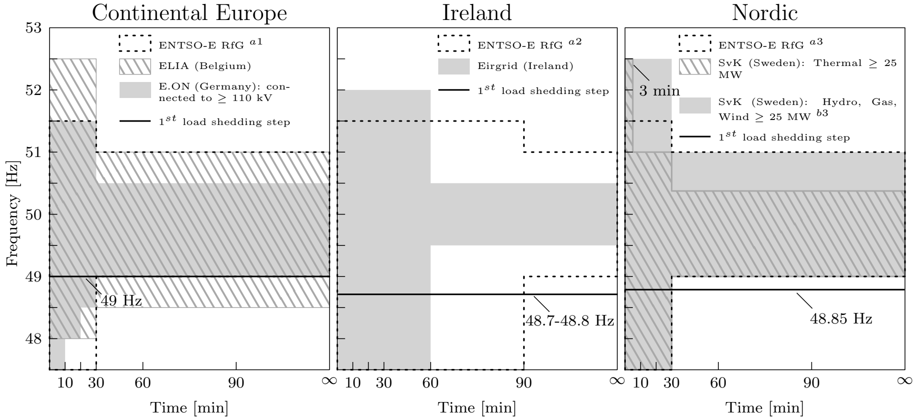

[a1] 47.5-48.5 Hz: To be specified by each TSO (≥ 30 min)
[a1] 48.5-49 Hz: To be specified by each TSO (≥ the period for 47.5-48.5 Hz)
[a2] 48.5-49 Hz: To be specified by each TSO (≥ 90 min)
[a3] 48.5-49 Hz: To be specified by each TSO (≥ 30 min)
[b3] Wind allowed to trip at 52 Hz

(a) ENTSO-E synchronous areas [103, 104, 105, 102, 106, 10] (load shedding steps as proposed by the ENTOS-E network code on Emergency and Restoration)

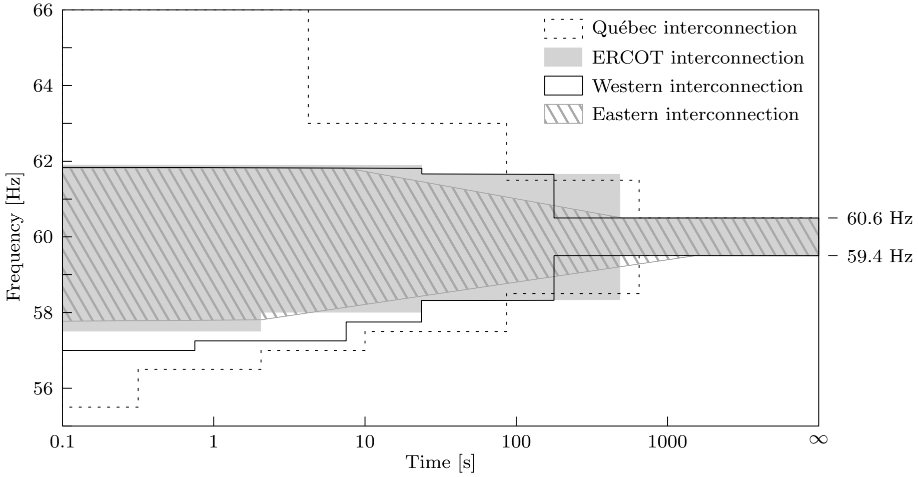

(b) North America [107]

Figure 3.9: Frequency capability curve for synchronous areas within ENTSO-E (a) and North American Electric Reliability Corporation (NERC) (b)

Due to the increasing penetration of distributed generation connected to the medium and low voltage network, it becomes increasingly important that these (smaller) units also become compliant with this RfG network code. In the early years of the installation of DG units, no appropriate standards and connection requirements were yet developed. Consequently, a substantial number of DG units have nowadays frequency disconnection settings in the range between 49.5 - 50.5 Hz, which can lead to cascading outages during a frequency event. In order to ensure system stability during major contingencies, ENTSO-E encourages all of it members to bring the frequency disconnection settings of the units in line with the network codes at transmission level. Two countries within ENTSO-E, Germany and Italy, have already launched large programs to retrofit the settings of non-compliant units [108].

With respect to load shedding, the specific frequency at which the first load shedding step is activated and the amount of load disconnected at each step depends on the implemented load shedding scheme, often designed nationally (see [109] for an extensive overview).

Besides the allowed frequency range, it is important to analyse the admissible ROCOF immediately after the imbalance. This ROCOF is often used in combination with the frequency deviation to trigger load shedding relays as it provides a more selective and/or faster operation. Due the rotor swings following an event, the ROCOF oscillates. Therefore, an average of the measured instantaneous ROCOF values is generally used [110].

Moreover, the ROCOF should be limited to prevent false tripping of ROCOF relays within low and medium voltage networks, often applied to protect distributed generation against islanding [111, 112]. Islanding occurs when a part of the power system becomes electrically isolated from the rest of the power system, yet continues to be energized by generators connected to the isolated subsystem. When islanding occurs, local generation does not exactly balance the remaining load. Consequently, frequency changes rapidly, depending on the power imbalance and the inertia of the islanded subsystem. This triggers the ROCOF relay and the islanded subsystem is disconnected. Typical ROCOF relays, installed in a 50 Hz system, are set between 0.1 and 1 Hz/s, depending on the inertia of the power system [113]. The amount of generation protected against islanding by this type of relay (instead of a vector shift relay for example) is system dependent. In Ireland for instance, almost half of the wind generation is connected to the distribution grid and uses this type of relay [114]. To prevent the risk of cascading disconnections, the ROCOF should in this system thus not exceed the trigger setting equal to 0.5 Hz/s.

Additionally, it is not yet clear what the impact of a high ROCOF event is on conventional generating units. For power systems within large synchronous areas, requirements of the allowed ROCOF range, ensuring a continuous and uninterrupted operation of the power plants, are often missing in the grid codes since large sustained frequency gradients are quite rare. In the power system of continental Europe for instance, ROCOF values of only 5 - 10 mHz/s are observed after a power plant outage of 1 GW. Also during more serious contingencies such as the system disturbance on 4 November 2006 or the Italian blackout of 2003, the frequency gradients remained below 1 Hz/s. Nevertheless, within the drafting process of the most recent ENTSO-E network code for generators (RfG), it was initially included that all generation units should remain connected up to an estimated 2 Hz/s in order to handle a system split with unbalances of at least 40% [104]. The limit was however removed from the last version and the responsibility for setting the maximum value was returned to the individual TSOs [13].

In smaller islanded systems on the other hand, a ROCOF limit is mostly already defined as these systems are likely to experience fast frequency transients [115]. Again in Ireland, power generation units must for instance remain connected up to 0.5 Hz/s (measured over a 500 ms time window) [114]. Further investigations are currently ongoing to study whether it is feasible to increase this limit to 1 Hz/s without leading to a catastrophic power plant failure or substantially impacting the plant-life [116, 117, 118]. However, as voltage dips during faults, which are common in power systems, lead to short-duration ROCOF values in excess of 1 Hz/s and the forces experienced on the machine shaft can be considered more severe than during a loss-of-generation event, the TSOs (EirGrid and SONI) do not expect any issues with increasing the limit. Moreover, bilateral discussions with wind turbine manufactures indicate that also wind turbines (DFIG and full converter) can easily handle ROCOF values up to 4 Hz/s [118], although further research is required to assess the impact of very high ROCOF on their control and protection systems.

In the following sections, the influence of a decreased system inertia on the inertial response and primary control action is investigated. Secondary control is not further discussed, since it is considered to be hardly affected by a variation in system inertia due to its operation on a longer time scale.

3.4.3 Inertial response

Before governor control is initiated, the frequency response at the COI upon power imbalances is largely influenced by the system inertia H_{sys}. The frequency in function of time is in per unit by[5]:

---

[5] In the following, it is always assumed that ΔP_L is positive, i.e. the load power is higher than the generated power ($P_L > P_G$). The same analysis can be made for negative ΔP_L.

$$\omega_{e,COI}(t) = 1 - \frac{\Delta P_L}{2H_{sys}} \cdot t \tag{3.10}$$

During this phase of the frequency response, the power imbalance is mainly covered by the kinetic energy, withdrawn from the synchronous machines. The system inertia provides in this way an energy buffer to allow sufficient time for the governor control to react. As the ROCOF and H_{sys} are inversely proportional, low system inertia can result in very high ROCOF values (Figure 3.10(a)).

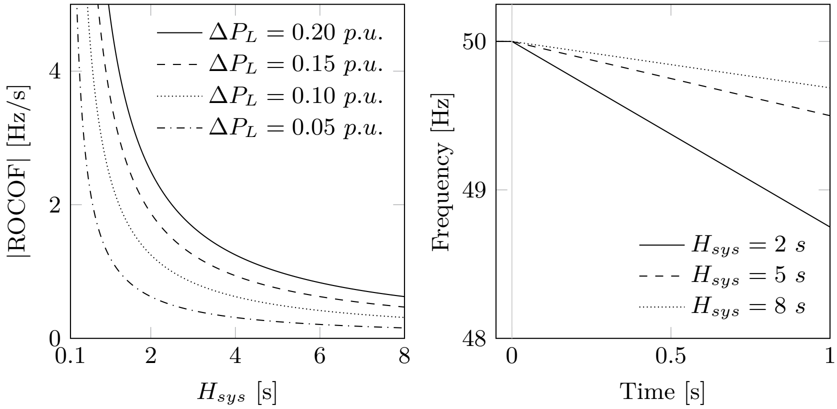

(a) Rate of change of frequency

(b) Frequency for $\Delta P_L = 0.1\ p.u.$

Figure 3.10: Inertial response: Rate of change of frequency (a) and frequency (b) at the center of inertia after a power imbalance

In Figure 3.10(b), the frequency as a function of time is given for a power imbalance of 0.1 p.u.. It highlights that for a given imbalance, the frequency drop is much larger and faster if inertia is decreased. For a lower H_{sys}, the governor control therefore needs to react sooner to cease the frequency decline before it reaches critical values. Taking for instance the load shedding settings as defined within the ENTSO-E grid code for continental Europe (Figure 3.9(a)), a substantial power imbalance of 0.1 p.u. and a system inertia of 2 s results in the activation of the first load shedding step after ≈ 0.8 s if no additional control actions are applied.

3.4.4 Primary control action

Equivalent governor/turbine model

Using the equivalent governor/turbine model to represent the total primary control action (Figure A.2), the influence of system inertia on the minimum frequency after a power imbalance is illustrated in Figure 3.11. It shows that the minimum frequency (f_{min}) decreases as the system inertia drops. Furthermore, decreasing inertia also reduces the time to reach this f_{min}, denoted by t_{min} (Figure 3.11(b)).

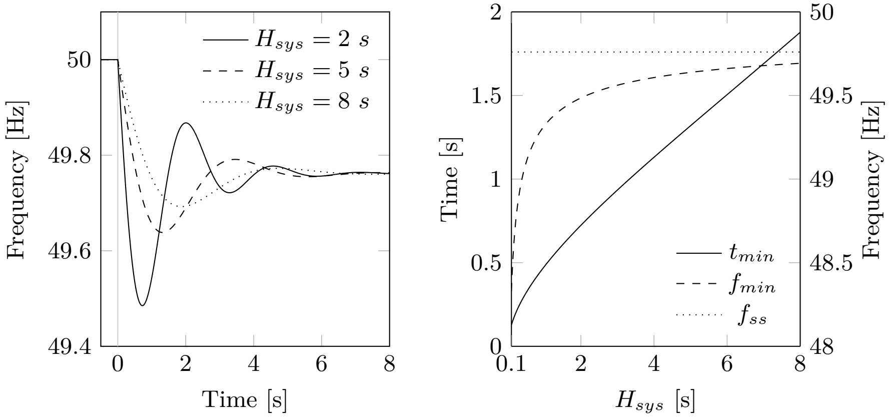

(a) Frequency

(b) Minimum frequency and time to reach this value

Figure 3.11: Frequency response due to primary control action (a) and minimum frequency in function of inertia (b) ($\Delta P_L = 0.1\ p.u.$, $R_{sys} = 0.05$, $D_{sys} = 1$ and $\tau_{sys} = 0.8\ s$)

On the contrary, the steady state frequency, f_{ss}, remains unaltered if the inertia and the systems primary control time constant τ_{sys} is varied. It is only a function of the system droop and load damping:

$$f_{ss} = 1 - \frac{\Delta P_L}{\frac{1}{R_{sys}} + D_{sys}} \tag{3.11}$$

To compensate for the decreasing system inertia, the load-frequency control parameters can be adjusted in order to keep the frequency within certain limits. The results of this analysis, using the equivalent governor/turbine model, are shown in Figure 3.12.

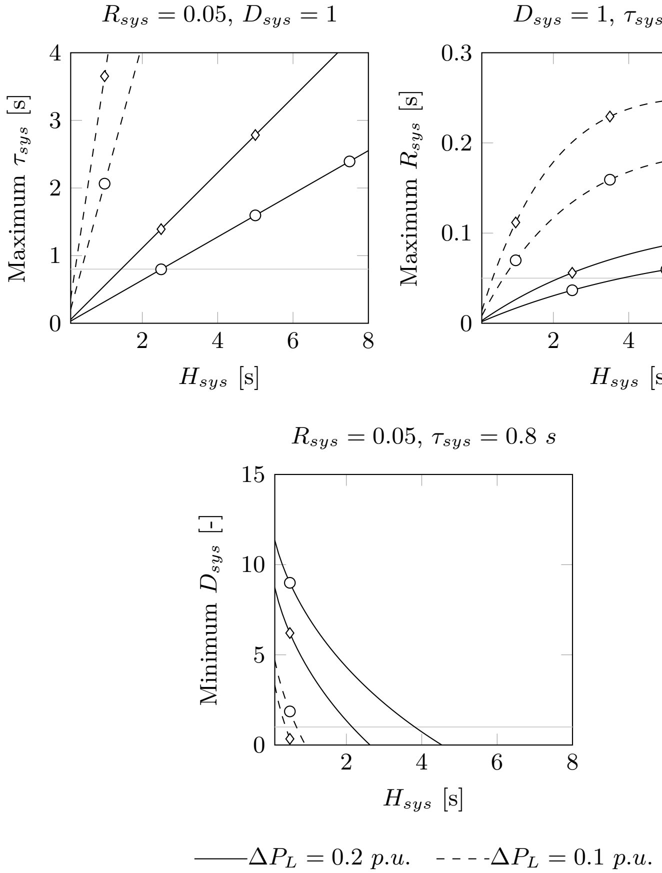

Figure 3.12: Variation of frequency control parameters in order to keep $f_{min} \geq$ 49 Hz ($\circ$) and 49.2 Hz ($\diamond$)

The first subfigure for instance, shows the variation of the (maximum) primary control time constant in function of system inertia in order keep the frequency above a certain level. It indicates that the relationship between τ_{sys} and H_{sys} is almost linear. However, this time constant is mostly a function of the type of power plants (gas, hydro, thermal,...) providing primary reserves to the system. The time constants related to each type of turbine and governor system are generally fixed. Therefore, unless slow reacting units are replaced by units with a fast prime mover response, it is not feasible to substantially reduce this parameter.

Secondly, also damping, related to the variation in load power due to frequency sensitivity, is mostly uncontrollable and highly depends on the type and amount of load connected to the system. Damping values above 5 do generally not occur, unless the load is explicitly controlled to react upon frequency deviations by altering its power setpoint.

Finally, the system droop can be reduced to compensate for the decrease in system frequency. This can be achieved by increasing the amount of units providing primary control or reducing the droop of each individual generators. The latter option is mostly restricted by various technical limits, and typical droop values are between 0.04 and 0.09 with the lower values corresponding to thermal and the higher to hydropower plants [33].

Different power plants models

Contrary to the former section in which the total governor response was represented by an equivalent governor/turbine model, three distinct types of power plants are now considered in the load-frequency study, i.e. a power plant with a steam, hydro or gas turbine. A detailed model of the governor and turbine model of each power plant type can be found in Appendix A.3.

Steam turbines are applied in fossil fuel and nuclear units to convert the steam at high temperature and pressure into mechanical energy. Numerous turbine configurations and types exist, depending for instance on the amount of turbine stages or whether or not a reheater is used to improve the efficiency. Furthermore, a turbine with multiple stages may be either of the cross-compound or tandem-compound type, with respectively the different stages mounted on a single shaft or two shafts. Here, a model of a tandem-compound single reheat turbine with three turbine stages is used. The dynamic response from a change in steam flow to a change in turbine power can be represented by a combination of first order transfer functions (Figure A.3). The largest time constant within this model is related to the reheater.

The response of the hydropower plant is quite different from a steam turbine as their performance is mainly influenced by the characteristics of the water column feeding the turbine. The most detailed representation of this water column is a travelling wave model, taking into account the water hammer effects due to elasticity of the water and the penstock. In power system studies, the penstock is usually considered to be inelastic and only the effect of the water inertia is included [119]. Due to inertia of the water, the change in turbine power is initially opposite to a change in the position of the gate at the foot of the penstock. This non-minimum phase behaviour of the turbine requires the governor to be equipped with a large transient droop compensation to allow a stable operation. Consequently, the primary response of the turbine is relatively slow.

Gas turbines are of two basic types, i.e. the open cycle (OCGT) or combined cycle (CCGT) gas turbine. In the latter configuration, the exhaust gases of the gas turbine are fed into a heat recovery steam generator which produces steam to drive a steam turbine. To obtain maximum efficiency, the air and fuel flows are controlled by the temperature controller to maintain the gas exhaust temperature at its maximum allowable level. The incoming air flow is adjusted by changing the position of variable inlet guide vanes, mounted at the inlet of the compressor. In general, these gas turbines are considered to be fast responding units which can rapidly react on frequency deviations by injecting more fuel into the combustor [95]. However, as already touched upon in section 3.4.1, the frequency dependency of the incoming airflow can also impact the frequency control in a detrimental way.

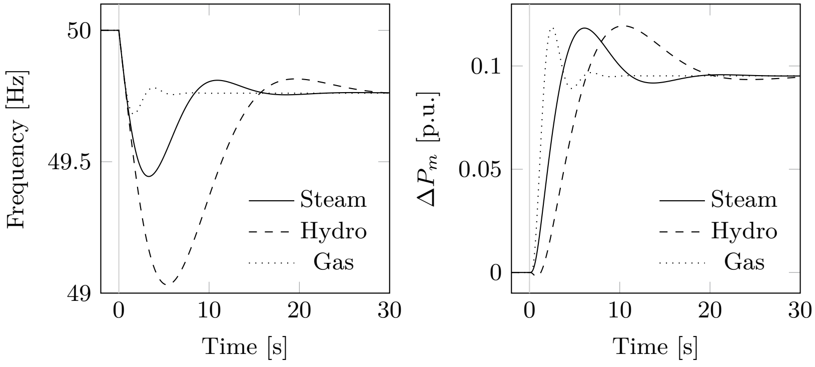

(a) Frequency

(b) Turbine response

Figure 3.13: Frequency (a) and turbine response (b) for three different type of power plants ($\Delta P_L = 0.1\ p.u.$, $R_{sys} = 0.05$, $D_{sys} = 1$ and $H_{sys} = 8\ s$)

The response of the different turbines and the corresponding frequency when subjected to a load change is shown in Figure 3.13. It demonstrates that, although the inertia and permanent droop are equal in the three cases, the different plant characteristics significantly influence the transient frequency response. Due to the non-minimum phase behaviour and slow response of the hydro turbine, the frequency drop is much larger compared to the case where the steam or gas turbine provide primary control.

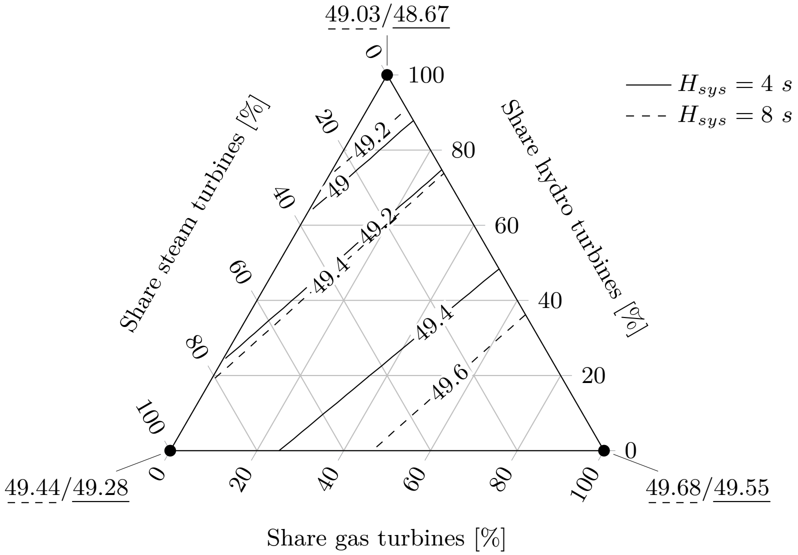

(a) Minimum Frequency in Hz

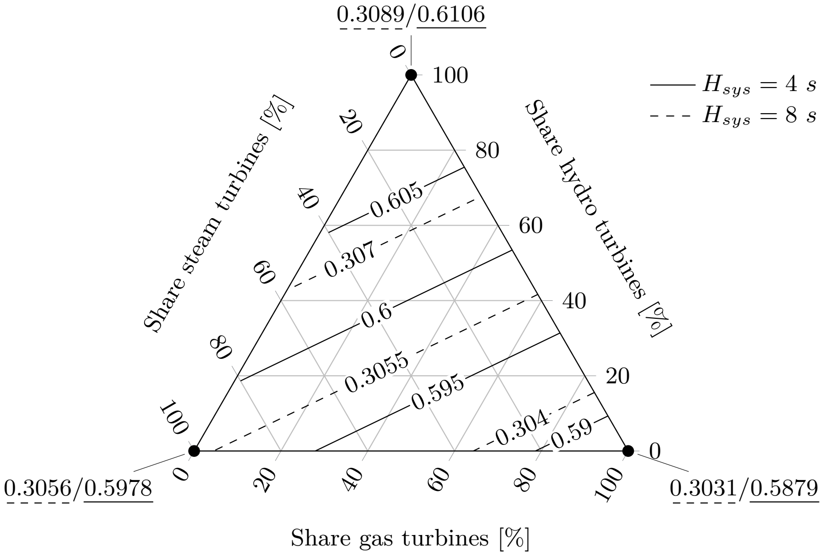

(b) Maximum |ROCOF| in Hz/s (measured over 500 ms)

Figure 3.14: Minimum frequency and |ROCOF| after a load step of $\Delta P_L = 0.10$ $[p.u.]$ ($D_{sys} = 1$, $R_{sys} = 0.05$)

By combining the different generation technologies for primary frequency control, for the same load step, system droop, load damping and inertia, a hydro dominated system leads to the lowest minimum frequency (Figure 3.14). Here both the minimum frequency and the rate of change of frequency (averaged over 500 ms) after a load imbalance are given for different combinations of gas, hydro and steam turbines providing primary control. The ROCOF averaged over the first 500 ms after the event is only slightly altered as the generation technology changes as it is mainly determined by the inertia within the system.

Up till now, it is assumed that each generation unit has sufficient power reserve available to compensate for the power imbalance. The minimum frequency shown in the previous figures would even drop more in case part of the generation park reaches its power limits during the frequency response. Moreover, the power plants that do not participate in the primary control, are considered to be frequency insensitive. However, if the proportion of base-load gas turbines increases, the frequency control becomes more challenging [95]. This is mainly due to the incapability of the inlet guide vanes to open further in order to compensate for the reduced airflow during a frequency drop. As the fuel-to-air ratio decreases, the exhaust temperature increases. This rising exhaust temperature then activates the temperature controller to reduce the fuel flow in order to restore the fuel-to-air ratio. This finally leads to a reduced power output aggravating the initial power imbalance.

3.5 Reduced inertia: how low can we go?

From the former analysis, it can be concluded that a reduction in system inertia mainly influences the frequency stability of the power system as it leads to increased ROCOF and lower minimum values for the same power imbalance. The minimum inertia thus depends on the ROCOF withstand capability of the system, to ensure a proper functioning of the protection system, generator operation and converter unit controllers. Furthermore, the higher this initial ROCOF following an event, the greater the risk of the system frequency dropping below load-shedding thresholds and heading towards system collapse. Consequently, system inertia is one of the important parameters to determine the maximum time delay for governor and prime movers to react and cease the frequency decline.

As this time constant is directly linked to the physical characteristics of the different power plants, it is almost fully determined by the energy mix of the system. Additional measures such as a fast power injection by converter connected units or a rapid reduction in load power, often grouped under the name of fast frequency response, could reduce this time constant. However, they also require some time for frequency detection and event identification before they can provide the response (of the order of 150 - 200 ms [120]). Even in case the frequency drops to a level at which the first load shedding is activated, a certain amount of inertia is required to allow the underfrequency load shedding to operate in time in order to prevent a total blackout.

In the following, the constraints on the allowed ROCOF and nadir (i.e. lowest, minimum) frequency are subjected to two power systems, i.e. the continental Europe and Nordic power system, in order to estimate the required inertia. Next, the relationship between inertia and the share of converter connected generation is further described. Finally, some options to operate a system with lower (synchronous) inertia are proposed.

3.5.1 Minimum inertia for the continental Europe and Nordic power system

As the ROCOF and frequency limits, speed of droop control action, power plant mix, the assumed reference incident, ... vary from system to system, a very case specific approach is often required to determine the minimum inertia. By making some simplifications and assumptions, e.g. applied to the synchronous area of continental Europe and Nordic power system, we can however already give a rough idea of the required amount.

It is assumed that 1 Hz/s (as proposed in the Irish grid code) becomes the standard in the future European generator grid connection codes. Secondly, the total network power frequency characteristic, corresponding to the total droop action within the current systems, is set to 22560 MW/Hz (continental Europe) and 6000 MW/Hz (Nordic) [49, 97]. Finally, the reference incident is taken equal to respectively 3 GW (continental Europe) and 1.4 GW (Nordic). The latter corresponds to the rating of the largest HVDC interconnector currently under construction. This link will connect the power systems of Norway and Denmark and is expected to be operational in 2020 [121].

In Figure 3.15, the minimum required inertia as a function of the maximum allowed ROCOF is shown. The inertia is given here in terms of the kinetic energy, which can be converted into a system inertia constant using (2.5). For both reference incidents, a minimum kinetic energy stored in the synchronous machines of 35 GWs and 75 GWs is required for respectively the Nordic and continental European system in order to remain below the 1 Hz/s limit. The total kinetic energy within the Nordic system is estimated to be currently in the range of 120-250 GWs (Figure 2.11), which is thus more than sufficient for

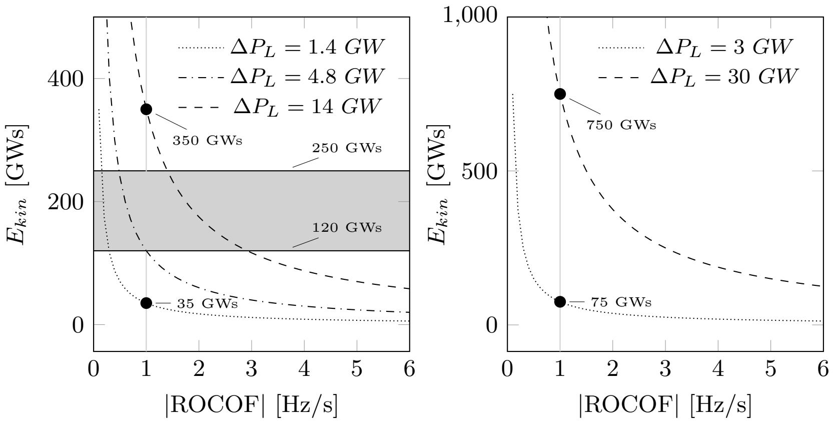

(a) Nordic system (b) Continental European system

Figure 3.15: Minimum required kinetic energy in function of maximum allowed ROCOF

the considered reference incident. Even for 120 GWs, power imbalances up to 4.8 GW do not result in a violation of the ROCOF operating range. If however a more severe incident is assumed with a power imbalance 10 times higher then the current reference incident, a kinetic energy of 350 GWs is required.

Also for the continental European system, as the system is substantially larger in size compared to the Nordic system, the current stored energy can be assumed more than sufficient for the considered reference incident.

In Figure 3.16, the minimum required inertia is given as a function of τ_{sys} in order to keep the nadir frequency above 48.8 Hz (Nordic) and 49 Hz (Continental Europe), corresponding to the frequency limit at which the first load shedding step is activated. Using the required minimum stored kinetic energy to keep the ROCOF above 1 Hz/s, τ_{sys} is respectively 5.7 s and 7.1 s, which can be considered feasible looking at the time constants associated within the different governor and turbine models.

Also other studies on the frequency stability of large interconnected systems demonstrate that there is at this moment sufficient inertia available (see e.g. [122] and [123] for respectively the Western and Eastern Interconnection in North America). In [123], it is concluded that the loss of inertia in the Western Interconnection due to the increased converter connected generation is of little consequence for up to at least 50% levels of instantaneous penetration as long as adequately fast primary frequency control is implemented.

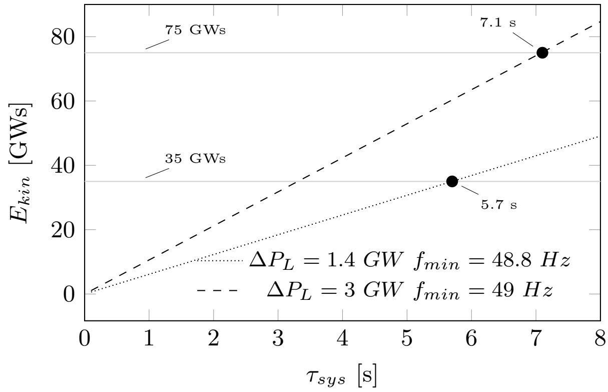

Figure 3.16: Minimum required kinetic energy in function of maximum τ_{sys} in order to $f \geq f_{min}$

3.5.2 Inertia and share of converter connected generation

In general, it is already quite challenging to define a minimum required inertia as it depends on numerous system parameters, but it is even more difficult to translate this to a certain amount of converter connected generation. In Figure 3.17, two distinct scenarios are depicted. The real future trend of the inertia decline will probably be situated somewhere between them.

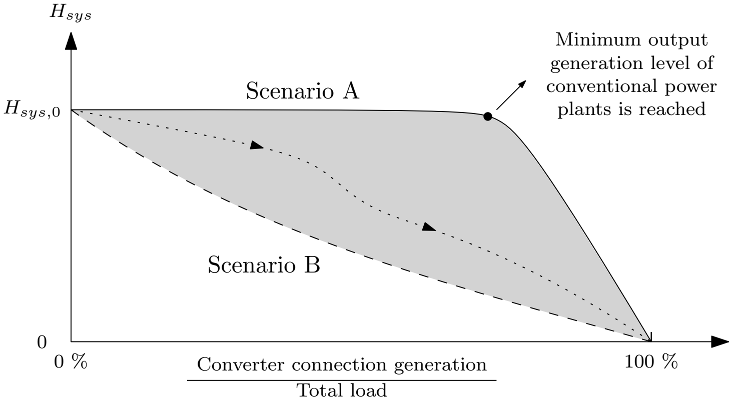
H_{sys}
$H_{sys,0}$
0
Scenario A
Scenario B
Minimum output generation level of conventional power plants is reached
0 %
100 %
$\frac{\text{Converter connection generation}}{\text{Total load}}$

Figure 3.17: Inertia in function of the penetration of converter connected generation

In scenario A, the amount of converter connected generation is increased while the inertia from the spinning conventional power plants is only slightly lowered or even kept constant. This can be achieved by lowering the minimum generation level of the conventional units, also indirectly providing an increased margin to deliver frequency control. The efficiency may be compromised in this way, but the turbine is probably the limiting factor at lower loads (turbine blades fluttering, economizer misting or issues of mixed flow). As an example of what might be achievable, the output of a test plant in North America was brought down to 19% instead of the minimum of 40-50% of the rated power [114]. By dispatching the plant to lower output levels instead of decommissioning, the synchronous system inertia is maintained up to a certain level of converter connected generation. Additionally, the system inertia could be kept constant by installing more synchronous compensators, typically been used to absorb or generate reactive power, supporting the voltage of the grid. Although they represent a quite traditional solution to the decline in inertia, they are currently experiencing a revival of interest. In Denmark for instance, a 270 MVA compensator was installed in 2013, the first one in the country for over 40 years. A flange was connected to the rotor shaft in order to connect an additional flywheel at a later stage which would increase the inertia of the system [114].

In scenario B, the conventional power plants are gradually displaced and the corresponding system inertia decreases. It is assumed that the primary control reserve is mainly provided by converter connected units (wind, PV, storage, ...) and consequently most of the spinning generation units can operate at maximum power level. Although 100% of converter connected generation corresponds to zero synchronous inertia, these two scenarios indicate that in between zero and 100% instantaneous penetration, the inertia can vary over a broad range.

3.6 Options to operate a system with low synchronous inertia

Several approaches can be taken to operate a power system with low inertia from synchronous generation corresponding to scenario B of Figure 3.17.

A first approach mostly focuses on adapting the current power system equipment, grid codes and protection to cope with higher ROCOF and larger frequency swings. Further investigations are however required to find out how far these ROCOF and frequency limits could possibly be stretched without jeopardizing power system stability, or damaging the turbines and auxiliary equipment in conventional power plants. As stated before, no major issues are foreseen with respect to converter connected generation.

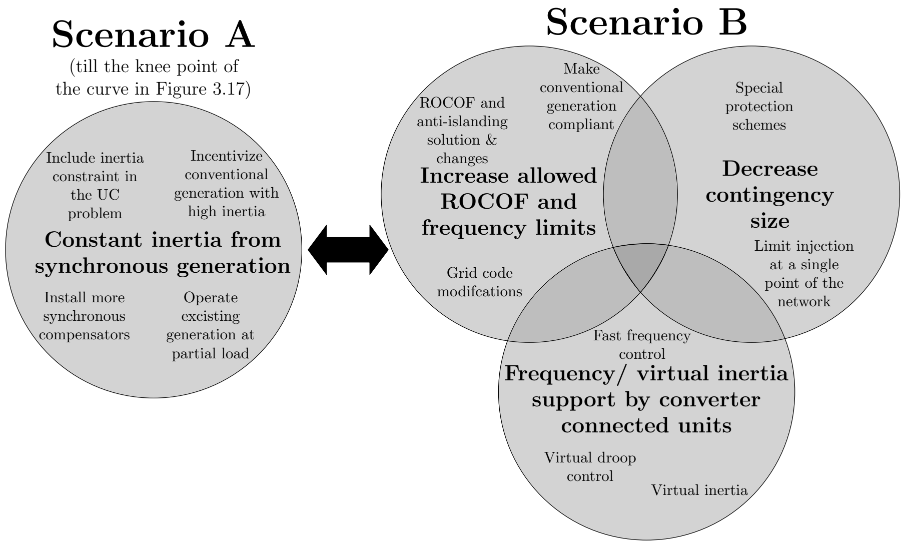
Scenario A
(till the knee point of the curve in Figure 3.17)
Include inertia constraint in the UC problem
Incentivize conventional generation with high inertia
Constant inertia from synchronous generation
Install more synchronous compensators
Operate excisting generation at partial load
Scenario B
ROCOF and anti-islanding solution & changes
Make conventional generation compliant
Increase allowed ROCOF and frequency limits
Grid code modifcations
Special protection schemes
Decrease contingency size
Limit injection at a single point of the network
Fast frequency control
Frequency/ virtual inertia support by converter connected units
Virtual droop control
Virtual inertia

Figure 3.18: Options to operate system with high penetration of converter connected generation: scenario A and B (see Figure 3.17)

The second approach tries to accommodate more converter connected generation by delivering virtual inertia and frequency control by renewable generation units. Different options are possible, going from emulating the behaviour of conventional power plants to delivering a fixed power injection after the frequency has dropped below a certain threshold. The optimal control which will be adopted at large scale in a power system is still unknown, but is an area of active research [124, 125].

Finally, a third approach, often disregarded, is decreasing the size (and probability) of the contingency by limiting the power injected at a single point in the network or implementing special protection schemes to prevent system splits and cascading outages [120]. The two considered scenarios and solutions with respect to system inertia in order to accommodate more converter connected generation are summarized in Figure 3.18.

3.7 Conclusion

The relevance of inertia in power systems is described by discussing the effect of the reduced amount of synchronous inertia on power system stability. Although this inertia plays an important role in different forms of stability, it is found that issues mainly arise in terms of frequency control as the ability of the system to resist to large power imbalance decreases. It results in high ROCOF values and substantial frequency deviations which can lead to instability of the system.

It is thus clear that new approaches are necessary to cope with the reduced synchronous inertia in order to accommodate more converter connected renewable generation in the current system. Different possible measures are proposed of which the virtual inertia support is further elaborated in the subsequent chapters.

Finally, it must be emphasized that, besides the reduced inertia, the increased converter connected generation impacts the operation and control of modern power systems in many other ways, including voltage stability and control, fault contribution, system protection, reserve provision, to name but a few. The optimal techno-economic solution or approach to tackle these challenges and to adequately operate a system with a high penetration of non-synchronous generation is therefore not only very system dependent, but also consists of a mix of existing and future technologies bounded to a wide range of system requirements and constraints.

Chapter 4

Control and modelling of converter connected units

"Essentially, all models are wrong, but some are useful."
- George E.P. Box

4.1 Introduction

The lack of inertia due to the displacement of synchronous generation can be compensated by modifying the control of converter connected units. Before proposing and analysing such inertia support techniques, a clear understanding of the underlying control structure is required. This chapter principally aims to provide a comprehensive overview, classification and description of the control approaches, with the main focus on the dynamic interactions with the power system.

The overall control structures, based on its primary energy source, of different converter units are firstly discussed. Thereafter, the available control approaches according to their role in a power system and operation mode are investigated. Two modes, namely the voltage and current source based control are dealt with in the subsequent sections. Also distinct techniques to estimate the grid frequency are discussed and compared as the grid frequency is an essential input to inertial support scheme. Finally, the aerodynamic and converter model of a Type 4 wind turbine is presented in more detail, which is used in the next chapters.

4.2 General control structure

4.2.1 Overview

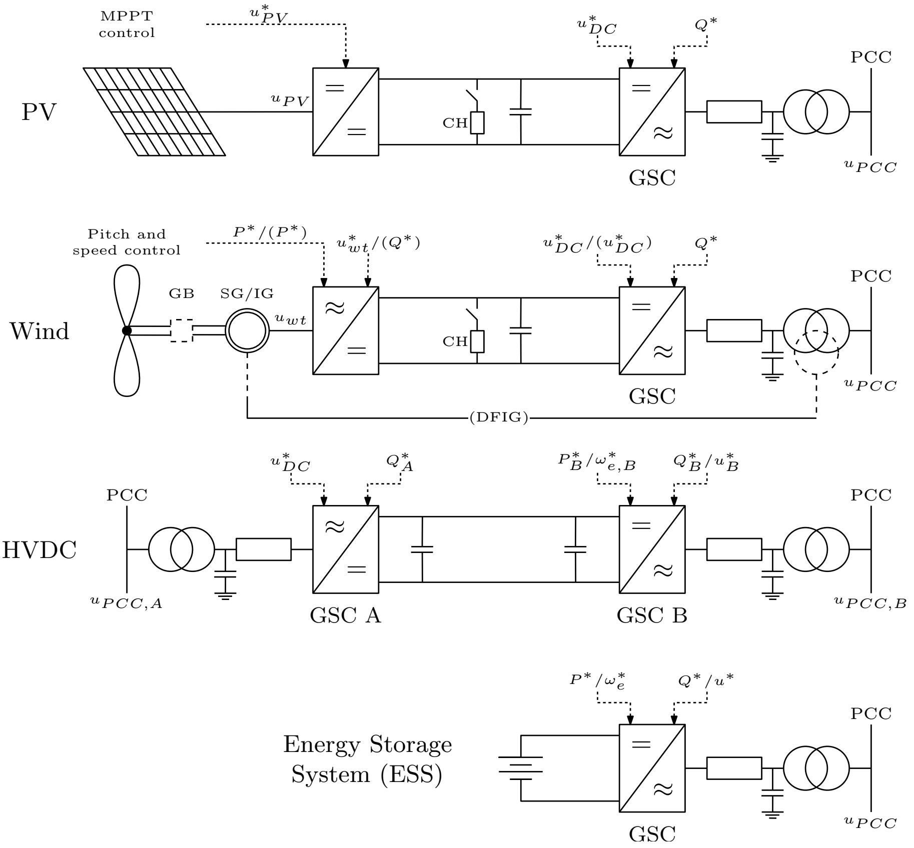
MPPT control
u^*_{PV}
PV
u_{PV}
CH
u^*_{DC}
Q^*
PCC
GSC
u_{PCC}
Pitch and speed control
$P^*/(P^*)$
$u^*_{wt}/(Q^*)$
$u^*_{DC}/(u^*_{DC})$
Q^*
Wind
GB
SG/IG
u_{wt}
CH
PCC
GSC
u_{PCC}
(DFIG)
u^*_{DC}
Q^*_A
$P^*_B/\omega^*_{e,B}$
Q^*_B/u^*_B
PCC
HVDC
$u_{PCC,A}$
GSC A
GSC B
PCC
$u_{PCC,B}$
P^*/ω^*_e
Q^*/u^*
Energy Storage System (ESS)
PCC
GSC
u_{PCC}

Figure 4.1: Overview of the control structure of a PV, Wind, HVDC and energy storage system (CH: chopper, GB: gearbox, GSC: grid side converter, MPPT: maximum power point tracking)

In Figure 4.1, the overall (simplified) control structure of a PV unit, a wind turbine (Type 3 and 4), an HVDC point-to-point link and a storage unit is given (Reference values are denoted by *). All units are connected to the AC grid through a phase reactor and a transformer. The filter is considered to be purely capacitive at the fundamental frequency and therefore represented by a shunt connected capacitor [70].

For a PV and wind turbine, the converter at the primary side is used to manage the conversion of the power from the primary source to DC power, either through a rectifier for a wind unit or a DC-DC converter in the case of PV [10]. For a wind turbine topology with a DFIG (Type 3), the stator of the induction generator is directly connected to the grid and only part of the generator power (15 - 30% depending on the slip) is exchanged through this rectifier which is connected to the rotor windings of the generator [49].

The control of the grid side converter (GSC) looks quite similar for PV and wind units as they are both typically assigned to keep the DC voltage at a constant level and to manage the reactive power injection into the system. Alternatively, in case of a Type 4 wind turbine, the GSC can be employed to control the active power while the other converter regulates the DC voltage [126, 127, 53, 128]. The GSC considered here is a three-leg voltage source converter (VSC) commonly used within most distributed generation, expect for small single-phase units such as residential PV [75]. When a fault occurs close to the converter, the active power injected in the system is in general substantially smaller than the amount of power from the primary energy source. Therefore, a DC chopper is often applied, which limits, in combination with acting on the primary source, the DC voltage during faults.

When modelling these PV and wind units, a distinction is made based on the level of modelling detail. Within electromagnetic transient (EMT) programs, all electrical parts of the unit are represented in great detail to simulate e.g. the switching dynamics of the converter, the DC link voltage variations or the electromagnetic transients within the generator. For power system stability studies, it is however generally not relevant to take into account all dynamics in detail as the fast transients do merely influence the slower ones. Furthermore, including all details in the modelling would lead to long calculation times when simulating large power networks with multiple converter units. Actually, in the stability analysis of the system, mainly a model is required that correctly represents the active and reactive power output at the PCC, influencing the electromechanical and voltage dynamics within the system. Furthermore, in case a full power electronic coupling is used, the dynamics of the primary source are to a large extend decoupled from the grid and vice versa. Therefore, some simplifications when applying a full power converter in the previous presented model of PV and Type 4 wind turbines can be made.

By for instance assuming an ideal (very fast) DC controller, both converters can be represented by a single GSC, fed by a constant DC voltage source [126]. The power from this GSC to the grid is now a direct function of the power coming from the PV panels or turbine, taking into account constant converter losses. The simplified model is shown in Figure 4.2.

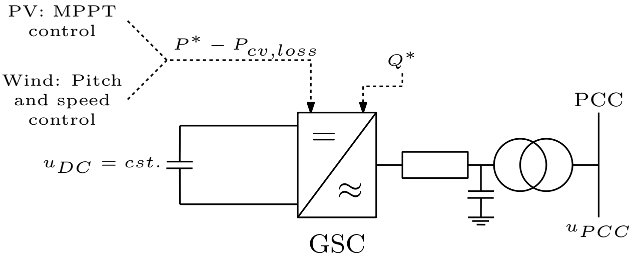

Figure 4.2: Simplified model of PV and wind (Type 4) GSC converter for power system stability studies

Within an HVDC point-to-point link, one of the converters usually controls the DC voltage and the other the active power in case it interconnects two asynchronous systems or when it is embedded in a single AC system. However, if no synchronous connected generation is present, such as for instance in offshore wind farms connected through HVDC, the offshore converter is operated in grid forming mode by setting the local voltage and frequency of the offshore grid (ω^* and u^*). Also for storage units, one can usually chose to operate the GSC to feed a certain amount of power into the system (P^* and Q^*) or to set the reference speed and voltage for the remaining PV and wind units (ω^* and u^*).

4.2.2 Classification of GSC control

Irrespective of the applied primary energy source, one can make another classification of the different GSCs (Figure 4.3), which is important to take into consideration for the provision of inertia support, as will be illustrated in the subsequent chapters of this work. This classification is based on the way converters are generally controlled or operated (voltage source or current source based) and their role towards the system (grid forming, grid feeding or grid supporting).

Currently, almost all converter connected generation units within large interconnected power systems, used to convert the energy from wind turbines or PV panels to the grid, are specifically designed to provide power to an energized grid. They can therefore be represented as equivalent controlled current sources (current source based or CSB) synchronized with the AC voltage at its terminals using a precise synchronization mechanism (e.g. a phase locked loop (PLL), see section 4.3.2). These type of converters do not inherently alter their power setpoint in function of the frequency and can therefore be considered inertialess from a power system point of view ($H_V = 0$).

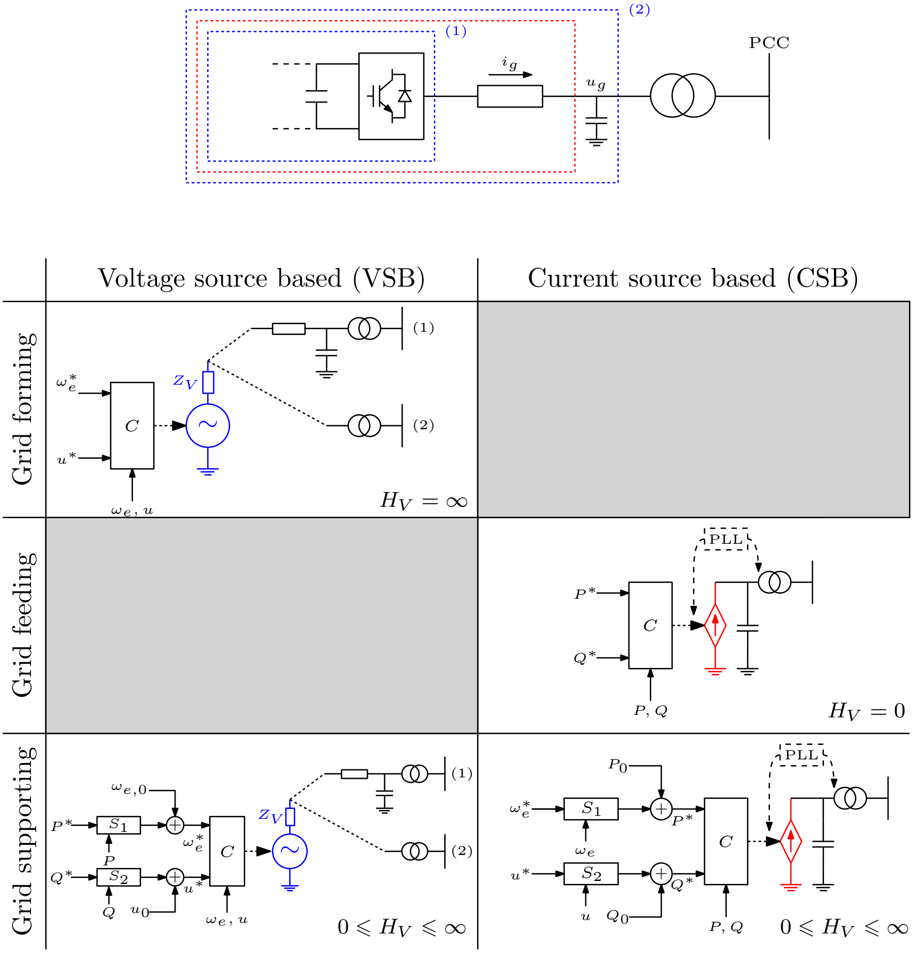
(2)
(1)
i_g
u_g
PCC
Voltage source based (VSB)
Current source based (CSB)
Grid forming
Grid feeding
Grid supporting
ω_e^*
u^*
C
Z_V
ω_e, u
(1)
(2)
$H_V = \infty$
PLL
P^*
Q^*
C
P, Q
$H_V = 0$
$\omega_{e,0}$
P^*
S_1
P
Q^*
S_2
Q
u_0
ω_e^*
u^*
C
ω_e, u
Z_V
(1)
(2)
$0 \leqslant H_V \leqslant \infty$
P_0
ω_e^*
S_1
ω_e
P^*
u^*
S_2
u
Q_0
Q^*
C
PLL
P, Q
$0 \leqslant H_V \leqslant \infty$

C: Lower control level
S_1: Frequency/active power support function
S_2: Voltage/reactive power support function
Z_V: Virtual impedance

Figure 4.3: Classification of GSC control approaches: simplified representation (based on [9])

In case the converter is applied to support the regulation of the local grid voltage or frequency, e.g. by means of the provision of inertia support, the converter is classified as a grid supporting CSB, with $0 \leqslant H_V \leqslant \infty$. Also large storage units and HVDC links, connected to the transmission or distribution system, are currently mostly CSB controlled as other synchronous machines within conventional power plants are applied to energize the system and consequently set the local voltage and frequency for the remaining converter units.

The main merit of CSB control is its control flexibility as it can provide a fast and accurate control of the reactive and active power under various grid conditions. Even during faults, the currents can fairly easily be limited by the controller in order to avoid damage to the power electronic equipment. Furthermore, applying CSB control allows the converter to be operated in parallel with other units. Moreover, to comply with the current grid connection codes, a CSB control is considered to be the only feasible control approach since often a specific amount of reactive or active power (current) needs to be provided during grid disturbances [9, 10].

Another control approach comprises the voltage source based (VSB) converters. Grid forming VSB converters operate as an ideal voltage source as they set the local voltage and frequency of the system. Since the frequency at their terminals remains constant, these grid forming converters can be considered to deliver an infinite amount of (virtual) inertia ($H_V = \infty$). However, due to their low output impedance, it is practically impossible to operate them in parallel with other grid forming converters, but they mostly define the reference frequency and voltage for other CSB converters instead. This type of control is for instance applied within uninterruptible power suppliers (UPS) or HVDC converters linked to offshore wind farms [9].

In order to allow parallel operation and to offer frequency and voltage regulation by VSB converters, a self-synchronizing droop based power controller is often included in the model (section 4.4.2), resulting in a grid supporting VSB approach. As the active and reactive power exchange of a VSB converter is a function of the AC grid voltage and frequency, it is inherently required to have a flexible amount of energy (storage) available to provide the required power and energy almost instantaneously. Otherwise the self-synchronizing capability is lost. Therefore, standard wind and PV units are mostly not eligible for this type of control. Consequently, to the best of the author's knowledge, it has not yet been implemented commercially within power converters connected to the transmission or distribution system, and is up till now mainly employed for units operating in stand-alone operation or to provide communication-less load sharing amongst parallel converters within micro-grids.

4.3 Current source based (CSB) control of grid side converters

4.3.1 Control implementation

An overview of the control structure for the model presented in Figure 4.2 (PV and full converter wind unit) is given in Figure 4.4. For the control of an HVDC link, the DC voltage is not constant, but usually controlled by one of the two GSCs. The power controller has in that case u_{DC}^* as input instead of P^*.

The voltage of the converter (u_{cv}) imposed to the AC grid is created by self-commutated pulse-width modulated (PWM) circuits. By acting on the amplitude and phase of u_{cv}, the active and reactive power over the complex impedance $r_g + j \cdot \omega_e l_g$, comprising both reactance and resistance of the phase reactor, is controlled.

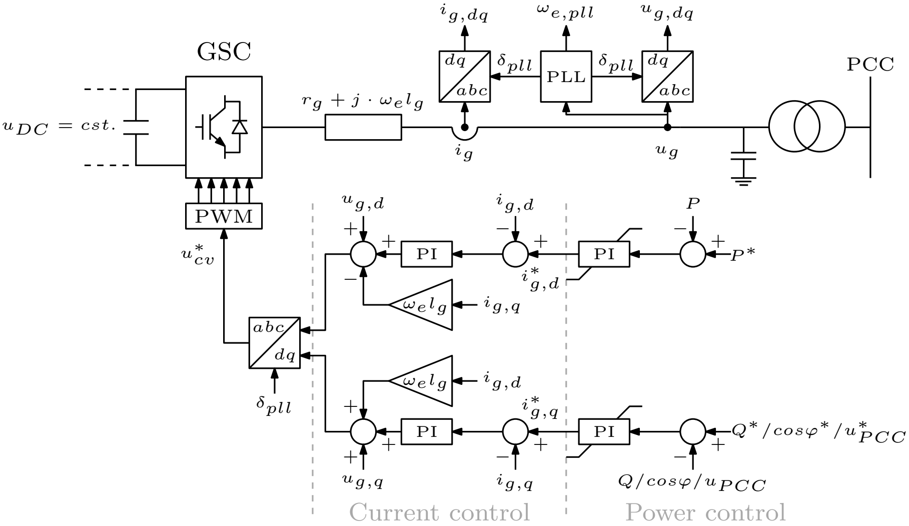

$i_{g,dq}$
$\omega_{e,pll}$
$u_{g,dq}$
GSC
dq
abc
δ_{pll}
PLL
δ_{pll}
dq
abc
PCC
$r_g + j \cdot \omega_e l_g$
$u_{DC} = cst.$
i_g
u_g
PWM
u_{cv}^*
$u_{g,d}$
$i_{g,d}$
P
+
+
−
+
−
+
PI
PI
P^*
$i_{g,d}^*$
−
$\omega_e l_g$
$i_{g,q}$
abc
dq
$\omega_e l_g$
$i_{g,d}$
δ_{pll}
+
$i_{g,q}^*$
PI
PI
$Q^*/cos\varphi^*/u_{PCC}^*$
+
+
−
+
−
+
$u_{g,q}$
$i_{g,q}$
$Q/cos\varphi/u_{PCC}$
Current control
Power control

Figure 4.4: Simplified control model of GSC: current source based control

A first control loop is the fast inner current control that regulates the AC currents whereas an upper slower control loop manages the active and reactive power output. A further simplification can actually be made by discarding this current control loop, as its response is much faster than the electromechanical dynamics of the power system. However, this can cause issues when faults close to the converter are simulated as the active and reactive current can not be distinguished [53].

Different options are feasible for implementing the current and power control loops, such as resonant controllers working on a $\alpha\beta$-stationary reference frame or PI-based controllers operating in a dq-synchronous reference frame adopted in this work [9].

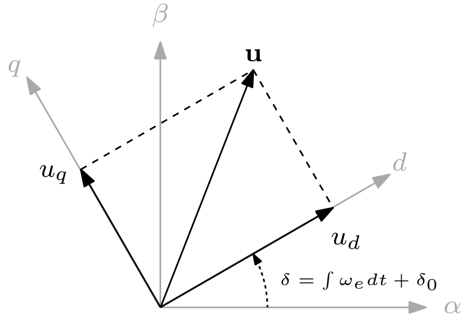

Figure 4.5: Voltage vector representation in the dq synchronous reference frame

By means of a combined Clarke ($abc \rightarrow \alpha\beta$) and Park transformation ($\alpha\beta \rightarrow dq$), all three-phase current and voltage signals (abc) being fundamental frequency AC signals during normal operation, are represented as DC values with one component aligned with the direct axis (d) and one along the quadrature axis (q) as illustrated in Figure 4.5. The transformation from the abc to the dq values is [10]:

$$\mathbf{u_{dq}} = \sqrt{\frac{2}{3}} \begin{bmatrix} cos\delta & cos(\delta - \frac{2\pi}{3}) & cos(\delta + \frac{2\pi}{3}) \\ -sin\delta & -sin(\delta - \frac{2\pi}{3}) & -sin(\delta + \frac{2\pi}{3}) \end{bmatrix} \cdot \mathbf{u_{abc}} \tag{4.1}$$

with δ the angle of the d-axis. Applying this transformation, the converter equations used to design the current controller, become in per unit [23, 129]:

$$u_{cv,d} - u_{g,d} = r_g \cdot i_{g,d} + l_g \cdot \left(\frac{di_{g,d}}{dt} - \omega_e \cdot i_{g,q} \right) \tag{4.2a}$$

$$u_{cv,q} - u_{g,q} = r_g \cdot i_{g,q} + l_g \cdot \left(\frac{di_{g,q}}{dt} + \omega_e \cdot i_{g,d} \right) \tag{4.2b}$$

The current in the $d(q)$-axis can be directly controlled by the $d(q)$ component of the converter voltage (u_{cv}). Since the dq values are DC signals in steady state, simple PI-controllers are applied. A grid voltage feed-forward and decoupling term (e.g. $u_{g,d}$ and $-\omega_e l_g$ in the d-axis) are added to improve the performance of the controller (Figure 4.4)[23].

The reference values for the current controller (i_d^* and i_d^*) are provided by the power controller. The instantaneously generated active and reactive power are calculated in per unit:

$$P = u_{g,d} \cdot i_{g,d} + u_{g,q} \cdot i_{g,q} \tag{4.3a}$$

$$Q = u_{g,q} \cdot i_{g,d} - u_{g,d} \cdot i_{g,q} \tag{4.3b}$$

As the angle of the grid voltage, usually estimated by a synchronization system such as a phase locked loop (PLL), is taken equal to the reference angle (δ) of the synchronous reference frame, the grid voltage is fully aligned with the d-axis and $u_{g,q}$ becomes 0. Consequently, the active and reactive power (or alternatively the voltage at the PCC or the power angle as shown in the figure) can respectively be controlled by the d- and q-component of the current vector. The output of the PI-controllers is finally limited to keep the total current below its maximum allowed value. In order to prevent integration wind-up, an anti-windup is used for the PI-controllers. Different approaches are possible to prioritize one of the two controllers once the converter current limit is reached [23].

4.3.2 Grid synchronization and frequency estimation

In order to ensure an appropriate operation of the CSB converters and to provide an accurate control of the active and reactive power to the grid, a precise synchronization technique is required to correctly estimate the grid voltage parameters, i.e. the grid voltage amplitude and phase angle. Moreover, a proper monitoring of the grid conditions is vital for the provision of additional grid support or to determine the most suitable operation mode of the converters [9].

The most extensively applied technique in three-phase systems to track the phase angle is through phase locked loops (PLLs). In general, this PLL is a feedback system that regulates the phase difference between its reference and output signal to zero, such that the phase of the output is locked to the phase of the reference. It consists of three fundamental blocks, a phase detector, a loop filter and a voltage-controlled oscillator (VCO) (Figure 4.6). The phase detector in the diagram generates an output signal proportional to the phase difference between the input signal and the output of the VCO. The output of the VCO is an oscillating signal which frequency is shifted with respect to a given central frequency, as a function of the output signal of the loop filter. Finally, the loop filter is applied to attenuate noise and high frequency signals, and is responsible for the control of the PLL [70]. As frequency is the time derivative of the phase angle, it can immediately be obtained as a byproduct of the phase detection.

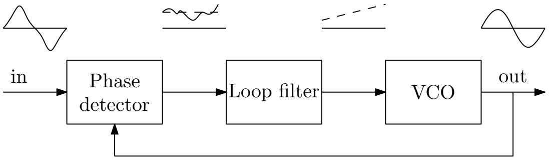

Figure 4.6: General structure of PLL [10]

One type of PLL commonly used to synchronize power converters is the synchronous reference frame phase locked loop (SRF-PLL) [130, 9]. This PLL transforms first the grid voltage into the dq-frame and then regulates the d- or q-component by means of the loop filter (PI-controller in this case) to zero, such that the reference angle of the rotating dq-frame is locked to the phase angle of the grid voltage. Whereas the PLL performs well under balanced undistorted grid voltages, the performance deteriorates under non-ideal conditions as it is very sensitive and susceptible to harmonics and unbalances due to its basic loop-filtering. To overcome this drawback, more advanced PLLs have been proposed in the literature which divide the unbalanced voltage into a combination of balanced components. It has for instance given rise to the double decoupled synchronous reference frame PLL (DDSRF-PLL) or the double second order generalized integrator PLL and frequency locked loop (DSOGI-PLL and DSOGI-FLL).

The DDSRF-PLL is an effective grid synchronization method in the presence of network faults as it exploits two rotating reference frames instead of one in order to represent an unbalanced voltage vector as a combination of a negative- and a positive-sequence component prior to the loop filter. The phase angle of the positive-sequence component is taken to synchronize the converter control and to calculate the grid frequency [131, 132].

In the DSOGI-PLL on the other hand, an adaptive filter based on a second order generalized integrator is used to obtain two pairs of orthogonal signals in the stationary reference frame ($\alpha\beta$) [11, 10]. The signals are then passed to a positive-negative calculation block calculating the sequence components in the $\alpha\beta$- and subsequently in the dq-frame. In [10] it is shown, that the DSOGI and DDSRF in combination with a PLL are actually two equivalent systems. However, as the SOGI is a frequency-variable adaptive filter tuned in such a way that it resonates when the grid frequency is equal to the natural frequency of the SOGI, it is often used in combination with a frequency locked loop, leading to a DSOGI-FLL. One of the main advantage of this FLL is its good performance under abnormal grid conditions as it is less sensitive to phase angle jumps compared to a PLL [9].

Apart from using PLLs or FLLs, a broad range of other synchronization or frequency measurements techniques can be applied [133, 134]. The most simple one, popular method in protection, is the zero-crossing detection method. Although it is relative easy to implement, it is very inaccurate and unreliable during distorted conditions [134]. Another way of estimating the grid frequency is for instance done through a spectral analysis, by taking the discrete fourier transformation of the input voltage. To further reduce the computational complexity, it is mostly implemented in a recursive way [135]. More advanced methods including the use of Kalman Filters, Prony estimation or numerical methods such as least square estimation can be found in the literature [133, 136, 137].

In the following, two of the commonly used PLL/FLL methods are described in more detail and their frequency measurement capability is compared, both during normal as distorted grid conditions.

SRF-PLL

The block diagram of the SRF-PLL is given in Figure 4.7(a). In order to study its dynamics, the non-linear model can be linearized by considering the transformation $(abc \rightarrow dq)$ (4.1) around the tracking point:

$$\begin{bmatrix} u_d \\ u_q \end{bmatrix} = \begin{bmatrix} u \cdot cos(\delta - \delta_{pll}) \approx u \\ u \cdot sin(\delta - \delta_{pll}) \approx u \cdot (\delta - \delta_{pll}) \end{bmatrix} \tag{4.4}$$

Assuming $u = 1\ p.u.$ leads to the model shown in Figure 4.7(b). The closed-loop transfer function of this second-order system is:

$$H(s) = \frac{2\zeta\omega_n \cdot s + \omega_n^2}{s^2 + 2\zeta\omega_n \cdot s + \omega_n^2} \tag{4.5}$$

with $\omega_n = \sqrt{\frac{K_p}{T_i}}$ and $\zeta = \frac{\sqrt{K_p T_i}}{2}$. This transfer function reveals that the SRF-PLL actually contains a low-pass filtering characteristic useful to cancel noise and high order harmonics in the input signal [10]. However, as shown later in the comparison of the different PLLs, the harmonic rejection properties are substantially degraded in case the PLL is tuned to have a good transient performance, i.e. rapidly tracking the DC component of the frequency and phase angle. Its transient performance can be expressed by means of the settling time τ_s, defines the time required for the system to stay within 1% of its steady-state response following a step input:

$$\tau_{s,pll} = \frac{4.6}{\omega_n \zeta} \tag{4.6}$$

By decreasing the settling time (corresponding to increasing the bandwidth of the PLL), higher harmonics in the input signal are less attenuated. Especially when there is a negative sequence component in the three-phase grid voltage (e.g. due to an unbalanced grid voltage), it leads to a substantial loss of performance.

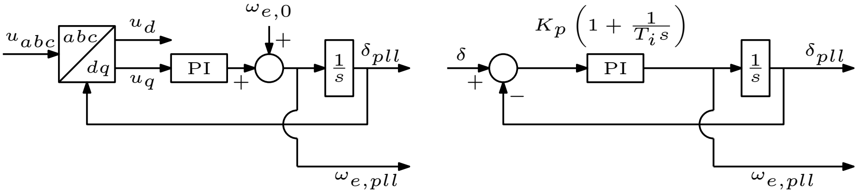

(a) Full model (b) Small-signal model

Figure 4.7: Block diagram of SRF-PLL [10]

DSOGI-PLL/FLL

In the DSOGI-PLL or DSOGI-FLL (Figure 4.8), the negative sequence component of the grid voltage is canceled using adaptive filters based on second order generalized integrators.

By applying the method of symmetrical components in the time domain (also denoted by Lyon transformation [10]), the positive and negative sequence components expressed in the stationary reference frame are:

$$\begin{bmatrix} u_\alpha^+ \\ u_\beta^+ \end{bmatrix} = \frac{1}{2} \cdot \begin{bmatrix} 1 & -q_p \\ q_p & 1 \end{bmatrix} \cdot \begin{bmatrix} u_\alpha \\ u_\beta \end{bmatrix} \qquad \begin{bmatrix} u_\alpha^- \\ u_\beta^- \end{bmatrix} = \frac{1}{2} \cdot \begin{bmatrix} 1 & q_p \\ -q_p & 1 \end{bmatrix} \cdot \begin{bmatrix} u_\alpha \\ u_\beta \end{bmatrix} \tag{4.7}$$

with $q_p = e^{-j\frac{\pi}{2}}$ the phase-shifting operator to obtain the in-quadrature representation of the input signal. This operator is implemented by means of a second order frequency adaptive filter based on a SOGI, which not only generates a set of two in-quadrature output signals but also attenuates the distorting higher harmonics of the input signal. The filtering capability of the DSOGI is further illustrated in Figure 4.9, clearly showing that it acts as a notch or low pass filter depending whether respectively the negative or positive sequence component of the voltage is applied as input.

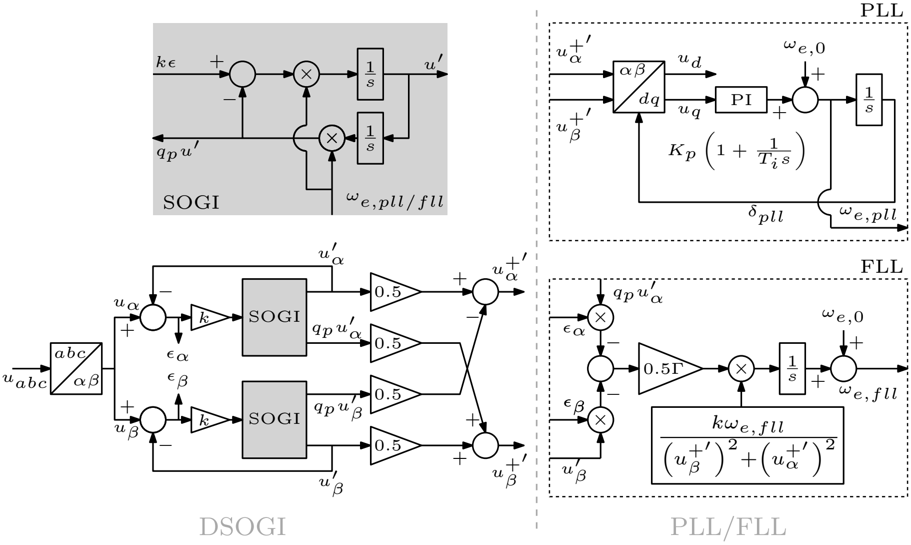
$k\epsilon$
u'
$q_p u'$
$\frac{1}{s}$
SOGI
$\omega_{e,pll/fll}$
PLL
$u_\alpha^{+'}$
$u_\beta^{+'}$
$\alpha\beta$
dq
u_d
u_q
PI
$\omega_{e,0}$
$K_p\left(1+\frac{1}{T_i s}\right)$
δ_{pll}
$\omega_{e,pll}$
u_{abc}
abc
u_α
u_β
k
ϵ_α
ϵ_β
u'_α
u'_β
$q_p u'_\alpha$
$q_p u'_\beta$
0.5
FLL
0.5Γ
$\omega_{e,fll}$
$\frac{k\omega_{e,fll}}{\left(u_\beta^{+'}\right)^2+\left(u_\alpha^{+'}\right)^2}$
DSOGI
PLL/FLL

Figure 4.8: Block diagram of DSOGI-PLL/FLL [11, 10]

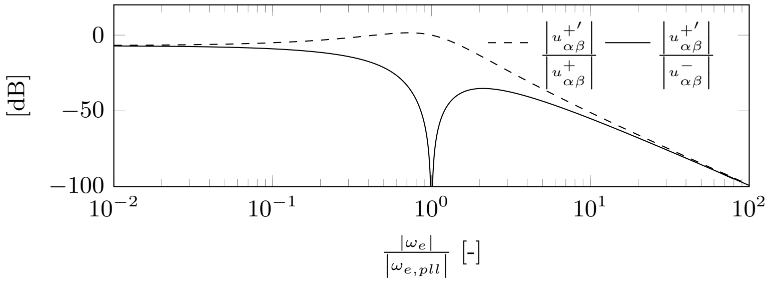

Figure 4.9: Frequency response of DSOGI ($k = \sqrt{2}$ to obtain a good trade-off between settling time and overshoot) [10]

The frequency for the SOGI can be provided by a PLL or an FLL. As both SOGI for the α and β component have the same frequency as input, only a single FLL is used. The FLL (Figure 4.8) includes a gain normalization and as reported in [133], it can be approximated by a first order system with a settling time:

$$\tau_{s,fll} \approx \frac{4.6}{\Gamma} \tag{4.8}$$

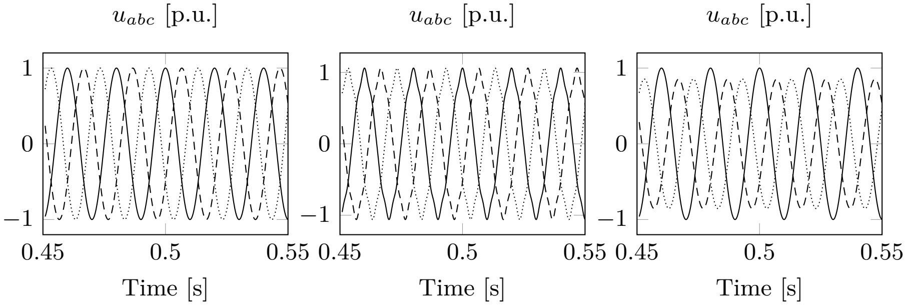

(a) Balanced (b) With harmonics (c) Unbalanced

Figure 4.10: Voltage waveforms as input to PLL/FLL: frequency drop with ROCOF of 4 Hz/s applied at t=0.5 s

The performance of the SRF-PLL, DSOGI-PLL and DSOGI-FLL is finally compared by taken three different voltage waveforms as input. The voltage waveforms are given in Figure 4.10 and correspond respectively to a perfectly balanced three-phase voltage, a grid voltage with harmonics and an unbalanced voltage waveform. The voltage with harmonics has a total harmonic distortion of 4.3% and is distorted by 7^{th} and 5^{th} harmonics, whereas the unbalanced case has a fundamental frequency positive and negative sequence voltage amplitude of respectively 0.9 and 0.1 p.u.. Due to e.g. a generation outage in the system, the frequency of the voltage rapidly decreases at t=0.5 s with a ROCOF equal to 4 Hz/s, which is actually a rather extreme case compared to the considered ROCOF values in the previous chapter. To determine the ROCOF, the frequency estimation is first passed through a second order low pass filter with a cut-off frequency of 20 Hz before its time derivative is calculated.

The results of the frequency and ROCOF measurements are given in Figure 4.11 and the mean absolute error of the frequency measurements as a function of the settling time is shown in Figure 4.12. Both figures clearly highlight that the SRF-PLL can only properly track the frequency in case of undistorted grid voltages. Decreasing the settling time of the SRF-PLL leads to better results (i.e. faster tracking) in the balanced voltage case, but reduces its filter capability

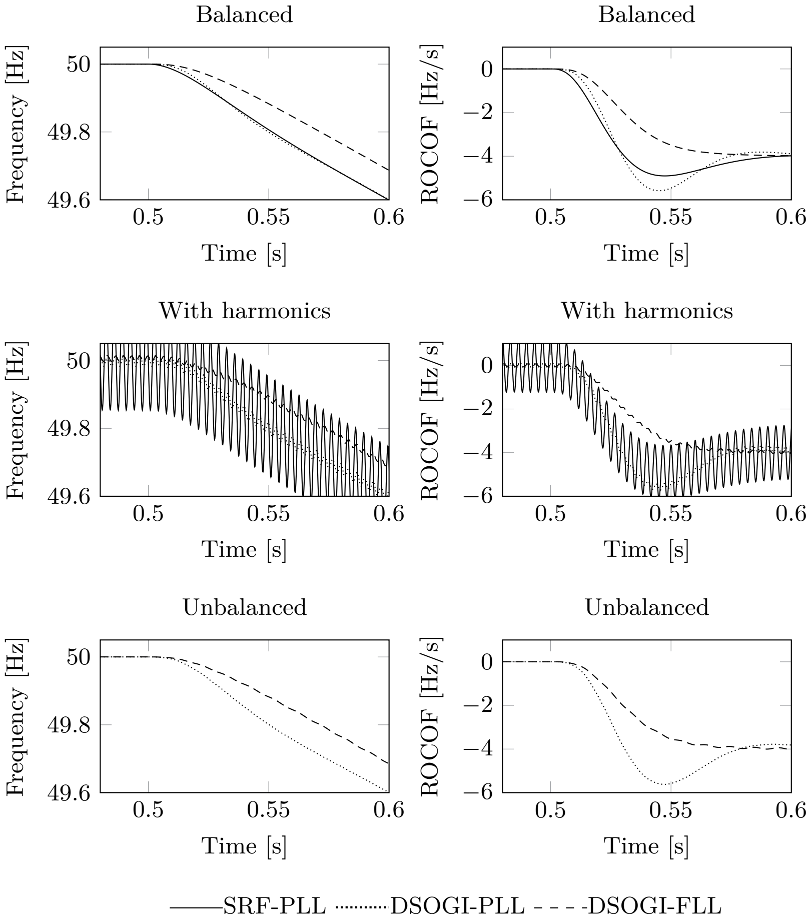

Figure 4.11: Frequency and ROCOF measurements for the voltages given in Figure 4.10 ($\tau_s = 100\ ms$), the results of the SRF-PLL are not given for the case of unbalanced voltages due to the high oscillating measurements

for distorted grid voltages leading to large errors in the ROCOF and frequency estimation (see e.g. the oscillations for the harmonic distorted voltage in Figure 4.11 associated with the 5^{th} and 7^{th} harmonic of the input voltage).

The DSOGI-PLL fully cancels the negative sequence component of the unbalanced voltage waveforms, such that the frequency and ROCOF estimation for the balanced and unbalanced case are almost identical. Also for the case with harmonics, the frequency estimation is substantially improved compared

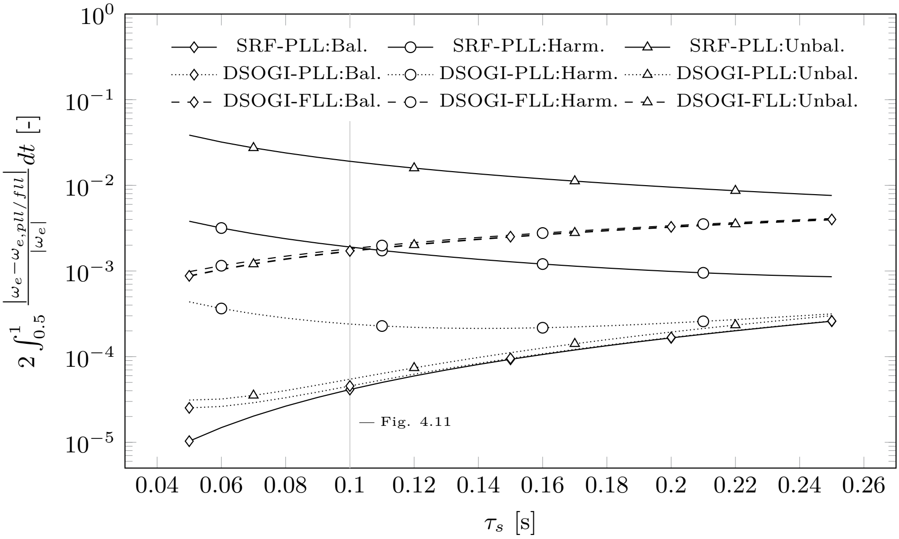

Figure 4.12: Comparison of the mean absolute error of the frequency measurements in function of the total settling time (with $k = \sqrt{2}$, the settling time of the DSOGI loop is fixed, equal to 18 ms)

to the SRF-PLL. The FLL is not able to track the frequency ramp without a steady state error as it only consists of a single integrator. The ROCOF on the other hand is correctly estimated for the three cases with sufficiently damping higher harmonics. An even better filtering can be achieved by adding more SOGIs tuned at different harmonics of the fundamental frequency [11].

Within power system stability studies, the influence of the PLL/FLL is often neglected or just a basic SRF-PLL is applied in the converter model to estimate the phase angle and grid frequency since no harmonics or unbalances are considered in the simulations. However, as given in [70], the PLL generally introduces a time delay between 10 - 100 ms, slightly influencing the active and reactive power output of the converter [138]. Also for studying the inertial support of these converters, it is important to take into account the PLL as the frequency measurement is not instantaneous due to time delays introduced by the limited bandwidth of the PLL/FLL and the additional filtering.

4.4 Voltage source based (VSB) control of grid side converters

4.4.1 Control concept

Grid forming converters are controlled to keep the frequency and voltage at the converter or filter bus (Figure 4.3) constant in time. Grid supporting converters using VSB control on the other hand vary their voltage and frequency depending on the measured active and reactive power by means of a droop control action. To explain this control concept, consider the equivalent electric circuit (Figure 4.13) representing the converter connected to a power system network modelled by its equivalent impedance (z), neglecting any shunt elements. The active and reactive power flow through this circuit with $z = r + j \cdot x$ is (in quasi-steady state):

$$P = \frac{u_1}{r^2 + x^2}\left[r(u_1 - u_2 cos\delta) + x u_2 sin\delta\right] \tag{4.9a}$$

$$Q = \frac{u_1}{r^2 + x^2}\left[-r u_2 sin\delta + x(u_1 - u_2 cos\delta)\right] \tag{4.9b}$$

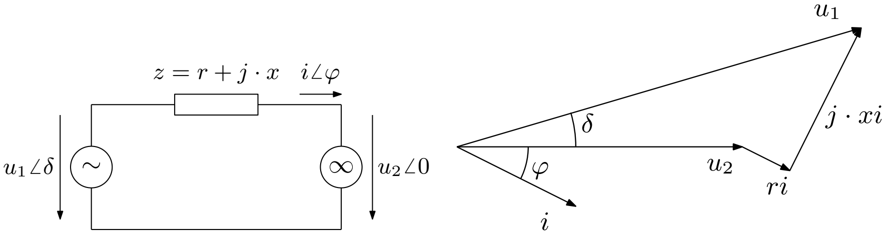

(a) Circuit (b) Phasor diagram

Figure 4.13: Power control of voltage-source base converter connected to a power system

High voltage transmission systems are mainly inductive in nature ($x >> r$) and the resistance can therefore be neglected. If also the power angle (δ) is small,

$sin\delta \approx \delta$ and $cos\delta \approx 1$. This way, (4.9a) and (4.9b) can be transformed to:

$$\delta \approx \frac{xP}{u_1 u_2} \tag{4.10a}$$

$$u_1 - u_2 \approx \frac{xQ}{u_1} \tag{4.10b}$$

These equations and the above analysis show that Q and u on the one hand and P and δ on the other hand are strongly coupled. Hence, changing δ (or ω_e) mainly alters the active power flow, the reactive power is predominantly influenced by the voltage difference and vice versa. Therefore, the most simple and commonly implemented control technique for these kind of converters to regulate the reactive and active power is based on standard droop control. The control expressions (S_1 and S_2 in Figure 4.3) can therefore be defined as:

$$\omega_e^* = R_P \cdot (P^* - P) + \omega_{e,0} \tag{4.11a}$$

$$u^* = R_Q \cdot (Q^* - Q) + u_0 \tag{4.11b}$$

with R_P and R_Q the droop gains for the active and reactive power. Using this control principle, the self regulation capability of synchronous machines is mimicked. When for instance the grid frequency is suddenly increased, also the exchanged/measured power P increases due to (4.10a). This in turn results in an higher frequency setpoint by the droop controller, automatically tracking the frequency of the external system. A PLL or another synchronization system is therefore not directly required.

4.4.2 Control implementation

The control scheme of the converter is given in Figure 4.14. The outer loop consists of the droop based active and reactive power controller as presented in the former section. The reference angle/frequency and voltage can be used as a direct input for the PWM converter (u_{cv}^*) corresponding to (1) in Figure 4.3, or an additional cascade current and voltage controller can be implemented as shown in the scheme. Hence, the voltage over the filter capacitance is regulated instead ((2) in Figure 4.3), which allows to explicitly limit the converter currents.

The virtual impedance (Z_V) control can serve different goals. It is for instance used to increase the decoupling between the active and reactive power controller applied to ensure an adequate control in case the converter is connected to grids with a moderate to high r/x ratio such a low voltage systems.

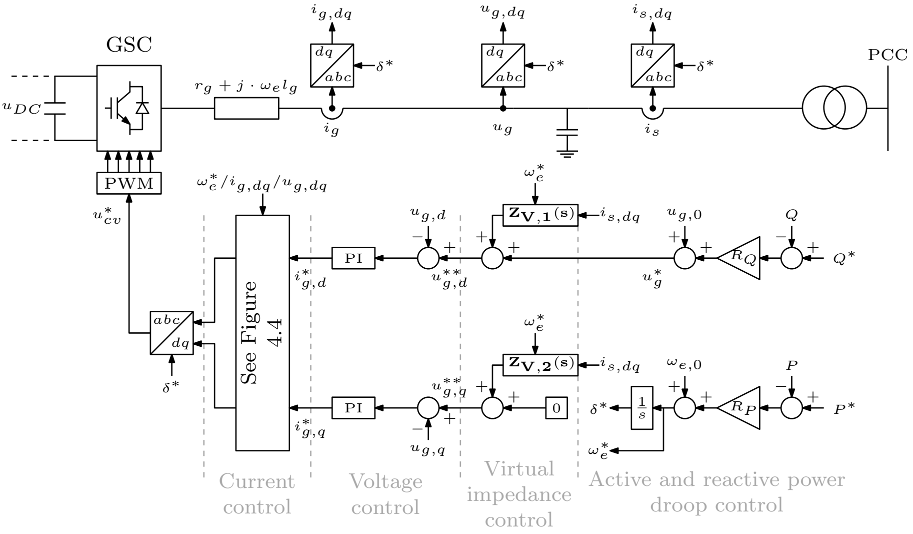
GSC
PCC
u_{DC}
$r_g + j \cdot \omega_e l_g$
$i_{g,dq}$
$u_{g,dq}$
$i_{s,dq}$
dq
abc
δ^*
i_g
u_g
i_s
PWM
u_{cv}^*
$\omega_e^*/i_{g,dq}/u_{g,dq}$
See Figure 4.4
PI
$i_{g,d}^*$
$i_{g,q}^*$
$u_{g,d}$
$u_{g,d}^{**}$
$u_{g,q}^{**}$
$u_{g,q}$
ω_e^*
$\mathbf{Z_{V,1}(s)}$
$\mathbf{Z_{V,2}(s)}$
0
$u_{g,0}$
u_g^*
$\omega_{e,0}$
$\frac{1}{s}$
R_Q
R_P
Q
Q^*
P
P^*
Current control
Voltage control
Virtual impedance control
Active and reactive power droop control

Figure 4.14: Simplified control model of GSC: voltage source based control

The issue for such systems is that equation (4.10a) and (4.10b) are not valid any more, as r can no longer be neglected. The active power depends on the voltage and the angle. In the extreme case, i.e. a purely resistive grid, the active power is even fully depending on the voltage instead of the angle difference. Large inductors could improve the decoupling, while increasing the size of the converter, and results in an increased cost. Other methods, such as advanced grid parameter estimation can also be applied, but virtually introducing the effect of the additional line inductance comprises often a more simple solution. The reference filter bus voltages, $u_{g,d}^{**}$ and $u_{g,q}^{**}$, are in this case:

$$u_{g,d}^{**} = u_{g,d}^{*} + \mathbf{Z_{V,1}}(\mathrm{s}) \begin{bmatrix} i_{s,d} \\ i_{s,q} \end{bmatrix} = u_{g,d}^{*} + \begin{bmatrix} 0 & \omega_e^* \cdot l_V \end{bmatrix} \begin{bmatrix} i_{s,d} \\ i_{s,q} \end{bmatrix} \tag{4.12a}$$

$$u_{g,q}^{**} = 0 + \mathbf{Z_{V,2}}(\mathrm{s}) \begin{bmatrix} i_{s,d} \\ i_{s,q} \end{bmatrix} = 0 + \begin{bmatrix} -\omega_e^* \cdot l_V & 0 \end{bmatrix} \begin{bmatrix} i_{s,d} \\ i_{s,q} \end{bmatrix} \tag{4.12b}$$

with l_V the virtual inductance.

In high voltage grids, the r/x ratio is sufficiently high. Therefore the virtual impedance control is mostly applied to shape the dynamic characteristics of the system. Additional damping can for instance be provided as proposed in [139, 140], by adding a virtual resistance coupled to first order high pass filter. Hence, the virtual resistance only acts on current transients and does not influence the control in steady state. $u_{g,d}^{**}$ and $u_{g,q}^{**}$ become:

$$u_{g,d}^{**} = u_{g,d}^{*} + \mathbf{Z_{V,1}(s)} \begin{bmatrix} i_{s,d} \\ i_{s,q} \end{bmatrix} = u_{g,d}^{*} + \begin{bmatrix} -r_V \cdot \frac{\tau_f s}{1+\tau_f s} & 0 \end{bmatrix} \begin{bmatrix} i_{s,d} \\ i_{s,q} \end{bmatrix} \tag{4.13a}$$

$$u_{g,q}^{**} = 0 + \mathbf{Z_{V,2}(s)} \begin{bmatrix} i_{s,d} \\ i_{s,q} \end{bmatrix} = 0 + \begin{bmatrix} 0 & -r_V \cdot \frac{\tau_f s}{1+\tau_f s} \end{bmatrix} \begin{bmatrix} i_{s,d} \\ i_{s,q} \end{bmatrix} \tag{4.13b}$$

with r_V the virtual resistance and τ_f the time constant of the filter.

4.5 Wind turbine modeling

The wind turbine applied in this work is a variable speed wind turbine equipped with a full scale power converter (Type 4 wind turbine). The model (Figure 4.15) is based on the turbine model proposed by the IEC Committee in IEC 61400-27-1 [141] and on the models presented in [128, 142, 143][1]. The simplified simulation model is intended to be used for power system stability studies and is tailored to take into account the main dynamics and controllers of interest in the provision of active power services to the system. The dynamics include the behaviour of the turbine blades, in terms of speed and (available) power, during frequency and inertia support.

As there is no specific need to model the electrical part of the generator in detail since it is fully decoupled with the grid, the proposed wind turbine model only includes a representation of the upper speed and power control level, the aerodynamic behaviour of the turbine and a simplified model of the converter corresponding to the one presented in section 4.3. The general speed and power control, encoloured in grey in the block diagram, can be implemented in many different ways [53, 100]. In this work, the pitch system is employed to limit the speed to its maximum value ($\omega_{m,gen}^{max}$) during high wind speeds and the converter is used to track the optimal power setpoint provided by the maximum power point tracking (MPPT).

---

[1] While the remainder of the text considers only full converter connected turbines, the same (inertia) control techniques can be achieved by other types of variable speed wind turbines such as the one equipped with a DFIG

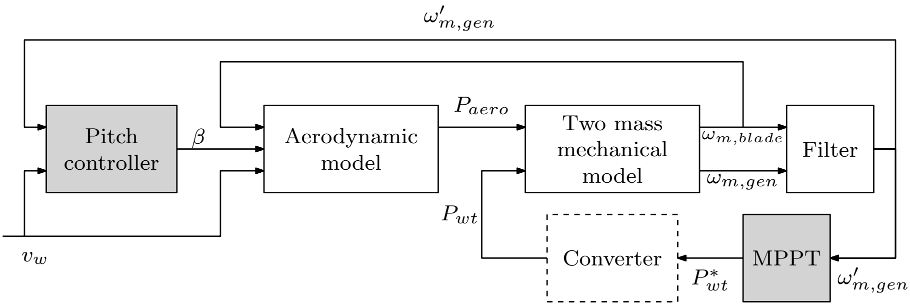
$\omega'_{m,gen}$
Pitch controller
β
Aerodynamic model
P_{aero}
Two mass mechanical model
$\omega_{m,blade}$
$\omega_{m,gen}$
Filter
P_{wt}
Converter
P^*_{wt}
MPPT
$\omega'_{m,gen}$
v_w

Figure 4.15: Block diagram of wind turbine model

4.5.1 Aerodynamic model

The aerodynamic model of the wind turbine converts the kinetic energy from the wind flow to rotational mechanical energy. The available power in the airflow passing through the rotor blades is:

$$P_w = \frac{1}{2}\rho_{air}A_{blade}v_w^3 \tag{4.14}$$

with ρ_{air} the density of the air, A_{blade} the swept area of the rotor blades and v_w the wind speed. Only a part of this power can be extracted by the blades, since fully converting P_w to kinetic energy would imply that the air stands still behind the turbine blades which not allows any air to flow away from the turbine. The wind speed is only partly reduced by the turbines and a fraction of the available power is converted, represented by the the power coefficient, C_p [49]:

$$P_{aero} = C_p P_w = C_p\frac{1}{2}\rho_{air}A_{blade}v_w^3 \tag{4.15}$$

The maximum C_p value is determined by the Betz-limit which states that the rotor blades can never extract more than 59% of the available power in the airflow. Typical C_p values for modern wind turbines are in the range of 25-45% [144]. The power coefficient is a function of the pitch angle, β and the tip speed ratio λ which is given by:

$$\lambda = \frac{\omega_{m,blade}R_{blade}}{v_w} \tag{4.16}$$

with R_{blade} the radius and $\omega_{m,blade}$ the rotational speed of the turbine blades. The pitch angle is defined as the angle between the rotor surface and the airfoil chord.

There are different ways to model the non-linear characteristic of the power coefficient such as using the blade element method, a loop-up table or an analytical approximation which is applied in this work. The $C_p(\beta,\lambda)$ is approximated by [53]:

$$C_p(\beta,\lambda) = 0.22\left(\frac{116}{\gamma} - 0.4\beta - 5\right)e^{\frac{-12.5}{\gamma}} \tag{4.17a}$$

$$\text{with} \quad \frac{1}{\gamma} = \frac{1}{\lambda + 0.08\beta} - \frac{0.035}{\beta^3 + 1} \tag{4.17b}$$

In Figure 4.16, the power coefficient in function of the tip speed ratio and pitch angle is displayed. It shows that the maximum C_p is obtained with $\beta = 0°$ and $\lambda = 6.3$.

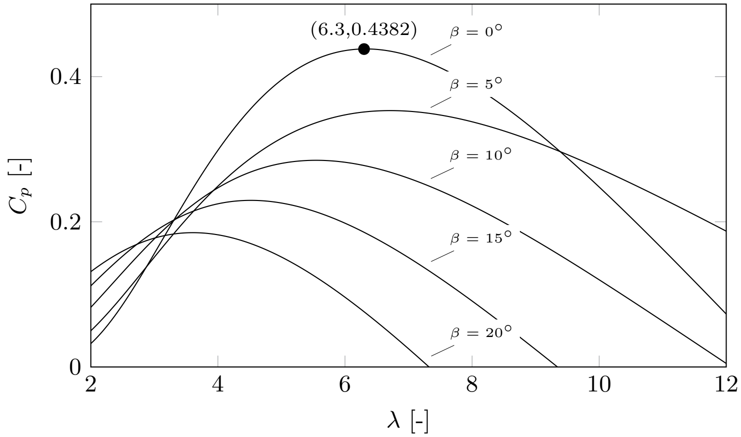

Figure 4.16: Power coefficient as a function of β and λ

4.5.2 Two mass mechanical model & filter

In the mechanical model, only the drive train of the turbine is included, modelled as a two mass model, namely a large mass corresponding to the inertia of the blades (H_{blade}) and a much smaller mass representing the generator inertia (H_{gen}). The dynamics of the shaft, neglecting self damping, are described in per unit by [53]:

$$2H_{blade}\frac{d\omega_{m,blade}}{dt} = T_{blade} - K_s\left(\theta_{blade} - \theta_{gen}\right) - D_s\left(\omega_{m,blade} - \omega_{m,gen}\right) \tag{4.18a}$$

$$2H_{gen}\frac{d\omega_{m,gen}}{dt} = K_s\left(\theta_{blade} - \theta_{gen}\right) + D_s\left(\omega_{m,blade} - \omega_{m,gen}\right) - T_{gen} \tag{4.18b}$$

$$\frac{d\theta_{blade} - \theta_{gen}}{dt} = \omega_{m,blade} - \omega_{m,gen} \tag{4.18c}$$

with K_s and D_s respectively the stiffness and mutual damping coefficient of the speed shaft rotating at a low speed. The torque on the blades (T_{blade}) and generator (T_{gen}) are:

$$P_{aero} = T_{blade} \cdot \omega_{m,blade} \tag{4.19a}$$

$$P_{wt} = T_{gen} \cdot \omega_{m,gen} \tag{4.19b}$$

In case a gearbox is present, the same equations are applicable, since the high speed shaft is mostly assumed to be very stiff [142]. Before the generator speed ($\omega_{m,gen}$) is used as input to the maximum power point tracker and pitch controller, it is passed to a first order low pass filter of which the output is denoted by $\omega'_{m,gen}$.

4.5.3 Pitch controller

In the high wind speed region, the pitch controller (Figure 4.17) keeps the speed of the turbine below its rated speed by pitching the blades. To realistically model the pitch control system, its servomechanism is represented by a first order system with a time constant τ_{pitch}. As both the pitch angle as its gradient are limited, the PI-controller regulating the input to the servomechanism is equipped with an anti-windup. Additionally, also the gain of the PI-controller is altered depending on the operating point of the system (i.e. gain scheduling) in order to compensate for the existing non-linear aerodynamic characteristics [142, 128]. This way, the total gain of the system is kept constant irrespective of the operating condition.

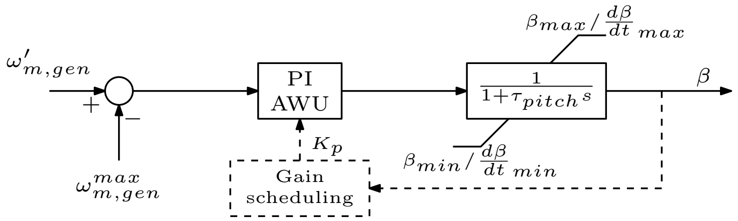
$\omega'_{m,gen}$
+
−
$\omega^{max}_{m,gen}$
PI
AWU
K_p
Gain
scheduling
$\frac{1}{1+\tau_{pitch}s}$
$\beta_{max}/\frac{d\beta}{dt}_{max}$
$\beta_{min}/\frac{d\beta}{dt}_{min}$
β

Figure 4.17: Block diagram of pitch controller (AWU: Anti-windup)

4.5.4 Maximum Power Point Tracking (MPPT)

The MPPT applies the power-speed characteristic as presented in Figure 4.18 to determine the power setpoint of the converter (P^*). In this figure, the MPPT curve and the ideal control curve which connects the points of optimal efficiency over different wind speeds is given. In Figure 4.19, the same curves are drawn, but now as a function of the wind speed. The parameters of the wind turbine used to compose the curves can be found in appendix B.2.

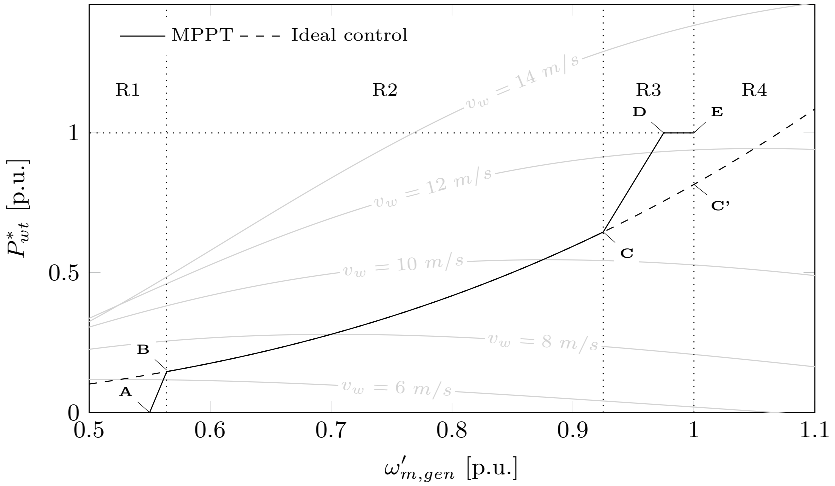

Figure 4.18: Power-speed control curves for MPPT and ideal operation. The latter connects the points of highest efficiency of the power-speed curves corresponding to a fixed wind speed (shown in grey)

Looking at the MPPT curve, four different regions can be distinguished (R1-R4). In R1, starting from the cut-in wind speed (point A), the rotor speed is kept almost constant, equal to its minimum value. Consequently, the turbine is operating at a sub-optimal operating point. Region 2, also called the variable speed region, begins at point B. From here on, the rotor speed is varied proportional with the increasing wind speed in order to achieve a constant tip speed ratio ($\lambda = 6.3$) corresponding to an optimal C_p. Consequently, maximum power is captured in this region. Theoretically, the rotor speed could be further increased following the ideal curve until maximum rotor speed (1 p.u.), but this would result in a vertical curve between point C' and E. Instead, in order to ensure a single power setpoint for every rotor speed, the MPPT curve is no longer following the ideal control curve from point C onwards, but the power setpoint is ramped up proportionally with the rotor speed until rated power is reached (point D). Region 3 is therefore a transition zone between the operation at optimal efficiency and the activation of the pitch system at point E. The latter point is generally chosen slightly higher than point D to prevent interference between the MPPT and the pitch control system [100]. Finally in region 4, the power setpoint is kept equal to its maximum rated value. At the same time, the pitch angle is increased in order to keep the rotor speed below its maximum value (Figure 4.19).

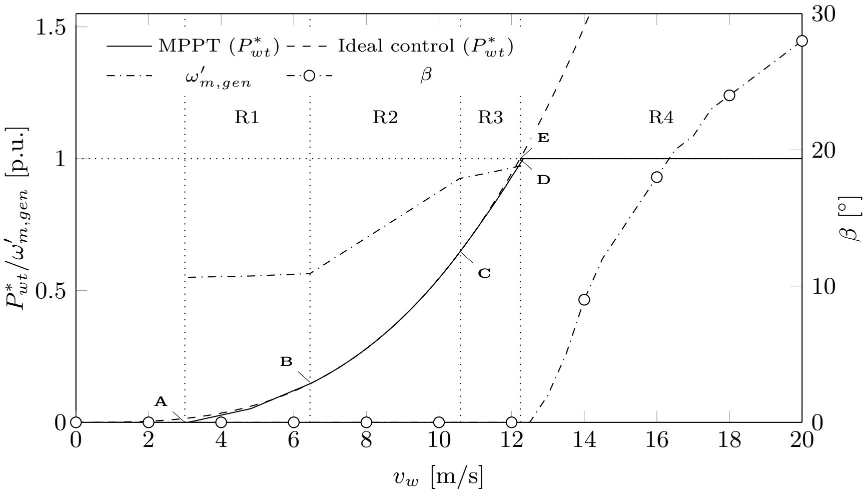

Figure 4.19: Power, rotor speed and pitch angle in function of wind speed

The proposed model is finally implemented in DIgSILENT Power Factory and a varying wind profile is applied. The simulation results in terms of active power, speed and pitch angle are given in Figure 4.20. For wind speeds above the rated speed (equal to 12.24 m/s), the pitch control is activated and both power and speed are limited to 1 p.u..

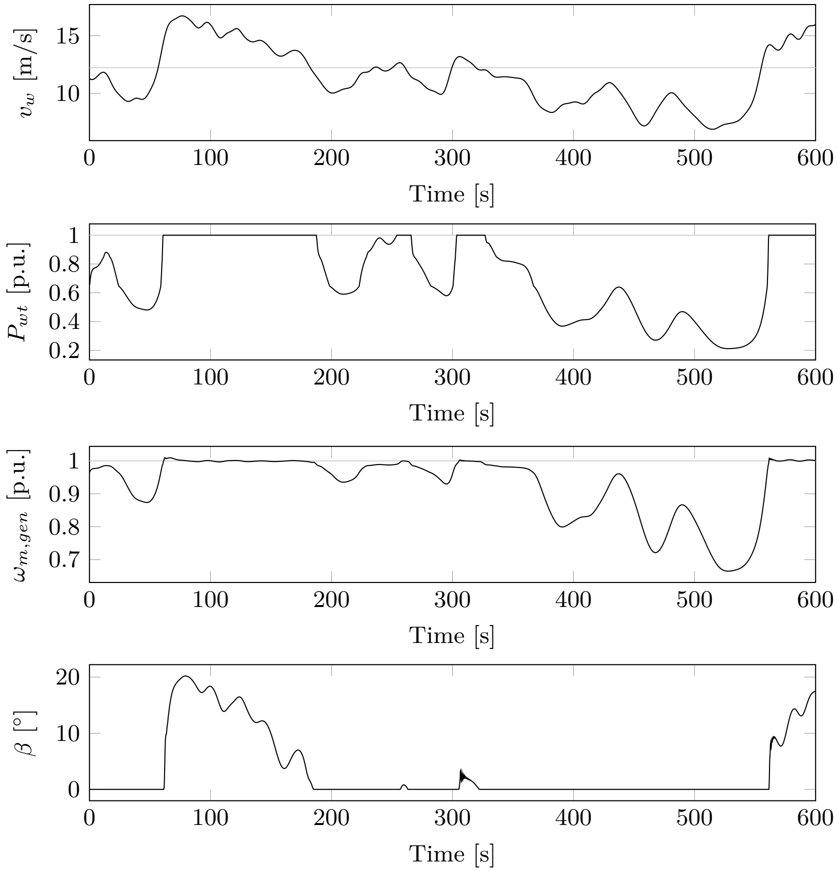

Figure 4.20: Wind turbine active power, speed and pitch angle for a varying wind profile

4.6 Conclusion

An overview of the various control structures of converter connected units is given and the available options to operate such converters depending on their role towards the system, i.e. grid forming, grid feeding or grid supporting, are discussed. The clear differences between the current or voltage source based grid supporting approach are highlighted, of which the control structure and implementation are described in more detail.

With respect to the current source based approach, the available synchronization techniques are assessed. It is shown that standard SRF-PLLs are not suitable to accurately and quickly track fast frequency deviations during distorted grid conditions, in terms of unbalances and harmonics. More advanced frequency tracking mechanisms are therefore required.

Finally, a mathematical representation of the aerodynamic characteristics, mechanical model and turbine control system of a Type 4 wind turbine is presented which can be applied in power system stability studies.

Chapter 5

Inertia support by converter connected units

> *"In science one tries to tell people, in such a way as to be understood by everyone, something that no one ever knew before.*
> *But in poetry, it's the exact opposite."*
> - Paul Dirac

5.1 Introduction

One of the options to operate a system with reduced inertia consists of altering the power output of converter connecting units as a function of the measured frequency and/or ROCOF. By providing this inertia support, the power imbalance causing the synchronous generators to exchange their kinetic energy is rapidly decreased, leading to a lower ROCOF and higher nadir frequency after a given negative power imbalance. Numerous control schemes can be implemented to this end, going from emulating the behaviour of synchronous machines to stepwise altering their power setpoints as soon as a frequency event is detected.

The available energy buffers within converter units are quantified. Based on this analysis, the inertia support mechanisms are grouped depending whether they are applied under optimal operation using their available energy buffers or under deloaded operation using the energy from the primary energy source.

Furthermore, also the control of transferring inertia by means of HVDC links is described. Finally, the potential issues with integrating the proposed controllers on system level is further addressed and an overview of the current grid codes related to the provision of inertia support is given.

5.2 Quantifying available energy buffers

Conventional power plants, equipped with synchronous machines, deliver an inertial response to the system by releasing part of their kinetic energy stored in the rotating generator and/or turbine. To provide an equivalent response by converter connected generation, an energy buffer and power margin need to be available or created.

This can be accomplished in three different ways. In a first approach, the PV or wind units are operated in a non-optimal operating point (i.e. deloading the unit). However, this deloading of renewable energy units is mostly considered undesirable as it results in a lower energy yield during normal operation.

A second approach comprises the use of the intrinsically available energy buffers within these converter connected units. In Figure 5.1(a), an overview is given of the stored mechanical and/or electrical energy for several generation technologies over a broad range of power ratings. The solid lines connect the points with the same inertia constant, used to normalize the stored energy for different ratings. The grey area, bounded by the lines of 2 and 9 s, corresponds to the inertia of conventional power plants.

Looking at wind turbines (DFIG and full converter), although some energy is stored in the DC link capacitor of the converter, most of the available energy comes from the rotating blades. In [145], an approximate relationship between the rating of the turbine and the moment of inertia of its blades is defined:

$$J_{blade} \approx 1.74 \cdot 10^{-7} S^{2.13} \tag{5.1}$$

The stored energy within the blades of a 2 MW turbine rotating at a rated speed of 1.8 rad/s is almost 7.3 MWs. Adding the inertia from the generator ($H \approx 1\ s$ [145]), the total inertia constant becomes 4.65 s comparable with the one of conventional power plants. The energy buffer of other converter units, such as PV and HVDC, is mainly coming from the energy stored in the DC link capacitors. The energy within other parts of the power electronic system (filters, line reactors,...) is negligible.

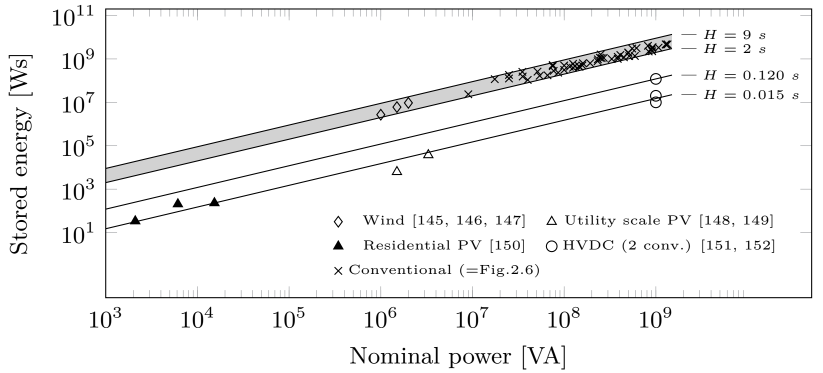

(a) Energy buffers in function of capacity for different generation technologies

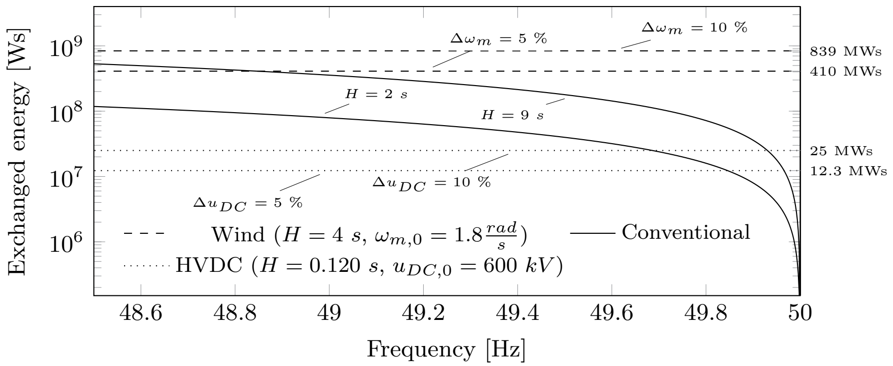

(b) Kinetic energy exchange for conventional units compared with converter connected units (S=1000 MVA)

Figure 5.1: Overview of available energy buffers in converter connected units (a) and the required exchanged energy during a frequency transient (b)

Similar to the inertia constant of rotating machines (2.5), an equivalent inertia constant can be defined for the DC link (with u_{DC} expressed here in volt):

$$H_{DC} = \frac{E_e}{S} = \frac{c \cdot u_{DC,0}^2}{2S} \tag{5.2}$$

Both the capacitor (c) as voltage level, influenced by the converter technology and rating of the unit, determine the total stored electrical energy E_e. Regarding HVDC, an equivalent inertia constant between 5-10 ms is obtained for the existing two- and three-level converters, whereas the increasingly popular modular multi-level converters (MMC) can have an inertia constant up to 60 ms (for a single converter) [151, 152][1]. PV units, both residential and utility scale, have an equivalent inertia constant only in the order of ms to tens of ms. It is thus clear that only the amount of stored energy within wind turbines (expressed with respect to their rating) comes close to that of conventional power plants (Figure 5.1(a)).

However, as the rotational speed of the synchronous machines is directly linked to the frequency, only a small part of their total stored energy is released during a frequency drop (Figure 5.1(b)). Here, the solid lines represent the amount of exchanged energy of a 1 GW power plant with an inertia constant of 2 and 9 s. The other horizontal lines indicate the maximum energy released by an equivalent wind farm or HVDC point-to-point link in case respectively a rotor speed or voltage deviation of 5 and 10% from the rated value (u_0 and ω_0) is allowed. This figure shows that, although the stored energy in for instance HVDC links (MMC) is far less than the energy in conventional power plants, it can still provide the same amount of energy as is released by a power plant (H=9 s) during a frequency drop down to 49.7 Hz if a 10% drop in DC link voltage is allowed. Furthermore, it also illustrates that wind appears again to be the perfect candidate to deliver inertia support as a similar energy exchange can be obtained for substantial frequency drops (below 49 Hz) with a rotor speed deviation of merely 5% [151].

Thirdly, also energy storage systems (ESS) or demand side management techniques might provide the required energy exchange (and buffer) to deliver inertial support. The latter approach, although out of the scope, can definitely be a viable option as it can for instance be realized by means of domestic thermostatic loads or by implementing a multi-stage underfrequency load shedding [153, 154]. However, additional infrastructure like communication and smart devices are required. Regarding energy storage systems, their rating and capacity mainly determine how much inertial support they can provide [155]. A broad range of storage technologies can be used such as short-term storage devices (e.g. ultracapacitors [156]) or other fast-acting technologies (e.g. li-ion batteries [157]).

Besides the energy buffer, the units also need to have a dynamic power margin available. Consider for instance a response identical to a synchronous machine with an inertia constant of 6 s. In case the grid experiences a frequency transient with a ROCOF of 0.5 Hz/s, the electrical output of the unit temporarily increases with 0.12 p.u..

---

[1] Actually, for HVDC links interconnecting two distinct synchronous areas, also the stored energy of one system can be used as an energy buffer to the other and vice versa.

Based on this analysis, three distinct categories of providing inertia support can be defined depending on the energy source:

1. Inertia support in deloaded operating point: Energy is taken from the primary energy source.
   - Wind power
   - PV
   - Demand side management
2. Inertia support in an optimal operating point: The intrinsic available energy buffers are applied.
   - Wind power (variable speed wind turbines): energy stored in blades, generator and gearbox
   - (HVDC grids: small amount of energy stored in the capacitors and cables)
3. Transfer of inertia: HVDC links

Storage can considered to be part of both category 1 and 2 as their primary energy source is equivalent to the available energy buffer. The type of energy source for inertia support that will be applied in future systems will largely depend on the available, installed generation units and storage facilities.

In the following, different inertia support mechanisms are presented. For the GSC control of PV and wind units, a current source based control is taken, as it assumed to be the present, standard control approach for such units. Virtual inertia by voltage source based converters is assessed in chapter 7.

5.3 Inertia support in an optimal operating point: wind power

Variable speed wind turbines (Type 3 and 4) do inherently not react to any changes in the grid frequency and therefore become completely inertialess from a power system perspective (section 2.3.3). However (see section 5.2), their available energy buffer in the form of rotational kinetic energy within the blades is quite substantial and comparable with the stored kinetic energy of conventional power plants. As a result, different control strategies can be applied in order to transfer this energy to the system during frequency transients and in this way provide some sort of inertia support.

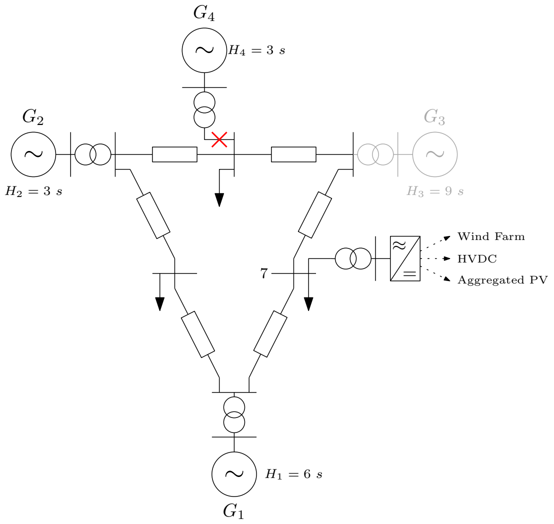

(a) Test system

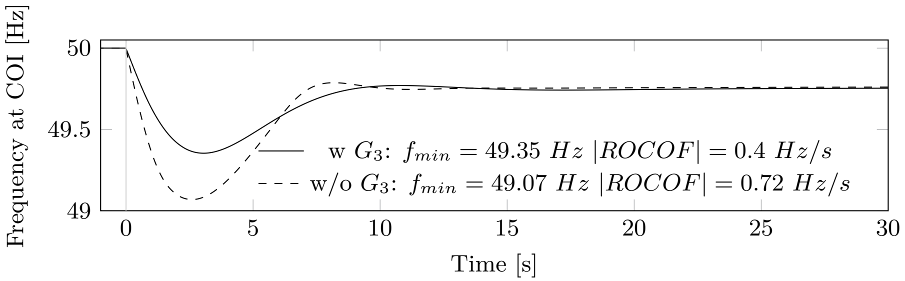

(b) Speed of synchronous machines

Figure 5.2: Test system: Frequency response after the outage of G_4 (27MW) with and without G_3 providing synchronous inertia (equivalent converter power is constant during frequency transient, equal to 50 MW)

These strategies are imposed to several constraints, such as the maximum and minimum allowed speed of the turbine, the current limits of the converter and the maximum torque of the generator. Furthermore, the inertia support can in most cases only be provided for a certain amount of time as a deviation in the rotational speed directly leads to a reduced aerodynamic performance of the turbine. The main advantage of applying these control methods employing the kinetic energy in the blades, is the high energy yield during normal operation as the turbine is operating at an optimal operating point.

In the following, some inertia support mechanisms are presented and the impact on the ROCOF and nadir frequency using the test system is analysed. It is assumed that a large amount of converter connected generation is connected at bus 7, represented by an equivalent converter. These added generation units displace plant 3 resulting in a decrease of synchronous inertia of about 48% compared to the original system (Appendix B.1). To demonstrate the influence of the inertia support on the frequency response, an outage of G_4 is taken as reference incident. In Figure 5.2, the test system including the converter connected generation are shown together with the frequency response with and without G_3 connected to the system. As active power support from the converters is not yet provided, the frequency response is substantially deteriorated with a lower nadir and higher ROCOF values when G_3 is displaced. The steady state frequency remains however almost unchanged since it is assumed that the droop factors of the remaining generators are modified in order to keep the total system droop (R_{sys}) constant.

5.3.1 Virtual inertia control

One way of providing inertia support is by simply mimicking the behaviour of synchronous machines through adding an additional power control loop acting on the frequency measured by the PLL. The proposed controller to provide the so called virtual inertia is given in Figure 5.3 with H_V the virtual inertia constant expressed in seconds. τ_V denotes the filter time constant of a first order filter to attenuate the high frequency oscillations in the measured grid frequency.

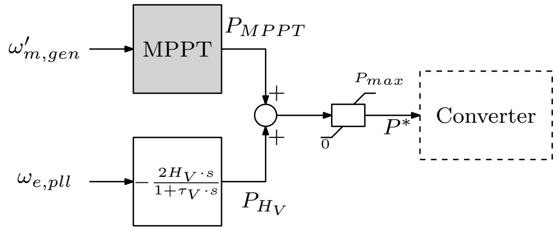

Figure 5.3: Virtual inertia control

In order to examine the effect of the virtual inertia control, a wind farm with a capacity of 100 MW, displacing G_3, is connected through a transformer to bus 7. The wind turbine model as proposed in the previous chapter is used to represent the aggregate response of the wind farm, assuming the same operating point, inertial controller and measured frequency for all turbines. A power imbalance at t = 0 s is simulated by assuming an outage of G_4.

All simulations are performed in DIgSILENT Power Factory. The simulation results for a wind speed equal to 10 $\frac{m}{s}$ with and without virtual inertia are given in Figure 5.4(a).

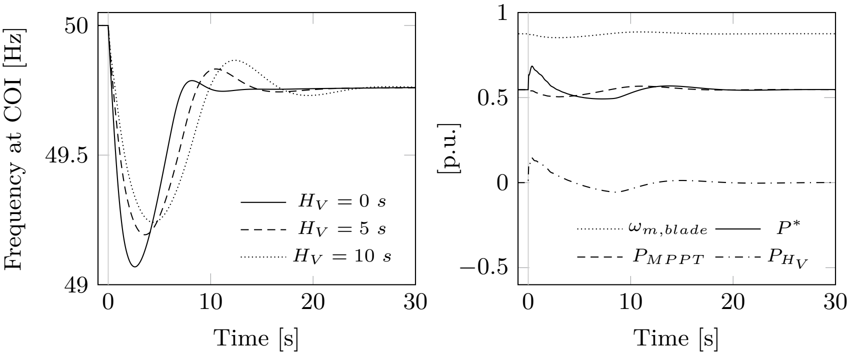

(a) Frequency (power imbalance of 27 MW at t = 0 s)

(b) Wind turbine: power and rotational speed for $H_V = 10\ s$

Figure 5.4: Results for a wind farm equipped with a virtual inertia controller ($v_w = 10\ \frac{m}{s}$ and $\tau_V = 0.2\ s$), wind farm covers 30% of total load

Before the imbalance, the wind turbines are operating at maximum C_p. As soon as the frequency changes, the power output of the turbine is increased proportionally with the measured ROCOF. As a result, the rotor speed drops (Figure 5.4(b)) releasing part of the kinetic energy of the blades. Consequently, the ROCOF is less than the case without inertial control and also the minimum frequency is slightly improved. The MPPT controller also acts on the decreasing rotor speed by lowering its output (P_{MPPT}) and in this way actually counteracts the setpoint coming from the inertial response controller (P_{HV}). As such, it provides some sort of self-stabilizing mechanism to prevent stalling and overspeeding.

The same simulation is performed for various H_V and τ_V over the whole wind speed range (Figure 5.5). In Region 1, no inertia support can be delivered as the rotor speed is close to its minimum value. In Region 2, virtual inertia can be provided and the ROCOF is decreased. Lowering the filter time constant further improves the measured ROCOF, but the rotor oscillations are less attenuated and consequently these oscillations also become more present in the inertial response of the wind turbine. Above rated wind speed, the power output is equal to the rating of the converter. Only if overloading is allowed, an inertial response can be delivered. In this case, an overloading of 10% is assumed and increasing H_V not further improves the ROCOF since the power output is

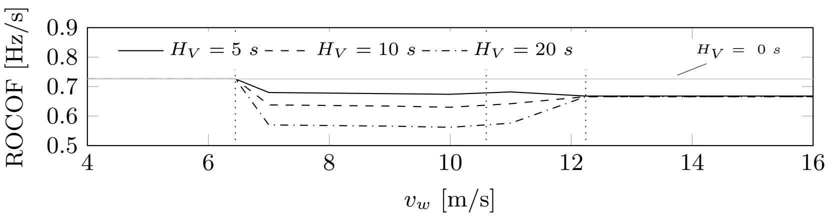

(a) ROCOF (measured over 500 ms) for $\tau_V = 0.1\ s$

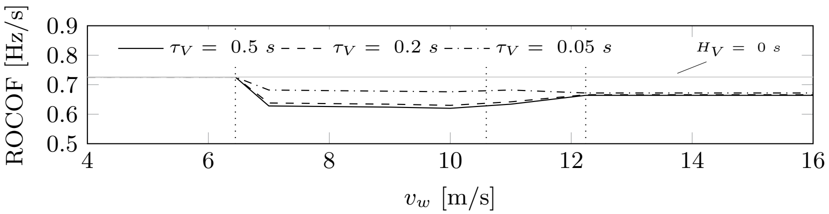

(b) ROCOF (measured over 500 ms) for $H_V = 10\ s$

Figure 5.5: Influence of virtual inertia control on ROCOF (Assuming that the converter can be overloaded by 10%)

capped (Figure 5.6) for a wind speed of 14 $\frac{m}{s}$. In region 4, the power to deliver inertia is no longer coming from the kinetic energy of the blades, but is released by reducing the pitch angle of the blades.

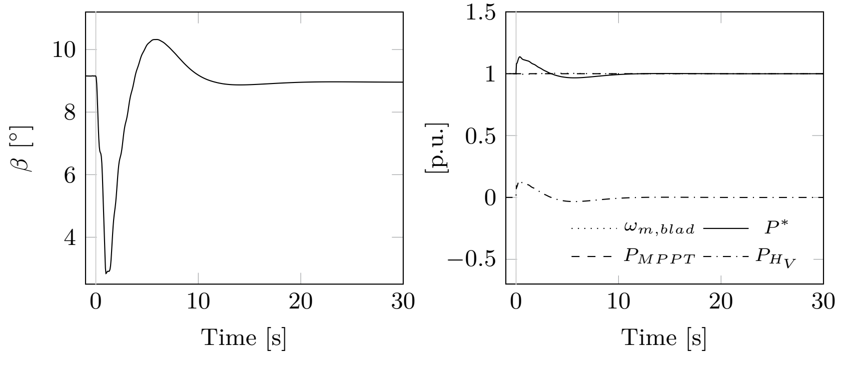

(a) Pitch angle

(b) Power and rotor speed

Figure 5.6: Results for a wind farm equipped with a virtual inertia controller ($v_w = 14\ \frac{m}{s}$, $H_V = 10\ s$ and $\tau_V = 0.2\ s$), wind farm covers 60% of total load

5.3.2 Fast frequency response control

The controller in the former section is designed to emulate the inertial response of synchronous machines. However, as the power converter is fully decoupled from the grid, any type of power response can be provided. One of the possible options consists of stepwise increasing the power output as soon as the frequency or ROCOF passes certain limits. Although this approach does not provide inertia in the way synchronous machines do, it can be considered as a form of inertia support since it will assist the system during the inertial response phase of the load-frequency control. The proposed implementation of such a controller is illustrated in Figure 5.7.

The controller switches the power setpoint from the MPPT controller to a pre-defined 'Fast frequency response (FFR) function', increasing the reference power with P_{up}. Since the kinetic energy within the blades is used to provide this power, the rotor speeds drops. Therefore, after a time period of t_{up}, the power output is lowered again in order to accelerate the turbine and return it to its optimal operating point. When the rotor speed is restored to its pre-disturbance value, the power reference is again provided by the MPPT controller. For wind speeds above rated, P_{down} can be set equal to zero as no recovery of the rotor speed is required.

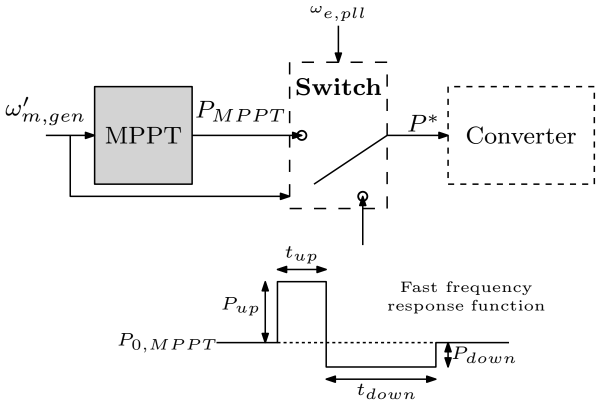

Figure 5.7: Fast frequency response control

The influence of the controller on the frequency response is given in Figure 5.8, taking the same operating points and power imbalance as in the previous section. It illustrates that not only the initial ROCOF is improved (0.58 $\frac{Hz}{s}$ measured over 500 ms) compared to the case of no support, but also the minimum frequency is increased due to the sustained power support provided during the first seconds after the detection of the frequency event. The downside of applying this controller is the secondary dip that occurs when the power drops to regain speed. Especially if a large number of units reduce their power output at the same time, this secondary dip can become a real challenge since it can possibly even drop below the initial frequency dip.

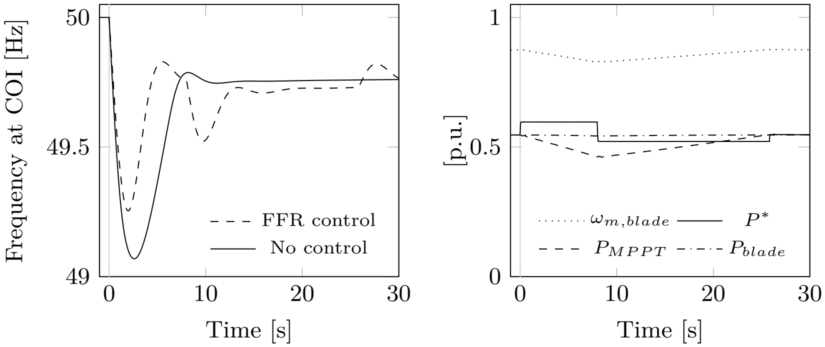

(a) Frequency (power imbalance of 40.5 MW at t = 0 s)

(b) Wind turbine: power and rotor speed

Figure 5.8: Results for a wind farm equipped with a fast frequency response controller ($v_w = 10\ \frac{m}{s}$, $t_{up} = 8\ s$, $P_{up} = 0.05\ p.u.$ and $P_{down} = 0.025\ p.u.$), controller is triggered at 49.8 Hz

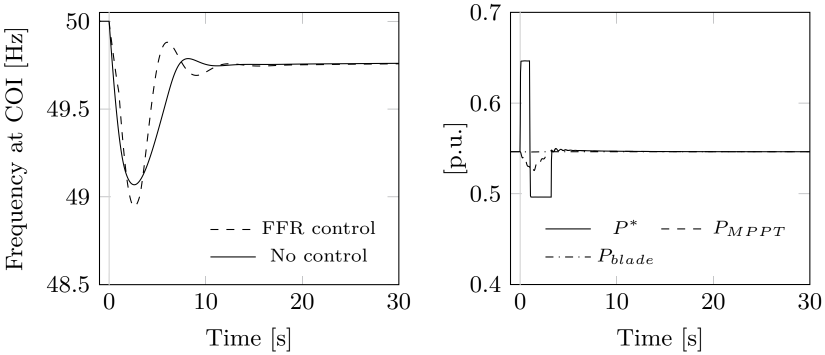

(a) Frequency (power imbalance of 27 MW at t = 0 s)

(b) Wind turbine: power and rotor speed

Figure 5.9: Results for a wind farm equipped with a fast frequency response controller ($v_w = 10\ \frac{m}{s}$, $t_{up} = 1\ s$, $P_{up} = 0.1\ p.u.$ and $P_{down} = 0.05\ p.u.$)

Also in case the output power from the wind drops too soon after the start of the frequency event, i.e. before the governor reaction has ceased the frequency decline, it can possibly jeopardize the frequency stability as the power drop leads to a reduction of the nadir frequency (Figure 5.9). It is therefore important to properly select the parameters of the fast frequency response function.

Besides constraints with respect to the maximum generator torque and converter current, increasing P_{up} leads to a lower t_{up} as the rotor speed drops more quickly due to the increased imbalance of converter power and the power captured from the wind. The latter is also reduced as a decreasing rotor speed directly impacts the aerodynamic performance of the turbine. This further aggravates the decline of the rotational speed of the blades during t_{up}.

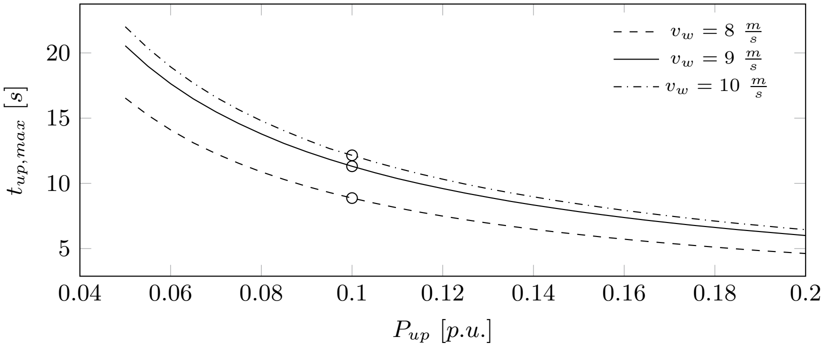

(a) Maximum t_{up} in function of the magnitude of the power step

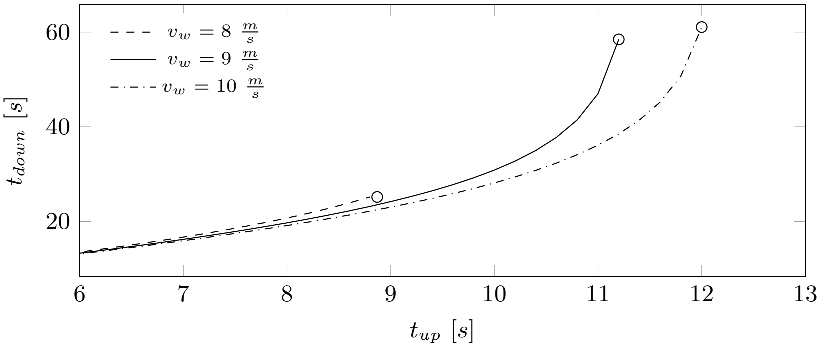

(b) t_{down} in function of t_{up} for $P_{up} = 0.1\ p.u.$ and $P_{down} = 0.05\ p.u.$

Figure 5.10: Correlation between FFR control paramters

The correlation of the parameters for different wind speeds is further illustrated in Figure 5.10. It demonstrates that the maximum time period delivering the power boost is limited depending on the magnitude of the power step and the wind speed before the minimum rotor speed is reached. For a given power step, t_{down} is given in function of t_{up} in Figure 5.10(b).

Besides the virtual inertia and fast frequency support control, numerous other control options are available which harness the kinetic energy in the blades in order to lower the ROCOF and/or increase the nadir frequency after a major negative power imbalance in the system. In [145, 158, 159, 160, 48] for instance, the power output of the wind turbine is varied proportional to both the ROCOF as well as to the deviation in the frequency. The latter control is similar to the droop control of conventional generation and mainly reduces the maximum frequency deviation after the event.

Variations on the FFR control are presented in [100, 50, 161, 162] where the shape of the function given in Figure 5.7 has been modified. In [100] for example, the MPPT controller is kept activated during the FFR support, leading to a power boost reduced over time compared to the constant P_{up}. A further optimization of the shaping parameters by means of a particle swarm optimization is presented in [163], with as main objective to limit the impact of the kinetic energy regain during t_{down}.

Other ways of reducing the secondary frequency dip caused by the power drop to restore the rotor speed are given in [159, 164]. Here, the inertial response is applied in a coordinated way, i.e. not all turbines connected to the system deliver the same FFR. By defining a different t_{up} for each turbine, the power output is gradually reduced and spread out in time. If it is assumed that the operating points of all turbines in a wind farm or power system are known, it is in theory even feasible to determine the optimal control settings by a centralized control unit which sends the appropriate inertial control parameters to each turbine individually [164]. As such, the secondary dip is reduced in most cases since the inertia support is primarily provided by wind turbines operating in region 4, but additional communication between different wind turbines is required.

Finally, in [165, 166] a control method is proposed which harvests both the energy from the blades as well as from the DC link capacitor of the converter in order to dampen the high torque variations exerted on the generator during the inertial support. However, as the stored energy in this DC bus is very small, the use of the energy within the capacitor for inertia support is rather limited.

5.4 Inertia support in a deloaded operating point: deloading wind and PV units

By deloading the renewable generation unit, part of the available power from the primary power source is not converted into electrical power, but used as a buffer to provide additional services to the grid. Besides the provision of inertia support, the unit can also deliver grid support over a longer time period, which makes it even feasible to participate in the primary control of the power system. By for instance not only acting on the ROCOF, but also on the frequency deviation, both droop control as well as the inertial response of synchronous machines are emulated by the converter. The control is presented in Figure 5.11, with P_{del} the power setpoint during normal operation and P_{AV} the maximum available power. R_V represents the (virtual) droop constant of the converter.

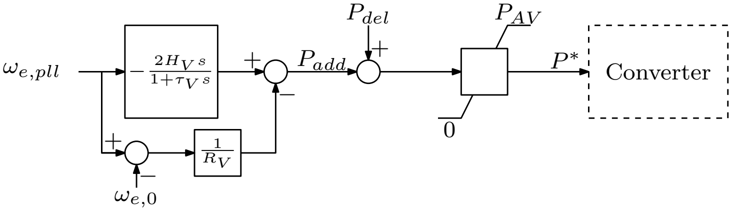

Figure 5.11: Droop and virtual inertia control

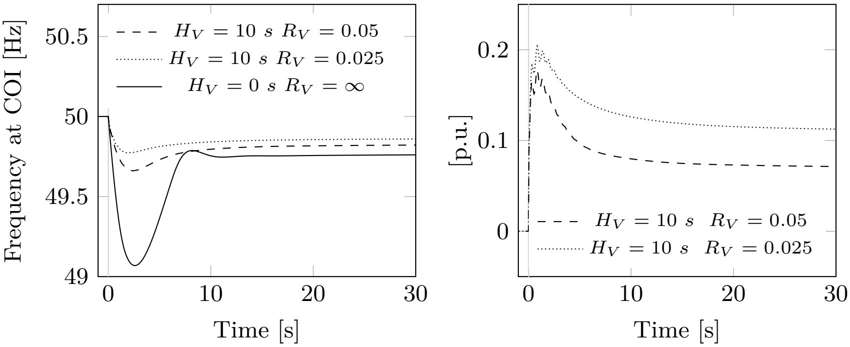

(a) Frequency

(b) Additional power reference

Figure 5.12: Results for converter units equipped with droop and virtual inertia support (power imbalance of 27 MW at t = 0 s)

Including this control in the converters connected to bus 7 of the test system, results in the frequency response given in Figure 5.12. The figure clearly shows that by applying droop control, also the nadir frequency and the steady state frequency are this time largely improved. The way in which both PV and wind can be deloaded to obtain P_{del} is shortly presented in the following.

Deloading wind turbines

To deliver frequency support over a longer time frame, the wind turbines need to have an up- and downward power margin. This margin can be created in different ways (Figure 5.13).

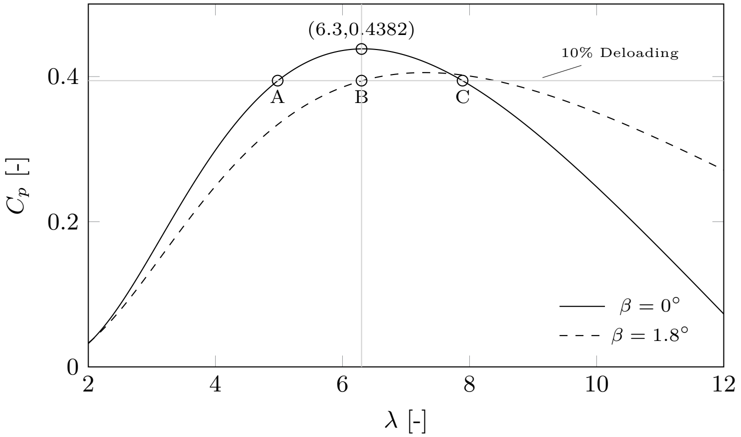

Figure 5.13: Providing a 10% power margin by underspeeding (A), pitching (B) or overspeeding (C)

Starting from the optimal operating point, three different approaches can be distinguished. A first approach consists in varying the pitch angle while keeping the rotor speed at its optimal value. As the pitch regulation is slow compared to the power control of the converter and may cause additional wear and tear, this method is mainly preferred in the high wind speed regions, where the pitch control is already activated and the rotor speed is at its maximum [167]. Also for fixed speed wind turbines, it is only feasible to apply deloading by altering the pitch angle. For variable speed turbines on the other hand, the control of the rotor speed can be modified. By over- or underspeeding the turbine away from its optimal tip speed ratio, the C_p drops and a certain power margin is created. Furthermore, in case of overspeeding, additional kinetic energy is stored in the blades compared to operation at optimal operating point. This way, kinetic energy is released to the power system in case frequency and inertia support is provided. To apply deloading by overspeeding, accurate and reliable wind speed measurements are however required [167].

The overspeeding approach can easily be integrated in the control of the turbine presented in figure 4.15 by changing the MPPT curve to a control curve connecting the operating points corresponding to a certain percentage of deloaded operation [168]. Alternatively, P_{AV} can simply be determined by a wind speed measurement and P_{del} is chosen depending on the required power reserve. Due to the mismatch in available power from the wind and the electrical output power, the wind turbine accelerates until it reaches the tip speed ratio corresponding to P_{del} (point B in Figure 5.13 for instance in the case of 10% deloading).

Deloading PV units

Since PV units have only a small amount of energy available in their DC link capacitor, they need to be deloaded in order to provide both up- as downward power reserves. Deloading can simply be achieved by modifying the MPPT control of the converter connected to the PV panels (Figure 4.1). This MPPT control normally alters the DC voltage of the panels (u_{pv}) in order to obtain maximum efficiency (point A in Figure 5.14(b)). The maximum power point and corresponding DC voltage vary with solar radiation, ambient temperature and solar cell temperature. Numerous MPPT techniques, such as the widely used perturb-and-observe algorithm, exist to extract the maximum power from the sun [169].

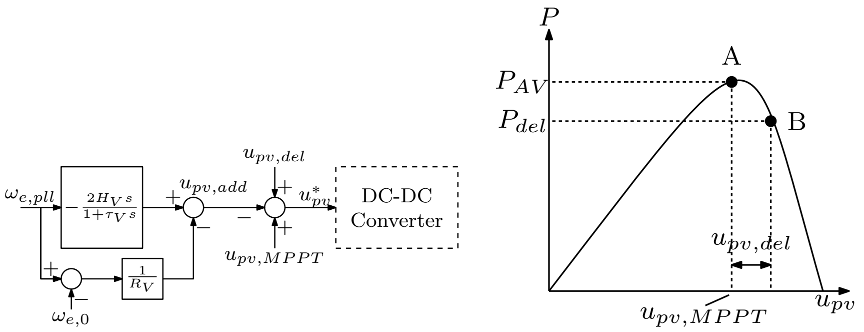

(a) Modified DC-DC controller to provide inertia support by PV

(b) Typical power versus DC voltage relationship of a PV unit

Figure 5.14: Inertia support by a PV unit [12]

To deload the unit, the PV voltage is increased above the MPPT point by $u_{pv,del}$ [170, 12]. Consequently, the power output is dropped (point B) and a power margin is created which can be applied to offer inertia and primary frequency support (Figure 5.14(a)). Since the relationship between power and voltage is nonlinear between points A and B, the proposed control delivers a slightly different power response compared to the one presented in Figure 5.11. Further research is however required to assess in detail the influence of the deloading on the losses and heat production.

5.5 Transfer of inertia by HVDC links

VSC HVDC links can be applied to connect independent asynchronous AC systems or can be embedded into a single AC system. The latter configuration, although many control options exist to provide for instance additional damping of the electromechanical modes of the system [171], offers no clear opportunities to support the inertial response of the system. However, when VSC HVDC technology is used to link two asynchronous systems, the inertia of one system can be transferred to the other by simply adding an additional control loop. In the following, the control in order to transfer the inertia is presented. Also the potential of including the use of the energy stored in the DC link for inertia support is discussed. Finally, the way HVDC grids can offer inertia support is further elaborated.

5.5.1 Inertia support by HVDC point-to-point links

In general, two distinct control strategies to provide inertia support by HVDC links can be considered, using the DC bus voltage as a inherent communication path to transfer the frequency signal from one system to another. Other communication channels can be applied, but may influence the effectiveness of the scheme, as it involves a certain delay that need to be small with respect to the time frame of inertia control [172].

Strategy 1

In a first strategy, applied to a link connecting two separate synchronous machine based power systems, the controller (Figure 5.11) is simply added to the outer control loop of the GSC responsible for controlling the active power over the DC line (Strategy 1 in Figure 5.15). As the other GSC keeps the DC voltage constant, the power required to provide inertia support is transferred from system B to A. Both converters are current source based controlled (CSB).

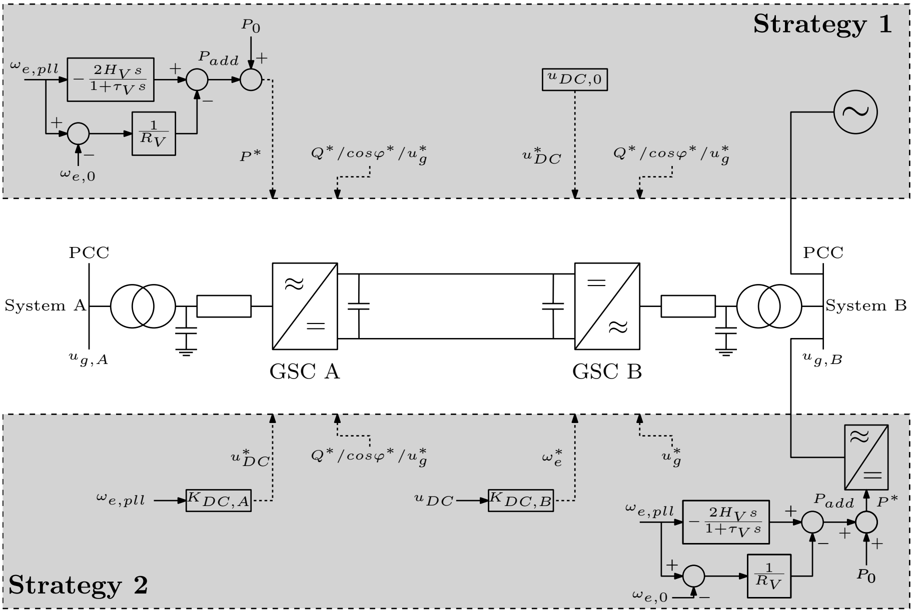
Strategy 1
P_0
P_{add}
$\omega_{e,pll}$
$-\frac{2H_V s}{1+\tau_V s}$
$\frac{1}{R_V}$
$\omega_{e,0}$
P^*
$Q^*/cos\varphi^*/u_g^*$
$u_{DC,0}$
u_{DC}^*
$Q^*/cos\varphi^*/u_g^*$
PCC
System A
$u_{g,A}$
GSC A
GSC B
PCC
System B
$u_{g,B}$
u_{DC}^*
$Q^*/cos\varphi^*/u_g^*$
ω_e^*
u_g^*
$\omega_{e,pll}$
$K_{DC,A}$
u_{DC}
$K_{DC,B}$
$\omega_{e,pll}$
$-\frac{2H_V s}{1+\tau_V s}$
P_{add}
P^*
$\frac{1}{R_V}$
P_0
$\omega_{e,0}$
Strategy 2

Figure 5.15: Inertia support from system B to A by point-to-point HVDC links: control overview

Strategy 2

The second strategy is applied to HVDC links connecting system A with a converter unit based power system, such as a wind farm for instance. Here, GSC A is controlling the DC voltage while GSC B is responsible for setting the AC voltage and frequency of system B (grid forming: voltage source based controlled). For strategy 2, the frequency of system A is duplicated to system B through subsequently altering the DC voltage and frequency setpoint of GSC B [172]. The inertia support itself is provided by the converters within system B equipped by the controller (Figure 5.11). $K_{DC,A}$ and $K_{DC,B}$ can be applied to define a proportional relationship between the frequency of system A and B.

Consequently, the actual virtual inertia and droop constant are:

$$H_{V,A} = K_{DC,A} \cdot K_{DC,B} \cdot H_V \tag{5.3a}$$

$$\frac{1}{R_{V,A}} = K_{DC,A} \cdot K_{DC,B} \cdot \frac{1}{R_V} \tag{5.3b}$$

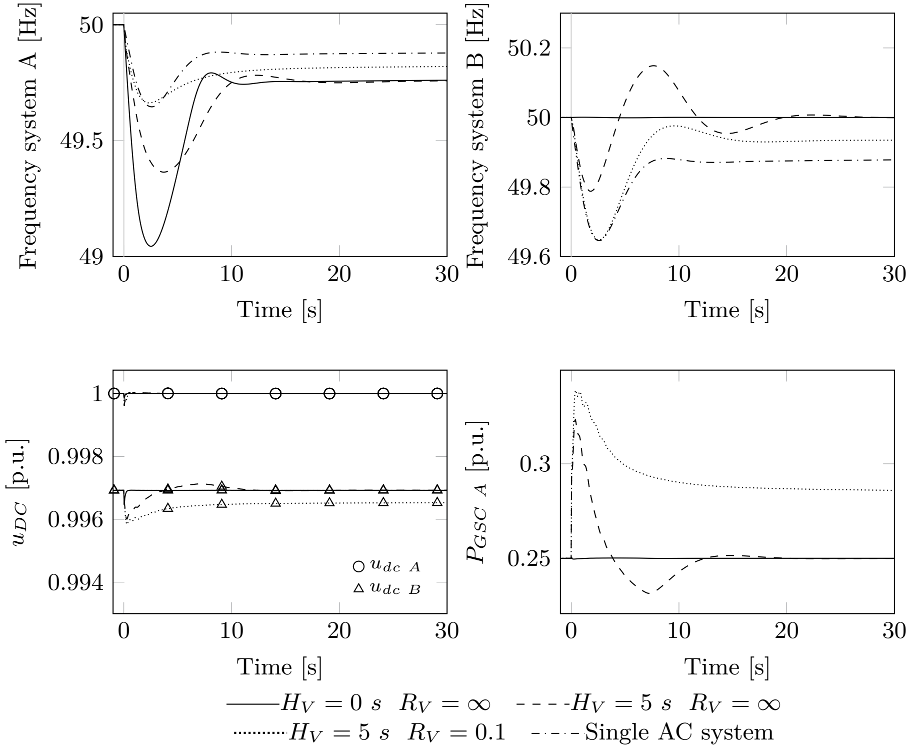

Figure 5.16: Results strategy 1

To illustrate how both strategies provide inertia support, the test network in appendix B.1 is used for system A. Instead of integrating a wind farm, an HVDC link of 200 MVA is now connected to bus 7 with an initial power transfer of 50 MW towards system A. This link displaces G_3. Also with respect to system B, the same test network (active power of load A, B and C decreased to 30 MW) is applied for strategy 1. For strategy 2, an equivalent converter model with a power output of 50 MW is used to represent the aggregated response of all converters within system B. A list of the parameters of the HVDC link is given in appendix B.3.

The results for the loss of G_4 within system A at $t = 0\ s$ are given in Figures 5.16 and 5.17. As H_V and R_V are expressed in per unit with respect to the rated power of the unit (200 MVA), they are scaled in this simulation to provide the same response as previously considered by the wind farm (100 MVA) in Figure 5.12 ($H_V = 5\ s$ and $R_V = 0.1$).

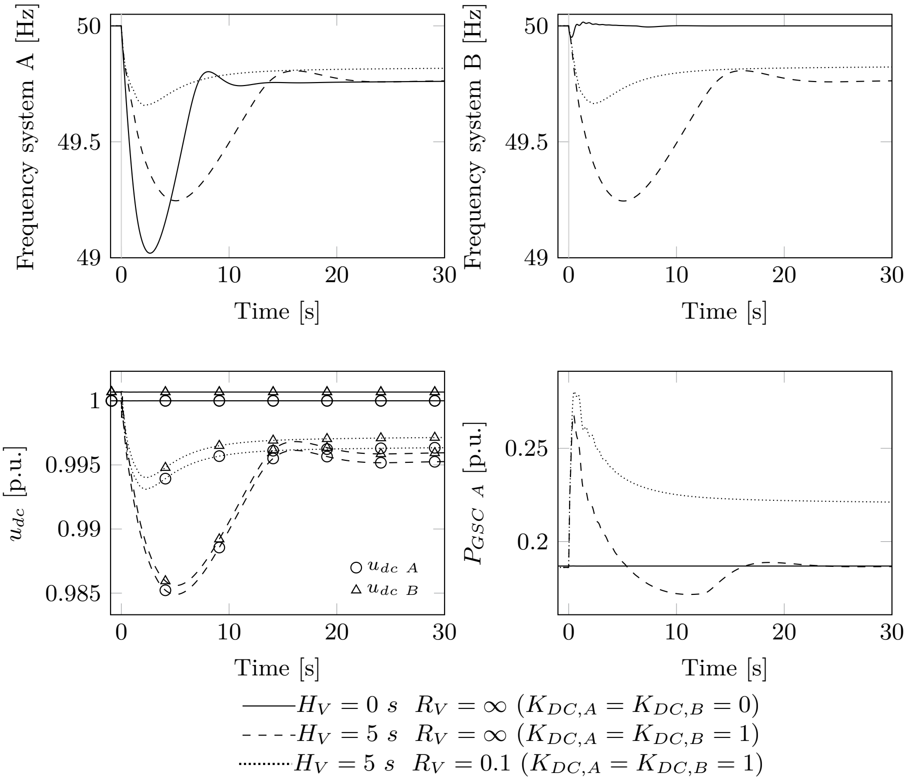

Figure 5.17: Results strategy 2

While the frequency response of system A and the power transfer of GSC A are quite similar for both strategies, the frequency within system B is different. In strategy 1, this frequency is determined by the synchronous machines connected to system B. As the power for inertia support is fully provided by them, a negative power imbalance occurs in system B and the frequency varies according to the inertia, droop control and turbine characteristics of the generators within system B. Applying strategy 2 and in case the inertia support is activated (e.g. $K_{DC,A} = K_{DC,B} = 1$), the frequency of system B is set equal to the one of system A through altering the DC voltage.

In Figure 5.16, the frequency response in system A and B in case they would be interconnected by an AC link is given as well. Since H_V is taken almost equal to the equivalent inertia constant of system B (5.7 s on a 200 MVA base), the initial frequency trajectory in network B is almost the same as when a single AC system is considered.

5.5.2 Potential of HVDC link energy storage in inertia support

Besides transferring power from one AC system to another, controlling the energy stored in the DC link by altering the DC voltage offers an alternative way of providing the required power for the inertial support. Although some studies [173] suggest to solely apply this energy stored in the DC link for inertia support, it is generally considered to be infeasible since much larger capacitance values compared to the one of current DC links are required. As shown in section 5.2, the equivalent inertia constant of an HVDC link is an order of ten to hundred times smaller than the one of conventional units. To asses the amount of virtual inertia and virtual droop possibly providing this available stored energy, the power required by the control loop is taken equal to the additional power from the DC link in case the output from the other terminal is fixed (all variables are expressed in per unit):

$$-2H_V\frac{d\Delta\omega}{dt} - \frac{1}{R_V}\Delta\omega = -2H_{DC}u_{DC}\frac{du_{DC}}{dt} \tag{5.4}$$

By integrating both sides and rewriting the equation in function of $\Delta u_{DC} = u_{DC} - 1$, H_{DC} becomes:

$$H_{DC} = \frac{2H_V\Delta\omega + \frac{1}{R_V}\int_0^t \Delta\omega dt}{\Delta u_{DC}^2 + 2\Delta u_{DC}} \tag{5.5}$$

This equation can be applied to determine the required H_{DC} to deliver inertia support acting on the ROCOF and deviation of the frequency, respectively characterized by H_V and $\frac{1}{R_V}$. The results are shown in Figure 5.18. In the first figure, the droop control is deactivated and only virtual inertia is delivered. H_{DC} is in that case depending on H_V, the allowed voltage deviation of the DC link and the maximum frequency deviation of the system. The grey horizontal lines corresponds to the $H_{DC} = 0.12\ s$, corresponding to the stored energy in two MMC converters. The results illustrate that only small values in the order of hundreds of milliseconds for H_V can be chosen in case the voltage variation over the DC link is limited to 10%. In Figure 5.18(b), also droop control is

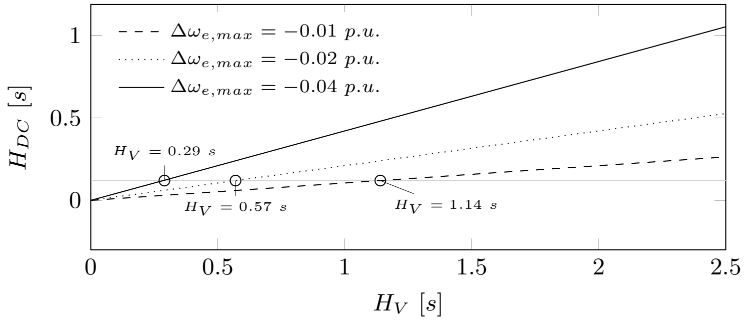

(a) Required H_{DC} in function of H_V for $\Delta u_{DC,max} = -0.1\ p.u.$ and $R_V = \infty$

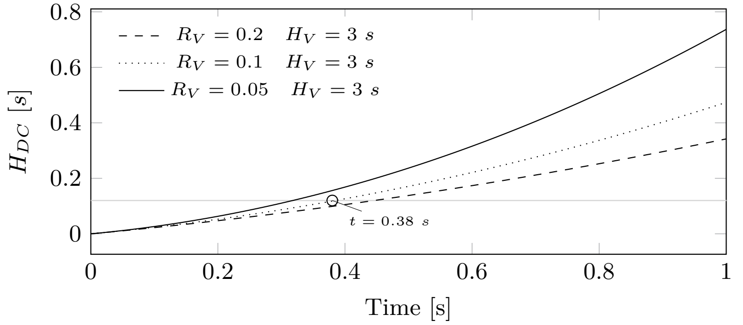

(b) Required H_{DC} in function of time to provide inertia support (assuming $ROCOF = -0.5\ \frac{Hz}{s}$)

Figure 5.18: Required H_{DC} to deliver inertia support

considered. As the energy related to the droop action of the controller is equal to the integral of the frequency, H_{DC} will also depend on the way the frequency varies after a power imbalance. Here, a frequency drop with a constant ROCOF of -0.5 $\frac{Hz}{s}$ is assumed. Again, it illustrates that the energy stored in the DC link is quite limited as it can only be applied to support the frequency during a few hundreds of milliseconds.

Although the stored energy is insufficient for frequency support, the variation of the DC link voltage to extract additional power can be integrated within the control loop (Figure 5.15) in order to offer a small time delay for the GSC_B to transfer the power from system B to A, which can be very useful when strategy 2 is applied [174]. By providing a small time delay using the energy stored in the DC link, the constraints with respect to the communication and response times of the turbines become less stringent.

5.5.3 Inertia support within HVDC grids

By interconnecting several HVDC links, a multi-terminal DC grid or even a fully meshed DC grid is formed. Multiple (a)synchronous AC systems, (offshore) wind farms and even large oil rigs can all be linked (Figure 5.19(a)), offering more degrees of freedom with respect to the provision of inertia support to the different power systems.

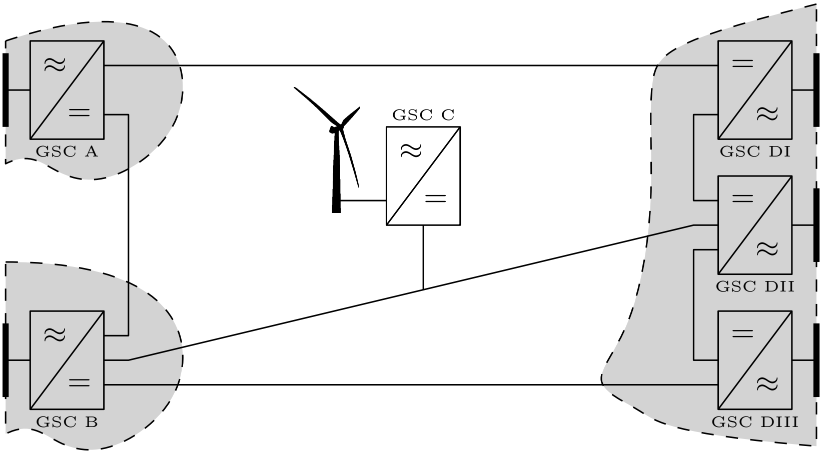
≈
=
GSC A
GSC C
≈
=
≈
=
GSC B
=
≈
GSC DI
=
≈
GSC DII
=
≈
GSC DIII

(a) Possible HVDC grid layout

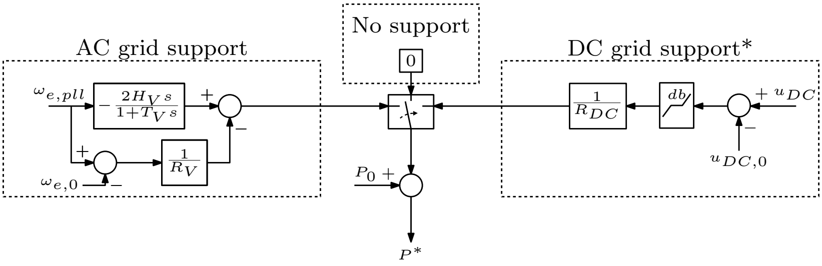
No support
AC grid support
DC grid support*
0
ωe,pll
− 2HV s / 1+TV s
+
−
+
−
ωe,0
1/RV
1/RDC
db
+ uDC
−
uDC,0
P0 +
P*

(b) Simplified representation of the active power control options for each converter (*Very basic DC droop control. Numerous other more advanced DC voltage controllers can be used, see [23])

Figure 5.19: Inertia support by HVDC grids

A detailed analysis of the control of the DC voltage within such a grid and the interactions of the converters is out of the scope of this work (an extensive overview can found in [23]). In general however, the active power control of each converter is designated to provide grid support (to the DC or AC grid) or to ensure a constant power transfer between the AC system and the DC system (no support), see Figure 5.19(b). As it is crucial for a stable operation of the DC grid to keep the DC voltage within certain limits, at least one converter should be equipped with a DC grid support control function in order to stabilize the voltage after a global power imbalance within the DC grid occurs. When multiple converters are involved in this task, the burden of the DC voltage regulation task can be shared among them, with each converter equipped with a droop control based voltage controller. Consequently, the DC voltage control is established in a similar way as the primary frequency control within an AC system.

Multiple converter combinations designated to offer DC or AC grid support are feasible (Figure 5.19(a)). Inertia support can for instance be provided by GSC A and B, while the converters connected to system D (I, II and III) are used to control the DC voltage. As the frequency can be considered a global parameter within a single AC system, in case one or multiple HVDC converters within a single synchronous system such as system D are used for inertia support, the other converters can not be applied for DC voltage control since their control action would result in a counteracting power exchange with the system.

Moreover, since multiple converters are connected to the same DC network, the total energy stored in the DC link is increased substantially compared to a standard DC point-to-point link. Therefore, as the number of converters rises, it becomes increasingly feasible to employ this energy for inertia support [151]. The DC grid controller can be simply adapted to accommodate the use of this energy through for instance adding a dead band (db: Figure 5.19(b)) to the DC voltage controller. This way, firstly the energy stored in the DC capacitors is harvested before the power reserves within other systems are employed to stabilize the DC voltage.

5.6 Large scale implementation of inertia support

Throughout this chapter, numerous control principles to provide inertia support by different converter connected generation units have been presented. However, the potential impact of the incorporation of such support at scale has not yet been addressed. Therefore, vital considerations and issues are identified when implementing inertia support in future power systems and some implementation approaches from a transmission system operator point of view are proposed. Before outlining these future steps, a short overview of current grid code requirements with respect to inertia support are presented.

5.6.1 Inertia support within current grid codes

In most countries, converter connected generation sources are still exempted to provide grid support. In light of stability concerns related to the high penetration of renewable generation sources, many TSOs are considering an adaptation of the current grid code to require converter units to participate in ancillary services. Some TSOs, such as those in Ireland, Germany and UK, have each already defined a specific set of requirements for wind power units regarding for instance the provision of primary frequency control during grid disturbances. In the UK, large wind farms (>50 MW) must have the capability to provide frequency support by continuously adjusting their active power output. To be able to ramp up their power output during a frequency dip, the units are required to have a certain power margin available. In Ireland, the TSOs have defined a droop characteristic for the activation of primary reserves by wind power units, both during under- as overfrequency events with a minimum response of 1% rated power per second [167]. In Germany, wind farms only need to respond to over frequencies by reducing their active power output with a gradient of 0.4 p.u./Hz when the frequency exceeds a certain threshold [10].

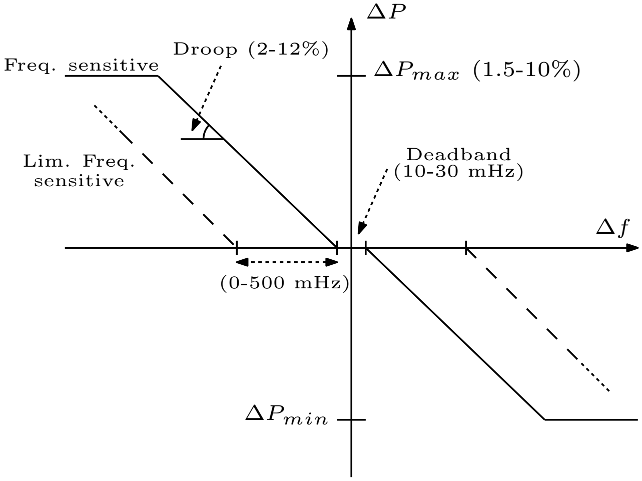

Figure 5.20: Active power frequency response characteristic according to ENTSO-E RfG network code (type C) [13]

ENTSO-E aims to harmonize these requirements in the different network codes of the countries within a single synchronous zone (the RfG code, [13]). Newly connected generating units are classified depending on their grid connection point, rated power and voltage level. According to the code, a generator unit of type C for instance, corresponding to a power plant with rated power above 50 MW in continental Europe, above 10 MW in the UK and above 5 MW in Ireland, should offer a frequency response corresponding to the droop characteristic given in Figure 5.20 [167].

As shown, the power plants must be capable of regulating their active power according to the system frequency, with or without a dead band corresponding respectively to the limited frequency or frequency sensitive mode. The time delay to provide the power response must be determined in accordance with the relevant TSO (a maximum time delay of 2 s for type C is proposed in the network code).

On the contrary, the provision of inertia support, which takes place in a much smaller time frame compared to this droop control, is not yet been (clearly) defined as a requirement in the European grid codes. Although the concept of virtual (or synthetic) inertia is for instance introduced in the RfG ENTSO-E code, no clear description of how such a virtual response should be provided has been set. Only a vague description implying that each unit should inject active power proportional to the severity of the disturbance in a very short time (200 ms) has been given [13].

Within the Canadian Hydro-Quebec transmission system on the other hand, a mandatory inertia support from wind farms with a rated power output higher than 10 MW is already introduced in the grid code early 2006. Here, the wind turbines need to provide an active power response equivalent to that of synchronous machines with an inertia constant of 3.5 s for a period of at least 10 s [175]. Manufactures adapted their control to fulfill these requirements and the first inertia-compliant wind turbines (from Enercon and Senvion) were installed in 2011. The control scheme which was finally implemented looks similar to the FFR control, i.e. the power is immediately increased (stepwise or proportional to the frequency deviation) as soon as the frequency goes outside a predefined deadband. The provision of this support has already proven to be very useful in the Hydro-Quebec system. During a generation outage of 1600 MW caused by a transformer failure in December 2015 for instance, 126 MW of additional power was provided by the wind turbines resulting in an increased nadir of 0.1-0.2 Hz compared to the case of no support [176].

Although some small steps have been taken to include the inertia support besides the (standard) primary frequency support as a requirement in the different grid codes, it is clear that there is no clear agreement yet among TSOs world-wide on how inertia support should optimally be look like. Unclear terms as e.g. “a response similar to” or “proportional to the severity of the event” still allow the inertia support to be implemented in many distinct ways.

5.6.2 Future pathways for inertia support

With respect to the adaptation of current grid codes by the TSOs or the creation of some market mechanism to enforce the real integration of inertia support within converter connected units at scale, the key questions that actually still need to be solved are: When, how much and what kind of inertia support should be provided depending on the penetration of converter connected generation and remaining synchronous inertia?

It is not feasible to provide a general and concrete answer to these questions as it depends on many different aspects. Therefore, some side-notes have to be made.

The required inertia support likely varies from system to system, depending on specific characteristics. Even systems of comparable size have distinct requirements, due to the different power plant portfolio, inertia of spinning synchronous machines, primary control speed, ... Furthermore, it is also key to accurately specify the power system requirements, i.e. what is the main objective of providing inertia support from a power system point of view? The main driver to offer inertia support is to keep the nadir and ROCOF between certain limits as they are considered the main metrics for frequency stability. Other metrics, such as the time to reach the steady state frequency after a major power imbalance or the presence of a secondary dip due to the speed recovery of wind turbines in case fast frequency control is implemented, could also be addressed.

Even if it is defined how the frequency trajectory should optimally be look like, numerous options are available to achieve this desired response as the power control of each converter can be tuned in many different ways. Whereas the response of conventional power plants is mostly constrained by physical characteristics such as synchronous inertia, governor speed, ramp rates of turbines, ... the active power output can be regulated to offer almost any kind of power response.

Besides these technical requirements, the (cost of the) energy yield lost should be taken into account as well. Deloading every single renewable energy unit offers a significant power reserve that can be applied for inertia and long term frequency support. However, it is probably not the best approach from an economical point of view.

The potential issues and considerations when implementing virtual inertia at scale are illustrated. Instead of using the formerly presented small test system, a large interconnected power system with a total generation capacity of 100 GVA is used, suppling the total load equal to 70 GW. Half of the power plant capacity is hydro based, the other half is thermal based. In the long run, it is expected that the conventional generation is gradually displaced such that 35 GW of the load could in theory be covered by wind power and 35 GW by solar PV. Two different scenarios (A and B), see Figure 5.21, are considered for the decrease of inertia in function of the converter connected penetration, corresponding to a fast and delayed decrease (section 3.5.1). The available primary reserves and droop action of conventional generation on the other hand, are assumed to remain unchanged. The aggregated single machine equivalent together with the governor and turbine models (appendix A.2 and A.3) are used to analyze the frequency response. To avoid load shedding and tripping of protection equipment, the minimum nadir and maximum ROCOF are set respectively to 48.8 Hz and 1 Hz/s. The considered power imbalance in the system is taken equal to 10% (of S_{sys}=100 GVA).

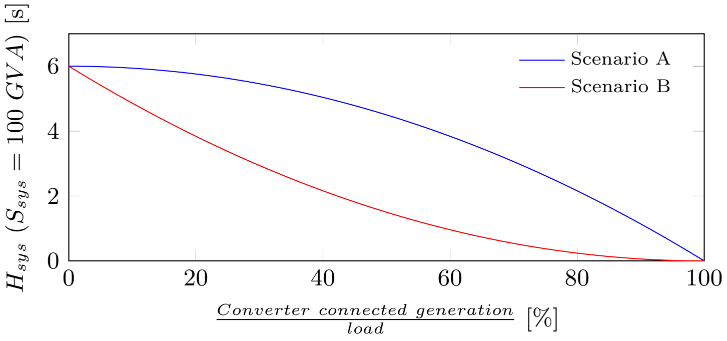

Figure 5.21: Assumed decrease of inertia as a function of the penetration of converter connected generation (without any support)

The inertia support provided by the PV and wind units is split in three categories, corresponding to:

1. Virtual inertia control (H_V): emulating the inertial response of synchronous machines, based on the measured ROCOF at the PCC
2. Virtual droop control (R_V): mimicking the primary control action of conventional power plants by acting on the deviation of the frequency
3. Fast frequency control (FFR): a fixed power response is delivered, triggered by a certain frequency threshold. In case units are working in an optimal operating point, also an energy regain phase is included.

Applying these control approaches, the frequency stability is investigated for penetration levels up to 80% in the subsequent sections.

Case 1: Deloading approach

Inertia support is included in the grid codes such that every converter in the system is required to be deloaded by 10% (of its optimal power output) in order to offer support. The penetration of converter connected generation is gradually increased and all converters are equipped with one of the three inertia support control functions presented in the list above ($H_V = 6\ s$, $R_V = 0.05$ and FFR with $P_{up} = 0.1\ p.u.$). Figure 5.22 illustrates the impact of the increased converter connected generation on the nadir and ROCOF. Without any support, the maximum share of converter connected generation is almost 75% for scenario A and 35% for scenario B, taking into account the constraints on ROCOF and nadir (48.8 Hz and 1 Hz/s).

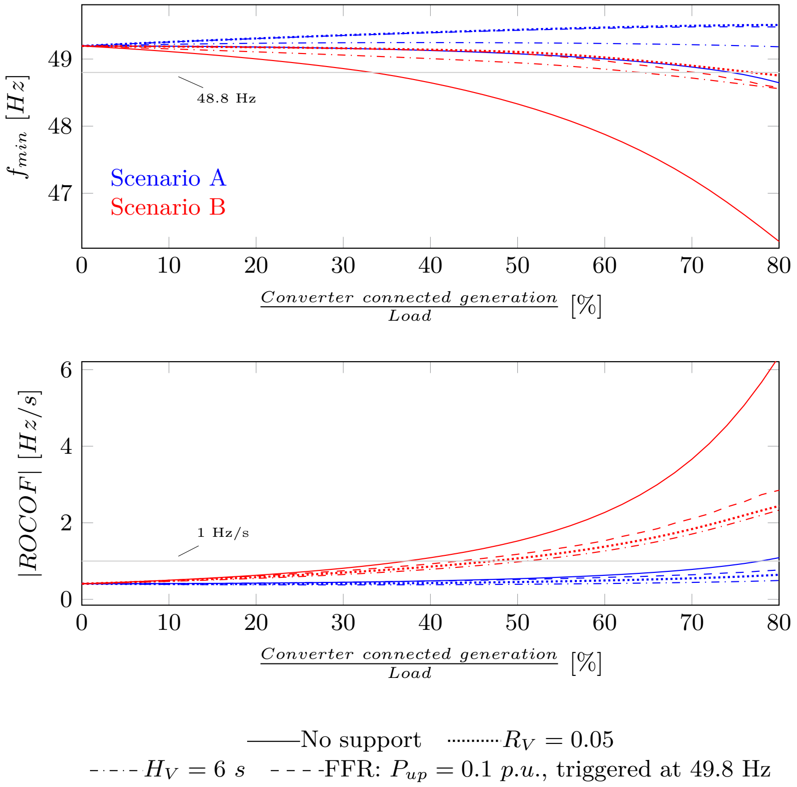

Figure 5.22: Results case 1: Deloading approach

However, for a certain amount of converter connected penetration, numerous combinations with respect to the power output of each converter exist to cover the remaining load. For instance 35 GW (38.8 GW - 3.8 GW reserve), can be produced by a total capacity of 50 GVA (operating at low wind speeds or solar radiation) or just by 38.8 GVA of converter connected units. As the virtual inertia and droop factor H_V and R_V are generally expressed with respect to the capacity of each unit, 50 GVA of generation provides much more support than 38.8 GVA, assuming that the applied power reserve is sufficient. Therefore the worst case is always considered, i.e. the remaining load is covered by converter units which normally operate at their maximum power output if no power reserve would have been required.

Applying inertia support, both ROCOF (measured over 500 ms) and nadir are substantially improved. The three inertia support controllers considered, perform almost equally, but the FFR and virtual droop raises the nadir slightly more than the virtual inertia control. Virtual inertia, as expected, is on the other hand more effective for lowering the initial ROCOF. For scenario A, the nadir frequency is even higher compared to the case of no converters.

Case 2: Optimal power point approach

In a second case, no unit is deloaded and the system fully relies on the inertial response provided by wind using the FFR control. This FFR can only be delivered within R2-4 (Figure 4.19). Moreover when the turbine is operating in R2 and R3, the turbine has to regain its optimal speed after the power boost which resulting in a secondary frequency dip. The amount of inertial support thus varies depending on the numbers of turbines enabled to respond, corresponding to a wind speed within R2-4.

Again only the worst case scenario is considered. All PV units operate at maximum power and the remaining part of the converter connected generation is covered by wind units. If all wind turbines experience the same wind speed, a maximum converter connected penetration of about 60% can be obtained without any converter unit capable of delivering inertia support since all wind turbines are still operating in R1. Above 60% all wind turbines deliver inertia support by FFR (Figure 5.23). As only the wind turbines are providing support, the improvement above 60% penetration is less compared to case 1.

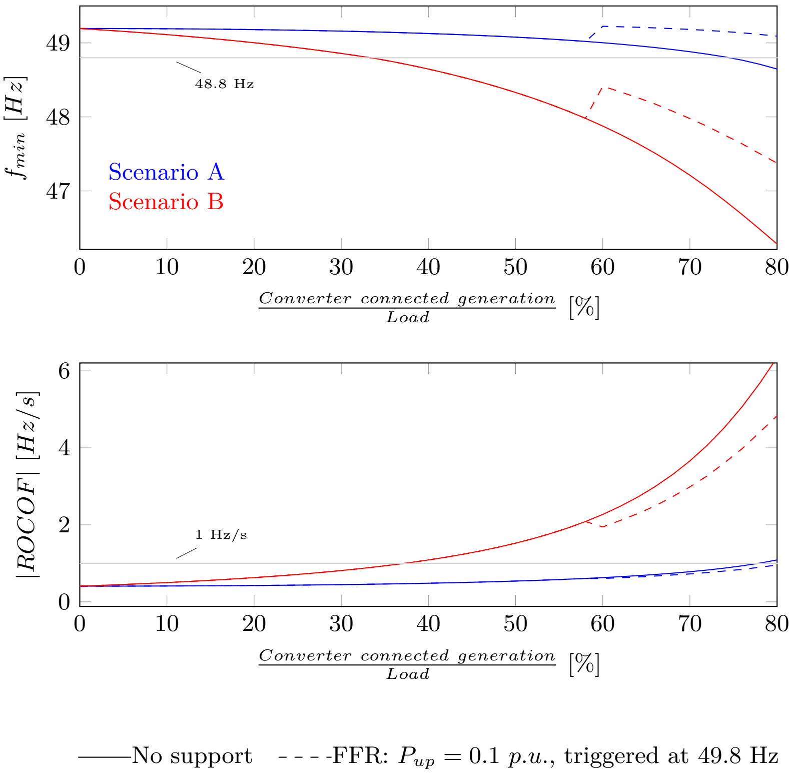

Figure 5.23: Results case 2: Optimal power point approach

Case 3: Tuning of control parameters

Instead of providing inertia support by every converter, the required power reserve, virtual inertia constant and droop are defined to obtain a frequency profile that meets the requirements in terms of maximum ROCOF and minimum nadir. The requirements are already met without any support up till 75% penetration for scenario A (Figure 5.22). Therefore only scenario B is considered.

The tuning parameters for virtual inertia and droop are given in Figure 5.24. The required H_V and R_V together with the maximum power change is expressed on the system base equal to 100 GVA. They represent the total support from all converters, i.e. the burden can for instance be shared among a small amount of units, as long as the H_V (or R_V) together with the required power reserve are properly chosen.

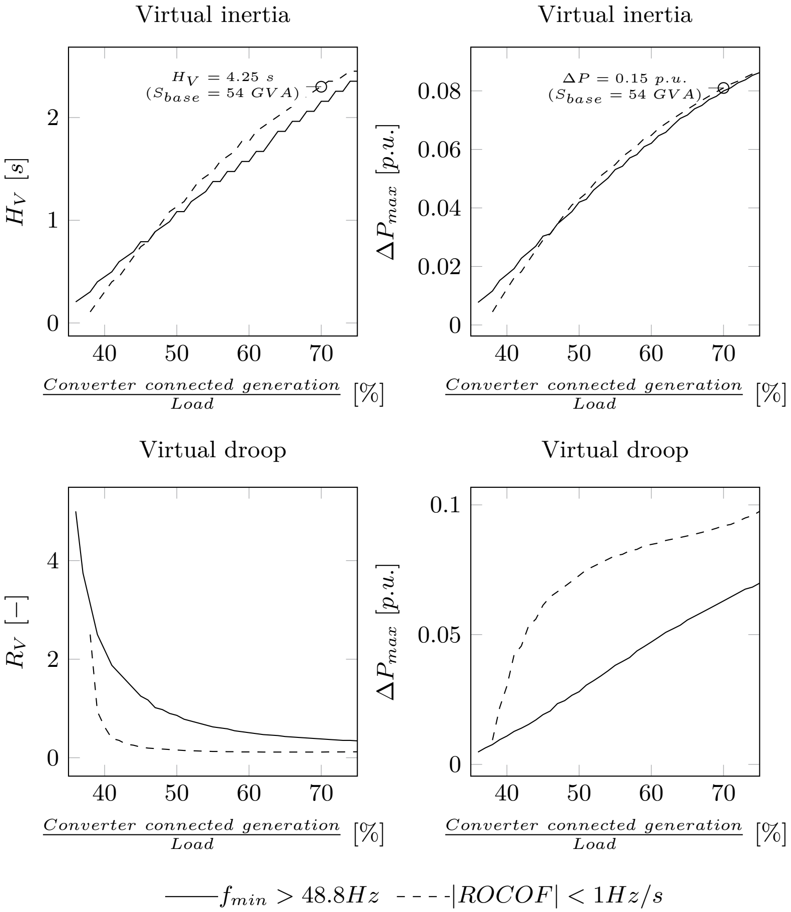

Figure 5.24: Results case 3: Optimal tuning of inertia support (H_V and R_V) for scenario B (expressed on a system base equal to 100 GVA)

The values for H_V are for instance less than the H_V defined in case 1, using the same base values. A penetration level of 70% for instance, corresponding to a total converter connected generation of 54 GVA in case 1. Although, an inertia constant of 6 s was assumed in case 1, only 4.25 s in combination with a power reserve of 0.15 p.u. is required to keep the ROCOF below 1 Hz/s.

5.6.3 Discussion & Guidelines for TSOs

Currently, inertia support is merely considered as a way to improve the frequency response of a system by rapidly increasing the power output of the converters in function of the ROCOF or frequency deviation. For low levels of converter connected penetration, it is relevant, though mostly not yet essential, to provide such support in most power systems. However, for higher shares, the appropriate provision and tuning of the inertia support becomes of utmost importance to fulfill the different objectives related to predefined frequency metrics.

As these three cases demonstrate, there are multiple approaches to eventually implement the inertia support on a large scale. The implementation presented in case 1 and 2 could be achieved by adapting the current grid code and defining additional requirements for wind and/or PV units. While deloading all units would offer a substantial potential to deliver inertia support, it results in a constant loss in energy yield during normal preparation. Furthermore, for high shares of converters, deloading by 10% is insufficient. An appropriate tuning of the response and the required power reserve is therefore important. Case 2 could be an interesting approach with respect to the obtained energy yield, but as the capability highly dependents on the wind speed, it seems not to be reliable since in the worst case scenario, insufficient support is delivered. However, improved forecasting of the wind speed could help to get a good estimate on the available amount of virtual inertia at each moment in time.

In case 3, the optimal tuning and reserve provision are presented for the considered control mechanisms. This approach can be used as a base for the development of an ancillary service market mechanism for inertia support. As the tuning parameters are likely to vary depending on the system characteristics, a detailed monitoring of the operating points of the system is vital.

In the end, it is the role of the TSO to form a bridge between the inertia support mechanisms developed by industry and academia, and their implementation in the power system. The essential steps to be undertaken before finally setting up for instance a market mechanism to provide the inertia response in case of high shares of converter connected generation are:

- Improved system monitoring: It is of utmost importance to have a good estimate of the available synchronous inertia in the system in order to define the required inertia support. Furthermore, a detailed knowledge of the system conditions in terms of plant portfolio, largest infeed size, primary frequency control dynamics, ... is vital.
- The key metrics to ensure frequency stability should be clearly defined, i.e. how should the frequency response look like? In the former cases,

only the nadir and ROCOF are considered, while some TSOs could place higher importance to the time to recover to the steady state or the impact of a secondary frequency dip.

- Based on both former steps, it can be determined whether or not inertia support becomes an essential tool to ensure system stability. It can already be implemented at low levels of converter connected generation by means of a grid code requirement in order to gain some experience with the impact of the controllers on system level.
- Once it is expected that the system is at the edge of stability after a power imbalance and the system really relies on virtual inertia support, it is important to guarantee the provision of the support and to correctly tune the parameters. Creating an ancillary service market to ensure a reliable support can be part of the solution.

5.7 Conclusion

The capability of different types of converter connected generation to offer inertia support is assessed. Based on the quantification of the energy buffers within these units, it is illustrated that, besides energy storage systems, only wind power units inherently have a sufficient amount of energy available to provide inertia support. Other types of generation need to be deloaded to create the required energy buffer and power margin. Moreover, several control methods together with their advantages and disadvantages are presented. These controllers basically mimic the behaviour of synchronous machines or provide a fast power boost once the frequency or ROCOF exceeds certain thresholds. The beneficial impact on the frequency stability and the influence of parameter tuning is demonstrated by means of the test system.

Additionally, the different control strategies of HVDC converters within a point-to-point link or a DC grid are described in more detail and the integration of the inertia support controller, in order to transfer the kinetic energy from one system to another, is presented. To what extend the energy stored in the DC link can be applied for inertia support is further elaborated. It is concluded that this energy can merely been used in the context of a DC grid when the stored energy of multiple converters is added up. Some considerations and potential issues of the implementation of inertia support at scale are also presented. The importance of proper tuning of the control parameters is illustrated and analyzed. Issues related to definition and quantification of the optimal response are finally highlighted and future steps and approaches towards implementation at system level are proposed.

Chapter 6

Receding horizon control of wind power to provide frequency regulation

"In the middle of difficulty lies opportunity."
- Albert Einstein

6.1 Introduction

The inherent amount of stored kinetic energy within the blades, generator and gearbox of the wind turbines offers the potential to provide virtual inertia support to the system after a sudden power imbalance (contingency). With the increased penetration of wind generation in power systems, there is a rising interest to also deliver frequency control during normal operation, further denoted by frequency regulation, in order to relieve the burden on remaining conventional generation units.

As a first step, the possible contribution of wind power to frequency regulation, by optimally anticipating load imbalances in the power system without substantially reducing the energy yield, is investigated. This ability is studied by implementing a receding horizon controller (RHC) taking future load and wind

---

This chapter is based on: P. Tielens and D. Van Hertem, "Receding Horizon Control of Wind Power to Provide Frequency Regulation," *IEEE Transactions on Power Systems*, vol. 32, no.4, pp. 2663-2672, 2017.

variations into account. The available energy reserves of the wind turbine over a certain time horizon are optimally exploited to damp frequency oscillations while keeping the energy losses within defined limits.

A general overview is given of the motivation and methodology to apply wind power for frequency regulation. Next, modeling and convex formulation of the optimization problem applied in the RHC are presented. The general potential of wind power kinetic energy reserves to damp frequency variations is examined and the setup of the RHC and the results for a random load profile are given. Finally, the possible application of the RHC in real-time operation is discussed.

6.2 Motivation and methodology

Renewable electricity generation is generally perceived as merely a contributor to frequency variability, although the power electronic interface offers an increased flexibility for grid support as the power output can be fully controlled. With respect to wind power units, such controllability can be applied to optimally manage the exchange of kinetic energy stored in the turbine and generator to offer grid support. Especially if multiple wind turbines are aggregated over a large geographical area, this amount of energy becomes quite substantial and highly relevant for offering grid services [177, 40].

The potential of using this kinetic energy to deliver frequency control and to stabilize the frequency after major load imbalances (contingencies) is already studied by developing different basic controllers creating an additional power reference proportional to the measured frequency deviation or rate of change of frequency [178, 179, 180, 46, 167, 158] (Chapter 5). An optimized frequency response by means of a particle swarm optimization can be found in [163].

In this chapter we try to exploit the flexibility of wind power units to provide frequency control during normal operation, i.e. frequency regulation. A first theoretical feasibility study on the use of kinetic energy stored in wind turbines to provide frequency regulation is performed in [181]. However, rotor speed and power limits were not taken into account. Furthermore, the proposed control was only tested for a single operating point assuming an optimal forecast.

Therefore, in order to take into account the turbine limits and forecast errors, a novel RHC controller which strives to achieve an optimal damping of frequency variations while keeping the energy loss within limits is developed. Otherwise, without setting a limit to the loss, the turbines would continuously be operating at a suboptimal point in order to have a large reserve capacity available to reduce the frequency variations. In a first step, perfect forecast is assumed in order to have a better insight in the value of using the available kinetic energy of wind turbines to damp frequency variations. The damping potential for load variations with a different energy content is evaluated over the whole wind speed range. Thereafter, the influence of forecast errors and parameter settings on the performance of the controller are studied using a random load and wind profile. Also the use of multiple (groups of) turbines is assessed.

A simplified power-frequency model (appendix A.2) is used which consists of an equivalent thermal power plant unit and an equivalent wind turbine that respectively aggregates all thermal and wind power units in the system. By assuming no congestion and the same frequency within the whole power system, the network is not taken into account as it not significantly influences the results. To model the primary control action of the thermal units, an equivalent thermal power plant is equipped with a droop controller. Secondary control actions are omitted as the aim is not to correct the area control error.

The equivalent wind turbine is represented by a reduced model of a variable speed turbine, including the aerodynamic and mechanical part of the turbine neglecting all electrical dynamics as they are orders of magnitude faster than the dynamics of interest. Rotor speed and power output limits are imposed to the model to correctly assess the (kinetic) energy exchange potential of the wind power units. Moreover, besides using rotor speed deviations, pitching is allowed as well to create the required power reserves.

6.3 Convex formulation of wind turbine and power system model

The optimization objective is to damp frequency variations limited by a defined reduction in energy yield. The formulation of the dynamic optimization problem over a time period $0 < t < t_{sim}$ is:

$$\begin{aligned} &\min_{T_{gen}(t),\ \beta(t)} && \int_0^{t_{sim}} [\Delta f(t)]^2 \, dt \qquad (6.1) \\ &\text{subject to} && \int_0^{t_{sim}} [P_{wt}(t)] \, dt \geqslant \epsilon \cdot EY_{wt,max} \\ & && \text{\& Wind turbine and power system dynamics} \end{aligned}$$

with $P_{wt}(t)$ the output power of the equivalent wind turbine and $\Delta f(t)$ the deviation from rated frequency (50 Hz). $T_{gen}(t)$ and $\beta(t)$ represent the control variables, namely generator torque and pitch angle. $\epsilon \in [0...1]$ is used to set a limit to the energy losses compared to the maximum energy yield $EY_{wt,max}$ over the considered time horizon. The dynamics of the equivalent wind turbine and power system are included as constraints. In this form, it is a nonconvex, nonlinear optimization problem which is very challenging to solve. Therefore a change of variables is applied to convert it to a convex optimization problem that can easily be solved with a high degree of efficiency and reliability combined with a low computational burden [182].

6.3.1 Wind turbine model

In order to include the dynamics of the (equivalent) wind turbine and power system as constraints, a convex formulation of the wind turbine model is applied in this work [183]. The control variables, pitch angle and generator torque of the turbine are converted to power and energy: $E_{kin}(t)$, $P_{wt}(t)$ and $P_{aero}(t)$. The latter denotes the aerodynamic power captured by the wind and $E_{kin}(t)$ the kinetic energy stored in the wind turbine. Assuming a single mass model ($\omega_m = \omega_{m,gen} = \omega_{m,blade}$), the energy is:

$$E_{kin}(t) = \frac{J \cdot \omega_m(t)^2}{2} \tag{6.2}$$

with ω_m the rotational speed and J the equivalent moment of inertia of the turbine blades and generator. The swing equation of the turbine is:

$$\frac{dE_{kin}(t)}{dt} = P_{aero}(t) - P_{wt}(t) \tag{6.3}$$

The limits of the rotor speed ($\omega_{m,min}, \omega_{m,max}$) can be set by limiting the kinetic energy. In the same way, the maximum generator torque ($T_{gen,max}$) determines the limit of the generated electrical power:

$$\frac{J \cdot \omega_{m,min}^2}{2} \leq E_{kin}(t) \leq \frac{J \cdot \omega_{m,max}^2}{2} \tag{6.4}$$

$$0 \leq P_{wt}(t) \leq \sqrt{\frac{2 \cdot E_{kin}(t)}{J}} \cdot T_{gen,max} \tag{6.5}$$

This constraint is convex, as $\sqrt{\frac{2 \cdot E_{kin}(t)}{J}}$ is a concave function of $E_{kin}(t)$. $P_{aero}(t)$ is finally limited by the maximum available power for a certain wind speed and kinetic energy content.

$$0 \leq P_{aero}(t) \leq P_{aero,max}(v_w(t), E_{kin}(t)) \tag{6.6}$$

with $P_{aero,max}(v_w(t), E_{kin}(t))$ a nonlinear function of the wind speed and kinetic energy:

$$P_{aero,max}(v_w(t), E_k(t)) = \\ \underset{\beta_{min} \leq \beta \leq \beta_{max}}{max} \frac{1}{2} \cdot \rho \cdot \pi \cdot R_{blade}^2 \cdot C_p(\lambda(t), \beta(t)) \cdot v_w(t)^3 \tag{6.7}$$

with R_{blade} the rotor radius, ρ the air density, $\lambda(t) = \frac{\sqrt{\frac{2 \cdot E_{kin}(t)}{J}} \cdot R_{blade}}{v_w(t)}$ the tip speed ratio and $C_p(\lambda(t), \beta(t))$ the aerodynamic coefficient of performance. The latter is approximated by the function given by equation (4.17).

The constraint on the extracted aerodynamic power (6.6) is finally also convex since $P_{aero,max}$ can be approximated by a concave function of E_{kin} for every wind speed (Figure 6.1(a)). In Figure 6.1(b), this approximation is illustrated in more detail for a wind speed of 8 m/s. The global maximum is attained at $\beta = 0°$ and at the kinetic energy content corresponding to the optimal tip speed ratio. By further increasing the kinetic energy, the pitch angle should however be slightly increased in order to capture maximum power. The shape of this curve connecting the maximum power points, highly depends on the aerodynamic design of the blades, but in general an accurate concave fitting is possible for realistic C_p data [14, 183].

$P_{aero,max}$ gives the maximum available power for every combination of kinetic energy and wind speed. In case conventional maximum power point tracking control is applied, only the global optimum of this function is tracked by altering the kinetic energy of the turbine. The operating points of maximum power point tracking are finally marked in Figure 6.1(a) for the sake of completeness.

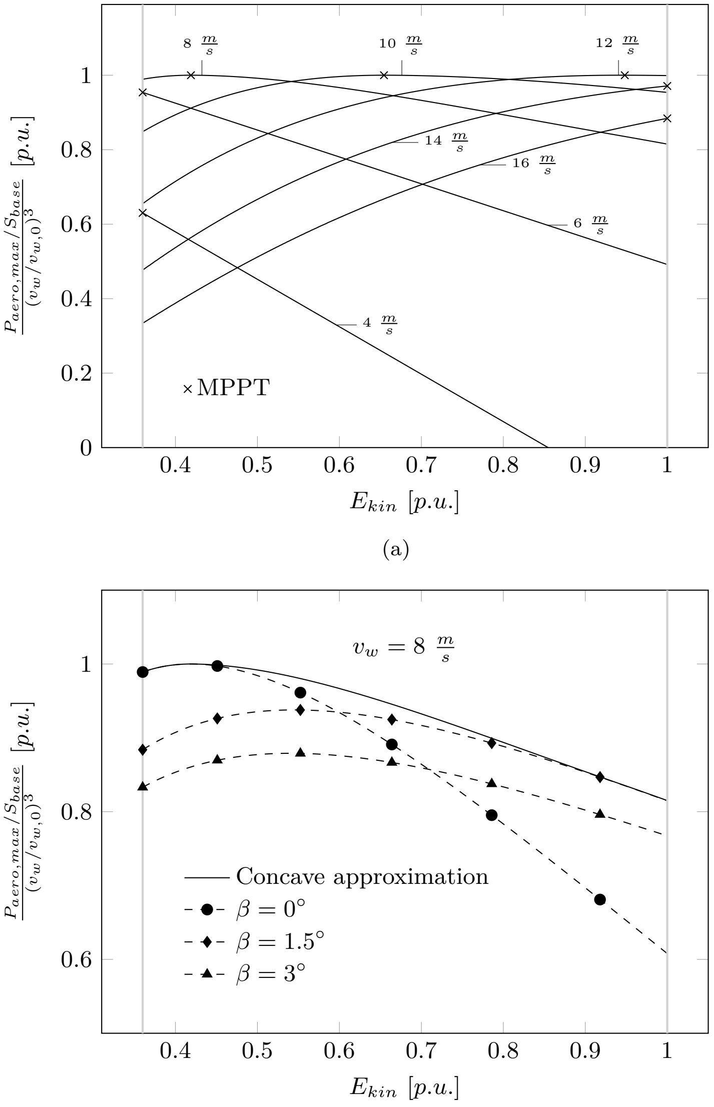

(a)

(b)

Figure 6.1: Normalized maximum available aerodynamic power as a function of kinetic energy for different wind speeds (a) and concave approximation for $v_w = 8\ \frac{m}{s}$ (b), the grey lines indicate the limits of the kinetic energy

Once the optimal values of $E_{kin}(t)$, $P_{wt}(t)$ and $P_{aero}(t)$ are determined, the control variables $\beta(t)$ and $T_{gen}(t)$ can be recalculated:

$$T_{gen}(t) = \frac{P_{wt}(t)}{\sqrt{\frac{2 \cdot E_{kin}(t)}{J}}} \tag{6.8}$$

$$P_{aero}(t) = \frac{1}{2} \cdot \rho \cdot \pi \cdot R_{blade}^2 \cdot C_p(\lambda(t), \beta(t)) \cdot v_w(t)^3 \tag{6.9}$$

6.3.2 Power system model

To represent the power system, a simplified power-frequency model is used combining the system's swing equation and governor action of all spinning generation units (appendix A.2). For frequency studies, the response of a system to variations in load and generation is expressed in terms of power:

$$2H(1-\alpha)\frac{\mathrm{d}\Delta f(t)}{\mathrm{d}t} = (1-\alpha)\Delta P_G(t) + \alpha \Delta P_{wt}(t) - \Delta P_L(t) \tag{6.10}$$

where $\alpha \in [0...1]$ denotes the share of wind generation and $2H(1-\alpha)$ represents the equivalent system inertia. Moreover, $\Delta f(t)$, $\Delta P_G(t)$, $\Delta P_{wt}(t)$ and $\Delta P_L(t)$ denote the deviation of respectively the system frequency $f(t)$, conventional generation $P_G(t)$, wind power generation $P_{wt}(t)$ and system load $P_L(t)$ with respect to their references. These references are set to the initial values. $P_{wt}(0)$ is fixed to the maximum power output for the given wind speed.

The conventional units are aggregated into a single thermal unit equipped with a governor, defined by a droop action R, subjected to two time constants τ_{gov} and τ_{tur}, representing respectively governor and turbine. The model for the droop control comprises two differential equations [85]:

$$\tau_{gov}\frac{\mathrm{d}\Delta y(t)}{\mathrm{d}t} = \frac{-\Delta f(t)}{R} - \Delta y(t), \tag{6.11}$$

$$\tau_{tur}\frac{\mathrm{d}\Delta P_G(t)}{\mathrm{d}t} = \Delta y(t) - \Delta P_G(t) \tag{6.12}$$

where Δy is the deviation of the control valve from its initial position. Combining the objective function from (6.1) and the constraints listed in (6.3)-(6.6) and (6.10)-(6.12) leads to the convex optimization problem. In the following simulations, this convex optimization problem is solved with CVX, i.e. a MATLAB-based modeling system for specifying and solving convex problems [184, 185]. All state and control variables are sampled every 0.2 s and the differential equations (6.3), (6.10)-(6.12) are discretized.

6.4 Potential of wind power kinetic reserves to damp frequency variations

Frequency deviations resulting from load variations are reduced by means of an optimization. Taking into account load forecasts, the optimization primarily exploits the kinetic energy reserves as they can be applied to compensate for the varying load with low overall energy losses. To better understand the potential of applying kinetic energy reserves for frequency regulation and the extent to which they can be applied to damp frequency oscillations, the case of perfect forecast is studied first. In Figure 6.2, the amount of reserves of a standard variable speed wind turbine is illustrated over the whole wind speed range when maximum power point tracking is applied. The arrows indicate the up and downward reserves in terms of kinetic energy (a) and power (b). For low wind speeds, the kinetic energy of the turbine is fixed at $E_{kin,min}$ corresponding to the minimum rotor speed and only downward reserves equal to $E_{kin,max} - E_{kin,min}$ can be delivered by means of speeding up the turbine to its maximum kinetic energy $E_{kin,max}$. As the wind speed increases, the rotor speed is raised proportionally to the wind by the maximum power point tracker in order to follow the optimal tip speed ratio. Consequently, upward reserves equal to $E_{kin} - E_{kin,min}$ are created and downward reserves are reduced. Finally at the rated wind speed $v_{w,0}$, the turbine reaches $E_{kin,max}$ corresponding to maximum up- and zero downward kinetic energy reserves.

(a) Kinetic energy reserve

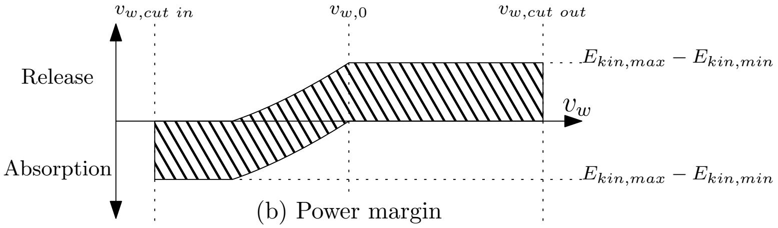

(b) Power margin

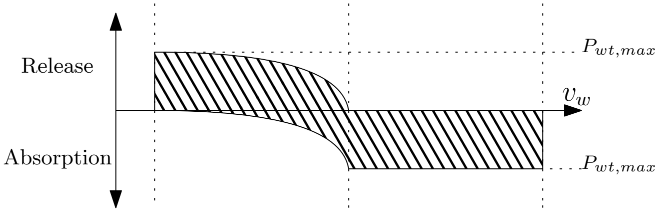

Figure 6.2: Schematic of the kinetic energy reserves and power margin referred to MPPT operation taken into account wind turbine operating limits.

Assuming the output power of the turbine to be limited to its rated power, the reserves can however not always be released (Figure 6.2 (b)). At low and high wind speeds, the reserves can not be used, as the power output is restricted to respectively zero and rated power. Only in the mid-speed range the power limits of the turbine allow to exploit these reserves. Therefore at first sight, it seems feasible to use the kinetic energy reserves solely within this mid-speed range. Moreover, the provision of kinetic exchange influences the aerodynamic power output of the turbine (Figure 6.1(a)). Deviating from the optimal kinetic energy directly leads to a reduction in aerodynamic power.

To investigate the ability in more detail, a sinusoidal load profile ($\Delta P_L(t) = A \cdot sin(\frac{2\pi}{50} \cdot t)$) is used as input for the optimization described in the previous section with t_{sim} =100 s. The energy content of this load is increased and for each step it is studied to what extent the turbines can damp the frequency variations while keeping the energy losses below 5% (ϵ =0.95). This optimization is repeated for different wind speeds with the results shown in Figure 6.3. The maximum damping is given for different wind speeds and loads. The energy content of the load is compared to the maximum available kinetic energy of the wind turbines ($E_{kin,av}$). This ratio together with the damping are defined as:

$$D = \frac{\int_0^{t_{sim}} \left[\Delta f_{nc}(t)\right]^2 dt - \int_0^{t_{sim}} \left[\Delta f_c(t)\right]^2 dt}{\int_0^{t_{sim}} \left[\Delta f_{nc}(t)\right]^2 dt} \tag{6.13}$$

$$\frac{E_{load}}{E_{kin,av}} = \frac{\int_0^{25} \left[A \cdot sin(\frac{2\pi}{50} \cdot t)\right] dt}{\alpha \cdot (E_{kin,max} - E_{kin,min})} \tag{6.14}$$

With $f_{nc}(t)$ and $f_c(t)$ the measured frequency with no control (optimal power tracking) and (damping) control. The period of the load fluctuation is fixed at 50 s. The amplitude A is gradually increased to determine the damping over a range of loads. The results (Figure 6.3(a)) clearly indicate that, mainly in the mid-speed range, a high potential is present to damp sinusoidal load variations while still keeping the energy yield at 95% compared to the case with optimal power point tracking. E.g. for wind speeds around 10 m/s, load imbalances with an energy content less than the maximum available kinetic energy are fully damped (Figure 6.3(b)). Even doubling the energy content of the load variations leads to a damping of 75%. The trajectories of the wind turbine variables for the point indicated in Figure 6.3(b) are given in Figure 6.4. The kinetic energy of the turbine has optimally been used to damp frequency variations as it oscillates between its limits. Figure 6.4(a) proves that no deloading is applied since the aerodynamic power (P_{aero}) is following the curve of maximum available power ($P_{aero,max}$).

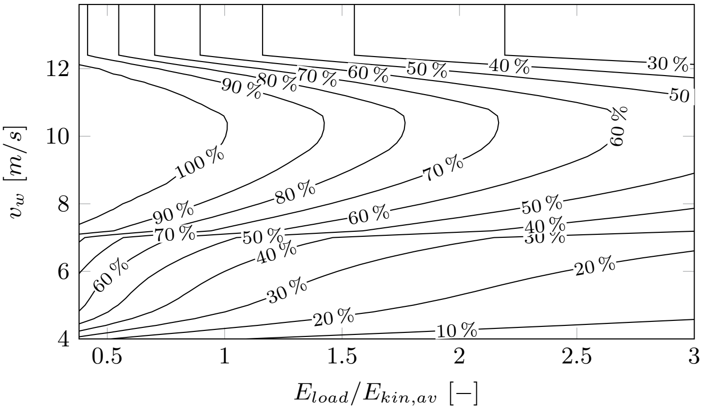

(a) Contour plot of % damping

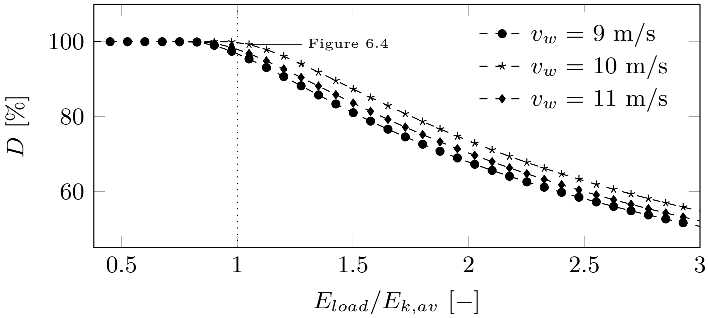

(b)

Figure 6.3: Damping potential of wind turbines over the whole wind speed range (a), for $v_w = 9$, 10 and 11 m/s (b)

In the low and high wind speed region, the damping potential is significantly reduced. This can be explained by two main reasons. Kinetic energy reserves can not be fully exploited as the electrical power output of the turbines must stay within strict limits. Although the optimization attempts to use these reserves by operating at a non-optimal point, it does not lead to a high damping since the loss in energy yield is restricted to 5%. In the remainder, it is investigated to what extent the power system can take advantage of these reserves in a non-optimal context, i.e. non-perfect forecast over a limited time horizon, by means of a receding horizon controller.

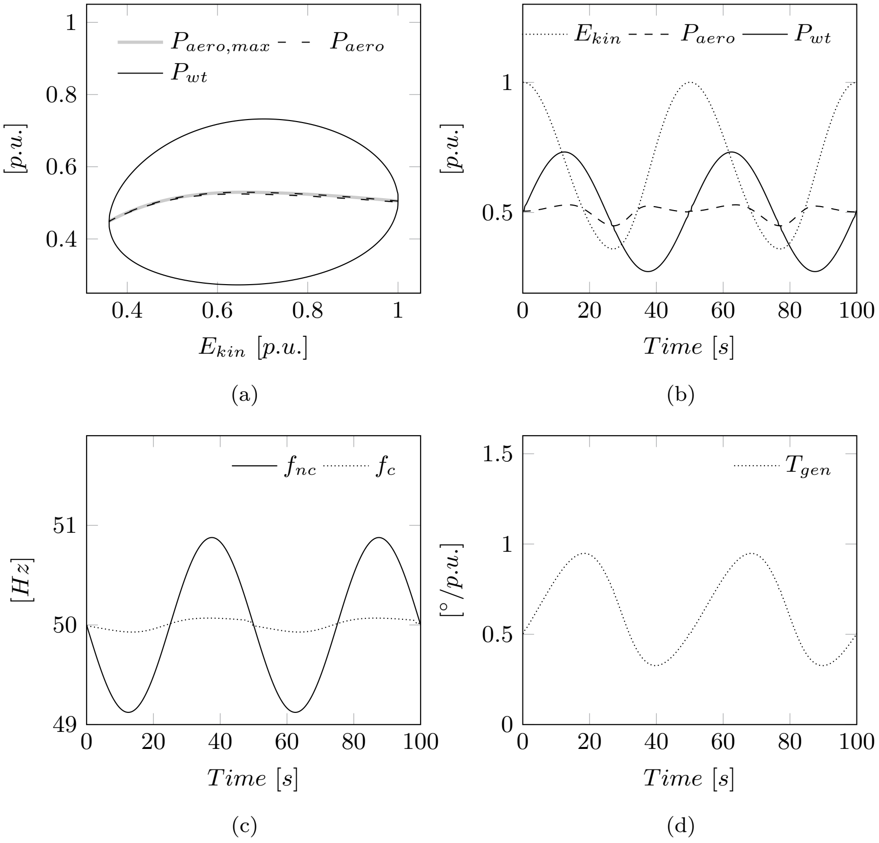

Figure 6.4: Optimization results for the point indicated in Figure 6.3(b) over a time horizon of 100 s

6.5 Receding horizon controller

To calculate the optimal control sequence of the wind turbine variables to damp frequency variations, a receding horizon controller is implemented using the same objective (Section 6.3). An overview of the controller is given in Figure 6.5. At each time t_i, the maximum energy yield $EY_{wt,max}|_{t_i}^{t_i+t_{RHC}}$ over a fixed future time or prediction horizon t_{RHC} is calculated using forecasted wind speeds. Next, an optimal control problem is solved over this time horizon taking into account predicted wind speeds and load changes:

$$\min_{T_{gen}(t),\ \beta(t)} \quad \int_{t_i}^{t_i+t_{RHC}} [\Delta f(t)]^2 \, dt \tag{6.15}$$

$$\text{subject to} \quad \int_{t_i}^{t_i+t_{RHC}} [P_{wt}(t)] \, dt \geqslant \epsilon \cdot EY_{wt,max}|_{t_i}^{t_i+t_{RHC}}$$

$$\text{Constraints (6.3)-(6.6) and (6.10)-(6.12)}$$

Thereafter the control variables ($T_g(t)$ and $\beta(t)$) calculated from $E_{kin}(t)$, $P_{wt}(t)$ and $P_{aero}(t)$ ((6.8) and (6.9)) between t_i and t_{i+1}, are taken to determine the operating points of the wind turbine and the power system using the measured wind speeds and load variations. The operating points at t_{i+1} are used to initialize the subsequent optimization considering the shifted prediction horizon $[t_{i+1}...(t_{i+1}+t_{RHC})]$ as optimization window. By iteratively solving the optimization problem, an optimal sequence of control variables is derived.

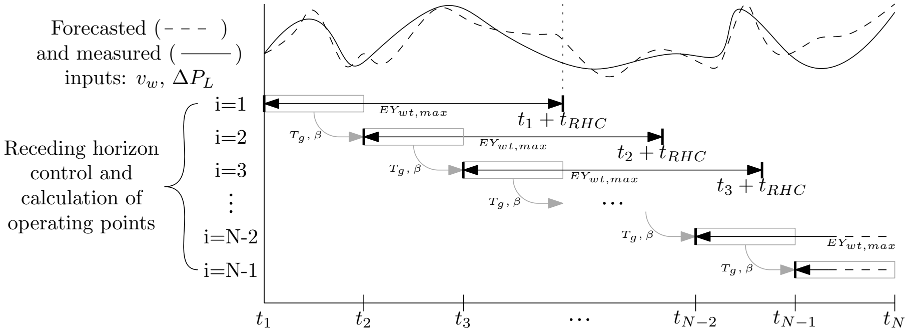
Forecasted (- - -) and measured (——) inputs: v_w, ΔP_L
Receding horizon control and calculation of operating points
i=1
i=2
i=3
⋮
i=N-2
i=N-1
$EY_{wt,max}$
$t_1 + t_{RHC}$
$t_2 + t_{RHC}$
$t_3 + t_{RHC}$
T_g, β
…
t_1
t_2
t_3
…
t_{N-2}
t_{N-1}
t_N

Figure 6.5: Overview of the implemented receding horizon control

6.6 Simulation results

6.6.1 Random load profile

The ability of the wind turbines to damp frequency variations arising from a random load profile over a time period of 600 s is analyzed (Figure 6.6(a)). Both measured and forecasted overall system load (expressed as deviations from their initial value) are shown.

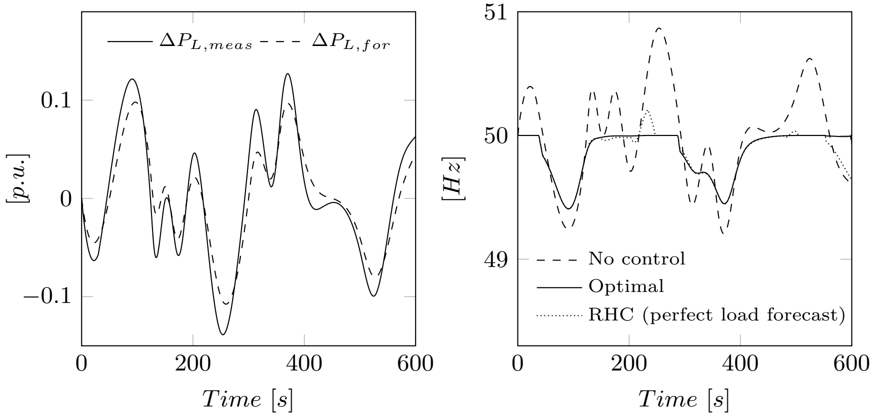

(a) Measured and forecasted load profile

(b) Frequency results: No frequency regulation by wind, Optimal frequency regulation and RHC with perfect forecast

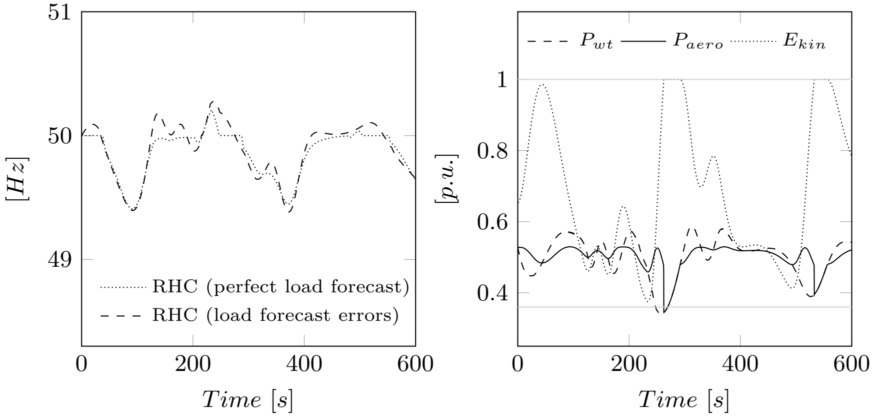

(c) Frequency results: RHC with and without forecast errors

(d) Power and kinetic energy for RHC (with load forecast errors)

Figure 6.6: Results for a random measured and forecasted load profile (RHC parameters: $\epsilon = 0.8$ & $t_{RHC} = 60\ s$)

It is assumed that the load is the only source of variability in the power system as the wind speed is perfectly forecasted and kept constant equal to 10 m/s. The results of applying the RHC to damp the frequency deviations for $t_{RHC} = 60\ s$ and $\epsilon = 0.8$ are shown in Figures 6.6(b) and 6.6(c). In Figure 6.6(b), the frequency trajectories assuming perfect forecast are compared for the case of no frequency regulation by wind (corresponding to optimal power tracking), optimal frequency regulation (optimization time horizon equal to 600 s without restricting the loss in energy yield) and the RHC. When optimal control is applied, the frequency deviations are significantly damped. Mainly frequencies above 50 Hz are fully attenuated since the wind turbines can easily reduce their power output. To damp load increases, the turbines release their stored kinetic energy. Since they are rapidly depleted, frequency dips are only slightly reduced compared to the case of no control by wind. However, if the energy content of the load increase is low, it can be fully attenuated as illustrated for the load swing around $t = 200\ s$.

The results of the RHC match quite well with the optimal control, except for frequency rises (e.g. around $t = 250\ s$) as the loss in energy yield is constrained ($\epsilon = 0.8$) directly limiting the delivery of downward reserves. Looking at the results for the RHC with forecast errors (Figure 6.6(c)), the forecast errors only slightly influence the performance of the controller and the frequency deviations are still considerably damped compared to the case of optimal power tracking (no frequency control by wind). It is assumed that these load forecast have mainly an error in magnitude.

The wind generator output power, aerodynamic power and kinetic energy as a function of time are given in Figure 6.6(d). As the RHC aims to damp frequency variations at a limited energy loss, the kinetic energy of the turbine is extensively used to compensate for load imbalances. E.g. around $t = 50\ s$, the kinetic energy level drops from almost 1 p.u. to 0.45 p.u. to reduce the frequency decline. Thereafter, during the recovery period coinciding with a drop in load power, the speed is back increased. The controller thus optimally controls the exchange of kinetic energy taking into account the variation in captured aerodynamic power.

6.6.2 Influence of control parameters and load forecast errors

In Figure 6.7, the influence of parameters ϵ and t_{RHC} on the damping (D) and energy yield (EY) is given. Damping is calculated using (6.13) and the energy yield is expressed as a percentage of the maximum available energy yield (corresponding to no frequency regulation or maximum power point tracking). By increasing t_{RHC} from 10 to 50 s for the case of perfect forecast, the damping increases significantly as the RHC incorporates load variations over a larger time horizon.

The energy yield (EY) is only slightly altered and remains well above 90%. Further increasing t_{RHC} is in this case not beneficial as the damping remains constant. The computational time to iteratively solve the optimization problem rises.

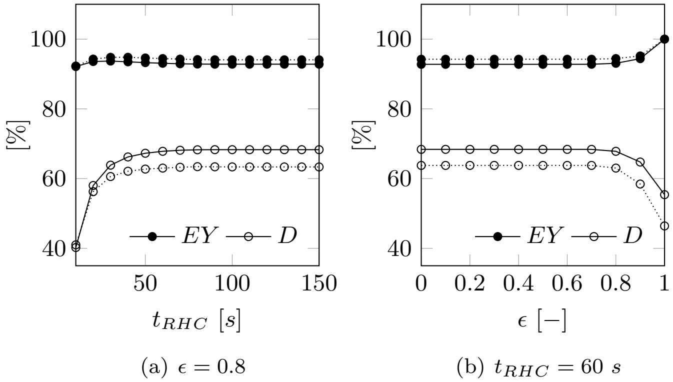

(a) $\epsilon = 0.8$

(b) $t_{RHC} = 60\ s$

Figure 6.7: Sensitivity analysis of parameters t_{RHC} with $\epsilon = 0.8$ (a) and ϵ with $t_{RHC} = 60\ s$ (b), with perfect load forecast (solid lines) and load forecast errors (dotted lines)

Parameter ϵ can be tuned to increase the energy yield even further, resulting in a lower damping (Figure 6.7(b)). The trade-off between damping and energy yield is clearly visible, mainly for values of $\epsilon \geq 0.8$. For this specific load profile, a maximum damping of 68% can be achieved with an energy loss of 7% if perfect forecast is assumed.

Looking at the results with load forecast errors, the damping is dropped by 5%. The energy yield on the other hand is marginally increased. To further investigate the influence on damping, the forecast errors are gradually increased by multiplying the forecasted load profile ($\Delta P_{L,for}$) from figure 6.6(a) by a factor $\sigma \in [1...0]$ or by shifting the profile in time defined by the parameter $\psi \in [0...50\ s]$. Different forecasted load profiles are created (Figure 6.8(a) and 6.8(b)). The case in which the controller has no forecast of the load available corresponds to $\sigma = 0$.

The damping further drops for smaller values of σ corresponding to a larger forecast error (Figure 6.8(c)). Also when the forecast profile is out of phase with the measured load profile, damping is reduced as illustrated in Figure 6.8(d).

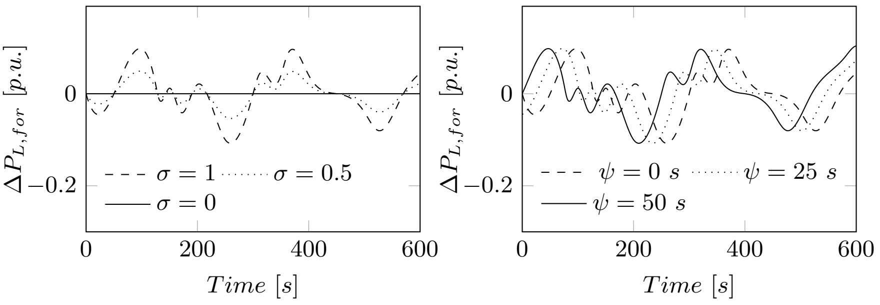

(a) Load forecast profiles for different σ values

(b) Load forecast profiles for different ψ values

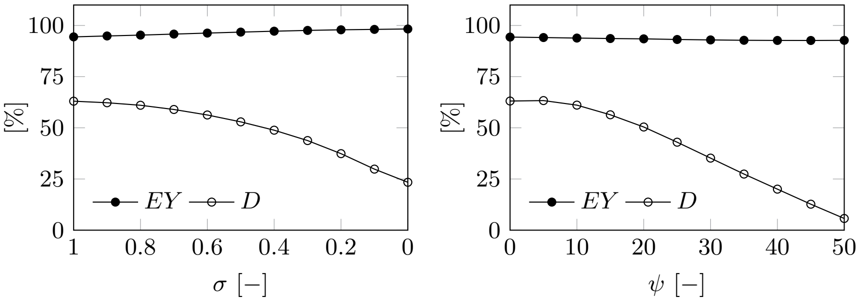

(c) Damping and energy yield in function of σ

(d) Damping and energy yield in function of ψ

Figure 6.8: Sensitivity analysis of load forecast errors ($\epsilon = 0.8$ & $t_{RHC} = 60$ s)

Even with no forecast ($\sigma =$ 0), the RHC still damps the frequency variations by 25%, while keeping the energy loss below 3%. This controller can thus significantly contribute to frequency regulation, even in the case no accurate forecast of the load is available.

6.6.3 Multiple turbines with variable wind speed profile

The optimal control of multiple turbines with a different, variable wind speed is elaborated. The wind profiles for two aggregated turbines with an equal share to the total wind power capacity are given in Figure 6.9(a). Due to the changing wind speeds, two sources of variability, load and wind power fluctuations influence the system frequency. Forecasted and measured load profile are the same as in Figure 6.9.

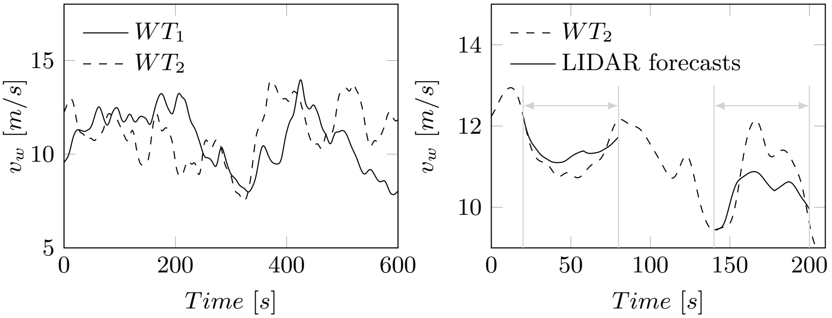

(a) Wind profiles

(b) Wind profile for WT_2 together with the LIDAR forecasts at $t =$ 20 & 140 s

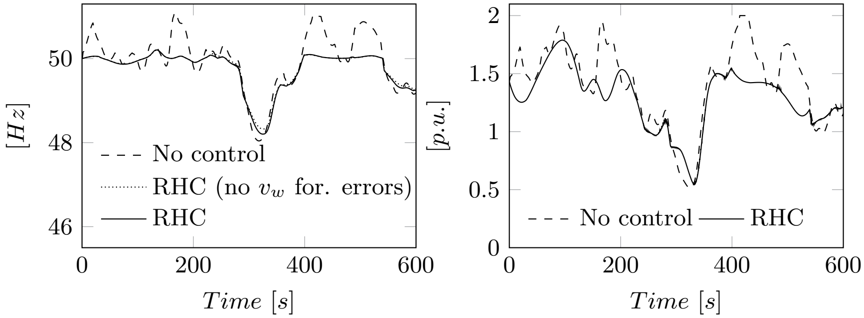

(c) Frequency results

(d) Total wind power: no control and RHC

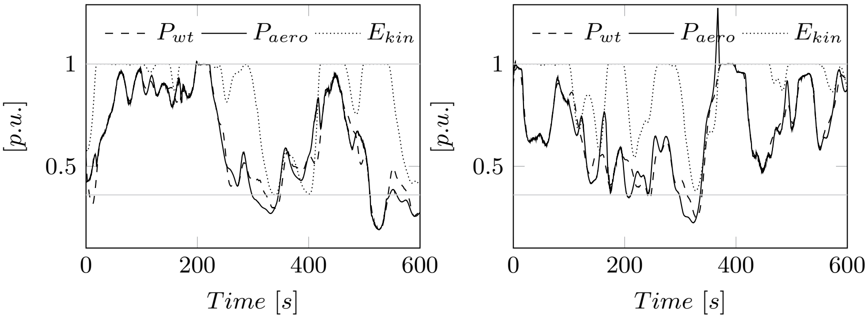

(e) Power and kinetic energy for RHC (WT_1)

(f) Power and kinetic energy for RHC (WT_2)

Figure 6.9: Results for two aggregated wind turbines with a variable wind profile

Contrary to previous simulations though, the wind speed at the turbines is not perfectly known. At each time step, only an estimate of the future wind speeds is available. A light detection and ranging (LIDAR) sensor can for instance be applied to accurately measure the wind speed at a certain distance in front of the turbine and provide a time history of future wind speeds. This data is very valuable in the design of complex feed forward turbine controllers to further reduce the loading or increase the performance of the turbine [186, 187]. An estimate of the future wind speeds over the considered time horizon is available every second (see Figure 6.9(b) for $t = 20$ and 140 s). At the time the wind speed prediction is made, it is assumed that its forecast is quite accurate for the first couple of seconds, thereafter only a rough estimate of the upcoming wind speed is available.

The frequency results (Figure 6.9(c)) show that these forecast errors only slightly influence the performance of the controller since the curves with and without wind forecast errors almost coincide. The results with and without RHC control indicate that the frequency variations are again significantly reduced. The controller is able to calculate the optimal operating points of the turbines in oder to reduce the total variability in the system (reflected in terms of frequency deviations). The kinetic energy of both turbine is extensively used and exchanged with the system (Figure 6.9(e) and 6.9(f)).

6.7 Discussion

Results show that integrating an RHC controller in wind turbines can support the frequency regulation of a system, mainly to damp over-frequencies. Damping of under-frequencies is rather limited to short power deviations with a low energy content. Applying this controller leads to a restricted loss in energy yield, which can be tuned by the parameter ϵ.

This chapter aims to propose a possible controller to offer frequency regulation by wind, but further research in different areas is required to transfer this rather conceptual control method into practice.

The main critical requirement to apply this controller is the forecast of both load and wind variations. With recent development of advanced forecast systems such as LIDAR, accurate wind forecasts are becoming feasible [188]. Load forecast on the other hand have up until today mainly been used for long-term applications as load variations are highly unpredictable on the short-term. Nevertheless, the results reveal that even if no forecast is available, a considerable damping of frequency variations can be achieved without further reducing the energy yield of the wind turbines.

The simulation results make use of aggregated models of the load, wind and conventional generation. Further research is therefore required to investigate how this control can be implemented on system level, consisting of a large number of wind farms or turbines. The effectiveness of the controller is proven for multiple turbines, but the communication, distribution of setpoints, where and how to perform wind speed measurements are out of the scope of this work.

Finally, also the impact of the increased fatigue loading on the mechanical components of the turbine due to the excessive exchange of kinetic energy and the prolonged periods of suboptimal operation should be further investigated.

6.8 Conclusion

A novel RHC controller is proposed to provide frequency regulation by wind power. The controller takes future load and wind variations into account and therefore optimally exploits the kinetic energy reserves of the wind turbine over a certain time horizon.

To iteratively solve the optimization with a low computational burden, a convex formulation of the problem is presented. By implementing the controller, wind turbines are mainly capable of damping over-frequencies as the damping of under-frequencies, resulting from positive load imbalances, is limited by the kinetic energy content of the turbines depending on the wind speed.

The considered load and wind forecast errors only slightly influence the performance of the controller as it iteratively determines the optimal trajectory and in this way adjusts the control variables in each step in order to compensate for the forecast errors. Even in the case where no load forecast is available, the controller still damps the frequency variations by 25% while keeping the energy yield above 97% compared to maximum power point tracking for the load profile considered.

Chapter 7

Pathways to a converter based power system

"It's difficult to make predictions, especially about the future."
- Niels Bohr

7.1 Introduction

Within current power systems, the frequency and voltage angles throughout the network are still set by the synchronous machines installed in conventional power plants. Converters on the other hand use a synchronization unit (a PLL for instance) to synchronize to the grid voltage in order to accurately control their active and reactive power to the grid. Consequently, they do not set the frequency themselves, but can influence the speed of nearby synchronous machine by altering their power setpoint in function of the measured frequency deviation and ROCOF, i.e. inertia support.

In this chapter, it is assessed how far this inertia support can be stretched as more synchronous machines are displaced and the system eventually becomes completely converter based, i.e. a so called empty grid. Additionally, other converter control approaches are suggested which can be applied to provide inertia and frequency support in a system with zero synchronous inertia.

7.2 From synchronous machine based towards an empty grid

When converters displace synchronous machines and consequently the total inertia within the system drops, new methods (chapter 5) can be applied to provide inertia support by slightly modifying the controllers of the converter in order to obtain a minimum required amount of $H_{sys,min}$ (Figure 7.1). Present CSB control approaches (section 4.3) are retained. Furthermore, since the dynamics within the system are still predominantly determined by the behaviour of these synchronous machines, the traditional forms of power system stability and their classification (Figure 3.2), still apply.

On the contrary, if more converter connected generation and load is integrated in the system, the system becomes completely 'empty' in the end, i.e. without any synchronous machines setting voltage and frequency. Consequently, the stability assessment of such a system looks significantly different from before as the traditional forms of stability related to the electro-mechanical dynamics are no longer relevant. Frequency limits for instance, usually defined to avoid damage to different mechanical parts of the generator and steam turbine, do not need to be that stringent since a direct coupling between any generator and the grid is no longer present.

It is however infeasible to control a system without synchronous machines in a stable manner, solely applying power converters using CSB control since they always require other power converters or synchronous machines to set the local voltage amplitude and frequency within the grid. Distinct control approaches based on VSB control are therefore required which would provide the needed grid support, e.g. to keep the system inertia at a certain level. Moreover, the VSB converters should be compatible with the existing generation units and provide a seamless path between the present and a converter based system.

To evolve towards such a system, the following research questions are addressed:

- What amount of synchronous inertia or grid strength is still required to provide the support, i.e. define point (A) in Figure 7.1?
- Can such an empty grid be controlled using only CSB converters and who will set the frequency in this system (C)?
- What kind of approach is applied in zone (B)? Can the control of (C) be used or modified for this zone?

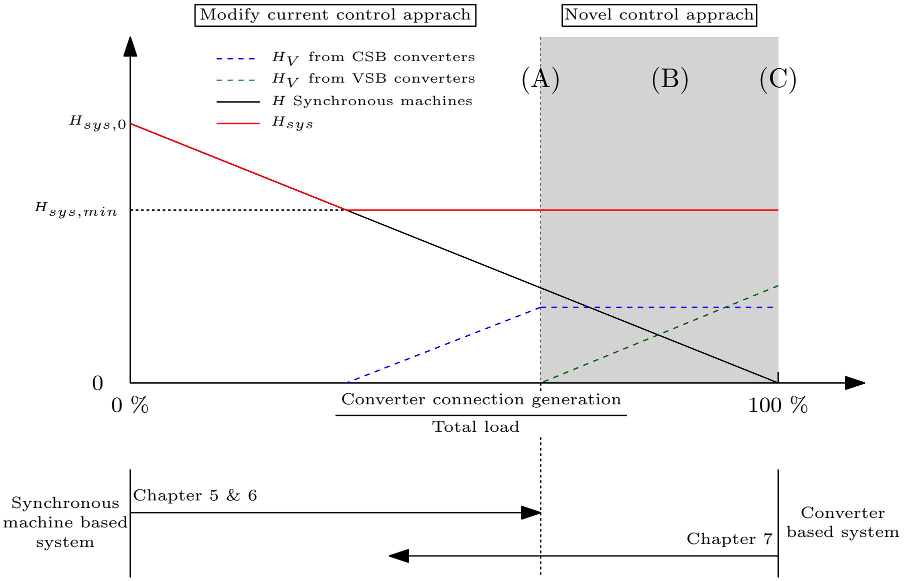

Figure 7.1: From synchronous machine based to an empty grid (assuming a linear relationship between converter connected penetration and inertia from synchronous machines)

7.3 Limits to provision of inertia support by CSB converters

The capability of the CSB converter to provide virtual inertia support generally depends on the strength of the AC system it is connected to. This external AC system can be considered weak either because of its high equivalent impedance (low short circuit ratio (SCR)) or low inertia.

In the following sections, stability issues related to the provision of inertia support are identified and the minimum required inertia and maximum SCR are quantified for a test system.

7.3.1 Test system and methodology

The test system represents a converter connected to an external grid through a transformer (Figure 7.2). The control of the converter is the one presented in section 4.3, with two decoupled inner current controllers and an outer power control loop. Contrary to previous RMS simulations, all electromagnetic dynamics within the grid are taken into account.

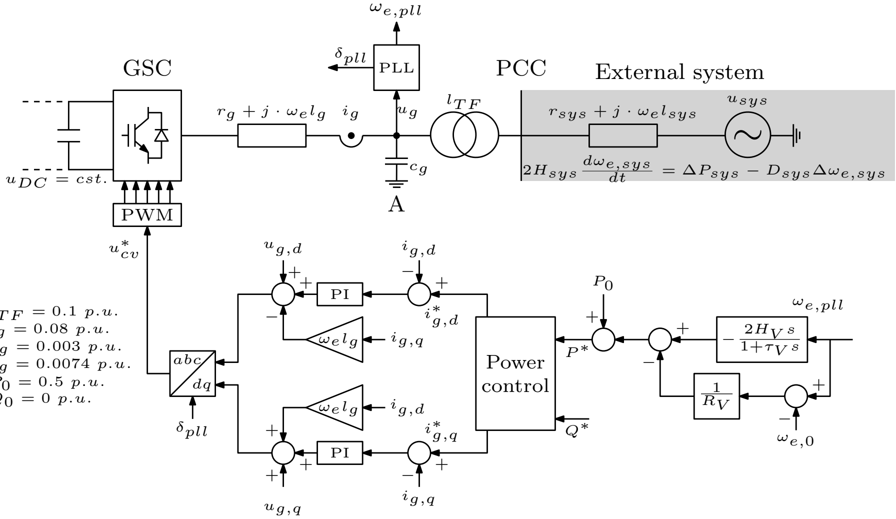
$\omega_{e,pll}$
δ_{pll}
PLL
GSC
PCC
External system
$r_g + j \cdot \omega_e l_g$
i_g
u_g
l_{TF}
$r_{sys} + j \cdot \omega_e l_{sys}$
u_{sys}
$2H_{sys}\frac{d\omega_{e,sys}}{dt} = \Delta P_{sys} - D_{sys}\Delta\omega_{e,sys}$
$u_{DC} = cst.$
c_g
A
PWM
u^*_{cv}
$u_{g,d}$
$i_{g,d}$
PI
$i^*_{g,d}$
$\omega_e l_g$
$i_{g,q}$
P_0
$\omega_{e,pll}$
$l_{TF} = 0.1\ p.u.$
$l_g = 0.08\ p.u.$
$r_g = 0.003\ p.u.$
$c_g = 0.0074\ p.u.$
$P_0 = 0.5\ p.u.$
$Q_0 = 0\ p.u.$
abc
dq
Power control
P^*
$-\frac{2H_V s}{1+\tau_V s}$
$\frac{1}{R_V}$
δ_{pll}
$\omega_e l_g$
$i_{g,d}$
$i^*_{g,q}$
Q^*
$\omega_{e,0}$
PI
$u_{g,q}$
$i_{g,q}$

Figure 7.2: CSB converter connected to a weak grid: test system

At the DC side, a perfect voltage source is connected to the DC bus. Hence, DC dynamics are neglected and the primary energy source is assumed to have an infinite power reserve available to provide inertial support (e.g. ideal storage unit). This inertial support is provided by altering the setpoint of the power control as a function of ROCOF and frequency deviation, using the measured frequency of the PLL (a standard SRF-PLL is applied here).

The external system is modelled by its Thévenin equivalent, i.e. a voltage source connected in series with the equivalent grid impedance. To represent the frequency dynamics within the external system, the frequency of the voltage source is determined by an equivalent swing equation (Figure 7.2). The controllers and mathematical representation of all system elements are modelled in the synchronous reference frame and implemented in MATLAB Simulink.

To assess the stability of the considered test system, it is linearised around its current operating point and converted to a standard feedback control system (Figure 7.3) [189]. Here, the input to the control system is the change in reference power (ΔP^*) and the output corresponds to the frequency deviation measured by the PLL. The open loop transfer function is denoted $G(s)$. The feedback loop on the other hand comprises the virtual inertia controller, with feedback gains equal to H_V and $\frac{1}{R_V}$. With this modelling concept, standard root locus techniques in order to determine the location of the poles of the closed loop system in function of the varying H_V and $1/R_V$ can be applied. To define the stability limits, it is analysed at which amount of support the poles cross the imaginary axis and move into the right half plane . This corresponds to the gain margin (Gm) of the open loop systems $G(s)$ and $G(s) \cdot H(s)$.

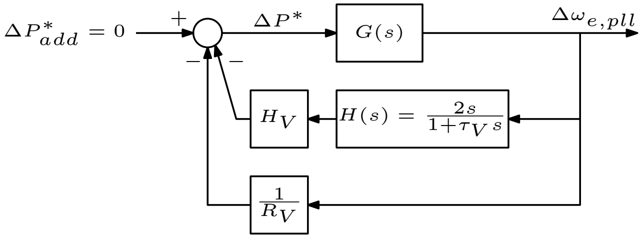

Figure 7.3: Feedback control system equivalent of test network

7.3.2 Minimum required synchronous inertia and SCR to deliver virtual inertia support

Case 1: Infinite strong grid w.r.t. equivalent impedance

The converter is directly connected to the equivalent voltage source, i.e. the transformer impedance is assumed zero and the SCR at the PCC is taken equal to infinity. The bode plots of $G(s)$ and $G(s) \cdot H(s)$ for this theoretical case are shown in Figure 7.4. Here, the dashed lines are used to represent a converter with an infinite control bandwidth. The gain margins of $G(s)$ and $G(s) \cdot H(s)$ are in this case equal to infinity irrespective of H_{sys}. Hence, stability is ensured for all values of H_V and $1/R_V$.

On the other hand, for a finite bandwidth of the controller (see solid lines in Figure 7.4), the gain margin is limited and a maximum amount of inertia support as a function of the available H_{sys} can be defined. The gain margin is however still sufficient. Hence, even for low values of H_{sys}, equal to 1 s for instance, H_V and $1/R_V$ can reach respectively 28.6 and 260.4 before the system becomes unstable.

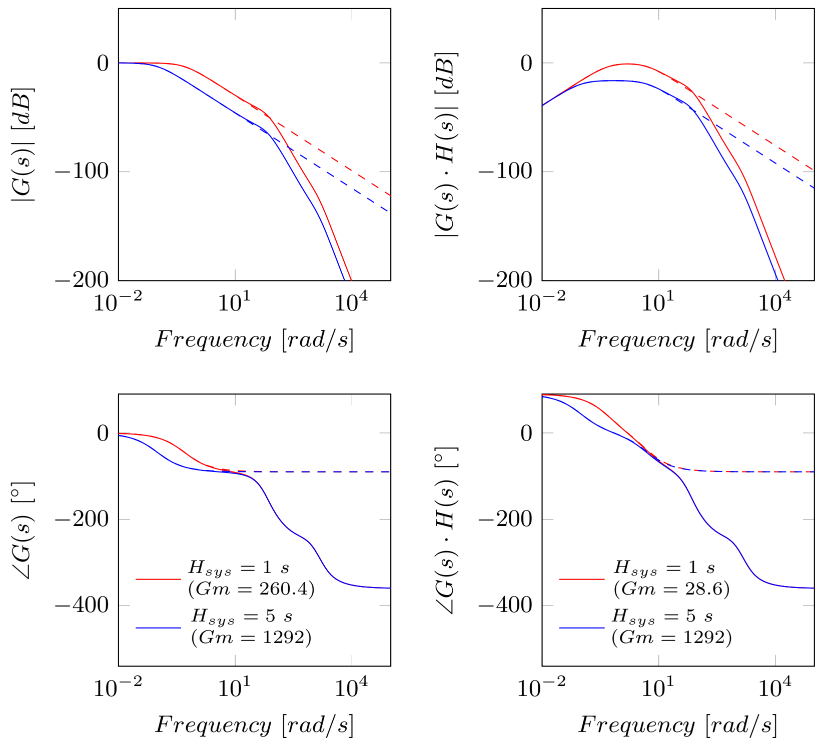

Figure 7.4: Bode plot of $G(s)$ and $G(s)\cdot H(s)$ (see Figure 7.3) for case 1 ($D_{sys}=1$, $\tau_V=0.2$ s and $\tau_{s,pll}=0.1$ s), dashed lines correspond to a converter with an infinite control bandwidth

Case 2: Varying SCR

The transformer and line impedance are in this case also taken into account. A bode plot of the open loop transfer function $G(s)$ for different grid parameters is given in Figure 7.5. In the low frequency range, the line parameters have no influence as the phase and magnitude plot of $G(s)$ are equal to the one of case 1, corresponding to the response of an aggregated single machine equivalent, $\frac{1}{2H_{sys}s+D_{sys}}$.

However, within a higher frequency range, between 10 and 100 Hz, $G(s)$ behaves as a notch filter, sharply attenuating $\Delta\omega_{e,pll}$ when ΔP^* varies with a frequency equal to the centre frequency of the filter. The magnitude peak at higher frequencies ($\approx 10^4 Hz$) is due to the electromagnetic resonance of the LCL-circuit.

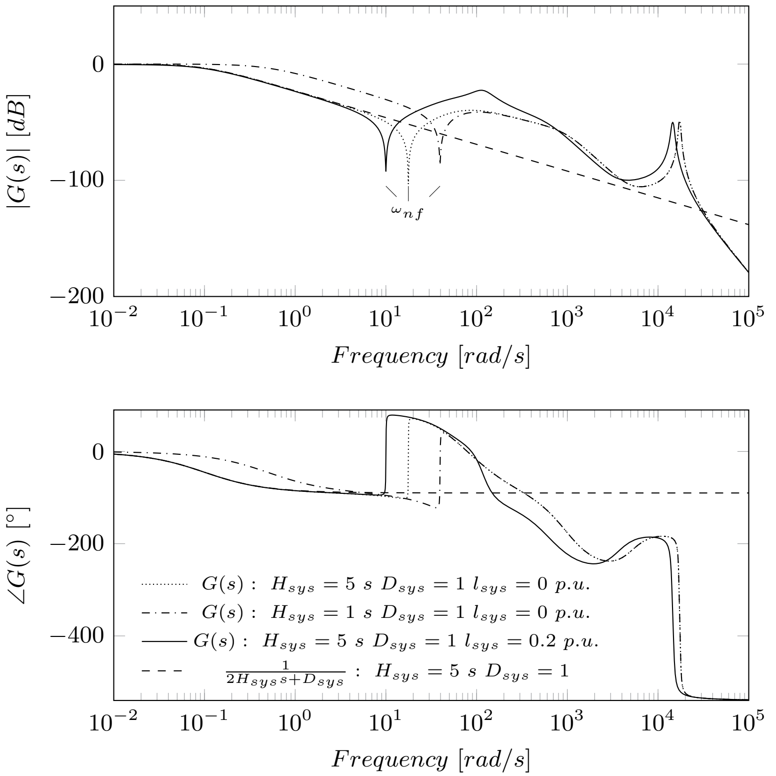

Figure 7.5: Bode plot of $G(s) = \frac{\Delta\omega_{e,pll}}{\Delta P^*}$ for different grid parameters

To explain this filter-like behaviour of $G(s)$ and in order to calculate the centre frequency of the notch filter, a simplified mechanical equivalent of the test system is used (Figure 7.6). A mass with inertia H, placed on a frictionless surface, represents the external system. It is connected on one side through a damper (D) with the reference frame moving at a constant speed, equal to the rated system ‘speed’ of 50 Hz. At the other side is it linked with the (inertialess) converter bus (A) through a spring representing the equivalent grid impedance.

Neglecting the resistance of the impedance, the spring constant k is equal to the synchronizing power coefficient as defined by (A.2). The power delivered by the converter is considered equivalent to a force exerted on the inertialess filter bus to which the PLL is connected. The angle of u_s and u_g is represented by the deflection with respect to the moving reference frame. To denote the relationship between P_{cv}^* and P_{cv}, a first order filter with a very small time constant is used. The transfer function in this case between ΔF $(= \Delta P_{cv}^*)$ and the frequency deviation measured at point A, has two complex conjugated zeros $(\alpha \pm \omega j)$, with ω corresponding to ω_{nf} (Figure 7.5):

$$\omega_{nf} = \sqrt{\frac{k}{2H_{sys}} - \frac{D_{sys}^2}{16H_{sys}^2}} \tag{7.1}$$

Referring to the mechanical equivalent, exerting a force F with frequency ω_{nf} at point A thus perfectly counteracts the force by the spring (F_k) due to the moving mass it is connected to, such that the deflection of point A (δ_g) with respect to the moving reference frame remains constant. The same applies for the test system, the PLL does not measure a frequency oscillation within the equivalent system when the active power varies with frequency ω_{nf}.

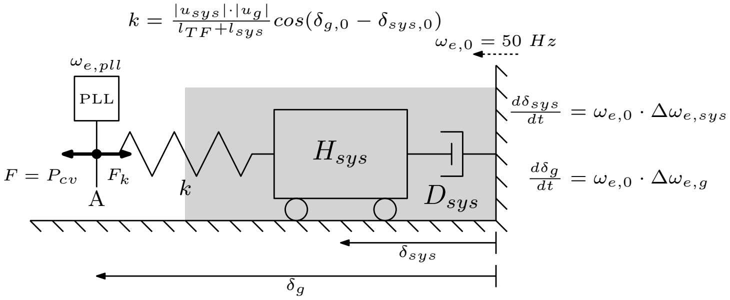
$k = \frac{|u_{sys}|\cdot|u_g|}{l_{TF}+l_{sys}} cos(\delta_{g,0} - \delta_{sys,0})$
$\omega_{e,0} = 50\ Hz$
$\omega_{e,pll}$
PLL
$\frac{d\delta_{sys}}{dt} = \omega_{e,0} \cdot \Delta\omega_{e,sys}$
H_{sys}
$F = P_{cv}$
F_k
A
k
D_{sys}
$\frac{d\delta_g}{dt} = \omega_{e,0} \cdot \Delta\omega_{e,g}$
δ_{sys}
δ_g

Figure 7.6: Simplified mechanical equivalent of the test system shown in Figure 7.2

The maximum H_V and $\frac{1}{R_V}$ is determined by separately calculating the gain margin of the open loop function (1) and (2) of Figure 7.3, for different amounts of system inertia and varying grid strength. The grid strength is expressed in terms of SCR at the point A of the test system. An r/x ratio for the grid impedance of the external system equal to 0.1 is assumed, corresponding to a typical high voltage line [190]. The results are given in Figure 7.7 and 7.8. The plots show that $H_{V,max}$ and $1/R_{V max}$ depend almost linearly on the SCR. Reducing the settling time of the PLL increases both limits, obviously also detrimentally affecting the dynamic performance of the converter. Looking at the influence of varying H_{sys}, it just slightly affects the results as it only alters the limits under a certain threshold. Unless very low values for the system inertia are considered, it is mainly the grid strength that determines the maximum amount of virtual inertia support.

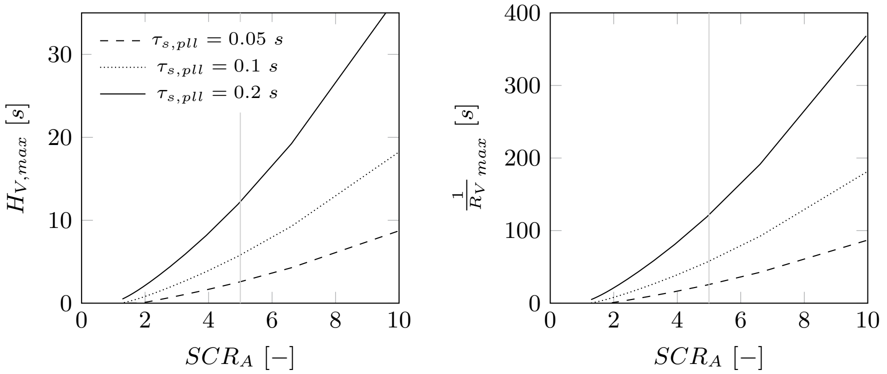

Figure 7.7: Maximum H_V and $\frac{1}{R_V}$ in function of the SCR at point A ($D_{sys} = 1$, $H_{sys} = 5\ s$ and $\tau_V = 0.2\ s$)

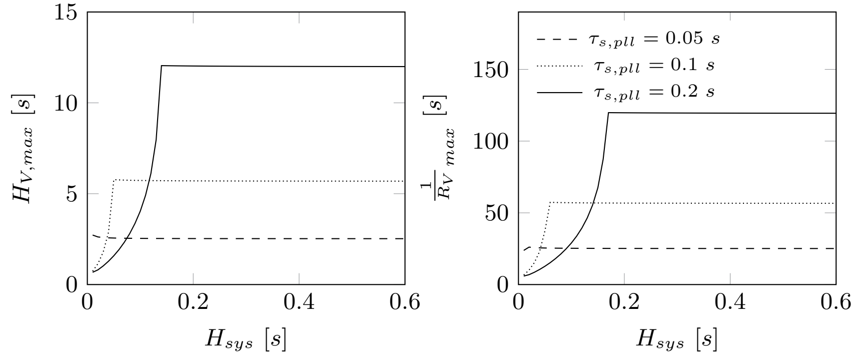

Figure 7.8: Maximum H_V and $\frac{1}{R_V}$ in function of H_{sys} ($D_{sys} = 1$, $SCR_A = 5$ and $\tau_V = 0.2\ s$)

7.3.3 Discussion

Providing virtual inertia, by altering the power setpoint as a function of the measured frequency at its terminals, seems quite challenging when CSB converters are operating in weak grids characterized by a low SCR. But even if no support is required, several studies have demonstrated that unstable dynamic interactions between the grid impedance and the converter control can occur when the conventional decoupled dq-control together with a SRF-PLL for synchronization is applied [191, 192, 193, 194, 195].

Several causes have been identified. In [195] for instance, it is shown that the control in a weak grid becomes very difficult due to the severe nonlinearities and highly coupled active power/voltage interactions. Other works mainly address the control issues in weak grids by analysing the input admittance of the converter [196, 197, 198]. Under the assumption that the power converter is controlled as a current source, this input admittance need to have non-negative conductance at all frequencies in order to act as a passive system, i.e. not amplifying any oscillations within the network [199, 200]. While this is mostly not the case over the whole frequency range considered, as long as the conductance is positive in the neighbourhood of each critical resonance and therefore attenuating the oscillations, stability is ensured. Within weak grids, positive damping of low frequency system modes can however occur, leading to resonance between the grid and the converter [196]. Changing the control parameters, adding additional filters or modifying the PLL settings can help to shape the input impedance in order to increase the damping capability at certain frequencies. With respect to the PLL, increasing its bandwidth however further extends the frequency range of the negative conductance behaviour [197]. Reducing the settling time of the PLL can therefore improve the stability, but results in a slower dynamic response.

Other stability issues specifically related to the application of PLLs in weak grids are addressed in [194, 201]. Stability problems occur because the local voltage used by the PLL become more influenced by the converter itself than by the grid voltage behind the equivalent grid impedance. It can provoke a positive feedback mechanism within the converter resulting in instability when the grid impedance is high.

The same applies for the provision of virtual inertia. As the line impedance increases, the frequency at the measurement point becomes more and more influenced by the active power output of the converter itself instead of the frequency set by the remaining synchronous machines. By increasing the loop gain by means of H_V or $1/R_V$, a positive feedback can occur, leading to system instability. Also in this case (Figure 7.8), reducing the settling time corresponding to a lower bandwidth extends the stability range.

Several options have been proposed to increase the power transfer and stability range in weak grids. Instabilities are avoided by means of virtually synchronizing the power converter to a stronger point in the system [202]. By introducing for instance an impedance-conditioning term in the PLL, the small signals stability is significantly improved, and the power transfer capability is increased equal to its static limit. An additional voltage feed forward loop within the current controller of the converter can also be used to improve the damping characteristic [192]. By properly tuning different lead lag elements in order to change the phase of the measured voltage before it is used as feed forward term in the current control, adequate damping is provided. Also modifying the outer power control loop based on an advanced gain-scheduling control system as proposed in [195] can tackle the issue of the instabilities related to the control in weak grids.

Finally, instead of adapting the conventional converter control approach using an inner decoupled current and an outer power/voltage loop, new distinct control techniques based on VSB control can be applied within weak grids. As the PLL is in most cases one of the main causes of instability, these PLL-less control approaches become more and more relevant for the operation of weak grids with low synchronous inertia. Furthermore, as they do not require any other synchronous machines to set the system frequency, they can operate in island mode or provide black start capability, see also sections 4.2.2 and 4.4.

7.4 Providing virtual inertia by VSB converters

The basics of VSB control have already been introduced in section 4.4.1. The standard controller was described which consists out of a droop based control action such that it can be operated in parallel with other converters. However, some additional modifications are required in order to also provide virtual inertia, which are presented in the following section.

7.4.1 Swing equation emulation

The active power (droop) control of the proposed control approach in section section 4.4.1 can be modified in order to provide inertia to the system by mimicking the swing equation of a synchronous machine [203]. As such, the reference frequency of the converter is determined by the following equation:

$$\underbrace{2H_V \cdot \frac{\mathrm{d}\omega_e^*}{\mathrm{d}t}}_{\text{Inertia}} = P^* - P - \underbrace{\frac{1}{R_P} \cdot (\omega_e^* - \omega_{e,0})}_{\text{Droop}} - \underbrace{K_D \cdot (\omega_e^* - \omega_{e,pll})}_{\text{Damping}} \tag{7.2}$$

where K_D denotes the damping constant used to represent the damping effect of a synchronous machine which acts here on the difference between the reference frequency and the actual frequency at the PCC, which is measured by a PLL at the filter bus. Using this approach, the converter can be considered to emulate the electromechanical behavior of a synchronous machine, in terms of damping and inertia, which is equipped with a governor having a droop constant equal to

R_P and a very small total time constant (turbine and governor) of the primary control action depending on the control bandwidth.

Although not implemented in this work, a higher order model representation of the synchronous machine can be included in the control to replicate its behaviour in more detail. In [204] for instance, an electrical model which emulates the electrodynamics within the stator, damper and field windings of the machine is included. This electrical machine model, together with the 2^{nd} order swing equation, results in a 7^{th} order machine representation [204]. Such emulation of the dynamics within a synchronous machine using a VSB is often grouped under the name 'Virtual Synchronous Machine' (VSM or VISMA) control, although many other terminologies, such as synchronverter [205] or power-synchronization control [206], are being applied in the literature depending on the control approach or modelling detail. A more elaborated classification can be found in [207].

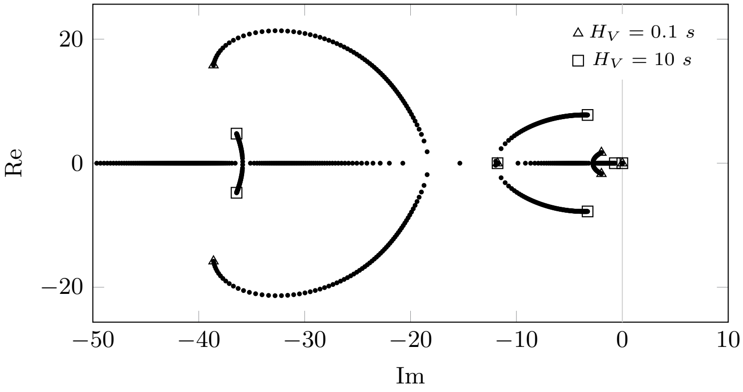

Figure 7.9: Root locus of the most critical poles (for test system as shown in Figure 7.2) using a VSB converter with virtual inertia H_V swept from 0.1 to 10 s ($R_P = 0.05$, $H_{sys} = 5$ s, $D_{sys} = 1$ and $SCR_A = 2$)

Besides its black start capability and the possibility to be operated in island mode, the voltage source based control allows to provide an improved inertia support in weak systems compared to the conventional current source based control approach, since it is not affected by the PLL-feedback loop. If we for instance use the same test network as shown in Figure 7.2 with $SCR_A = 2$, the system will remain stable for increasing values of H_V as illustrated in Figure 7.9. In this figure, the most critical poles of the linearised dynamic system model are shown for H_V going from 0.1 to 10 s. As all poles are located in the left half plane, small-signal stability is ensured.

Finally, in Figure 7.10, the frequency and active power variation from the converter after a power imbalance within the test system, $\Delta P_{sys} = 0.1$ $p.u.$, at $t = 1$ s is given for different values of H_V. It shows that the converter is able to reduce the initial ROCOF and also to stabilize the frequency. The steady state frequency is depending on the droop gain, which is taken equal to 0.05 in this simulation. In case $R_P = \infty$, the frequency would further decline.

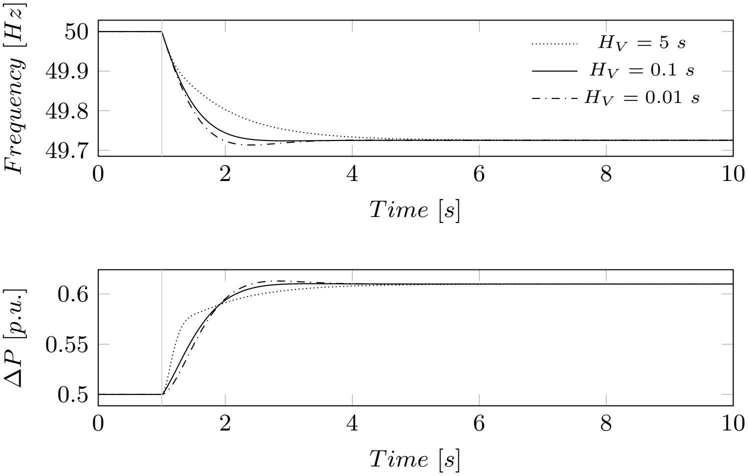

Figure 7.10: Frequency and converter active power variation after $\Delta P_{sys} = 0.1$ $p.u.$ ($R_P = 0.05$, $H_{sys} = 5$ s, $D_{sys} = 1$ and $SCR_A = 2$)

7.4.2 Discussion

As VSB control emulating a synchronous machine offers in most cases a lot of benefits compared to CSB control, one may ask themselves why not all converters should be controlled that way?

To answer this question, it is important to look at the main requirement to apply VSB control, i.e. it always requires additional storage. If the required energy or power are not available, any frequency dip within the system would directly result in a loss of synchronism of the converter, since it can not provide the required synchronizing power [208]. Or looking at it from a different perspective, setting a certain H_V implies that the power from the primary source is not transferred directly to the system, i.e. kind of smoothed by the virtual inertia, just like the power output from a large synchronous machine when a varying mechanical input power is applied. So, a storage unit is required to cope with the active power difference between the primary energy source and the output.

Secondly, as the output power is not directly controlled, many of the formerly proposed control mechanisms (see chapter 5), such as the fast frequency control, can not be applied. Furthermore, it is also impossible to set a certain deadband in which the frequency of ROCOF is allowed to vary without activating the inertia support controller.

Thirdly, and maybe the main reason why converters are mostly current source based is related to their fault behaviour. Contrary to synchronous machines, the converter currents need to remain within strict limits when a fault occurs in order to prevent damage to the power electronic components. The current controller as shown in Figure 4.14 can be used to limit these currents, but this will result in a loss off synchronism with the remaining system as the upper (droop) power control loops are unable to affect their controlled variables, i.e. the frequency and voltage output of the converter.

As a solution, in case the current limitation is reached or the available storage unit is unable to provide the required power or energy, the converter can be switched back to current based control as demonstrated in [206]. However, this can be quite challenging as additional control loops are required to allow a smooth transition between the two control modes. Since the active power control is kind of bypassed during the fault, no virtual inertia or droop control is provided.

Despite these issues, unless one single grid forming converter is used (which is quite unlikely from a reliability perspective), voltage source based grid supporting converters will become indispensable in the control and operation of a converter based power system as they are required to set the frequency for other current source based converters. Referring back to Figure 7.1, it is therefore expected that for a high penetration of converters (zone C), virtual inertia will not exclusively be provided by CSB converters within wind turbines and PV units, but also by large storage facilities or HVDC links using voltage source based control approach.

7.5 Converter based test system

Finally, we refer back to the test system as given in appendix B.1 and implement the formerly proposed control methods in order to operate the system without any synchronous generators directly connected to the network. All conventional generation is gradually ($G_4 \rightarrow G_1$) replaced by converter connected units with the same capacity and initial power setpoints, see Figure 7.11. By applying virtual inertia, the total system inertia is kept constant.

To this end, many combinations using different types of converter control approaches are feasible. When still some synchronous machines are connected to the system, the inertia support as proposed in chapter 5 can be applied. For even higher penetration of converters, close to 100%, some of the remaining generation is switched to voltage source based control using the inertia emulation proposed in 7.4.1, as at least one synchronous machine or converter has to set the system frequency. To improve the reliability, both the converters replacing G_1 and G_2 are voltage source based. Additionally, the converters $CV_{1,2,3}$ are equipped with an AC voltage controller, to take over the voltage control capability of the AVRs of the synchronous machines.

A power imbalance at t=1 s is simulated by assuming an outage of the line connected to $CV_4/G4$. All simulations are performed in DIgSILENT Power Factory and the results are presented in Figure 7.12.

The results for the different cases illustrate that the frequency response is improved as more and more synchronous machines are being displaced by converters, though the equivalent system inertia is remained unaltered. This can mainly be explained by the fast droop control action by means of $1/R_V$ and $1/R_P$ of the converters compared to the much slower turbine and governor response from the conventional units. In case 4 for instance, no synchronous machines are connected to the system such that the slow transient in the frequency trajectory is fully attenuated, resulting in an overdamped response. As the time constant of the droop action is in the order of ms to hundreds of a second, depending on the control bandwidth of the converter, the ROCOF (measured over 500 ms) will also be largely improved compared to the base case where only conventional units are connected.

Finally, it must be noted that between CV_1 and CV_2, the same synchronization mechanism as within a conventional system takes place (see section 2.2.2), as shown for case 4 in Figure 7.12. As soon as the power imbalance occurs, the frequencies of the converters will drop at a different rate depending on the electrical distance to the load. Thereafter, each converter will oscillate around the frequency at the centre of (virtual) inertia. Due to the damping included in the power controller of each converter, this oscillation is attenuated and the converters will finally acquire the same frequency.

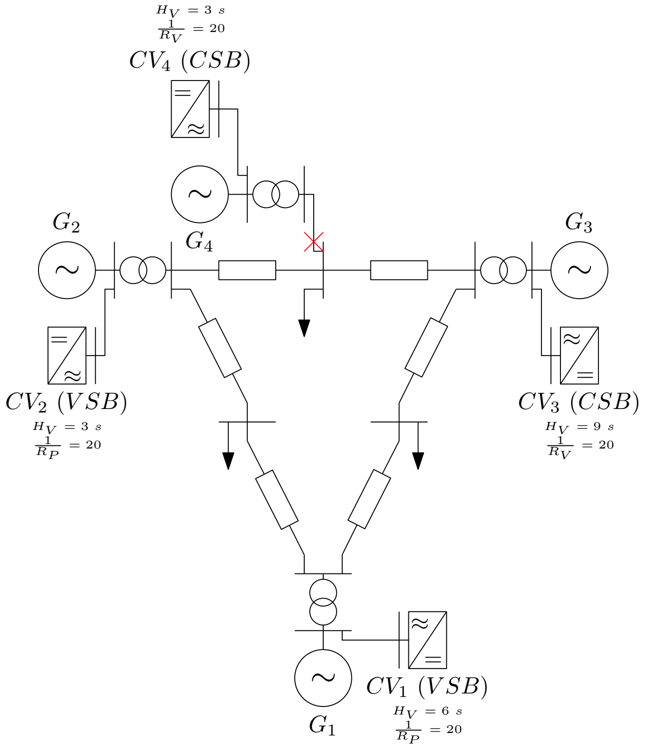
$H_V = 3\ s$
$\frac{1}{R_V} = 20$
$CV_4\ (CSB)$
G_2
G_4
G_3
$CV_2\ (VSB)$
$H_V = 3\ s$
$\frac{1}{R_P} = 20$
$CV_3\ (CSB)$
$H_V = 9\ s$
$\frac{1}{R_V} = 20$
$CV_1\ (VSB)$
$H_V = 6\ s$
$\frac{1}{R_P} = 20$
G_1

(a) Test system

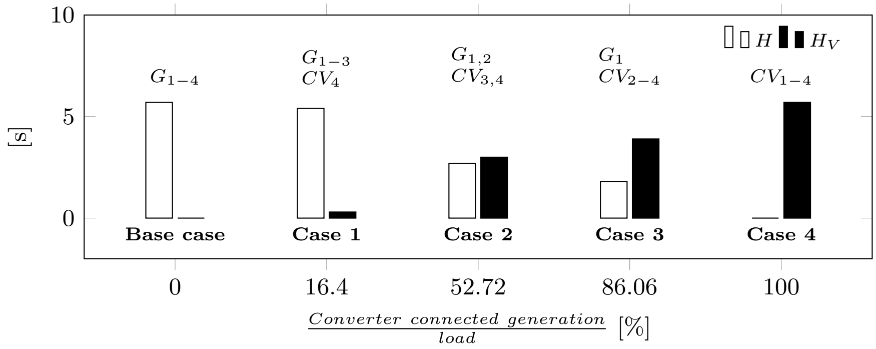

(b) Operating units together with the variation in synchronous inertia (H) and virtual inertia (H_V) for the different test cases. Total inertia is kept constant equal to 5.7 s (all values expressed on a system base of 300 MVA)

Figure 7.11: From synchronous to converter (CV) based system: test system and test cases (VSB: Voltage source based, CSB: Current source based)

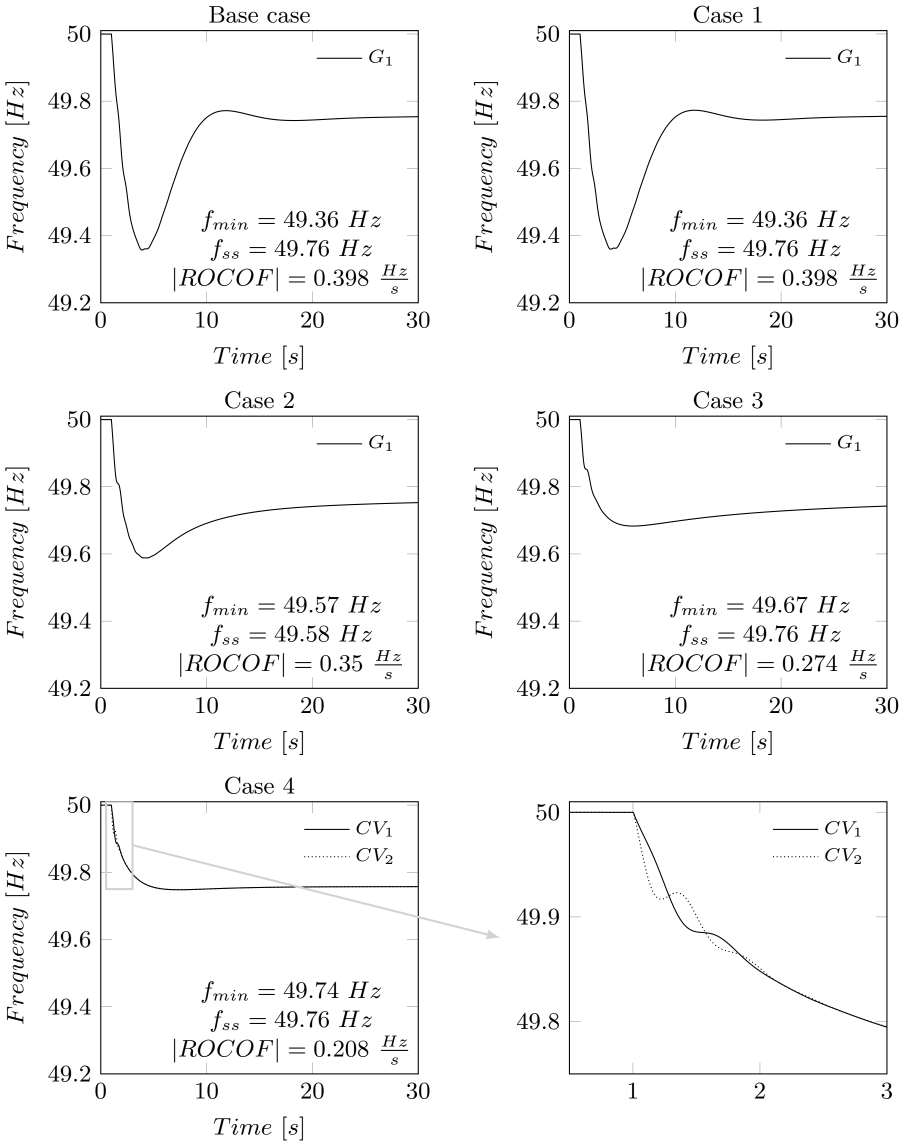
Base case

Case 1

Case 2

Case 3

Case 4

Figure 7.12: Frequency results after an outage of the line connecting G_4/CV_4 for the different test cases presented in Figure 7.11, $|ROCOF|$ is measured over 500 ms

7.6 Conclusion

As illustrated in this chapter, virtual inertia provision by applying current source based control will become very challenging in weak grids with a low SCR due to the fact that the frequency at the terminals of the converter will become more influenced by the control of the converter itself than by the external system. Hence, the control can become unstable, even for moderate values of H_V.

Modifying the currently applied controllers within HVDC links, wind and PV units, will therefore improve the frequency response of the power system, yet new approaches are required for very high levels of converter based generation. Furthermore, these conventional controllers do always require other devices to set the frequency within the system and can therefore not properly function in island mode.

To operate and control a fully converter based system, new approaches using voltage source based controllers are proposed and further analyzed. Applying these control approaches, it is demonstrated by means of the proposed test system how to provide inertia and frequency support in case there are no longer synchronous machine connected. While such an operation is feasible, it will require a fundamental change in the controls of the converters.

Chapter 8

Conclusion

8.1 General summary and conclusions

This thesis provides a clear understanding of the stability problems related to the reduced inertia from synchronous machines and presents different control methods which can be applied to deliver inertia support by converter connected generation. As such, this work covers the complete transition from a system perspective, from a conventional towards a converter based power system. Although only applied to small simple test systems, the findings are generic and instructive to set out (future) approaches for the operation and control of large-scale power systems with reduced synchronous inertia. The main conclusions related to the different parts of this work are summarized in the following.

By investigating the role, quantification and measurement of inertia in present power systems, it is shown that it is a vital parameter upon which power system operation is based and both the distribution as well as the amount of inertia have an impact on the different forms of power system stability. The total amount of inertia perceived by the system is however very challenging to accurately measure in real time.

Looking at the different forms of power system stability, it is illustrated that issues will mainly arise with respect to the frequency stability of the system as reduced inertia results in very high ROCOF values and a low nadir frequency after a negative power imbalance. Hydro based systems perform in this respect even worse, with increasing risk of reaching the frequency threshold at which load shedding is activated. Defining a general minimum of required inertia is quite difficult though since it is very system specific and depends on a wide range of parameters. Nevertheless, by for instance using the available data of the Nordic power system, it is concluded that current levels of kinetic energy stored in synchronous machines are sufficient to cope with power imbalances that are almost three times higher than the applied reference incident.

In order to operate and control such a power system with reduced inertia, multiple options are proposed, going from adapting the current protection equipment and grid codes to providing so-called virtual inertia by converter connected generation. With respect to the control approaches and modelling of these converter connected generation, a clear distinction is made between the current source based control, which is the most prevalent control method in use for RES-e sources and the voltage source based control, which is currently merely applied in small micro grids or to energize offshore wind power plants. As an accurate frequency measurement is required to provide inertia support by current source based converters, the different synchronization mechanisms have been discussed in more detail. It is demonstrated that additional time delays are involved due to the filtering in order to attenuate higher order harmonics and negative sequence components in the voltage waveform at the terminals of the converter.

By making a comparison of the inherently stored amount of energy within the distinct RES-e units, it is concluded that, without the integration of additional storage or curtailment, mainly wind turbines are eligible for inertia support. The kinetic energy in the blades and transmission system can be applied to deliver an inertial response similar to the one of synchronous machines such that the frequency stability in low inertia systems is improved. Alternative control methods, such as providing a step wise response are also effective, although a correct parameter tuning is required to make sure that power decrease in the recovery phase will not result in a severe secondary dip.

Furthermore, also the transfer of inertia through HVDC links connecting two asynchronous systems is considered as a feasible option to support the frequency response. To this end, different strategies are proposed. Moreover, the potential of applying the stored energy in the DC link and converters is analysed, however the amount of stored energy is insufficient and can merely be applied to provide inertia support during a very short time, in the order of hundreds of milliseconds. Interconnecting the different links such that a DC grid is formed will increase the potential, such that support can delivered over a longer time frame.

Using the different mechanisms, the provision of such support can be implemented at large scale. Care should however be taken when implementing inertia provision by wind units in an optimal operating point. As the capability of the support is depending on the wind speed, insufficient inertia will be provided if a large numbers of turbines are operating at low wind speeds.

The application of the kinetic energy within wind turbines to provide frequency regulation is further elaborated. To this end, a receding horizon controller is proposed in order to include forecast of load and wind speed variations. By implementing the controller, wind turbines can mainly damp over-frequencies as the damping of under-frequencies is limited by the kinetic energy content of the turbines, which is depending on the wind speed. Moreover, it has been proven that the controller substantially reduces the influence of load and wind forecast errors as it iteratively determines the optimal trajectory and in this way adjusts the control variables in each step.

Complete new control approaches using voltage source based control are finally required to provide virtual inertia in weak grids. In such systems, inertia provision by current source based control will lead to instability due to the positive feedback through the measured frequency and power controller. Hence, an inertia controller emulating the swing equation of a synchronous machine is proposed and implemented in the test system. Moreover, the use of such voltage source based control enables the operation of 100% converter based systems which has been demonstrated by converting the applied test system.

8.2 Recommendations to different stakeholders

The transition towards a RES-e based power system, with a substantial penetration of converter connected generation, will not take place overnight. To accommodate the increasing number of converter connected units and the reduction of inertia from synchronous machines which goes along with it, some recommendations to the involved stakeholders are made based on the findings of this work:

- **TSO**: As inertia is shared among other power systems within the same synchronous zone, a collaboration between different TSOs is required to conduct detailed system studies in order to define the minimum required system inertia, which involves sharing technical data, expertise and results. Since inertia mainly influences the frequency stability of the system, a consensus is needed on how the frequency response should optimally look like. Different operating scenarios and contingencies have to be taken into account, such as large power plant outages or even system splits.

  Additionally, new and better monitoring tools, which accurately estimate and measure the amount of inertia coming from synchronous machines and load, need to be implemented in order to determine the required provision of virtual inertia by converter connected generation at each moment in time. The burden of inertia provision, both from synchronous generators as well as (virtual inertia) from converter connected units, can be shared by different TSOs by requiring to deploy a certain amount of inertia within its own responsibility area.

The TSOs should also take action to modify the current grid codes in order to define technical specifications including the provision of inertia and frequency support by different types and sizes of converter connected units. Since frequency is a global system parameter, it is probably not imperative that all devices contribute equally to this support, as long as the total support is sufficient to keep the frequency and ROCOF within certain limits.

Moreover, as shown in this work, in case of reduced system strength or extreme high penetration of converter units, a change in mindset is required to pave the way for the transition of a CSB to VSB control approach.

- **DSO**: Furthermore, a close collaboration between DSO and TSO is essential to make sure that the settings of installed protection devices (such as ROCOF relays) are adapted to cope with the expected ROCOF after a power imbalance, which is closely related with the required minimum system inertia defined by the TSO.
- **Manufacturers of RES-e units**: Although some wind turbine manufacturers have already developed inertia support controllers, they should further investigate the impact of the inertia provision on the different mechanical components and related lifetime of the turbines. Incorporating wind forecast and additional storage should also be considered to increase the reliability and flexibility of the support.

8.3 Future work

During this thesis, several issues and challenges were identified that need further optimization or research.

A first interesting field of future research is the mathematical modelling of large-scale power systems with an increased number of converter connected generation. Normally, power system engineers mostly rely on phasor based modelling to analyse the stability of large-scale power systems. This modelling approach assumes that sufficient inertia is present in the system such that the time scales of electromechanical dynamics within the synchronous machines are order of magnitudes larger than the time scales involved in the electromagnetic dynamics occurring in the network. As the inertia decreases, these assumptions may not be valid any more and new modelling approaches have to be considered. Although a detailed EMT simulation may be suited to analyse small power systems, it is not a feasible solution for large-scale studies due to its computational burden. A fundamental new mathematical framework for converter based power systems is needed, which accurately represents the dynamics of interest with the required level of detail.

Further investigation is also required to determine which approach and steps should optimally be taken to implement inertia support at a large scale. Besides imposing it as a requirement through the different grid codes, a new ancillary service market can for instance be created at which virtual inertia becomes a service product that is contracted or traded among different market participants. Additional research is however required on how such a market will look like and who can participate in it, taken into account different constraints.

In this work, mainly large wind farms or HVDC links were assumed to provide virtual inertia to the system. The role of smaller units integrated in the distribution system still need to be addressed. A key aspect here is to further investigate the robustness and reliability of the control algorithms and communication if numerous distributed units take part in the inertia provision. Moreover, the optimal way and location of providing inertia need to be assessed in more detail. Should they fulfil a more active role in the future, with providing ancillary services to support the stability of the transmission system?

Further research is finally required in the area of VSB converter controllers and their implementation in transmission systems. Not only the robustness of the control should be further assessed, but also the required characteristics of the attached storage unit need to be defined in more detail. With respect to robustness, using real time simulation platforms could e.g. help to reveal the underlying stability and control issues during grid disturbances due to the time delays and filtering involved in the measurements.

Appendix A

Power system and power plant modelling

A.1 Classical multi-machine system representation

To model the electromechanical dynamics between synchronous machines, the power system can be represented with various levels of detail, depending on the accuracy, severity of disturbance or length of simulation required. The most simple representation is the so-called classical multi-machine model [4, 14, 32]. This model presented here is used to describe the frequency and rotor angle deviations upon a small load change in the system. Although it leads only to approximate results, it is considered to be useful and instructive in the analysis of the influence of inertia on electromechanical transients.

The main assumptions of the model are:

- Generators are represented by their classical machine model of constant voltage behind transient reactance
- The power network has a very high x/r ratio
- All loads are represented by constant impedances and have a negligible reactive component
- The effect of generator controls are neglected (i.e. constant mechanical infeed and excitation voltage)

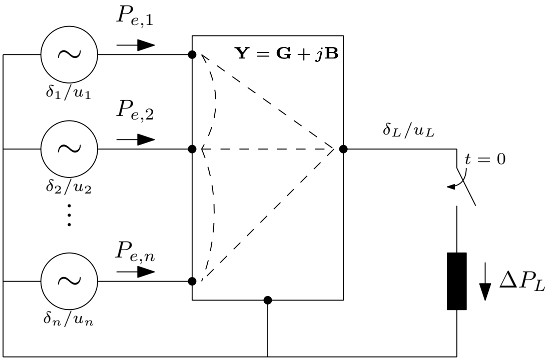

Figure A.1: Classical multi-machine system representation to study a sudden load change at node L [14, 4]

Consider now a power system network which has been reduced to its internal generator nodes and one additional node L, to which a small load change of ΔP_L is suddenly applied. The network is given in Figure A.1. For small disturbances, the change in electrical power from each node can be expressed as:

$$\Delta P_{e,i} = \sum_{j=1}^{n} P_{S,ij} \cdot (\Delta\delta_i - \Delta\delta_j) \tag{A.1}$$

with $P_{S,ij}$ the synchronizing power coefficient representing the active power change between bus i and another bus j due to a change in power angle between the two buses, while keeping all other bus angles constant:

$$P_{S,ij} = \left.\frac{\partial P_{ij}}{\partial \delta_{ij}}\right|_{\delta_{ij,0}} = u_i u_j b_{ij} cos(\delta_{ij,0}) \tag{A.2}$$

A.2 Aggregated single machine equivalent for load-frequency studies

Corresponding to section 2.2.2, all the synchronous machines can be aggregated into a single machine for the analysis of the frequency response at the COI due to a power imbalance. As a result, a simple power system equivalent model can be used for load-frequency studies in which the transmission network performance is not taken into account, see Figure A.2 [32]. Accordingly, equation (2.15), including governor control and system load damping, becomes:

$$2H_{sys}\frac{\mathrm{d}\Delta\omega_{e,COI}}{\mathrm{d}t} = \Delta P_G - \Delta P_L - D_{sys}\Delta\omega_{e,COI} \tag{A.3}$$

with D_{sys} the % change in system load per % change in grid frequency. Typical values are 1-2% [32]. $\Delta P_G = \sum_{i=1}^{n}\Delta P_{m,i}$ represents the change in generator power of all units participating in the primary control action of the system. ΔP_G is composed out of the governor action of the different power plant types, e.g. thermal, hydro, gas, ... each having a distinct dynamic behaviour.

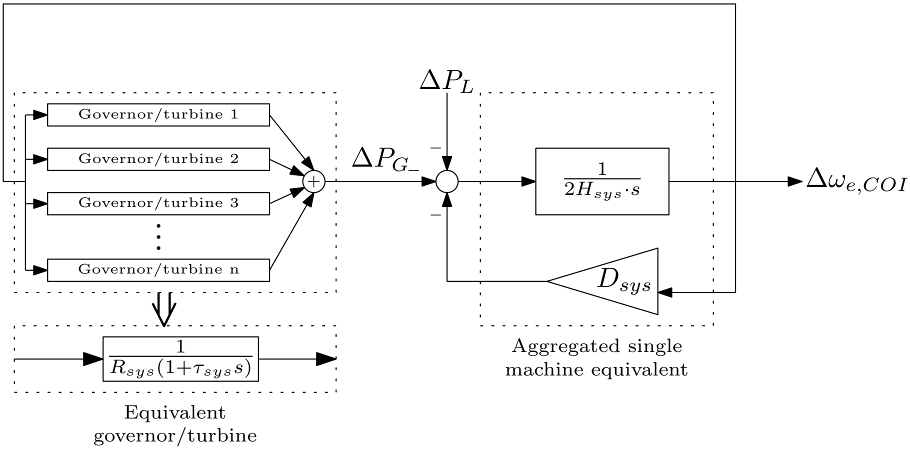
Governor/turbine 1
Governor/turbine 2
Governor/turbine 3
Governor/turbine n
ΔP_G
ΔP_L
−
−
+
$\frac{1}{2H_{sys}\cdot s}$
$\Delta\omega_{e,COI}$
D_{sys}
$\frac{1}{R_{sys}(1+\tau_{sys}s)}$
Aggregated single machine equivalent
Equivalent governor/turbine

Figure A.2: Power system equivalent for load-frequency studies

To simplify the complexity of the different governor and turbine models, it can be assumed that the governor action of all power plants can be approximated by an equivalent first order transfer function with time constant τ_{sys} as shown in the figure [14]. R_{sys} denotes here the composite frequency droop and is given by:

$$\frac{1}{R_{sys}} = \sum_{i=1}^{n}\frac{S_i}{R_i \cdot S_{sys}} \tag{A.4}$$

The droop of each individual machine, R_i, represents the % change in grid frequency that causes 100% change in valve position or power output of the corresponding generation unit.

A.3 Turbine and governor models

Detailed models of the turbines and governors considered in this work can be found below. The steam turbine model of Figure A.3 corresponds to the IEEEG1 model and represents in this work a tandem-compound single reheat turbine with parameters taken from [119, 32].

The hydro turbine model of Figure A.4, neglecting the effects of pipe elasticity and water compressibility, is based on the models presented in [32]. Due to the non-minimum phase behaviour of the hydro turbine, a transient droop compensation is included in the governor model.

The gas turbine model finally represents an open cycle gas turbine (OCGT) equipped with governor, acceleration and temperature control. The model is adapted from the one developed by Rowen [209, 210], by making reference to more recent OCGT models [211, 95, 212]. The same model can be applied in load-frequency studies (up till secondary control action) for a combined cycle gas turbine (CCGT) since the heat recovery generator and steam turbine will have little impact on the overall unit response within this time frame, due to the long time constants associated with their dynamics [95].

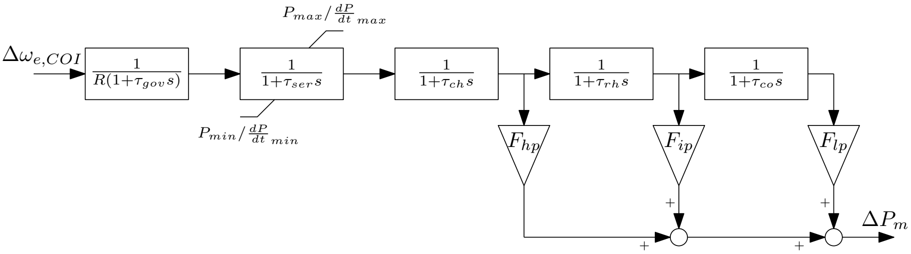

R	Droop [-]	0.05	F_{ip}	Intermediate pressure turbine factor [-]	0.3
τ_{gov}	Governor time constant [s]	0.1	F_{lp}	Low pressure turbine factor [-]	0.4
τ_{ser}	Servo time constant [s]	0.3	P_{max}	Maximum valve limit [p.u.]	1
τ_{ch}	Time constant of steam chest [s]	0.3	P_{min}	Minimum valve limit [p.u.]	0
τ_{rh}	Time constant of reheater [s]	7	$\frac{dP}{dt}_{min}$	Maximum valve closing rate [p.u./s]	0.3
τ_{co}	Time constant of crossover piping [s]	0.5	$\frac{dP}{dt}_{min}$	Minimum valve closing rate [p.u./s]	-0.3
F_{hp}	High pressure turbine factor [-]	0.3			

Figure A.3: Steam turbine and governor model

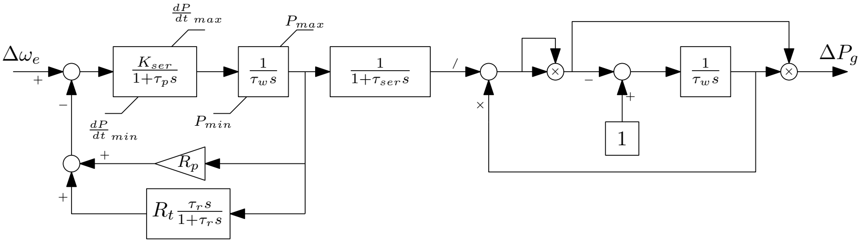
$\Delta\omega_e$
$\frac{K_{ser}}{1+\tau_p s}$
$\frac{dP}{dt}_{max}$
$\frac{dP}{dt}_{min}$
P_{max}
P_{min}
$\frac{1}{\tau_w s}$
$\frac{1}{1+\tau_{ser} s}$
R_p
$R_t \frac{\tau_r s}{1+\tau_r s}$
1
ΔP_g

R_p	Permanent droop [-]	0.05	τ_r	Reset time [s]	5
R_t	Transient droop [-]	0.2	τ_w	Water starting time [s]	1
K_{ser}	Servo gain [-]	5	P_{max}	Maximum gate limit [p.u.]	1
τ_{ser}	Servo time constant [s]	0.2	P_{min}	Minimum gate limit [p.u.]	0
τ_p	Pilot valve time constant [s]	0.05	$\frac{dP}{dt}_{min}$	Maximum gate closing rate[p.u./s]	0.16
			$\frac{dP}{dt}_{min}$	Minimum gate closing rate [p.u./s]	-0.16

Figure A.4: Hydro turbine and governor model

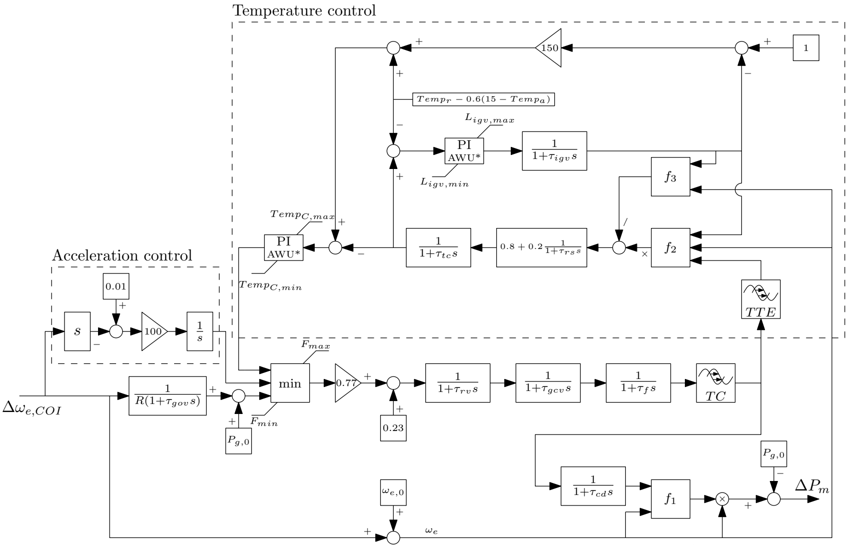
Temperature control
Acceleration control
150
1
$Temp_r - 0.6(15 - Temp_a)$
$L_{igv,max}$
PI AWU*
$L_{igv,min}$
$\frac{1}{1+\tau_{igv} s}$
f_3
f_2
$Temp_{C,max}$
$Temp_{C,min}$
$\frac{1}{1+\tau_{tc} s}$
$0.8 + 0.2\frac{1}{1+\tau_{rs} s}$
TTE
0.01
s
100
$\frac{1}{s}$
$\Delta\omega_{e,COI}$
$\frac{1}{R(1+\tau_{gov} s)}$
$P_{g,0}$
F_{max}
min
F_{min}
0.77
0.23
$\frac{1}{1+\tau_{rv} s}$
$\frac{1}{1+\tau_{gcv} s}$
$\frac{1}{1+\tau_f s}$
TC
$\frac{1}{1+\tau_{cd} s}$
f_1
$\omega_{e,0}$
ω_e
ΔP_m

*AWU=anti-windup

$f_1(u_1, u_2) = \frac{1}{0.77}(u_1 - 0.23) + 0.5(1 - u_2)$

$f_2(u_1, u_2, u_3) = \frac{T_r - 453(u_2^2 - 4.21u_2 + 4.42)0.82(1-u_3) + 722(1-u_2) + 1.94(i_{gv,max} - (50u_1 + 34))}{1 + 0.005(15 - T_a)}$

$f_3(u_1, u_2) = \frac{u_1 u_2^{0.257} 288}{Ta + 273}$

R	Droop [-]	0.05	$Temp_a$	Ambient temperature [°]	15
τ_{gov}	Governor time constant [s]	0.05	τ_{igv}	IGV actuator time constant [s]	3
τ_{rv}	Ratio valve positioner time constant [s]	0.05	$L_{igv,max}$	Maximum inlet guide vane [p.u.]	1
τ_{gcv}	Gas control valve time constant [s]	0.05	$L_{igv,min}$	Minimum inlet guide vane [p.u.]	0.46
τ_f	Gas fuel system time constant [s]	0.4	IGV_{max}	Angle maximum inlet guide vane [°]	84
TC	Combustion time delay [s]	0.01	IGV_{min}	Angle minimum inlet guide vane [°]	57
TTE	Turbine and exhaust time delay [s]	0.04	F_{max}	Maximum fuel limit [p.u.]	1
τ_{cd}	Compressor discharge time constant [s]	0.2	F_{min}	Minimum fuel limit [p.u.]	0.15
$Temp_r$	Rated exhaust temperature [°]	510	$Temp_{C,max}$	Maximum limit temperature controller [p.u.]	1.1
τ_{tc}	Thermocouple time constant [s]	0.5	$Temp_{C,min}$	Minimum limit temperature controller [p.u.]	0
τ_{rs}	Radiation shield time constant [s]	15			

Figure A.5: Gas turbine and governor model

Appendix B

System data

B.1 Test system

The test system shown in Figure B.1 is a modified version of the nine bus system model presented in [4]. A complete set of system parameters can be found in Table B.1, B.2, B.3 and B.4. G4 corresponds to a local hydro generation unit which is not equipped with a governor or exciter.

Parameter	Description	G1	G2	G3	G4
Type	Power plant type	Hydro	Steam	Steam	Hydro
S [MVA]	Rated power	90	90	90	30
u [kV]	Nominal voltage	16.5	18	13.8	13.8
x_d [p.u.]	d-axis synchronous reactance	0.36	1.72	1.68	0.38
x'_d [p.u.]	d-axis transient reactance	0.15	0.23	0.23	0.13
x''_d [p.u.]	d-axis subtransient reactance	0.1	0.2	0.2	0.08
x_q [p.u.]	q-axis synchronous reactance	0.24	1.66	1.60	0.22
x'_q [p.u.]	q-axis transient reactance	0.24	0.38	0.32	0.22
x''_q [p.u.]	q-axis subtransient reactance	0.1	0.1	0.2	0.1
x_l [p.u.]	Leakage reactance	0.083	0.1	0.095	0.075
R_a [p.u.]	Armature resistance	0.003	0.005	0.002	0.002
τ'_{d0} [s]	d-axis transient open circuit time constant	8.96	6	5.89	7.23
τ''_{d0} [s]	d-axis subtransient open circuit time constant	0.075	0.0575	0.0575	0.068
τ'_{q0} [s]	q-axis transient open circuit time constant	/	0.535	0.6	/
τ''_{q0} [s]	q-axis subtransient open circuit time constant	0.15	0.0945	0.08	0.13
$SG1.0$ [p.u.]	Machine saturation at 1 p.u. voltage	0.13	0.13	0.13	0.13
$SG1.2$ [p.u.]	Machine saturation at 1.2 p.u. voltage	0.32	0.32	0.32	0.32
H [s]	Inertia constant	6	3	9	3

Table B.1: Generator parameters

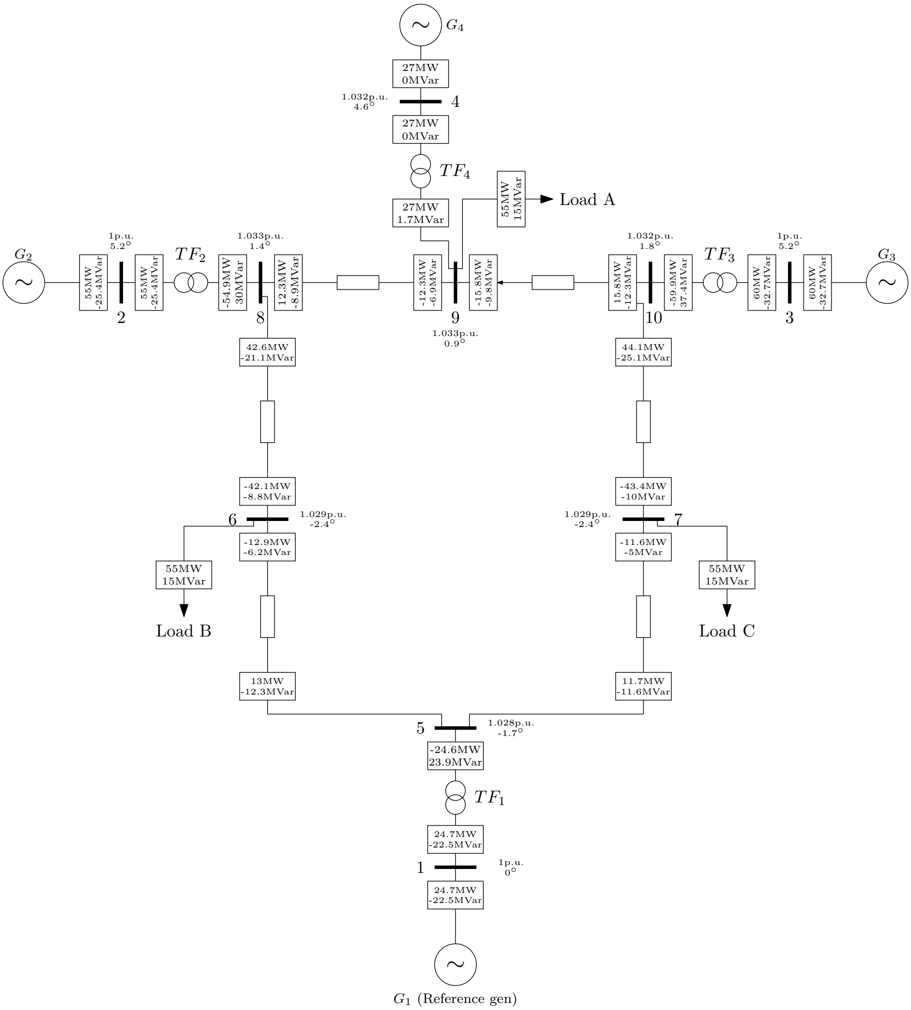
G_4
27MW 0MVar
1.032p.u. 4.6°
4
27MW 0MVar
TF_4
27MW 1.7MVar
55MW 15MVar
Load A
G_2
1p.u. 5.2°
55MW -25.4MVar
2
55MW -25.4MVar
TF_2
1.033p.u. 1.4°
-54.9MW 30MVar
8
12.3MW -8.9MVar
-12.3MW -6.9MVar
9
-15.8MW -9.8MVar
1.033p.u. 0.9°
1.032p.u. 1.8°
15.8MW -12.3MVar
10
-59.9MW 37.4MVar
TF_3
1p.u. 5.2°
60MW -32.7MVar
3
60MW -32.7MVar
G_3
42.6MW -21.1MVar
44.1MW -25.1MVar
-42.1MW -8.8MVar
6
1.029p.u. -2.4°
-12.9MW -6.2MVar
55MW 15MVar
Load B
-43.4MW -10MVar
1.029p.u. -2.4°
7
-11.6MW -5MVar
55MW 15MVar
Load C
13MW -12.3MVar
11.7MW -11.6MVar
5
1.028p.u. -1.7°
-24.6MW 23.9MVar
TF_1
24.7MW -22.5MVar
1
1p.u. 0°
24.7MW -22.5MVar
G_1 (Reference gen)

Figure B.1: Test system with power flow results

Parameter	Description	L8-9	L9-10	L8-6	L6-5	L10-7	L7-5
u [kV]	Nominal voltage	230	230	230	230	230	230
r [Ω]	Resistance	4.496	6.295	16.928	5.29	20.631	8.993
x [Ω]	Reactance	38.088	53.323	85.169	44.965	89.93	48.668
b [μS]	Susceptance	281.66	395.08	578.45	332.7	676.75	298.69

Table B.2: Line parameters

Parameter	Description	G1	G2	G3
Type	Exciter type	IEEE AC4A	IEEE AC4A	IEEE AC4A
τ_b [s]	Filter time delay	10	10	10
τ_c [s]	Filter derivative time constant	1	1	1
K_a [/]	Controller Gain	200	200	200
τ_a [s]	Controller time constant	0,02	0,02	0,02
$V_{i,min}$ [p.u.]	Input signal minimum limiter	-10	-10	-10
$V_{i,max}$ [p.u.]	Input signal maximum limiter	10	10	10
$V_{r,min}$ [p.u.]	Control minimum output	-4.53	-4.53	-4.53
$V_{r,max}$ [p.u.]	Control maximum output	5.46	5.46	5.46
Parameter	Description	G1	G2	G3
Type	Governor type	IEEE HYGOV*	IEEE G1*	IEEE G1*

*Parameters as given in section A.3

Table B.3: Exciter and governor parameters

Parameter	Description	T1	T2	T3	T4
S [MVA]	Rated power	100	100	100	30
u_1 [kV]	Primary voltage	230	230	230	230
u_2 [kV]	Secondary voltage	16.5	18	13.8	13.8
u_k [%]	Short circuit voltage	12.5	13.18	10.04	10.1
u_{k0} [%]	Zero sequence short circuit voltage	3	4	3	3
P_c [kW]	Copper Losses	210	250	250	100
Parameter	Description	Load A	Load B	Load C	
P [MW]	Active power	55	55	55	
Q [MVar]	Reactive power	15	15	15	

Table B.4: Load and transformer parameters

B.2 Wind turbine model

Parameter	Description	Value
S [MVA]	Rated power	2
$v_{w,0}$ [m/s]	Nominal wind speed	12.24
$\omega_{m,0}$ [rad/s]	Nominal turbine speed	2
R [m]	Rotor radius	36
H_{gen} [s]	Generator inertia constant	1
H_{blade} [s]	Turbine inertia constant	4
K_s [s]	Stiffness coefficient	85
D_s [s]	Mutual damping coefficient	4

Table B.5: Aerodynamic parameters

Parameter	Description	Value
S [MVA]	Rated power	2
u [kV]	Nominal voltage	0.690
r_g [p.u.]	Grid filter resistance	0.003
x_g [p.u.]	Grid filter reactance	0.08

Table B.6: Wind turbine GSC parameters

B.3 HVDC model

The VSC HVDC model and parameters are based on the Hydro Quebec model within Matlab/Simulink [16].

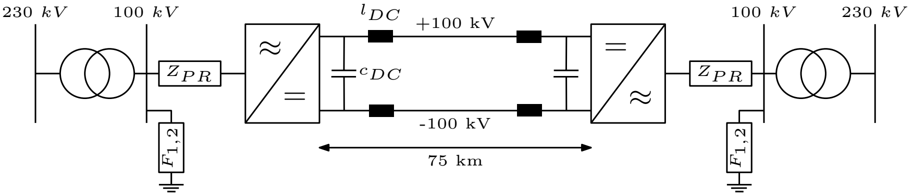

Figure B.2: HVDC link

Parameter	Description	Value
S [MVA]	Rated power	200
r [Ω/km]	DC cable resistance	$1.39{\cdot}10^{-2}$
l [H/km]	DC cable inductance	$1.59{\cdot}10^{-4}$
c [F/km]	DC cable capacitance	$2.31{\cdot}10^{-7}$
c_{DC} [F]	DC capacitor	$35{\cdot}10^{-6}$
l_{DC} [H]	DC reactor	$8{\cdot}10^{-3}$
l_{PR} [p.u.]	Phase reactor inductance	0.15
r_{PR} [p.u.]	Phase reactor resistance	0.0015
Filter F_1	Rated reactive power [MVAr]	18
	Resonance frequency [Hz]	1350
	Quality factor	15
Filter F_2	Rated reactive power [MVAr]	22
	Resonance frequency [Hz]	2700
	Quality factor	15

Table B.7: VSC HVDC link parameters [16]

Bibliography

[1] European Commision (EC), "EU energy in figures - statistical pocketbook 2016," EC, Tech. Rep., 2016.

[2] ——, "EU reference scenario 2016 - energy, transport and GHG emissions trends to 2050," EC, Tech. Rep., 2016.

[3] Eurostat. (2016) Energy statistics: Main indicators. [Online]. Available: http://ec.europa.eu/eurostat/en/data/database

[4] P. Anderson and A. Fouad, *Power System Control and Stability.* Wiley - IEEE Press, 2002.

[5] J. Soens, "Impact of wind energy in a future power grid," Ph.D. dissertation, Katholieke Universiteit Leuven, Belgium, 2005.

[6] E. Ørum, M. Kuivaniemi, M. Laasonen, A. Bruseth, E. Jansson, A. Danell, K. Elkington, and N. Modig, "Future system inertia," ENTSO-E, Tech. Rep., 2015.

[7] F. Milano, *Power System Modelling and Scripting.* Springer-Verlag Berlin Heidelberg, 2010.

[8] T. Van Cutsem and C. Vournas, *Voltage Stability of Electric Power Systems.* Springer, 1998.

[9] J. Rocabert, A. Luna, F. Blaabjerg, and P. Rodriguez, "Control of power converters in ac microgrids," *IEEE Transactions on Power Electronics*, vol. 27, no. 11, pp. 4734–4749, Nov 2012.

[10] R. Teodorescu, M. Liserre, and P. Rodriguez, *Grid converters for photovoltaic and wind power systems.* Wiley-IEEE, 2011.

[11] P. Rodriguez, A. Luna, I. Candela, R. Teodorescu, and F. Blaabjerg, "Grid synchronization of power converters using multiple second order

generalized integrators," in *2008 34th Annual Conference of IEEE Industrial Electronics*, Nov 2008, pp. 755–760.

[12] P. Zarina, S. Mishra, and P. Sekhar, "Exploring frequency control capability of a PV system in a hybrid PV-rotating machine-without storage system," *International Journal of Electrical Power & Energy Systems*, vol. 60, no. 0, pp. 258 – 267, 2014.

[13] ENTSO-E, "Network code on requirements for grid connection applicable to all generators (RfG)," ENTSO-E, Tech. Rep., 2016.

[14] G. C. Tarnowski, "Coordinated frequency control of wind turbines in power systems with high wind power penetration," Ph.D. dissertation, Technical University of Denmark, 2011.

[15] M. Bollen and F. Hassan, *Integration of distributed generation in the power system.* Wiley - IEEE Press, 2011.

[16] Mathworks. (2014) VSC-based HVDC transmission system. [Online]. Available: https://nl.mathworks.com/help/physmod/sps/powersys/ug/vsc-based-hvdc-link.html

[17] European Commision (EC). (2009) 2020 climate & energy package. [Online]. Available: https://ec.europa.eu/clima/policies/strategies/2020_en#tab-0-0

[18] ——. (2014) 2030 climate and energy goals for a competitive, secure and low-carbon EU economy. [Online]. Available: http://europa.eu/rapid/press-release_IP-14-54_en.htm

[19] EurObserv'ER, "Photovoltaic barometer," EurObserv'ER, Tech. Rep., 2017.

[20] ——, "Wind energy barometer," EurObserv'ER, Tech. Rep., 2017.

[21] B. Kroposki, B. Johnson, Y. Zhang, V. Gevorgian, P. Denholm, B. M. Hodge, and B. Hannegan, "Achieving a 100% renewable grid: Operating electric power systems with extremely high levels of variable renewable energy," *IEEE Power and Energy Magazine*, vol. 15, no. 2, pp. 61–73, March 2017.

[22] ENTSO-E, "Ten-year network development plan 2016: executive report," ENTSO-E, Tech. Rep., 2016.

[23] J. Beerten, "Modeling and control of DC grids," Ph.D. dissertation, KU Leuven, 2013.

[24] P. Buijs, D. Bekaert, S. Cole, D. Van Hertem, and R. Belmans, “Transmission investment problems in Europe: Going beyond standard solutions,” *Energy Policy*, vol. 39, no. 3, pp. 1794 – 1801, 2011.

[25] D. Van Hertem and M. Ghandhari, “Multi-terminal VSC HVDC for the European supergrid: Obstacles,” *Renewable and Sustainable Energy Reviews*, vol. 14, no. 9, pp. 3156 – 3163, 2010.

[26] ELIA ASSET, “Le projet alegro: Interconnexion entre la belgique et l’allemagne,” ELIA, Tech. Rep., 2016.

[27] J. Mrosik, “Ultranet: The energytransition in Germany (Amprion, Siemens and Transnet BW),” Siemens, Tech. Rep., 2016.

[28] K. M. Rippel, A. Preuß, M. Meinecke, and R. König, “Netzentwicklungsplan strom 2030 - offshore-netzentwicklungsplan 2030: Zahlen, daten und fakten,” 50Hertz, Amprion, TenneT and Transnet, Tech. Rep., 2017.

[29] D. Van Hertem, O. Gomis-Bellmunt, and J. Liang, *HVDC Grids: For Offshore and Supergrid of the Future.* Wiley-IEEE Press, 2016.

[30] Eurelectric (Working Group on Security of Electricity Supply), “Security of electricity supply: Roles, responsibilities and experiences within the eu,” Eurelectric, Tech. Rep., 2006.

[31] R. Serway, R. Beichner, and J. Jewett, *Physics for Scientists and Engineers.* Holt Rinehart & Winston, 2000.

[32] P. Kundur, *Power System Stability and Control.* New York, US: McGraw-Hill, 1994.

[33] J. Machowski, J. Bialek, and J. Dumby, *Power system dynamics: stability and control.* Wiley, 2009.

[34] P. Tielens and D. Van Hertem, “Grid inertia and frequency control in power systems with high penetration of renewables,” in *Young Researcher Symposium Delft*, April 2012, pp. 1–6.

[35] P. Daly, N. Cunniffe, and D. Flynn, “Inertia considerations within unit commitment and economic dispatch for systems with high non-synchronous penetrations,” in *IEEE Power Tech*, June 2015, pp. 1–6.

[36] J. Driesen and K. Visscher, “Virtual synchronous generators,” in *Power and Energy Society General Meeting - Conversion and Delivery of Electrical Energy in the 21st Century, 2008 IEEE*, July 2008, pp. 1–3.

[37] J. Morren, S. De Haan, and J. Ferreira, “Contribution of DG units to primary frequency control,” in *Future Power Systems, 2005 International Conference on*, November 2005, pp. 1–6.

[38] H. Bevrani, T. Ise, and Y. Miura, “Virtual synchronous generators: A survey and new perspectives,” *International Journal of Electrical Power & Energy Systems*, vol. 54, pp. 244 – 254, 2014.

[39] J. Morren, “Grid support by power electronic converters of distributed generation units,” Ph.D. dissertation, TU Delft, 2006.

[40] B. Rawn and P. Lehn, “Wind rotor inertia and variable efficiency: fundamental limits on their exploitation for inertial response and power system damping,” in *EWEC-conference*, March 2008, pp. 1–10.

[41] W. Stevenson and J. Grainger, *Power System Analysis.* New York, US: McGraw-Hill, 1994.

[42] E. W. Kimbark, *Power System Stability.* Wiley-IEEE, 1995.

[43] W. Winter, K. Elkington, G. Bareux, and J. Kostevc, “Pushing the limits: Europe’s new grid: Innovative tools to combat transmission bottlenecks and reduced inertia,” *Power and Energy Magazine, IEEE*, vol. 13, no. 1, pp. 60–74, January 2015.

[44] W. Kramer, S. Chakraborty, B. Kroposki, and H. Thomas, “Advanced power electronic interfaces for distributed energy systems,” NREL, Tech. Rep., 2008.

[45] M. Mahmoud and F. Al-Sunni, *Control and Optimization of Distributed Generation Systems.* Springer, 2013.

[46] G. Lalor, A. Mullane, and M. O’Malley, “Frequency control and wind turbine technologies,” *IEEE Transactions on Power Systems*, vol. 20, no. 4, pp. 1905–1913, 2005.

[47] A. Mullane and M. O’Malley, “The inertial response of induction-machine-based wind turbines,” *IEEE Transactions on Power Systems*, vol. 20, no. 3, pp. 1496–1503, 2005.

[48] I. Moore, “Inertial response from wind turbines,” Ph.D. dissertation, Cardiff University, 2012.

[49] T. Ackermann, *Wind power in power systems.* Chichester, UK: John Wiley & Sons, 2005.

[50] M. Kayikçi and J. Milanović, "Dynamic contribution of DFIG-Based wind plants to system frequency disturbances," *Power Systems, IEEE Transactions on*, vol. 24, no. 2, pp. 859–867, 2009.

[51] V. Akhmatov, "Variable-speed wind turbines with doubly-fed induction generators: Part I: Modelling in dynamic simulation tools," *Wind Engineering*, vol. 26, no. 2, pp. 85–108, 2002.

[52] Y. Lei, A. Mullane, G. Lightbody, and R. Yacamini, "Modeling of the wind turbine with a doubly fed induction generator for grid integration studies," *IEEE Transactions on Energy Conversion*, vol. 21, no. 1, pp. 257–264, 2006.

[53] A. Perdana, "Dynamic models of wind turbines: a contribution towards the establishment of standardized models of wind turbines for power system stability studies," Ph.D. dissertation, Chalmers university of technology, Sweden, 2008.

[54] N. R. Ullah, "Wind Power – Added Value for Network Operation," Ph.D. dissertation, Chalmers university of technology, Sweden, 2008.

[55] P. Fairley, "Europe replaces old wind farms," *IEEE Spectrum*, vol. 46, no. 1, pp. 13–13, Jan 2009.

[56] The European Wind Energy Association (EWEA), "Powering Europe : wind energy and the electricity grid," EWEA, Tech. Rep., 2010.

[57] S. Chandrasekaran, "Grid connected doubly fed induction generator based wind turbine under lvrt," Ph.D. dissertation, University of Bologna, 2014.

[58] C. W. Taylor, *Power system voltage stability.* McGraw-Hill Ryerson, 1994.

[59] IEA, "Energy efficiency roadmap for electric motors and motor systems," IEA (4E Energy Efficient End-use Equipment), Tech. Rep., 2015.

[60] J. V. Milanović, K. Yamashita, S. M. Villanueva *et al.*, "International industry practice on power system load modeling," *IEEE Transactions on Power Systems*, vol. 28, no. 3, pp. 3038–3046, 2013.

[61] A. R. Khatib, M. Appannagari, S. Manson, and S. Goodall, "Load modeling assumptions: What is accurate enough?" in *2015 IEEE Petroleum and Chemical Industry Committee Conference (PCIC)*, October 2015, pp. 1–9.

[62] T. Inoue, H. Taniguchi, Y. Ikeguchi, and K. Yoshida, “Estimation of power system inertia constant and capacity of spinning-reserve support generators using measured frequency transients,” *Power Systems, IEEE Transactions on*, vol. 12, no. 1, pp. 136–143, 1997.

[63] P. Wall, F. González-Longatt, and V. Terzija, “Demonstration of an inertia constant estimation method through simulation,” in *Universities Power Engineering Conference (UPEC), 2010 45th International*, Augustus 2010, pp. 1–6.

[64] ——, “Estimation of generator inertia available during a disturbance,” in *Power and Energy Society General Meeting, 2012 IEEE*, July 2012, pp. 1–8.

[65] P. Wall and V. Terzija, “Simultaneous estimation of the time of disturbance and inertia in power systems,” *IEEE Transactions on Power Delivery*, vol. 29, no. 4, pp. 2018–2031, 2014.

[66] P. M. Ashton, C. S. Saunders, G. A. Taylor, A. M. Carter, and M. E. Bradley, “Inertia estimation of the GB power system using synchrophasor measurements,” *IEEE Transactions on Power Systems*, vol. 30, no. 2, pp. 701–709, 2015.

[67] D. Chassin, Z. Huang, M. Donnelly, C. Hassler, E. Ramirez, and C. Ray, “Estimation of wecc system inertia using observed frequency transients,” *Power Systems, IEEE Transactions on*, vol. 20, no. 2, pp. 1190–1192, 2005.

[68] A. Girgis and W. Peterson, “Adaptive estimation of power system frequency deviation and its rate of change for calculating sudden power system overloads,” *Power Delivery, IEEE Transactions on*, vol. 5, no. 2, pp. 585–594, 1990.

[69] P. Kundur, J. Paserba, V. Ajjarapu, G. Andersson, A. Bose, C. Canizares, N. Hatziargyriou, D. Hill, A. Stankovic, C. Taylor, T. Van Cutsem, and V. Vittal, “Definition and classification of power system stability IEEE/CIGRE joint task force on stability terms and definitions,” *Power Systems, IEEE Transactions on*, vol. 19, no. 3, pp. 1387–1401, 2004.

[70] S. Cole, “Steady-state and duynamic modelling of vsc hvdc systems for power system simulation,” Ph.D. dissertation, KU Leuven, 2010.

[71] M. Pavella, D. Ernst, and D. Ruiz-Vega, *Transient stability of power systems: A unified approach to assessment and control.* Springer Science & Business Media, 2000.

[72] M. Gibbard, P. Pourbeik, and D. Vowles, *Small-signal stability, control and dynamic performance of power systems.* University of Adelaide Press, 2015.

[73] M. Reza, “Stability analysis of transmission systems with high penetration of distributed generation,” Ph.D. dissertation, TU Delft, 2006.

[74] Y. Xue and M. Pavella, “Extended equal-area criterion: an analytical ultra-fast method for transient stability assessment and preventive control of power systems,” *International Journal of Electrical Power & Energy Systems*, vol. 11, no. 2, pp. 131 – 149, 1989.

[75] T. Wijnhoven, “Evaluation of fault current contribution strategies by converter based distributed generation,” Ph.D. dissertation, KU Leuven, 2015.

[76] N. W. Miller, “Keeping it together: Transient stability in a world of wind and solar generation,” *IEEE Power and Energy Magazine*, vol. 13, no. 6, pp. 31–39, November 2015.

[77] D. Gautam, V. Vittal, and T. Harbour, “Impact of increased penetration of DFIG-Based wind turbine generators on transient and small signal stability of power systems,” *Power Systems, IEEE Transactions on*, vol. 24, no. 3, pp. 1426–1434, 2009.

[78] A. Mitra and D. Chatterjee, “A sensitivity based approach to assess the impacts of integration of variable speed wind farms on the transient stability of power systems,” *Renewable Energy*, vol. 60, no. 0, pp. 662 – 671, 2013.

[79] M. Nunes, J. Peças Lopes, H. Zurn, U. Bezerra, and R. Almeida, “Influence of the variable-speed wind generators in transient stability margin of the conventional generators integrated in electrical grids,” *Energy Conversion, IEEE Transactions on*, vol. 19, no. 4, pp. 692–701, 2004.

[80] S. De Rijcke, H. Ergun, D. Van Hertem, and J. Driesen, “Grid impact of voltage control and reactive power support by wind turbines equipped with direct-drive synchronous machines,” *Sustainable Energy, IEEE Transactions on*, vol. 3, no. 4, pp. 890–898, 2012.

[81] S. Eftekharnejad, V. Vittal, G. Heydt, B. Keel, and J. Loehr, “Impact of increased penetration of photovoltaic generation on power systems,” *Power Systems, IEEE Transactions on*, vol. 28, no. 2, pp. 893–901, 2013.

[82] B. Tamimi, C. Canizares, and K. Bhattacharya, “System stability impact of large-scale and distributed solar photovoltaic generation: The case of

ontario, canada," *Sustainable Energy, IEEE Transactions on*, vol. 4, no. 3, pp. 680–688, 2013.

[83] R. Shah, N. Mithulananthan, R. Bansal, and V. Ramachandaramurthy, "A review of key power system stability challenges for large-scale PV integration," *Renewable and Sustainable Energy Reviews*, vol. 41, no. 0, pp. 1423 – 1436, 2015.

[84] P. Kundur, K. Morrison, J. Paserba *et al.*, *The Electric Power Engineering Handbook.* IEEE - CRC Press, 2001, ch. Power system dynamics and stability, pp. 1–34.

[85] P. Kundur, N. J. Balu, and M. G. Lauby, *Power system stability and control.* McGraw-hill New York, 1994.

[86] J. Slootweg and W. Kling, "The impact of large scale wind power generation on power system oscillations," *Electric Power Systems Research*, vol. 67, no. 1, pp. 9 – 20, 2003.

[87] D. Vowles, C. Samarasinghe, M. Gibbard, and G. Ancell, "Effect of wind generation on small-signal stability: A New Zealand example," in *Power and Energy Society General Meeting - Conversion and Delivery of Electrical Energy in the 21st Century, 2008 IEEE*, July 2008, pp. 1–8.

[88] S. Yuanzhang, W. Lixin, L. Guojie, and L. Jin, "A review on analysis and control of small signal stability of power systems with large scale integration of wind power," in *Power System Technology (POWERCON), 2010 International Conference on*, October 2010, pp. 1–6.

[89] P. G. Bueno, J. C. Hernández, and F. J. Ruiz-Rodriguez, "Stability assessment for transmission systems with large utility-scale photovoltaic units," *IET Renewable Power Generation*, vol. 10, no. 5, pp. 584–597, 2016.

[90] R. H. Byrne, R. J. Concepcion, J. Neely, F. Wilches-Bernal, R. T. Elliott, O. Lavrova, and J. E. Quiroz, "Small signal stability of the western North American power grid with high penetrations of renewable generation," in *2016 IEEE 43rd Photovoltaic Specialists Conference (PVSC)*, June 2016, pp. 1784–1789.

[91] EURELECTRIC - ENTSO-E, "Deterministic frequency deviations: root causes and proposals for potential solutions," EURELECTRIC - ENTSO-E, Tech. Rep., 2011.

[92] H. Bevrani, *Robust Power System Frequency Control.* Springer US, 2009.

[93] S. Prabakaran and G. Pradeep, "A study on turbine blade fatigue protection," in *Power Systems Conference (NPSC), 2014 Eighteenth National*, December 2014, pp. 1–4.

[94] IEEE, "Guide for abnormal frequency protection for power generating plants," *ANSI/IEEE Std C37.106-1987*, 1987.

[95] G. Lalor, J. Ritchie, D. Flynn, and M. J. O'Malley, "The impact of combined-cycle gas turbine short-term dynamics on frequency control," *IEEE Transactions on Power Systems*, vol. 20, no. 3, pp. 1456–1464, 2005.

[96] H. A. Bauman, G. R. Hahn, and C. N. Metcalf, "The effect of frequency reduction on plant capacity and on system operation [includes discussion]," *Transactions of the American Institute of Electrical Engineers. Part III: Power Apparatus and Systems*, vol. 73, no. 2, 1954.

[97] ENTSO-E, "Continental Europe operation handbook," ENTSO-E, Tech. Rep., 2009.

[98] Nordel, "The nordic grid code 2007 (nordic collection of rules)," Nordel, Tech. Rep., 2007.

[99] M. Milligan, P. Donohoo, D. Lew, E. Ela, B. Kirby, H. Holttinen, E. Lannoye, D. Flynn, M. O Malley, N. Miller *et al.*, "Operating reserves and wind power integration: an international comparison," in *9th international workshop on large-scale integration of wind power into power systems*, July 2010.

[100] S. De Rijcke, "Dynamic grid support by wind farms: Potential of rotating kinetic energy," Ph.D. dissertation, KU Leuven, 2014.

[101] ENTSO-E, "Operation reserve ad hoc team report: final version," ENTSO-E, Tech. Rep., 2012.

[102] T. Ackermann, N. Martensen, T. Brown *et al.*, "Scaling up variable renewable power: the role of grid codes," IRENA, Tech. Rep., 2016.

[103] ENTSO-E, "ENTSO-E network code on emergency and restoration," ENTSO-E, Tech. Rep., 2015.

[104] B. Genet, "Implementation EU netwerk code: Topic frequency management," ELIA, Tech. Rep., 2016.

[105] ENTSO-E, "Netwerk code for requirements for grid connection applicable to all generators: requirements in the context of present practices," ENTSO-E, Tech. Rep., 2012.

[106] EirGrid, “Eirgrid grid code v6.0,” EirGrid, Tech. Rep., 2015.

[107] D. Wenzhong Gao, E. Muljadi, W. Wang *et al.*, “Comparison of standards and technical requirements of grid-connected wind power plants in China and the United States,” NREL, Tech. Rep., 2016.

[108] ENTSO-E, “Dispersed generation impact on Continental Europe region security,” ENTSO-E, Tech. Rep., 2014.

[109] L. Young, “A collation of international policies for under-frequency load shedding,” Transpower, Tech. Rep., 2009.

[110] IEEE, “IEEE guide for the application of protective relays used for abnormal frequency load shedding and restoration,” *IEEE Std C37.117-2007*, pp. 1–55, Aug 2007.

[111] J. Vieira, W. Freitas, W. Xu, and A. Morelato, “Efficient coordination of rocof and frequency relays for distributed generation protection by using the application region,” *Power Delivery, IEEE Transactions on*, vol. 21, no. 4, pp. 1878–1884, 2006.

[112] W. Freitas, W. Xu, C. Affonso, and Z. Huang, “Comparative analysis between ROCOF and vector surge relays for distributed generation applications,” *Power Delivery, IEEE Transactions on*, vol. 20, no. 2, pp. 1315–1324, 2005.

[113] H. Kazemi Kargar and J. Mirzaei, “New method for islanding detection of wind turbines,” in *2nd International Power and Energy Conference*, December 2008, pp. 1633–1637.

[114] L. Ruttledge and D. Flynn, “Short-term frequency response of power systems with high non-synchronous penetration levels,” *Wiley Interdisciplinary Reviews: Energy and Environment*, vol. 4, no. 5, pp. 452–470, 2015.

[115] ENTSO-E, “Frequency stability evaluation criteria for the synchronous zone of Continental Europe (requirements and impact factors),” ENTSO-E, Tech. Rep., 2016.

[116] Eirgrid, System Operator for Northern Ireland (SONI), “ROCOF modification proposal - TSOs’ recommendations,” EirGrid, SONI, Tech. Rep., 2012.

[117] The Commision for Energy Regulation (CER), “Rate of change of frequency (ROCOF) modification to the grid code,” CER, Tech. Rep., 2014.

[118] Eirgrid, System Operator for Northern Ireland (SONI), “DS3 Joint Grid Code Working Group Position Paper on ROCOF,” EirGrid, SONI, Tech. Rep., 2012.

[119] P. Pourbeik, R. Boyer, K. Chan, G. Chown *et al.*, “Dynamic models for turbine-governors in power system studies,” IEEE, Tech. Rep., 2013.

[120] J. Riesz, “The future power system security program,” AEMO, Tech. Rep., 2016.

[121] Statnett. The nordlink cable to Germany. [Online]. Available: http://www.statnett.no/en/Projects/NORDLINK/

[122] N. Miller, M. Shao, S. Pajic, and R. D’Aquila, “Eastern frequency response study,” NREL, Tech. Rep., 2013.

[123] ——, “Western wind and solar integration study phase 3: Frequency response and transient stability,” NREL, Tech. Rep., 2014.

[124] REserviceS, “Economic grid support services by wind and solar PV,” REserviceS, Tech. Rep., 2014.

[125] J. Van de Vyver, J. D. M. De Kooning, B. Meersman, L. Vandevelde, and T. L. Vandoorn, “Droop control as an alternative inertial response strategy for the synthetic inertia on wind turbines,” *IEEE Transactions on Power Systems*, vol. 31, no. 2, pp. 1129–1138, 2016.

[126] S. Achilles and M. Pöller, “Direct drive synchronous machine models for stability assessment of wind farms,” in *Proc. of 4th International workshop on large-scale integration of wind farms*, October 2003, pp. 1–6.

[127] G. Michalke, A. Hansen, and T. Hartkopf, “Control strategy of a variable speed wind turbine with multipole permanent magnet synchronous generator,” in *Proc. European Wind Energy Conference and Exhibition 2007 (EWEC 2007)*, May 2007, pp. 1–6.

[128] A. D. Hansen and G. Michalke, “Modelling and control of variable-speed multi-pole permanent magnet synchronous generator wind turbine,” *Wind Energy*, vol. 11, no. 5, pp. 537–554, 2008.

[129] D. Ramasubramanian, Z. Yu, R. Ayyanar, V. Vittal, and J. Undrill, “Converter model for representing converter interfaced generation in large scale grid simulations,” *IEEE Transactions on Power Systems*, vol. 32, no. 1, pp. 765–773, 2017.

[130] P. Rodriguez, A. Luna, R. S. Muñoz-Aguilar, I. Etxeberria-Otadui, R. Teodorescu, and F. Blaabjerg, "A stationary reference frame grid synchronization system for three-phase grid-connected power converters under adverse grid conditions," *IEEE Transactions on Power Electronics*, vol. 27, no. 1, pp. 99–112, 2012.

[131] P. Rodriguez, A. Luna, R. Teodorescu, and F. Blaabjerg, "Grid synchronization of wind turbine converters under transient grid faults using a double synchronous reference frame PLL," in *2008 IEEE Energy 2030 Conference*, November 2008, pp. 1–8.

[132] P. Rodriguez, L. Sainz, and J. Bergas, "Synchronous double reference frame PLL applied to a unified power quality conditioner," in *10th International Conference on Harmonics and Quality of Power*, October 2002, pp. 614–619.

[133] P. Jayamaha, "Energy storage for frequency support in weak electrical grids," Ph.D. dissertation, The University of Nottingham, 2015.

[134] D. W. P. Thomas and M. S. Woolfson, "Evaluation of frequency tracking methods," *IEEE Transactions on Power Delivery*, vol. 16, no. 3, pp. 367–371, 2001.

[135] H. A. Darwish and M. Fikri, "Practical considerations for recursive dft implementation in numerical relays," *IEEE Transactions on Power Delivery*, vol. 22, no. 1, pp. 42–49, 2007.

[136] M. S. Padua, S. M. Deckmann, G. S. Sperandio, F. P. Marafao, and D. Colon, "Comparative analysis of synchronization algorithms based on PLL, RDFT and kalman filter," in *2007 IEEE International Symposium on Industrial Electronics*, June 2007, pp. 964–970.

[137] T. Lobos and J. Rezmer, "Real-time determination of power system frequency," *IEEE Transactions on Instrumentation and Measurement*, vol. 46, no. 4, pp. 877–881, 1997.

[138] A. H. Norouzi and A. M. Sharaf, "Two control schemes to enhance the dynamic performance of the statcom and sssc," *IEEE Transactions on Power Delivery*, vol. 20, no. 1, pp. 435–442, 2005.

[139] A. A. A. Radwan and Y. A. R. I. Mohamed, "Power synchronization control for grid-connected current-source inverter-based photovoltaic systems," *IEEE Transactions on Energy Conversion*, vol. 31, no. 3, pp. 1023–1036, 2016.

[140] S. I. Nanou and S. A. Papathanassiou, “Grid code compatibility of vsc-hvdc connected offshore wind turbines employing power synchronization control,” *IEEE Transactions on Power Systems*, vol. 31, no. 6, pp. 5042–5050, 2016.

[141] *EC 61400-27-1*, International Electrotechnical Commission Std.

[142] A. Hansen, C. Jauch, P. Sørensen *et al.*, “Dynamic wind turbine models in power system simulation tool digsilent,” Technical University of Denmark, Tech. Rep., 2004.

[143] A. Hansen, I. Margaris, G. Tamowski, and F. Iov, “Simplified type 4 wind turbine modeling for future ancillary services,” in *European Wind Energy Conference & Exhibition*, February 2013.

[144] O. Anay-Lara, N. Jenkins, J. Ekanayake *et al.*, *Wind energy generation: modeling and control.* Wiley, 2009.

[145] J. Morren, J. Pierik, and S. W. de Haan, “Inertial response of variable speed wind turbines,” *Electric Power Systems Research*, vol. 76, no. 11, pp. 980 – 987, 2006.

[146] T. Littler, B. Fox, and D. Flynn, “Measurement-based estimation of wind farm inertia,” in *Power Tech, 2005 IEEE Russia*, June 2005, pp. 1–5.

[147] L. Holdsworth, J. B. Ekanayake, and N. Jenkins, “Power system frequency response from fixed speed and doubly fed induction generator-based wind turbines,” *Wind Energy*, vol. 7, no. 1, pp. 21–35, 2004.

[148] M. S. El Moursi, W. Xiao, and J. L. Kirtley, “Fault ride through capability for grid interfacing large scale pv power plants,” *IET Generation, Transmission Distribution*, vol. 7, no. 9, pp. 1027–1036, 2013.

[149] M. J. Hossain, M. A. Mahmud, H. R. Pota, and N. Mithulananthan, “Design of non-interacting controllers for PV systems in distribution networks,” *IEEE Transactions on Power Systems*, vol. 29, no. 6, pp. 2763–2774, 2014.

[150] SMA, “PV inverter residential: datasheet overview,” SMA Solar Technology AG, Tech. Rep., 2006.

[151] R. H. Renner and D. Van Hertem, “Potential of using DC voltage restoration reserve for HVDC grids,” *Electric Power Systems Research*, vol. 134, pp. 167 – 175, 2016.

[152] J. Beerten, O. Gomis-Bellmunt, X. Guillaud, J. Rimez, A. van der Meer, and D. Van Hertem, “Modeling and control of HVDC grids: A key challenge for the future power system,” in *2014 Power Systems Computation Conference*, Augustus 2014, pp. 1–21.

[153] V. Trovato, S. H. Tindemans, and G. Strbac, “Demand response contribution to effective inertia for system security in the GB 2020 gone green scenario,” in *IEEE PES ISGT Europe 2013*, October 2013, pp. 1–5.

[154] W. Gu, W. Liu, C. Shen, and Z. Wu, “Multi-stage underfrequency load shedding for islanded microgrid with equivalent inertia constant analysis,” *International Journal of Electrical Power & Energy Systems*, vol. 46, pp. 36 – 39, 2013.

[155] V. Knap, S. K. Chaudhary, D. I. Stroe, M. Swierczynski, B. I. Craciun, and R. Teodorescu, “Sizing of an energy storage system for grid inertial response and primary frequency reserve,” *IEEE Transactions on Power Systems*, vol. 31, no. 5, pp. 3447–3456, 2016.

[156] G. Delille, B. Francois, and G. Malarange, “Dynamic frequency control support by energy storage to reduce the impact of wind and solar generation on isolated power system’s inertia,” *Sustainable Energy, IEEE Transactions on*, vol. 3, no. 4, pp. 931–939, 2012.

[157] M. Swierczynski, D. I. Stroe, A. I. Stan, R. Teodorescu, R. Laerke, and P. C. Kjaer, “Field tests experience from 1.6MW/400kWh li-ion battery energy storage system providing primary frequency regulation service,” in *IEEE PES ISGT Europe 2013*, October 2013, pp. 1–5.

[158] P. Tielens, S. De Rijcke, K. Srivastava, M. Reza, A. Marinopoulos, and J. Driesen, “Frequency support by wind power plants in isolated grids with varying generation mix,” in *Power and Energy Society General Meeting, 2012 IEEE*, July 2012, pp. 1–8.

[159] J. Conroy and R. Watson, “Frequency response capability of full converter wind turbine generators in comparison to conventional generation,” *Power Systems, IEEE Transactions on*, vol. 23, no. 2, pp. 649–656, 2008.

[160] Y. Wang, G. Delille, H. Bayem, X. Guillaud, and B. Francois, “High wind power penetration in isolated power systems - assessment of wind inertial and primary frequency responses,” *Power Systems, IEEE Transactions on*, vol. 28, no. 3, pp. 2412–2420, 2013.

[161] N. R. Ullah, T. Thiringer, and D. Karlsson, “Temporary primary frequency control support by variable speed wind turbines,” *IEEE Transactions on Power Systems*, vol. 23, no. 2, pp. 601–612, 2008.

[162] S. Engelken, A. Mendonca, and M. Fischer, “Inertial response with improved variable recovery behaviour provided by type 4 WTs,” *IET Renewable Power Generation*, vol. 11, no. 3, pp. 195–201, 2017.

[163] F. Hafiz and A. Abdennour, “Optimal use of kinetic energy for the inertial support from variable speed wind turbines,” *Renewable Energy*, vol. 80, pp. 629 – 643, 2015.

[164] D. Deroost, P. Tielens, K. S. Srivastava, G. Velotto, and D. Van Hertem, “Analysis and coordination of delivering inertial response by wind power plants,” in *Wind Integration Workshop Brussels*, September 2015.

[165] M. F. M. Arani and Y. A. R. I. Mohamed, “Analysis and mitigation of undesirable impacts of implementing frequency support controllers in wind power generation,” *IEEE Transactions on Energy Conversion*, vol. 31, no. 1, pp. 174–186, 2016.

[166] Y. Li, Z. Xu, and K. P. Wong, “Advanced control strategies of pmsg-based wind turbines for system inertia support,” *IEEE Transactions on Power Systems*, vol. PP, no. 99, pp. 1–1, 2016.

[167] F. Diaz-Gonzalez, M. Hau, A. Sumper, and O. Gomis-Bellmunt, “Participation of wind power plants in system frequency control: Review of grid code requirements and control methods,” *Renewable and Sustainable Energy Reviews*, vol. 34, pp. 551 – 564, 2014.

[168] R. G. de Almeida and J. A. P. Lopes, “Participation of doubly fed induction wind generators in system frequency regulation,” *IEEE Transactions on Power Systems*, vol. 22, no. 3, pp. 944–950, 2007.

[169] N. Karami, N. Moubayed, and R. Outbib, “General review and classification of different MPPT techniques,” *Renewable and Sustainable Energy Reviews*, vol. 68, Part 1, pp. 1 – 18, 2017.

[170] M. Dreidy, H. Mokhlis, and S. Mekhilef, “Inertia response and frequency control techniques for renewable energy sources: A review,” *Renewable and Sustainable Energy Reviews*, vol. 69, pp. 144 – 155, 2017.

[171] Y. Pipelzadeh, B. Chaudhuri, and T. C. Green, “Control coordination within a VSC HVDC link for power oscillation damping: A robust decentralized approach using homotopy,” *IEEE Transactions on Control Systems Technology*, vol. 21, no. 4, pp. 1270–1279, 2013.

[172] Y. Phulpin, “Communication-free inertia and frequency control for wind generators connected by an HVDC-link,” *IEEE Transactions on Power Systems*, vol. 27, no. 2, pp. 1136–1137, 2012.

[173] J. Zhu, C. D. Booth, G. P. Adam, A. J. Roscoe, and C. G. Bright, “Inertia emulation control strategy for VSC-HVDC transmission systems,” *IEEE Transactions on Power Systems*, vol. 28, no. 2, pp. 1277–1287, 2013.

[174] A. Junyent-Ferr, Y. Pipelzadeh, and T. C. Green, “Blending HVDC-Link energy storage and offshore wind turbine inertia for fast frequency response,” *IEEE Transactions on Sustainable Energy*, vol. 6, no. 3, pp. 1059–1066, 2015.

[175] L. Ruttledge and D. Flynn, “Emulated inertial response from wind turbines: Gain scheduling and resource coordination,” *IEEE Transactions on Power Systems*, vol. 31, no. 5, pp. 3747–3755, 2016.

[176] P. Fairley. (2016) Can synthetic inertia from wind power stabilize grids? [Online]. Available: http://spectrum.ieee.org/energywise/energy/renewables/can-synthetic-inertia-stabilize-power-grids

[177] L. Ruttledge and D. Flynn, “Co-ordination of frequency responsive wind plant in future power systems,” in *Renewable Power Generation Conference (RPG 2013), 2nd IET*. IET, 2013, pp. 1–4.

[178] J. Morren, S. W. H. De Haan, W. Kling, and J. Ferreira, “Wind turbines emulating inertia and supporting primary frequency control,” *IEEE Transactions on Power Systems*, vol. 21, no. 1, pp. 433–434, 2006.

[179] R. De Almeida and J. Peças Lopes, “Participation of doubly fed induction wind generators in system frequency regulation,” *IEEE Transactions on Power Systems*, vol. 22, no. 3, pp. 944–950, 2007.

[180] G. Ramtharan, J. Ekanayake, and N. Jenkins, “Frequency support from doubly fed induction generator wind turbines,” *IET Renewable Power Generation*, vol. 1, no. 1, pp. 3–9, 2007.

[181] S. De Rijcke, P. Tielens, B. Rawn, D. Van Hertem, and J. Driesen, “Trading energy yield for frequency regulation: Optimal control of kinetic energy in wind farms,” *Power Systems, IEEE Transactions on*, vol. 30, no. 5, pp. 2469–2478, 2015.

[182] S. Boyd and L. Vandenberghe, *Convex Optimisation.* Cambridge University Press, 2004.

[183] T. G. Hovgaard, S. Boyd, and J. B. Jørgensen, “Model predictive control for wind power gradients,” *Wind Energy*, vol. 18, no. 6, pp. 991–1006, 2015.

[184] M. Grant and S. Boyd, "Graph implementations for nonsmooth convex programs," in *Recent Advances in Learning and Control*, ser. Lecture Notes in Control and Information Sciences, V. Blondel, S. Boyd, and H. Kimura, Eds. Springer-Verlag Limited, 2008, pp. 95–110.

[185] M. Grant and S. Boyd, "CVX: Matlab software for disciplined convex programming, version 2.1," http://cvxr.com/cvx, Mar. 2014.

[186] M. Soltani, R. Wisniewski, P. Brath, and S. Boyd, "Load reduction of wind turbines using receding horizon control," in *2011 IEEE International Conference on Control Applications (CCA)*, September 2011, pp. 852–857.

[187] M. Harris, M. Hand, and A. Wright, "Lidar for turbine control," National Renewable Energy Laboratory (NREL), Tech. Rep., 2006.

[188] R. K. Newsom, L. K. Berg, W. J. Shaw, and M. L. Fischer, "Turbine-scale wind field measurements using dual-doppler lidar," *Wind Energy*, vol. 18, no. 2, pp. 219–235, 2015.

[189] M. Yu, A. J. Roscoe, A. Dysko, C. D. Booth, R. Ierna, J. Zhu, and H. Urdal, "Instantaneous penetration level limits of non-synchronous devices in the british power system," *IET Renewable Power Generation*, vol. 11, no. 8, pp. 1211–1217, 2017.

[190] D. Van Hertem, "The use of power flow controlling devices in the liberalized market," Ph.D. dissertation, KU Leuven, 2009.

[191] L. Sainz, J. J. Mesas, L. Monjo, J. Pedra, and M. Cheah-Mané, "Electrical resonance instability study in wind power plants," in *2016 Electric Power Quality and Supply Reliability (PQ)*, Augustus 2016, pp. 139–144.

[192] M. Zhao, X. Yuan, J. Hu, and Y. Yan, "Voltage dynamics of current control time-scale in a vsc-connected weak grid," *IEEE Transactions on Power Systems*, vol. 31, no. 4, pp. 2925–2937, 2016.

[193] J. Z. Zhou, H. Ding, S. Fan, Y. Zhang, and A. M. Gole, "Impact of short-circuit ratio and phase-locked-loop parameters on the small-signal behavior of a VSC-HVDC converter," *IEEE Transactions on Power Delivery*, vol. 29, no. 5, pp. 2287–2296, 2014.

[194] D. Dong, B. Wen, D. Boroyevich, P. Mattavelli, and Y. Xue, "Analysis of phase-locked loop low-frequency stability in three-phase grid-connected power converters considering impedance interactions," *IEEE Transactions on Industrial Electronics*, vol. 62, no. 1, pp. 310–321, 2015.

[195] A. Egea-Alvarez, S. Fekriasl, F. Hassan, and O. Gomis-Bellmunt, "Advanced vector control for voltage source converters connected to weak grids," *IEEE Transactions on Power Systems*, vol. 30, no. 6, pp. 3072–3081, 2015.

[196] L. Harnefors, M. Bongiorno, and S. Lundberg, "Input-admittance calculation and shaping for controlled voltage-source converters," *IEEE Transactions on Industrial Electronics*, vol. 54, no. 6, pp. 3323–3334, 2007.

[197] B. Wen, D. Boroyevich, R. Burgos, P. Mattavelli, and Z. Shen, "Analysis of D-Q small-signal impedance of grid-tied inverters," *IEEE Transactions on Power Electronics*, vol. 31, no. 1, pp. 675–687, 2016.

[198] M. Cheah-Mane, J. Liang, N. Jenkins, and L. Sainz, "Electrical resonance instability study in hvdc-connected offshore wind power plants," in *2016 IEEE Power and Energy Society General Meeting (PESGM)*, July 2016, pp. 1–5.

[199] L. Harnefors, L. Zhang, and M. Bongiorno, "Frequency-domain passivity-based current controller design," *IET Power Electronics*, vol. 1, no. 4, pp. 455–465, 2008.

[200] J. Sun, "Impedance-based stability criterion for grid-connected inverters," *IEEE Transactions on Power Electronics*, vol. 26, no. 11, pp. 3075–3078, 2011.

[201] D. Dong, B. Wen, P. Mattavelli, D. Boroyevich, and Y. Xue, "Grid-synchronization modeling and its stability analysis for multi-paralleled three-phase inverter systems," in *2013 Twenty-Eighth Annual IEEE Applied Power Electronics Conference and Exposition (APEC)*, March 2013, pp. 439–446.

[202] J. A. Suul, S. D'Arco, P. Rodrìguez, and M. Molinas, "Impedance-compensated grid synchronisation for extending the stability range of weak grids with voltage source converters," *IET Generation, Transmission & Distribution*, vol. 10, pp. 1315–1326(11), 2016.

[203] S. D'Arco, J. A. Suul, and O. B. Fosso, "A virtual synchronous machine implementation for distributed control of power converters in smartgrids," *Electric Power Systems Research*, vol. 122, pp. 180 – 197, 2015.

[204] C. Pelczar, "Mobile virtual synchronous machine for vehicle-to-grid applications," Ph.D. dissertation, Clausthal University of Technology, 2012.

[205] Q.-C. Zhong, Z. Ma, W.-L. Ming, and G. C. Konstantopoulos, “Grid-friendly wind power systems based on the synchronverter technology,” *Energy Conversion and Management*, vol. 89, pp. 719 – 726, 2015.

[206] L. Zhang, “Modeling and control of VSC HVDC links connected to weak AC systems,” Ph.D. dissertation, Royal Institute of Technology (KTH), 2010.

[207] S. D’Arco and J. A. Suul, “Virtual synchronous machines-classification of implementations and analysis of equivalence to droop controllers for microgrids,” in *2013 IEEE Grenoble Conference*, June 2013, pp. 1–7.

[208] H. Xin, L. Huang, L. Zhang, Z. Wang, and J. Hu, “Synchronous instability mechanism of P-f droop-controlled voltage source converter caused by current saturation,” *IEEE Transactions on Power Systems*, vol. 31, no. 6, pp. 5206–5207, 2016.

[209] W. Rowen, “Simplified mathematical representations of heavy-duty gas turbines,” *Journal of Engineering for Power*, vol. 105, pp. 865–869, 1983.

[210] ——, “Simplified mathematical representations of single shaft gas turbines in mechanical drive service,” in *Turbo Expo: Power for Land, Sea, and Air*, June 1992.

[211] A. Bagnasco, B. Delfino, G. B. Denegri, and S. Massucco, “Management and dynamic performances of combined cycle power plants during parallel and islanding operation,” *IEEE Transactions on Energy Conversion*, vol. 13, no. 2, pp. 194–201, 1998.

[212] L. Meegahapola and D. Flynn, *Gas Turbine Modelling for Power System Dynamic Simulation Studies.* Springer International Publishing, 2014, pp. 175–195.

List of publications

Reviewed journals

[1] **P. Tielens** and D. Van Hertem, "Receding Horizon Control of Wind Power to Provide Frequency Regulation," *IEEE Transactions on Power Systems*, vol. 32, no.4, pp. 2663-2672, 2017.

[2] **P. Tielens** and D. Van Hertem, "The Relevance of Inertia in Power Systems," *Renewable and Sustainable Energy Reviews*, vol. 55, pp. 999-1009, 2016.

[3] S. De Rijcke, **P. Tielens**, B. Rawn, D. Van Hertem and J. Driesen, "Trading Energy Yield for Frequency Regulation: Optimal Control of Kinetic Energy in Wind Farms," *IEEE Transactions on Power Systems*, vol. 30, no. 5, pp. 2469-2478, 2014.

[4] W. Leterme, **P. Tielens**, S. De Boeck and D. Van Hertem, "Overview of Grounding and Configuration Options for Meshed HVDC grids," *IEEE Transactions on Power Delivery*, vol. 29, no. 6, pp. 2467-2475, 2014.

International conferences

[1] M. Abedrabbo, M. Wang, **P. Tielens**, F. Dejene, W. Leterme, J. Beerten and D. Van Hertem, "Impact of DC grid contingencies on AC system stability," *13th IET International Conference on AC and DC Power Transmission (ACDC 2017)*, Manchester, February 2017, pp. 1-7.

[2] **P. Tielens** and D. Van Hertem, "Influence of system wide implementation of virtual inertia on small-signal stability," *2016 IEEE International Energy Conference (ENERGYCON)*, Leuven, April 2016, pp. 1-6.

[3] J. N. Sakamuri, **P. Tielens**, D. Kaushik, M. Altin, N. A. Cutululis, A. Hansen and D. Van Hertem, “Improved frequency control from wind power plants considering wind speed variation, ” *2016 Power Systems Computation Conference (PSCC)*, Genoa, June 2016, pp. 1-7.

[4] D. Deroost, **P. Tielens**, K. Srivastava, G. Velotto and D. Van Hertem, “Analysis and coordination of delivering inertial response by wind power plants, ” *Wind Integration Workshop*, Brussels, October 2015, pp. 1-6.

[5] J. Verveckken, F. Geth, B. Hunyadi, J. Beerten, N. Leemput, J. Van Roy, **P. Tielens**, V. De Smedt, S. Iacovella, N. Koolen, H. De Clercq, J. Driesen, G. Gielen, R. Puers, J. Vandewalle, S. Van Huffel, R. Belmans, G. Deconinck and W. Dehaene, “Developing engineering-oriented educational workshops within a student branch,” *Eurocon 2013*, Zagreb, July 2013, pp. 933-940.

[6] F. Geth, J. Verveckken, N. Leemput, J. Van Roy, J. Beerten, **P. Tielens**, V. De Smedt, S. Iacovella, B. Hunyadi, N. Koolen, H. De Clercq, G. Gielen, R. Puers, S. Van Huffel, R. Belmans, G. Deconinck, W. Dehaene and J. Driesen, “Development of an open-source smart energy house for K-12 education,” *2013 IEEE Power & Energy Society General Meeting*, Vancouver, BC, July 2013, pp. 1-5.

[7] S. De Boeck, **P. Tielens**, W. Leterme and D. Van Hertem, “Configurations and earthing of HVDC grids,” *2013 IEEE Power & Energy Society General Meeting*, Vancouver, BC, July 2013, pp. 1-5.

[8] **P. Tielens**, H. Ergun and D. Van Hertem, “Techno-economic Analysis of Large-scale Integration of Solar Power Plants in the European Grid,” *International Solar Integration Workshop*, Lisbon, November 2012, pp. 1-6.

[9] **P. Tielens** and D. Van Hertem, “Grid Inertia and Frequency Control in Power Systems with High Penetration of Renewables,” *Young Researchers Symposium in Electrical Power Engineering*, Delft, April 2012, pp. 1-6.

[10] **P. Tielens**, S. De Rijcke, K. Srivastava, M. Reza, A. Marinopoulos and J. Driesen, “Frequency Support by Wind Power Plants in Isolated Grids with Varying Generation Mix,” *2012 IEEE Power & Energy Society General Meeting*, San Diego, July 2012, pp.1-8.

[11] Nguyen Tuan Anh, D. Van Hertem, **P. Tielens** and J. Driesen, “Damping controller design of TCSC based on wide-area monitoring and supplement torque components,” *2012 IEEE International Energy Conference and Exhibition (ENERGYCON)*, Florence, September 2012, pp. 401-407.

Curriculum Vitae

Pieter Tielens
Born July 28, 1988 in Genk, Belgium.

2000 - 2006	Secondary School Science - Mathematics (8h) St.-Jan Berchmansinstituut, Zonhoven
2006 - 2011	Master of Science in Engineering: Energy Katholieke Universiteit Leuven
2011 - 2017	PhD in Engineering Science University of Leuven (KU Leuven) Department of Electrical Engineering (ESAT) Division of Electrical Energy and Computer Architectures (ELECTA)

FACULTY OF ENGINEERING SCIENCE
DEPARTMENT OF ELECTRICAL ENGINEERING
ELECTA
Kasteelpark Arenberg 10 B2445
B-3001 Heverlee
http://www.esat.kuleuven.be/electa